Università degli Studi di Bologna

Facoltà di Scienze Matematiche Fisiche e Naturali
Dottorato di Ricerca in Fisica, XVII Ciclo

Development and applications of algorithms for the analysis of Remote-Sensing measurements in the Atmosphere

Dr. Elisa Castelli

Advisors

Prof. Rolando Rizzi

Dr. Bianca Maria Dinelli

PhD Coordinator

Prof. Roberto Soldati

Bologna, Italy, March 2005

Università degli Studi di Bologna
Facoltà di Scienze Matematiche Fisiche e Naturali

Consiglio Nazionale delle Ricerche - Bologna
Istituto di Scienze dell'Atmosfera e del Clima

PhD Thesis
by
Dr. Elisa Castelli

March 2005

Introduction

SAFIRE-A (Spectroscopy of the Atmosphere using Far InfraRed Emission—Airborne) is a high-resolution Fourier transform spectrometer that performs limb sounding observations of atmospheric emission in the Far-Infrared spectral region, for the measurement of volume mixing ratio profiles of several stratospheric constituents. The instrument was integrated onboard the high-flying research aircraft M55 Geophysica within the framework of the Airborne Polar Experiment (APE).
SAFIRE-A observes the atmospheric spectrum with high spectral resolution through the far-infrared, where many of the trace gases, playing a major role in atmospheric chemistry, have important emission features. A scientific code for the routine analysis of the middle infrared emission spectra measured by SAFIRE-A (the Retrieval Algorithm for SAFIRE-RAS), was initially developed by Dr B.M.Dinelli of the institute ISAC (CNR-Bologna) where this thesis has been developed. The objective for which SAFIRE-A and RAS were developed is to perform the measurement of the volume mixing ratio profiles of H_2O, O_3, HNO_3, N_2O, ClO, HCl and H_2O.
The final goal of the RAS code was the operational analysis of the measurements performed by the SAFIRE-A instrument.
However, before applying a scientific code to operational analysis, several preliminary steps had to be performed: the code had to be validated, some improvements deriving from new insights in atmospheric spectroscopy had to be implemented and retrieval diagnostic tools had to be developed.
The subject of this thesis was the transformation of the RAS code from a scientific to an operational code and the analysis of several observation campaigns performed by the SAFIRE-A instrument.
An overview of the chapters of this thesis is reported below.

Chapter 1 provides a brief and general introduction to the remote sensing of the Earth's atmosphere with spectroscopic techniques.

Chapter 2 describes the SAFIRE-A instrument, with its measurement requirements and its main scientific objectives.

Chapter 3 In this chapter it is possible to find a description of the M55-Geophysica aircraft along with the on-board scientific instrumentation and the performed measurement campaigns. The APE-GAIA (Airborne Polar Experiment-Geophysica Aircraft in Antarctica) and ENVISAT (ENVironmental SATellite) Validation Campaign are described in more details.

Chapter 4 discusses the inverse problem theory which is required in the case of indirect measurements as for SAFIRE-A. The inverse methods describe the mathematical procedures which allow to obtain the wanted parameters from the measured data. An overview of the Averaging Kernel (AK) computation and of the retrieval quality parameters calculation is also given.

Chapter 5 provides the description of the models developed for the analysis of the SAFIRE-A spectra. A description of the features implemented into the code and of the input necessary for the retrieval procedure is reported here.

Chapter 6 describes the code validation activities carried out, and the development of new features implemented into the code. The validation activity is composed of two part. In the first part, an internal validation was performed: simulated spectra allow for the retrieval process to be started with an initial guess of the parameters perturbed by a known amount with respect to the values used to produce the synthetic spectra. The second part of the validation is a comparison of the spectra simulated by the RAS forward model and spectra simulated by a forward model code for a new instrument operating in the millimetre-wave region. In order to perform this comparison some update and modifications to the code were

necessary. The last part of the chapter reports the two new features implemented into the code: the pointing angle retrieval and the averaging kernel calculation. Some examples of the application of these features are also given.

Chapter 7 discusses the analysis of the data collected during two of the flights part of the APE-GAIA Campaign, held in Terra del Fuoco, Argentina in 1999 to observe the Antarctic polar vortex. The obtained profiles are compared with other measurements obtained by instruments onboard the Geophysica, in order to validate the SAFIRE-A results. These results are used to give an interpretation of the atmospheric scenario and of the chemical processes encountered in the lower polar stratosphere during the flights.

Chapter 8 reports the results of the data analysis for two of the flights part of the ENVISAT Validation Campaign, one performed at mid-latitude (Forli', Italy), and the other at high latitude (Kiruna, Sweden). A validation of the obtained profiles is carried out using measurements obtained by instruments onboard the Geophysica or assimilated measurements. The obtained results for O_3 and HNO_3 are compared with spatially and temporally coincident MIPAS-ENVISAT (Michelson Interferometer for Passive Atmospheric Sounding – ENVIronmental SATellite) profiles. For the mid-latitude flight, a further comparison of the two sets of measurements using trajectory calculation is also performed.

Chapter 1: Remote Sensing of the Atmosphere

The purpose of this chapter is to provide a brief introduction to the remote sensing of the Earth's atmosphere with spectroscopic techniques. The spectroscopy of the atmosphere consists in observing a large continuous portion of the atmospheric spectrum and using it either to identify the presence and the amount of specific molecular species in the atmospheric region under study, or to infer its physical characteristics.
The importance of the atmosphere surrounding the Earth has not been completely understood for a long time. So there was very little knowledge about its fundamental role in sustaining life on Earth and shaping the conditions of our existence. Until about 1950, it was assumed that the mean state of the atmosphere was stable, well balanced and not likely to be significantly affected by anthropogenic activity. Thanks to the accelerated development of new sounding methods and to the improvement in the sensitivity of the detectors and in the analytical capabilities, our knowledge of the atmospheric composition has considerably improved: it has not just become more detailed, but it has also revealed the complex interactions among different molecular species as well as their behaviour in the presence of solar radiation.
The chemical composition of the Earth's atmosphere varies to a large degree with local physical conditions, and therefore depends on recurring events such as diurnal, seasonal and solar cycles. At least 40 different molecular species have been identified as part of the atmospheric mixture. Together these gases control the global radiative and dynamical fields that dictate the characteristic physical conditions encountered on the Earth's surface (for example some act as a shield against harmful solar UV radiation, some other as a thermal blanket insulating the Earth from cold space). There are also gases present only as a result of human activities that can affect the atmospheric balance.
Nowadays the chemical composition and variability of the atmosphere in terms of latitude, longitude, altitude and time dependence is studied by progressively more sophisticated and sensitive techniques which provide global coverage, simultaneous measurements of many species, absolute concentration determinations and temporal variations.

1.1 Global composition and structure of the Atmosphere

The Earth's atmosphere is a gaseous envelope surrounding the planet. Like other planetary atmospheres, the Earth's atmosphere plays a central role in transfers of energy between the sun and the planet's surface and from one region of the globe to another; these transfers maintain thermal equilibrium and determine the planet's climate. However, the Earth's atmosphere is unique in that it is related closely to the oceans and to the surface processes, which, together with the atmosphere form the basis for life [1].
The Earth's atmosphere consists of a mixture of gases, mostly molecular nitrogen (78% by volume) and molecular oxygen (21% by volume); (see Table 1.1). Water vapour, carbon dioxide, and ozone, along with other minor constituents, comprise the remaining 1% of the atmosphere. Although they appear in very small abundance, trace species like water vapour and ozone play a key role in the energy balance of the Earth through their involvement in radiative processes. Because they are created and destroyed in particular regions and are closely linked to the circulation through transport, these and others minor species are highly variable. In addition, the atmosphere also contains various solid and liquid particles such as aerosols, water drops and ice crystals which are highly variable in space and time. These particles suspended in the atmosphere play an important role in absorption and scattering of solar radiation and in the physics of clouds and precipitation.

Constituent	Tropospheric mixing ratio[d]	Vertical distribution (mixing ratio)	Controlling processes
N_2	0.7808	Homogeneous	Vertical mixing
O_2	0.2095	Homogeneous	Vertical mixing
H_2O[b]	<0.030	Highly variable	Evaporation, condensation, transport, production by CH_4 oxidation
Ar	0.0093	Homogeneous	Vertical mixing
CO_2[b]	345 ppmv	Homogeneous	Vertical mixing, production by surface and anthropogenic processes
O_3[b]	10 ppmv[c]	Increases sharply in stratosphere, highly variable	Photochemical production in stratosphere, destruction at surface transport
CH_4[b]	1.6 ppmv	Homogeneous in troposphere, decreases in middle atmosphere	Production by surface processes, oxidation produces H_2O
N_2O[b]	350 ppbv	Homogeneous in troposphere, decreases in middle atmosphere	Production by surface and anthropogenic processes, dissociation in middle atmosphere, produces NO transport
CO[b]	70 ppbv	Decreases in troposphere, increases in stratosphere	Production antropogenically and by oxidation of CH_4 transport
NO[b]	0.1 ppbv[c]	Increases vertically	Production by dissociation of N_2O catalytic destruction of O_3
CFC-11[b]	0.2 ppbv	Homogeneuos in troposphere, decreases in stratosphere	Industrial production, mixing in troposphere, phototdissociation in stratosphere
CFC-12[b]	0.3 ppbv		

[a]Constituents are listed with volume mixing ratios representative of the Troposphere or Stratosphere, how the latter are distributed vertically, and controlling processes.
[b]Radiatively active.
[C]Stratospheric value.
[d]Mixing ratio = The fixed proportions in which two or more substances may become combined, such as the amount of nitrogen in the air compared to the rest of the air. Atmospheric scientists routinely discuss the gas phase concentrations of trace components in mixing ratios expressed in ratios of VOLUMES, as ppmv= Parts Per Million by Volume.

Table 1.1 Atmospheric Composition[a].

The starting point for describing atmospheric behaviour is the ideal gas law

$$\begin{aligned} pV &= nR^*T \\ &= \frac{m}{M}R^*T \\ &= mRT \end{aligned} \tag{1.1}$$

which constitutes the equation of state for a pure (single component) gas. In equation (1.1) p, T, and M denote the pressure, temperature, and molar weight of the gas, respectively, and *V, m*, and *n=m/M* refer to the volume, mass, and molar abundance of an air parcel, while *R** is the universal gas constant. An equivalent form of the ideal gas law that does not depend on the dimension of the system is

$$p = \rho RT \tag{1.2}$$

where ρ is the density of the gas.
By confining mass to a shallow layer above the Earth's surface, gravity exerts a profound influence on atmospheric behaviour. If vertical accelerations are ignored, Newton's second law of motion applied to the column of air between some level at pressure *p* and a level at *p+dp* (Figure 1.1) reduces to a balance between the weight of that column and the net pressure force acting on it

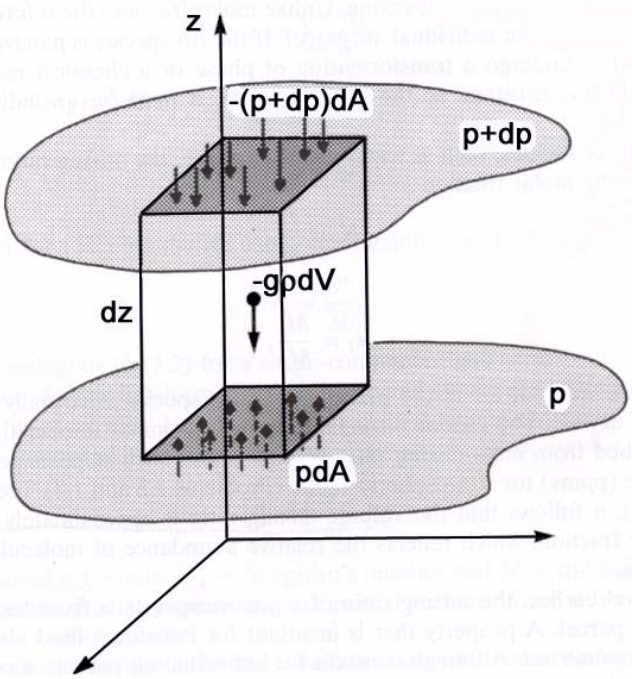

Figure 1.1: Hydrostatic balance for an incremental atmospheric column of cross-sectional area *dA* and height *dz*, bounded vertically by isobaric surfaces at pressures *p* and *p+dp*.

$$pdA - (p + dp)dA = \rho g dV \tag{1.3}$$

where g denotes the acceleration of gravity

$$-dpdA = \rho g dV \tag{1.4}$$

And from Figure 1.1

$$dV = dAdz \tag{1.5}$$

and finally

$$\frac{dp}{dz} = -\rho g \tag{1.6}$$

Known as *hydrostatic equilibrium*, this simple form of mechanical equilibrium is a good approximation even if the atmosphere is in motion because vertical displacements of air and their time derivatives are small compared to the forces in (1.6).
The compressibility of air makes the density in (1.6) dependent on the pressure through the gas law. Substituting ρ through eq. (1.2) and integrating from the surface to an altitude z yields

$$\frac{p}{p_s} = \exp\left[-\int_{z_s}^{z} \frac{dz'}{H(z')} \right] \tag{1.7}$$

where

$$H(z) = \frac{RT(z)}{g} \tag{1.8}$$

is the scale height and p_s is the surface pressure. As illustrated in equation (1.7), global-mean pressure and density decrease with altitude approximately exponentially. Above 100 km pressure and density also decrease exponentially, but at a rate which differs from that below (heterosphere). The distinct change of behaviour near 100 km marks a transition in the processes controlling the stratification of mass and the composition of air.

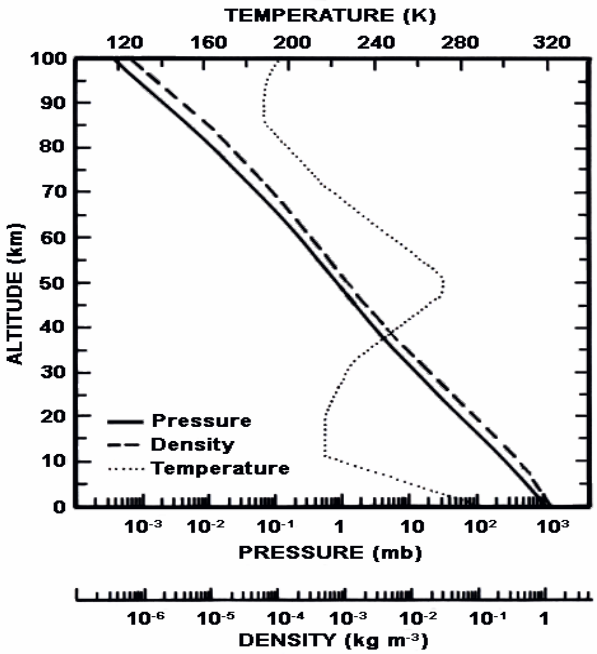

Figure 1.2: Global mean pressure (solid), density (dashed), and temperature (dotted), as functions of altitude. Source: U.S. Standard Atmosphere (1976).

The well-mixed region below 100 km is known as the homosphere and processes within it form the primary focus of this chapter.

The atmosphere is classified according to its thermal structure, which determines the dynamical properties of individual regions.

The atmosphere can be considered as made up of four layers on the basis of its vertical temperature profile (Figure 1.3): *troposphere, stratosphere, mesosphere* and *thermosphere*. The intermediate altitude regions (tops of these layers) where the temperature is approximately constant, are respectively called tropopause, stratopause and mesopause.

The troposphere (which means "turning sphere" and symbolizes the convective overturning that characterize this region) extends from the surface of the Earth to the tropopause at the approximate altitude of 18 km in the tropics, 12 km at mid-latitudes, and 6 to 8 km near the poles; it is characterised by a decrease of the mean temperature with increasing altitude with a typical decreasing rate of 6.5°C/km. This layer, which contains about 85-90% of the atmospheric mass, is often dynamically unstable with rapid vertical exchanges of energy and mass being associated with convective activity (globally the time constant for vertical exchanges is of the order of several weeks). Much of the variability observed in the atmosphere occurs within this layer.

Above the troposphere, through the transition region of the tropopause where the temperature is nearly constant, the atmosphere becomes very stable as the vertical temperature gradient reverses in a second atmospheric region: the stratosphere ("layered sphere"); this layer, which extends almost up to 50 km, contains 90% of the atmospheric ozone. Most of the ultraviolet radiation is absorbed by ozone, preventing this harmful radiation from reaching the Earth's surface, and increasing the temperature in this region. The stratopause separates the stratosphere from the mesosphere where the temperatures decrease with altitude from about 50 km to about 90 km; in this region dynamical instability occurs frequently and also rapid

vertical mixing is a typical phenomenon. Above about 90 km, in the so-called thermosphere, the temperature increases to reach maximum values that are strongly dependent on the level of solar activity. Here vertical exchanges associated with dynamical mixing become insignificant, instead molecular diffusion plays a major role by producing gravitational separation of species according to their molecular or atomic weight.

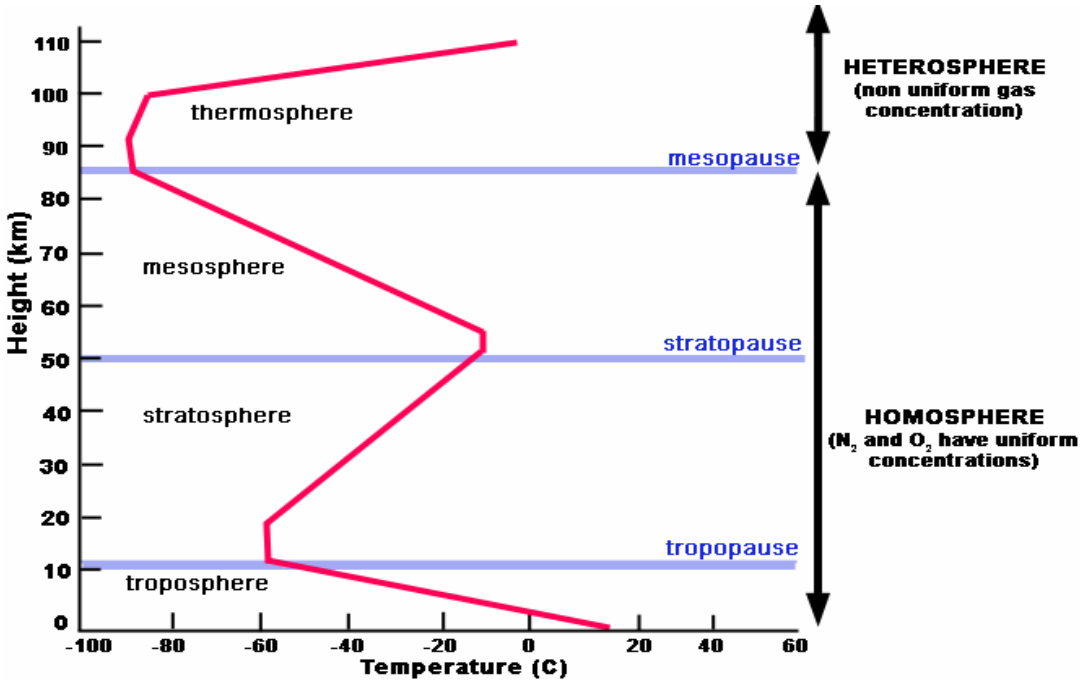

Figure 1.3: The vertical profile of the temperature (*temperature curve*) is typical of middle latitudes as defined in the U.S. Standard Atmosphere (1976). The name of each layer is also shown.

1.2 Observation techniques

The atmosphere can be investigated in situ, i.e. by bringing the instrument directly into the location where the measurements have to be performed (detailed reviews of these methods can be found in Gille [2] and Ehalt [3]). The atmosphere can also be sounded by remote sensing techniques, i.e. by instruments located at some distance from the air parcel to be studied; in this case the instruments allow global coverage and geographic variability though they suffer from some limitations in both spatial resolution and/or short-term variability.

Both remote sensing and in situ methods can be either passive or active; this distinction is due to the possible changes that the measurement technique does (active) or does not (passive) introduce in the observed sample of air.

Spectroscopy is a passive technique which provides an important tool to study the atmospheric chemistry. The spectrum of the atmosphere can be measured either in absorption (i.e. when the instrument observes how the atmosphere is transparent to the radiation coming from an external source) or in emission (i.e. when it observes the atmospheric signal itself). It contains features which are characteristics of its constituents and that can be thus used for their identification; furthermore the intensity of the observed features provides quantitative information on their amount. The features are due to electronic, vibrational and rotational transitions. Because of the relatively high energies usually associated with the electronic energy levels, the electronic spectra are typically observed in the visible and ultraviolet spectral regions (Figure 1.4); vibrational transitions within an electronic state (intermediate energies) are typically observed in the near and middle infrared and the pure rotational transitions within a vibrational state (low energies) in the far-infrared and microwave spectral regions (APPENDIX B).

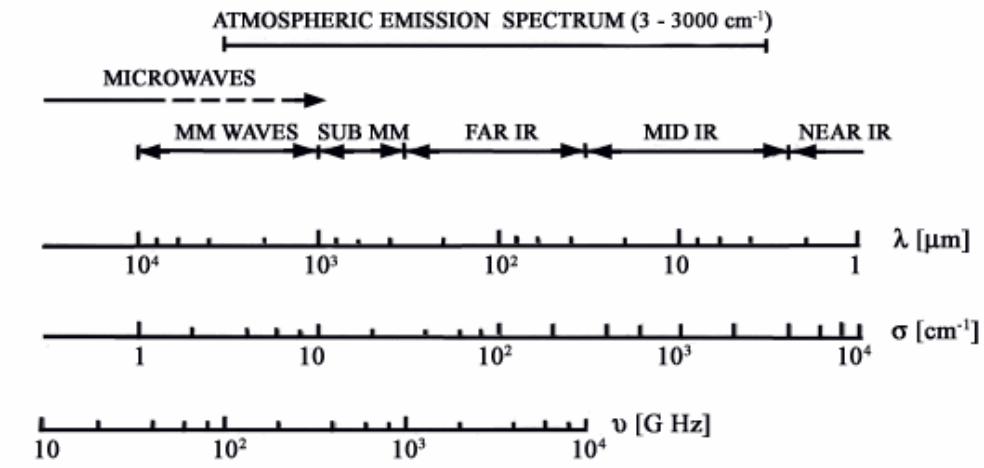

Figure 1.4: The spectral range in which the atmospheric emission spectrum shows significant features with indicated the conventional regions of the electromagnetic spectrum.

Because of the complex characteristics of the atmospheric environment no unique method-technique-instrument of investigation has the virtue to provide its complete characterisation in all its dimensions; therefore, the development of several complementary techniques is essential. Remote sensing with spectroscopic techniques has allowed to greatly increase our knowledge of the detailed composition and structure of the atmosphere. This coupling has been possible first of all thanks to the technological development (sensitive, fast-response detectors and compatible optical materials and fast computers); however it has been boosted by the emerging concern about the release of man-made chemicals in the atmosphere which could affect the atmospheric long-term stability and life condition in our planet.

1.2.1 Geometries and platforms

Different combinations of the observation platform (ground-based stations, high altitude platforms or satellites) and of the viewing geometry (vertical sounding or limb sounding) can be chosen, in principle, for remote sensing of the Earth's atmosphere.
Vertical sounding can be performed either from the ground, looking at the zenith, or from high altitude and space-borne platforms in nadir looking mode. Limb sounding measurements are possible from stratospheric balloon and aircraft, as well as from space, and generally provide a much higher vertical resolution with respect to vertical soundings. Each of these options offers specific advantages and disadvantages, as shown in Table 1.2, with limb sounding being particularly well suited for the study of upper tropospheric and lower stratospheric chemistry.
Vertical sounding can distinguish the contributions from different altitudes by exploiting the fact that the atmospheric spectral lines have a pressure (hence altitude) dependent line shape. Instruments with a very high spectral resolution are able to record the detailed shape of a spectral line: the signal in the far wings usually originates mainly from low altitudes, whereas the signal in the centre of the line from high altitudes. Therefore, by appropriate deconvolution methods the distribution of the constituent can be determined with a vertical resolution approximately equal to the atmospheric scale height. Two different looking directions can be used: *nadir* and *zenith*. Nadir vertical sounding measurements are possible from aircrafts, stratospheric balloons and satellites: the instrument is located on a floating platform and observes the atmosphere below so the signal-to-noise ratio is limited by the small contrast that exists between atmospheric and Earth's surface temperatures. In the case of zenith vertical soundings, the atmosphere is observed from below, either in emission or in absorption mode. In this case the background signal comes from the space and the narrow-

band signal from the farthest atmospheric layers may be covered by the near-field broadband signal.
Despite their wider spatial and temporal coverage, limb sounding observations from space have limited capability of capturing small scale features in the lowest altitude range. So, balloon and airborne instruments are usually the best choice for detailed investigations of the physical and chemical structure of the upper troposphere and lowermost stratosphere and for the study of local phenomena. There is not a unique view of which platform is the best: the operating altitude of large stratospheric balloons (approximately 40 km) is much higher than the maximum altitude reached by highflying aircraft (20 km) so balloon borne instruments offer a better altitude coverage for their measurements. On the other hand, the mobility and manoeuvrability of the aircraft, as well as the possibility of performing several flights within a relatively short time period cannot be obtained with balloon-borne instrumentation. Moreover, large scientific payload can be accommodated aboard an aircraft, making possible simultaneous measurements of several chemical compounds and other atmospheric parameters.

Geometry	Platform	Notes
Zenith	Ground based	only local measurements near station
Nadir	Space platform	global cover, low horizontal/vertical resolution
Nadir	Aircraft	high horizontal resolution, low vertical resolution
Limb	Space platform	global cover, low horizontal resolution
Limb	Aircraft/Balloon	optimal horizontal/vertical resolution for local phenomena

Table 1.2: Comparison between different observing platforms and geometries.

1.2.2 Limb sounding Technique

For remote sensing of the Earth's atmosphere, different combinations of the observation platform and of the viewing geometry can be used. In the limb sounding technique (Figure 1.5) the instrument is usually high up in the atmosphere and the line of sight is oriented below the horizontal direction, so that the Earth's surface is not reached and only the atmospheric limb is observed (at zenith angles[1] greater than 90°). The angle made by the Line Of Sight (LOS) with the horizontal direction is called the limb angle. In this way, the line of sight penetrates the atmosphere, and, after reaching a minimum altitude, that is called “tangent altitude” (h1 or h2), it emerges again to the open space (see Figure 1.5.a).
Limb sounding measurements generally maximise the observed signal and provide a good vertical resolution for the determination of vertical distributions, since in a spectrum relative to a given LOS the largest contribution to the signal is given by molecules near the *tangent point* (that is the minimum distance of the optical path from the Earth’s surface).
The spectra that are observed with the limb sounding geometry provide information about the composition of the atmosphere near the tangent altitude because the atmosphere has greater density at lower altitudes and because the optical path travels a long way at almost constant altitude near the tangent point. Therefore, measurements made with the limb sounding geometry are rather selective to the atmospheric composition at one specific altitude. A set of measurements performed at different limb angles (limb scanning sequence) provides information on the atmospheric composition at several altitudes and can then be used for the determination of the vertical distribution of the atmospheric composition. Various inverse procedures can be implemented (chapter 3) in order to retrieve the atmospheric composition as a function of altitude from the measured data [4].

[1] The zenith angle is defined as the angle between the zenith and the line of sight.

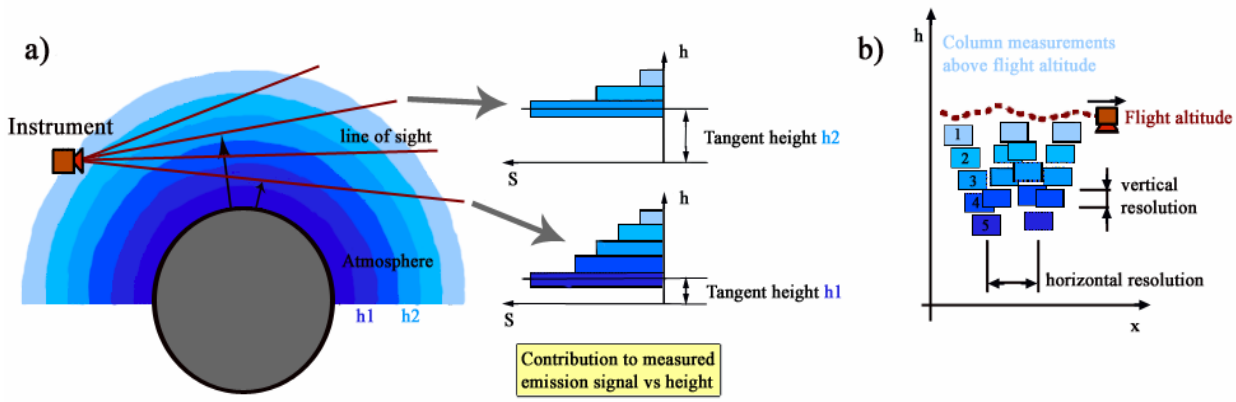

Figure 1.5: The limb sounding observation geometry. a) Vertical resolution. b) Horizontal resolution.

A drawback of a limb sounding measurement is the poor horizontal resolution along the viewing direction (typically about 500 km), due to the very long distances travelled by the line of sight in the atmosphere. To improve the horizontal resolution of airborne limb sounding instruments, the observations are made perpendicularly to the aircraft heading. In this case, the resolution along the flight path, as shown in Figure 1.5.b, is given by the product of the limb scanning sequence acquisition time and the aircraft ground speed and can be of fewer kilometres.

1.3 Emission and absorption measurements

Spectroscopic observations of the Earth's atmosphere can be performed either in emission, by observing the spontaneous thermal emission of the atmosphere, or in absorption by observing the attenuation of the signal of a bright external source like the sun or a star. In the latter case the source can either be observed directly or observed through the effect of radiation scattering. The atmospheric composition is derived from the spectroscopic features that the atmospheric constituents produce both in the emission and in the absorption spectra.

1.3.1 Absorption Spectroscopy of the atmosphere

Most of the high resolution spectroscopic observations, which have provided data for a large number of the infrared active constituents of the upper atmosphere, have been made in absorption (solar or stellar). The advantage of absorption spectroscopy is that a very bright source is exploited and spectra with very high signal-to-noise ratio can be obtained; unfortunately the measurements are constraint both in space and time: only the location of the observer can be used to improve the geographical coverage of these measurements and there is no way of improving the diurnal coverage (observations can only be made at two rather restrictive times of the day - sunset or sunrise). This makes almost impossible the study of diurnally varying species.

1.3.2 Emission Spectroscopy of the atmosphere

A number of chemical, dynamical and radiative processes, affecting the physical structure and the composition of the Earth's atmosphere, can be investigated by measuring spontaneous thermal emission of the atmospheric molecules. Emission spectroscopy benefits by a lot of advantages in comparison with other remote sensing methods [5], [6]. Being a passive technique, it does not introduce perturbations in the observed air masses and does not require energy demanding instruments. Moreover, emission measurements provide a better geographical and temporal coverage compared to absorption measurements. They do not need an external radiation source and can therefore be performed continuously (both at day and at night) in almost all the directions. This allows to overcome the poor latitude coverage of occultation measurements and makes it possible to monitor several key processes that involve

chemical species with a diurnal cycle. On the other hand, observations of the signal emitted by atmospheric molecules are only possible within the frequency range of the thermal emission of the atmosphere; this includes the middle/far infrared and the millimetrewave spectral regions. The boundaries of the operative range of emission measurements are defined by a low frequency cut-off (approx. 3 cm^{-1}) caused by the limits of optical instruments (to which this discussion is confined) and by a high frequency cut-off (approx. 3000 cm^{-1}) due to the low number of photons emitted by the atmosphere (Figure 1.4).

1.3.3 Spectral regions and units

Measurements can be made in a broad spectral range of the electromagnetic spectrum that is conventionally divided in regions with different names and where different units are often used for the measurement of either the frequency or the wavelength co-ordinate. Figure 1.4 provides a visual representation of the different intervals and of the different units. The wavelength is indicated with the letter λ and is measured in microns, the wavenumber is indicated with the letter σ and is measured in cm^{-1}, the frequency is indicated with the letter ν and is measured in GHz. The product λν is equal to the speed of light *c* measured in km/s (so that a wavelength of N micron corresponds to a frequency of $2.99792458 \cdot 10^5$/N GHz). The wavenumber is equal to the inverse of the wavelength measured in cm (a wavelength of x μm correspond to a wavenumber of (10^4/x) cm^{-1}). The region of atmospheric thermal emission corresponds to vibrorotational transitions (in the middle infrared) and rotational spectra (in the far infrared and sub-millimetre region). At longer wavelengths the spectroscopic features of atmospheric species are very rare, and weak and this explains the transparency of the atmosphere in the microwave regions and the possibility of using the microwaves for telecommunications. The millimetre region is an intermediate spectral region where only a few molecules of atmospheric interest have spectroscopic features, but at the same time the atmosphere is sufficiently transparent to allow observations at low altitudes [7].

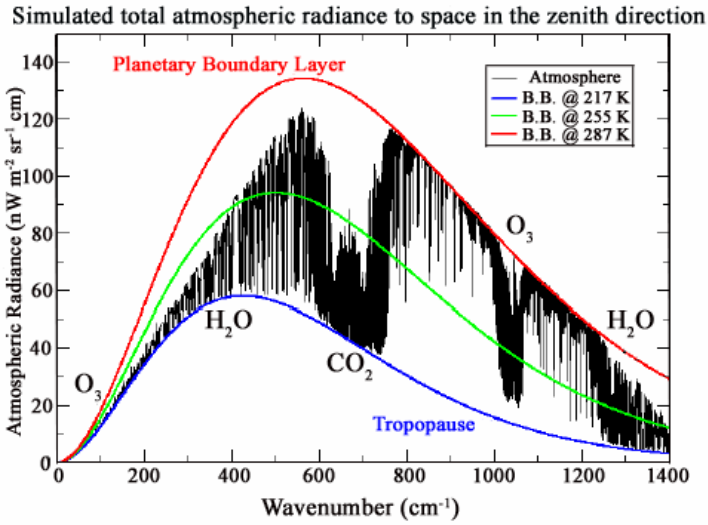

Figure 1.6: Simulated emission spectrum of the Earth's atmosphere in the zenith direction.

1.3.4 The Atmospheric emission spectrum

The emission spectrum of the Earth's atmosphere consists of spectral features that correspond to rotational and vibrational transitions of the atmospheric molecules (main gases and minor constituents). Pure rotational bands are associated to the millimetre (3-30 cm^{-1}) and the Far Infrared (FIR, 30-300 cm^{-1}) part of the spectrum, vibration bands to the Middle Infrared Region (MIR, 300-3000 cm^{-1}). The intensity envelope is given by the spectral distribution of a blackbody (indicated as B.B. in Figure 1.6) at the temperature of the emitting air masses (typically 250 K in the stratosphere), as shown in the figure below.

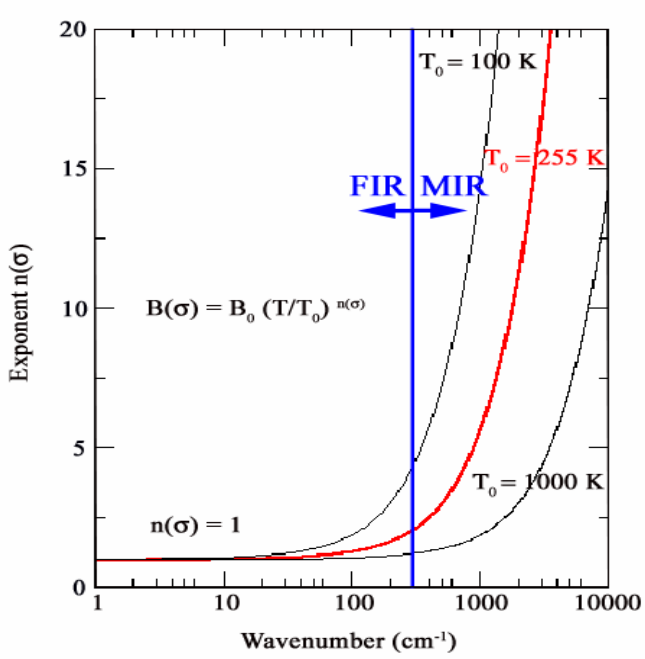

Figure 1.7: Temperature dependence of the Planck function.

The dependence of the Planck function $B(\sigma)$ on temperature can be expressed as a function of wavenumber σ according to the equation $B(\sigma)=c(\sigma)\ (T/T_0)^{n(\sigma)}$. If we plot the exponent $n(\sigma)$ versus the wavenumber σ we notice as this exponent is equal to 1 at low frequencies ($\sigma << 170\ cm^{-1}$) and increases greatly as the frequency is increased above that value (Figure 1.7). The emission in the MIR is, therefore, very sensitive to the atmospheric temperature. Temperature profiles can be retrieved with high accuracy by measuring the emission spectrum of a species with well known volume mixing ratio distribution. Conversely, a very good knowledge of the temperature profile is required for retrieving minor constituents concentration from emission measurements in the MIR. FIR measurements, on the other hand, have a weak dependence on temperature. From this perspective, measurements in the Far-infrared are relatively easier and can take advantage also from further aspects such as the freedom from scattering due to aerosols and clouds particles.

The complementarity of emission measurements in the MIR and FIR region can be recognised in the coverage of the chemical species. Apart from some main gases (for instance, water vapour and ozone), that have ubiquitous spectra in the infrared region, in the middle infrared it is possible to measure almost the entire nitrogen family, including the source gas N_2O and the important reservoir species $ClONO_2$. The detection of several compounds, that cannot be measured in the FIR, is also relatively easy in the MIR: for instance CO_2 NO_2 and CH_4 (which, having a dipole moment equal to zero, have not a pure rotational spectrum) or the chlorofluorocarbons. FIR remote sounders have their strength in the observation of the hydrogen family. (OH, HO_2, H_2O_2), but can also measure chlorine species (HCl, HOCl and ClO), bromine species (HBr, HOBr and BrO) and, even if with less sensitivity compared to the MIR, a few compounds of the nitrogen family (N_2O, HNO_3).

Chapter 2: The Instrument

SAFIRE-A (**S**pectroscopy of the **A**tmosphere using **F**ar **I**nfra**R**ed **E**mission—**A**irborne) is a high-resolution Fourier transform spectrometer (see APPENDIX A) that performs limb sounding observations of atmospheric emission in the Far-Infrared (FIR) spectral region for the measurement of volume mixing ratio (VMR) profiles of several stratospheric constituents from the tropopause to flight altitude (20 km for a high-altitude aircraft). The instrument was integrated onboard the high-flying research aircraft M55 Geophysica within the framework of the Airborne Polar Experiment (APE) and was flown, for the first time, as part of the M55 scientific payload during the Arctic campaign APE-POLECAT (Rovaniemi, Finland, Winter 1996–1997).

Figure 2.1: SAFIRE-A and the instrument onboard the M55 Geophysica.

2. SAFIRE-A

2.1 Instrument Structure

The mechanical structure of SAFIRE-A spectrometer consists of a box containing all the subsystems. The base plate of the box provides a rigid optical bench on which the optical components are assembled. This plate is suspended to the structure of the aircraft by means of three columns attached to the aircraft via antivibration mounts. The external walls of the box are made of honeycomb panels that limit the thermal and electromagnetic interference with the environment.

Dimensions	1800 mm X 800 mm X 650 mm
Weight	387 kg
Interferogram aquisition time	12, 24, 48, 96 s
Observation technique	Limb-sounding emission
Operating flight altitude	20 km
Field of view	0.57°
Optical channels	2
Spectral range	10-250 cm^{-1}
Spectral resolution	0.004 cm^{-1}

Table 2.1: SAFIRE-A Fourier Transform Spectrometer Specification.

Access to the instrument for ground operation is possible through a removable hatch on the left side of the aircraft. The instrument is installed in an unpressurized bay beneath the cockpit by suspension from the aircraft frame (see Figure 2.1). The viewing window is located on the right side of the aircraft with respect to the flight direction. A mechanical shutter in front of

the viewing port protects the input optics during ascent and descent and is opened by the pilot when the aircraft reaches the flight altitude.
In order to limit the possible cooling of the instrument during the flight, two heaters are mounted on the base plate. Mechanical vibrations are reduced by the antivibration mounts and acoustic noise, due to air turbulence entering the instrument cavity through the viewing port, is kept to a minimum by placing a limiting aperture at the focal plane of the input telescope [8].

2.2 Instrument Description

The instrument is a high spectral resolution Fourier transform spectrometer of the Martin-Puplett [9] type with a polarizing beamsplitter. The overall optical layout of the instrument is presented in Figure 2.2.
The atmosphere is viewed through a 200-by-40 mm open port located on the right side of the aircraft with respect to the flight direction. The atmospheric signal is collected by a flat limb-scanning mirror (M1 in Figure 2.2) that corrects for the aircraft roll and performs the limb-scan sequence.
An input telescope consisting of two confocal offaxis paraboloids (M2 and M3), provides a reduction in the solid angle of the interferometer relative to the solid angle of the atmospheric beam. An intermediate field stop located at the focal point of the telescope minimizes the thermal and turbulent exchange of atmospheric air between the instrument and the external environment.

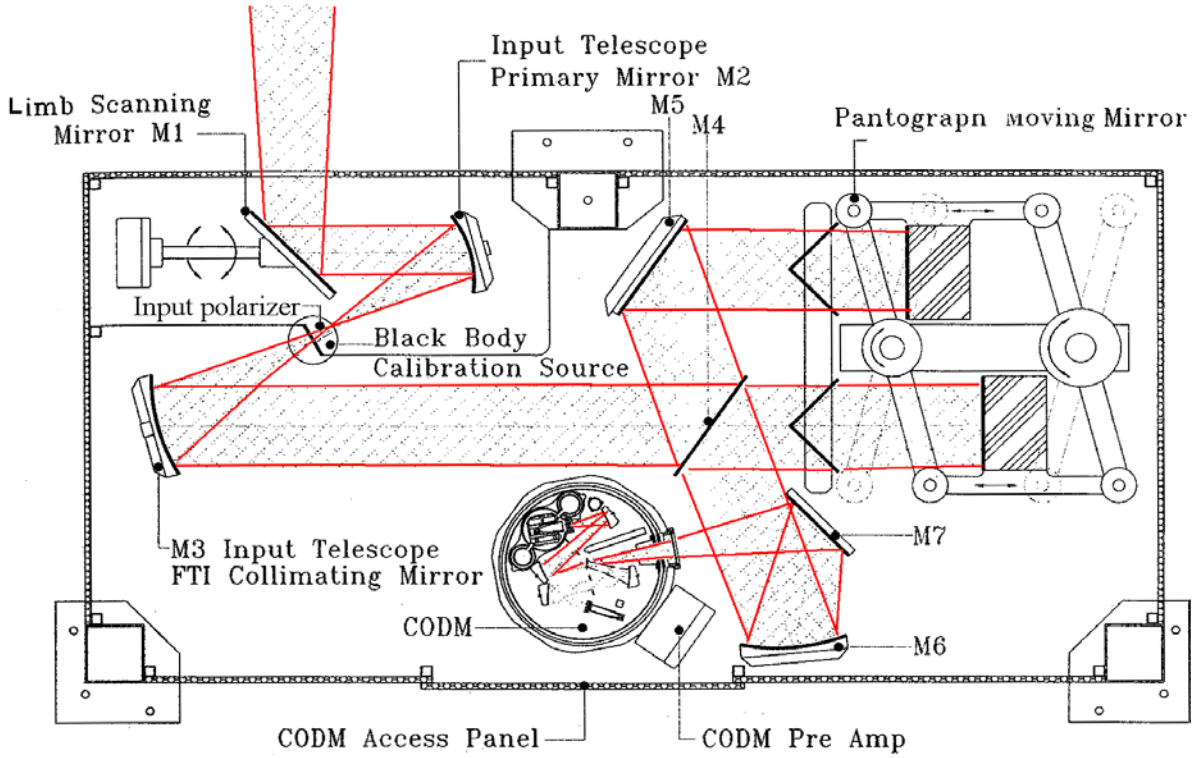

Figure 2.2: SAFIRE-A instrument.

The Martin–Puplett interferometer is characterized by the use of an input and output polarizer as well as the polarizing beamsplitter. The input polarizer of the Fourier Transform Interferometer (FTI), mounted beyond the focal point of the telescope, transmits the component of atmospheric radiation which is linearly polarized in the vertical plane. The radiation orthogonal linear polarization that is reflected by this polarizer originates from a calibration source and provides the second input port of the instrument. By rotating this input polarizer about an axis perpendicular to the optical axis of the beam, a second blackbody

source at a different temperature can be observed providing data for in-flight radiometric calibration (see section 1.2.1). The second off-axis paraboloid of the input telescope provides a collimated beam in which the sources at the two input ports (atmosphere and calibration blackbody) are superimposed with orthogonal polarizations.
The collimated beam enters the FTI through the polarizing beam splitter (M4), which has its principal axis oriented at 45° with respect to the directions of polarization of the two sources. Therefore each source is split into two polarized components (parallel and perpendicular to the principal axis of the beamsplitter) of equal amplitude. The parallel vector is transmitted to the moving fold mirrors and the perpendicular vector is reflected and folded by the flat mirror M5 toward the moving fold mirrors . Fixed roof top mirrors in each arm of the interferometer reflect the beams back (see Figure 2.2) and introduce a folding of the wavefront around the edge of the roof. When the polarized components recombine at the beamsplitter, after travelling different optical paths, the one that was transmitted is now reflected and the one that was reflected is now transmitted. The collimated output beam of the interferometer is condensed into the Cold Optics and Detector Module (CODM) by an off-axis paraboloid M6 and a folding flat mirror M7.
The FTI output polarizer creates two output channels (reflected and transmitted beam) in which the components that travelled different paths have now the same polarization and can interfere to produce interferograms. At both output ports we observe the interferogram of the spectral difference between the two input ports. The two interferograms have opposite phase (at zero path difference one interferogram has a positive signal, the other has a negative signal), and both in principle give access to the full spectral range (10–250 cm^{-1}). Two small condensing mirrors in each channel reimage the focal plane of the paraboloid onto the detector horn apertures (field stops), which are sized to provide the appropriate beam aperture on the sky when projected back through the optical system (a cold pupil is located in each of the parallel beam sections between the two small condensing mirrors and is used to limit the beam growth due to its solid angle at the middle position of the interferometer path). A cold narrowband filter is located in front of each detector, to select the atmospheric lines of interest, which together with the cold pupil and field stop is used to limit the radiation flux on the detector and hence the associated photon noise. By using different filters at the two detectors different spectral regions can be simultaneously observed [8].

2.3 Descriptions of Instrument Subsystems

The SAFIRE–A instrument is made of four main parts: the input optics system; the interferometer; the Cold Optics and Detector Module, including output optics and detectors; and the onboard computer and control unit. A summary of the main instrumental characteristics of the SAFIRE–A airborne Fourier transform spectrometer is shown in Table 2.1.

2.3.1 Limb Scanning Mirror

The control system of the limb-scanning mirror must be able to accurately set the limb view angle and correct for possible changes of the attitude of the platform. The SAFIRE-A pointing system has been designed for use an externally provided attitude signal. When used on an aircraft the attitude signal can be provided by the Aircraft Navigation System (ANS). However, there is an uncertainty associated with this control loop since SAFIRE-A is supported on antivibration mounts, which allow some flexure between the roll of the aircraft and the instrument. A study shows that the antivibration mounts introduce a negligible instability [8].

2.3.2 Onboard Calibration Unit

The baseline configuration adopted for in-flight radiometric calibration aims at the simultaneous measurements of the signals emitted by two alternated reference blackbodies

and by the atmosphere, which are respectively reflected and transmitted by the input polarizer on two different planes of polarization. The calibration system, located in the focus of the input telescope, selects the reference blackbody source, according to a pre-established calibration plan, by rotating the input polarizer. The two calibration sources are kept at temperatures of 0 and 140 °C, the first through a Peltier closed-loop circuit, the second through a stabilized heater. By switching the reflected input beam between the two reference blackbodies it is possible to calibrate the instrument response. By recording two consecutive limb emission measurements at the same pointing angle against the cold and hot blackbodies the calibration is achieved. The difference between the two measured spectra is the difference between the blackbodies of known radiance [8],[10].

2.3.3 Scanning Mechanism of the FTI

The scanning of the moving mirrors is implemented with a compact pantograph mechanism that moves the mirrors simultaneously in both arms of the interferometer so that as one path increases, the other path decreases (see Figure 2.2).

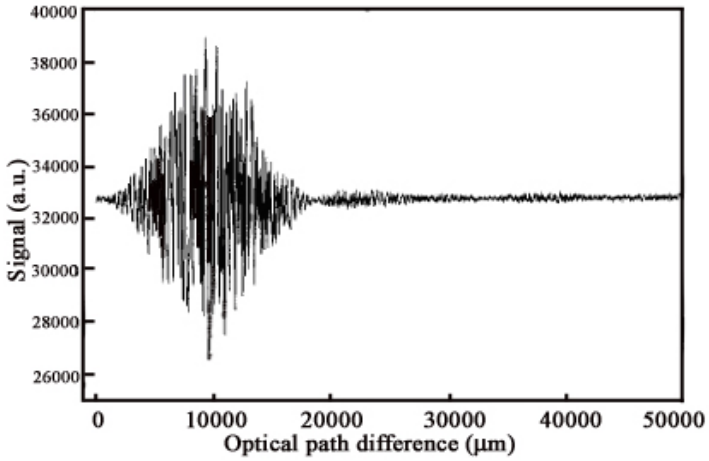

Figure 2.3: The central portion of an interferogram taken with a photolithographic polarizer.

The combination of the mechanical doubling of the effective optical path together with the beam folding provides a long optical path difference (125 cm), for a small mirror stroke (15.6 cm) in a compact instrument. A digital control of the angular speed provides a constant linear mirror speed. Interferograms are acquired both in forward and reverse motion.

2.3.4 Laser Interferometer

A reference laser interferometer, based on a frequency-stabilized diode laser source and following the same optical path as the far infrared radiation (FIR), is used for accurate measurements of the Optical Path Difference (OPD) between the two arms of the interferometer. The offset in the horizontal direction between the laser and the FIR optical path has been reduced to nearly zero. This greatly reduces sampling errors caused by the moving mirror tilt along the vertical axis that, in presence of a horizontal offset between the laser and the FIR beam, would lead to a difference between the measured and the effective OPD.

The laser reference source used for the laser interferometer is based on a 790-nm diode laser [11] that permits performance similar to the commonly used He-Ne system. The laser module and the collimating lens are mounted in a cylindrical laser head placed in an Invar mount. This kind of mounting permits laser head substitution with nearly no loss of alignment. The laser mount is thermally stabilized by means of a closed-loop circuit driving a Peltier cell. The laser drive current is also stabilized.

Interferogram points are acquired at equal OPD intervals, with stabilized scanning speed v. The average sampling frequency v_s is ~4.4 kHz. The instrument acquisition parameters, including the scanning speed v, the number of points N_p per interferogram, the acquisition time t_a, and the Nyquist wave number σ_n, for all four possible acquisition modes are shown in Table 2.2.

Scanning speed	v (mm/s)	σ_n (cm^{-1})	N_p	t_a (s)
0	14	1580	424000	96
1	28	790	212000	48
2	56	395	106000	24
3	112	198	53000	12

Table 2.2: Values of Fourier Transform Spectrometer scanning parameters

2.3.5 Cold Optics and Detector Module

The CODM is provided by University of Wales and encloses output optics, including output polarizer, pupils and field stops, blocking filters and collecting optics, and the two detectors corresponding to the two acquisition channels. All of these components are mounted on the cold plate of a liquid-helium cryostat and allow the full exploitation of photon-noise-limited detectors.

Two different kinds of infrared detector are used on SAFIRE–A: photoconductive detectors operating at 4 K make it possible to cover spectral intervals extending from 50 to 250 cm^{-1}, and bolometric detectors operating at 0.3 K make it possible to cover the 10–50-cm^{-1} region. In this case the detector is cooled through an additional closed circuit ^{3}Hecooling stage mounted on the cold plate of the cryostat (replenishment of the cryogenic in the cryostat requires that the cryostat is removed for servicing after the flight. Since the cryostat can operate for over 24 hours this activity has to be performed only once a day). The asymmetric pupil is a consequence of the presence of the laser interferometer and prevents the laser optics mounts to appear in the detector field of view. The circular field stop has been vignetted to increase the vertical resolution of the atmospheric measurements. The vertical aperture of 4 mm results in a beam divergence of 0.57°. The output polarizer is a photolithographic wire grid of the same type as the input polarizer; the narrowband filters are also obtained with a combination of different photolithographic meshes and are used in front of each detector and determine the trade-off between band coverage and photon noise. The characteristics of some of the most commonly used CODM narrowband filters are shown in Table 2.3. Along with line center and bandwidth, the table shows also the chemical species whose spectral lines are present inside the filter band.

Center Wave Number (cm^{-1})	Bandwidth (cm^{-1})	Chemical Species
23	1	O_3, ClO, N_2O, HNO_3
118	2	H_2O, OH, HOCl, O_3
125	2	H_2O, HCl, O_3

Table 2.3: Narrowband filters used in SAFIRE-A spectrometer for selecting the operating spectral region

2.3.6 Electronics

The SAFIRE–A spectrometer is designed to operate in a stand-alone mode during flight. This task is made possible by the onboard computer that stores a previously defined flight program, controls all the instrument subsystems, and provides data acquisition and storage. This arrangement guarantees total flexibility in choosing and changing the limb-sounding sequences, the acquisition speed, and the spectral resolution, by varying the moving mirror stroke, even during flight. According to the flight plan that is decided for each scientific flight, measurement configurations are chosen for each part of the flight itself.

The thermal behaviour of the system during a typical flight permits the use of a industry-standard PC-compatible computer with hard disk storage. Only the storage section of the system is enclosed in a pressurized case.

2.3.7 Instrument Line Shape

Instrument Line Shape (ILS) accounts for the finite spectral resolution of the instrument and distortion of the line-shape by the instrument. SAFIRE-A has a theoretical spectral resolution of 0.004 cm^{-1}, defined in terms of the period of independent spectral samples (equal to the inverse of twice the maximum optical path difference). The theoretical instrument line shape (ILS) is a $\sin(x)/x$ function convolved with a box car function due to the finite solid angle, and it has a Full Width at Half-Maximum (FWHM) of about 5 $X10^{-3}$ cm^{-1}.
The instrumental line shape of the SAFIRE–A spectrometer was estimated by analysing sharp atmospheric lines from spectra acquired from the higher atmospheric layers that can be observed by the instrument. The ILS was fitted using a linear combination of a sinc and a $sinc^2$ functions convolved with a Lorentzian atmospheric line shape. The result of the fit is shown in Figure 2.4.

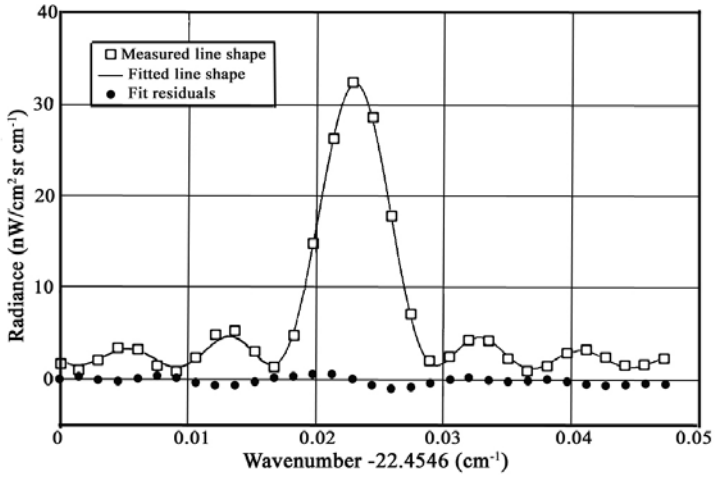

Figure 2.4: ILS of the SAFIRE-A spectrometer. The fitted ILS is a linear combination of $sinc^2$ and sinc functions.

2.3.8 Signal to Noise Ratio and Noise-Equivalent Spectral Radiance

The signal-to-noise ratio (S/N) of the spectra is defined as the ratio of the signal of the largest atmospheric emission (equal to about the emission of a 210 K blackbody) divided by the root mean squared (rms) of the noise measured in regions with no signal. The rms noise is less than 0.5 K and the S/N of the observed spectra is greater than 500:1.
The radiometric performances were measured on the ground in a thermobaric chamber. This chamber, hosted at the Institute CNR-TESRE (now CNR-IASF Institute) in Bologna, allows the control of both the temperature and the pressure down to 10 mbar. For the evaluation of the Noise-Equivalent Spectral Radiance (NESR is defined as that radiance that causes, in the measuring instrument, a signal to noise ratio of 1) a reference blackbody at 10 °C is used in front of the pointing mirror. Some tests were performed for various spectral channels and types of beam splitter.

Spectral channel (cm^{-1})	Beam Splitter	NESR (nW/cm^2 sr cm^{-1})
23	Photolithographic	0.22
118	Wire grid	9.5
118	Photolithographic	10
125	Photolithographic	13

Table 2.4: NESR measured under vacuum in a thermobaric chamber.

One of the useful tests performed in the thermobaric chamber was the comparison between wire grid and photolithographic polarizers. We found that the performances of both kind of polarizers are comparable at 118 cm^{-1} (see Table 2.4). Therefore for aircraft applications wire grid polarizers are to be preferred, because they allow less disturbance in the interferometric signal caused by the high levels of vibrations and acoustic noise expected onboard the aircraft.

2.4 Instrument Atmospheric Measurement Capabilities

The information about the VMR vertical profiles of atmospheric constituents retrieved by the SAFIRE-A instrument is obtained by means of an inversion process that operates on individual sequences of emission spectra acquired in the limb-sounding geometry. A limb-sounding sequence consists in a set of observations of the atmospheric signal performed at multiple elevation angles spanning the range of tangent heights between the tropopause and the aircraft altitude and including a few additional measurements above the horizontal for the estimate of the column content above the flight level and for calibration.

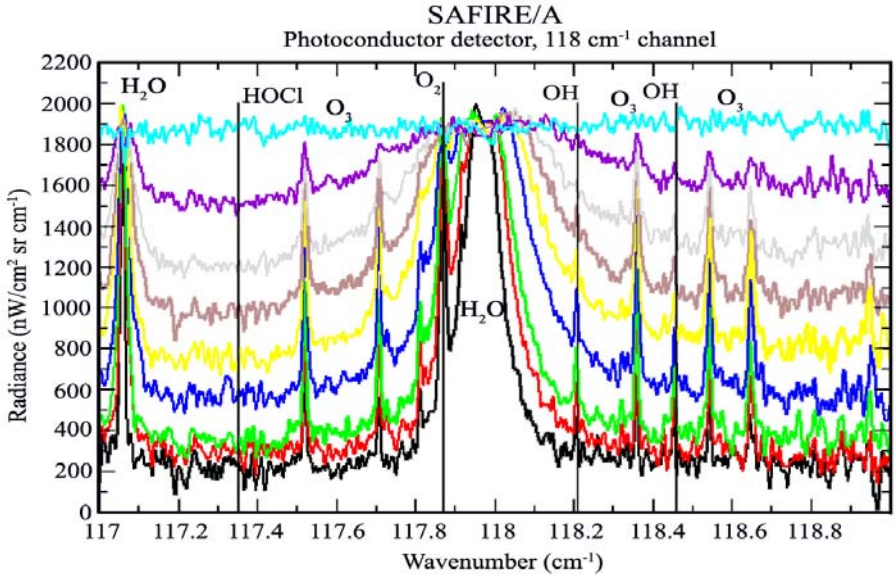

Figure 2.5: Limb scanning sequence of atmospheric emission spectra acquired in the 118 cm^{-1} window.

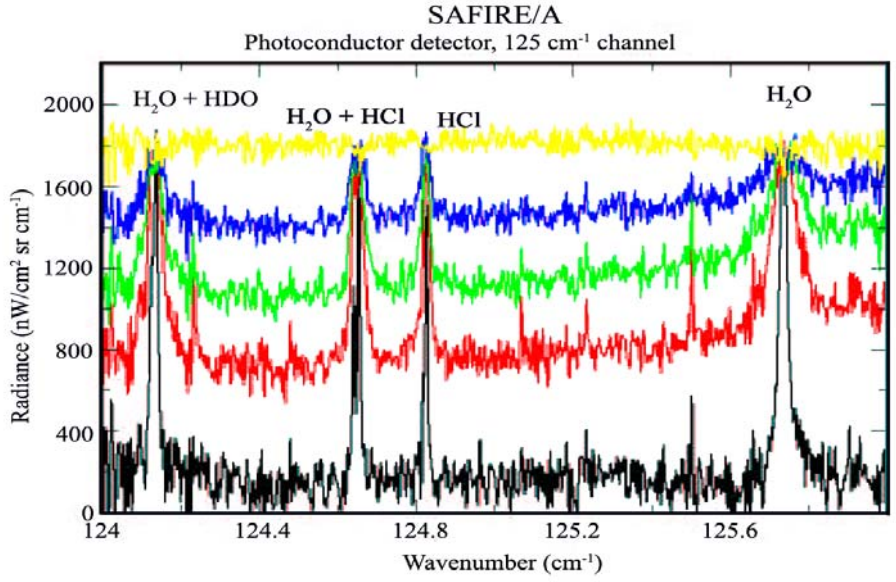

Figure 2.6: Limb scanning sequence of atmospheric emission spectra acquired in the 125 cm^{-1} window. Spectral features due to interesting molecular species are evidenced by vertical lines. In this case it is possible to use only a few limb angles near the horizontal; below tropopause, the atmospheric opacity due to water vapour limits sensitivity.

The typical SAFIRE-A acquisition strategy is based on a fixed sequence of observation angles, independent of the flight altitude. If a change of the sequence during the flight is wanted, it can be implemented in the predefined observation scheme stored on the on-board PC before takeoff. This scheme, normally called the flight program, is executed as soon as the instrument is powered, in such a way that the implementation of the selected plan of limb sounding observations is synchronized with SAFIRE-A switch-on time. The spacing between two contiguous angles below the horizontal is typically maintained at steps not greater than 0.3°; this results in a vertical oversampling of the order of 50% of the instrument Field of View (FOV), which is to be taken into account in the retrieval process where a suitable degree of profile regularisation is chosen. The calibration of the frequency scale of the spectra is performed with a fitting procedure that identifies the centers of well-known spectral lines within the selected interval. Radiometric calibration is achieved by recording, for each limb-scanning sequence, two consecutive measurements of the atmospheric signal at the highest viewing angle, normally a limb angle of 10°, against first the hot and then the cold blackbody reference sources. The difference between the two measured spectra must then be equal to the difference between the two blackbody sources of known radiance and might be used, therefore, to calibrate the instrument response in flight. Individual limb sequences of radiance and frequency-calibrated spectra are shown for the two short-wavelength channels at 118 cm^{-1} (Figure 2.5), and 125 cm^{-1} (Figure 2.6) and for the long-wavelength channel at 23 cm^{-1} (Figure 2.7), along with the assignment of the spectral features displayed by the target species in all the relevant microwindows [10].

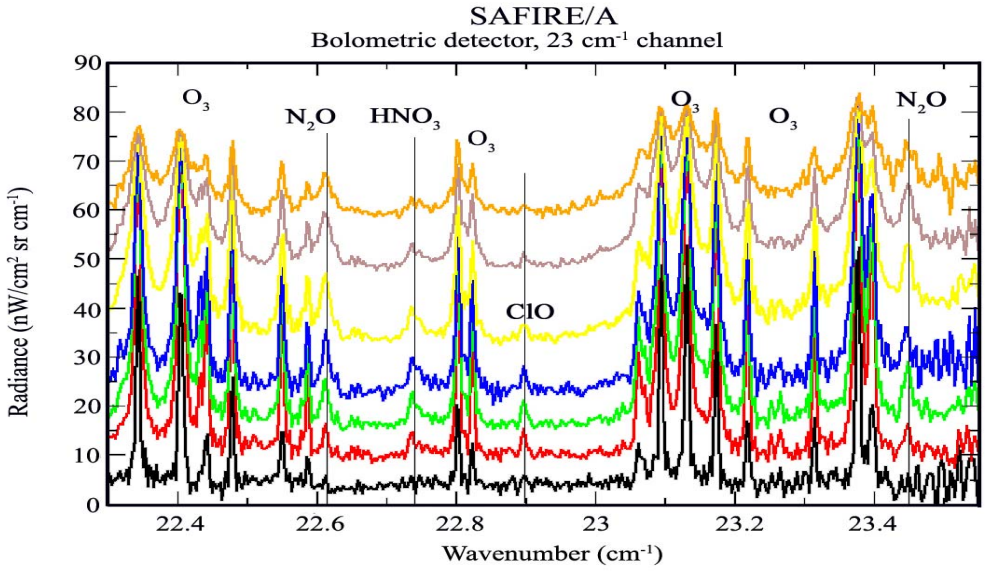

Figure 2.7: Limb scanning sequence of atmospheric emission spectra acquired in the 23 cm^{-1} window. Spectral features due to interesting molecular species are evidenced by vertical lines.

A retrieval code, (see Chapter 4) specifically developed for the analysis of airborne observations, is used for inverting the Earth-limb emission measurements and deriving the vertical distribution of minor atmospheric compounds. The retrieval process analyses the observations as a function of both spectral frequency and limb-scanning angle.

2.5 VMR Vertical Profile Measurements

As a final product of the retrieval process applied to the individual limb sequences measured by SAFIRE-A, vertical profiles of the volume mixing ratio for the observed species are obtained in the altitude range between the flight level (maximum 20 km) and the tropopause. Above the flight height the vertical distribution of the atmospheric constituents cannot be resolved, and only reduced information about the column content can be extracted.

The structures observed in the VMR profiles above the last retrieved point reflect the vertical distribution of the corresponding species, as described by the initial guess profile and re-scaled by the retrieval algorithm. Below the tropopause level, the limited transparency of the Earth's atmosphere, that is due to the higher values of the water vapour mixing ratio, prevents the possibility of extending the range of the observation to lower altitudes. As a consequence, the best performance of the instrument, in terms of the altitude coverage, are achieved at the highest latitudes (i.e., in the Arctic and Antarctic regions), where the tropopause might be located at heights as low as 8 km. Although limited by the occurrence of strong water vapour lines in the 10–200 cm^{-1} interval, the SAFIRE-A measurements are not significantly affected by aerosols and particles extinction and can be therefore carried out also in presence of high altitude clouds.

The vertical resolution of the single profile can be estimated to be approximately 1–2 km for ozone retrieval according to the Averaging Kernel calculations (see chapter 4.1.7). The horizontal resolution along the flight direction depends on the aircraft speed (approximately 650 km/h) and on the selected interferometric scanning speed. For an interferometric scan at maximum spectral resolution acquired in 30 s, the corresponding horizontal resolution in the flight direction of a complete limb sounding sequence (11 spectra) is about 60 km (much lower than 1° in latitude). This is sufficient, for instance, to resolve some of the atmospheric features that are due to vertical or horizontal transport, such as those connected with extrusion of lower-latitude air masses within the polar vortex region. Two-dimensional distributions of the atmospheric constituents observed during the flight can be built by combining the information of the individual profiles where the VMR values of the species are plotted versus altitude and time [10].

Chapter 3: Measurements Campaigns

3.1 The APE Project

Since the discovery of the so-called ozone hole over Antarctica in 1985, the question of stratospheric ozone depletion (APPENDIX C) has attracted the attention of the international scientific community. Observations from several experimental campaigns, carried out mainly in the polar regions, and the ongoing effort devoted to interpreting the data collected, have resulted in significant improvements in our understanding of this phenomenon. However, further significant progress is required in order to solve remaining uncertainties, and to obtain more quantitative information allowing to predict the future state of the ozonosphere with confidence.

Within this framework the Airborne Polar Experiment (APE) was initiated. This research programme was aimed at studying the physical and chemical processes responsible for the ozone loss in the polar stratosphere. The project started in 1995 as a result of an agreement of scientific co-operation between the Ente nazionale per le Nuove tecnologie, l'Energia e l'Ambiente (ENEA), on behalf of the Programma Nazionale di Ricerche in Antartide (PNRA), and the Russian organisations Myasishchev Design Bureau (MDB) and Central Aerological Observatory (CAO). It exploits the potential offered by the Russian M55-Geophysica high-altitude aircraft as a scientific platform to conduct observations in the upper troposphere and lower stratosphere at middle and high latitudes. Several universities and research institutes in the European Union, Russia, Switzerland and South America are involved in the project. They participate by operating their instruments on board the aircraft and by means of modelling activities and data analysis.

3.2 The M55 Geophysica Aircraft

The M55 was designed by the Russian company Myasishchev Design Bureau and was manufactured in the Smolensk factory on order from the Ministry of Defence of the former Soviet Union as a high-altitude reconnaissance aircraft. Its maiden flight was on 16th August 1988.

Figure 3.1: The M55 Geophysica aircraft (Kiruna, March 2003).

The M55-Geophysica is an all-weather single-seater stratospheric aircraft capable of operating both day and night for about 5 hours up to an altitude of 21 km, even in critical environmental conditions (e.g. temperatures down to -80°C, strong cross winds at take off/landing). The aircraft has a large reserve of electrical power for the instrumentation. Flight

parameters, necessary for the science mission, are regularly recorded by the aircraft and distributed to each instruments. Takeoff and landing lengths are less than 1000 m, but a runway of at least 2000 m is required for safe operation. With its two engines and triangular undercarriage, the Geophysica has a very robust design and so can operate in a wide range of ground weather conditions, notably tolerating a maximum crosswind of 10 m/s. These characteristics (see Table 3.1) together with the possibility of housing a scientific payload up to 1500 kg inside its bays (the main bay is over 5 m long and can accommodate bulky instruments) make the M55-Geophysica an ideal platform for research in the upper troposphere and lower stratosphere.

Length	22.9 m
Wing span	37.5 m
Speed	max. 750 km/h
Record altitude	21830 m
Operative radius	ca. 3500 km (17 km altitude)
Flight endurance	5 h 15' (17 km altitude)
Takeoff weight	max. 24700 kg
Payload weight	max. 1500 kg
Payload volume	max. 11.83 m3
Thrust	2 turbofan engines 5000 kgf
Takeoff/landing run	900 m
Runway required	1800m (asphalt)
Cross wind on takeoff/landing	max. 36 km/h The wide 6.6m track resulting from the twin-beam structure of the aircraft, provides stability during takeoff and landing.

Table 3.1: Geophysica Aircraft Technical characteristics.

Since the beginning of the co-operation between Italy and Russia in 1995, the M55-Geophysica has undergone several transformations in order to house the scientific payload and to increase its efficiency and flexibility as scientific laboratory. With this perspective, the bays of the aircraft have been modified according to a modular criterion, and have been equipped with standard interfaces with the instruments (attachment points, electrical connections, viewing windows, and servicing hatches). In addition, a number of dorsal bays, designed to lodge instruments, has been built onto the fuselage of the aircraft.
At present the M55-Geophysica is, together with the U.S. aircraft ER-2 (a modified version of the U-2 reconnaissance aircraft, managed by the NASA and used for scientific purposes) one of the two airborne platforms operating world wide for stratospheric research. While the ER-2 has a longer flight endurance than the M55-Geophysica, the latter has superior characteristics with respect to scientific payload capacity, power supply, manoeuvrability, and less dependence on ground meteorological conditions.

3.2.1 The Scientific Payload

The location of each instrument onboard the M55-Geophysica is indicated in Figure 3.2 (configuration used during APE-GAIA Campaign). The payload can be classified according to different measurement types: in situ aerosol instruments, remote sensing aerosol instruments, in situ chemical instruments, and remote sensing chemical instruments (Table 3.2 and Table 3.3).
The combination of two Fourier transform spectrometers, SAFIRE-A and MIPAS-STR (Michelson Interferometer for Passive Atmospheric Sounding/STRatospheric aircraft), operating in the Far and Medium Infrared respectively, is particularly important for remote sensing measurements of chemical species.
The two instruments perform emission measurements by using the limb sounding technique, and are capable of observing simultaneously a large number of constituents involved in the ozone depletion processes. MIPAS-STR measures almost all the compounds of the NO_y

family, and together with SAFIRE-A, covers Cl_y species (ClO, HCl and $ClONO_2$). SAFIRE-A has its strength in the observation of O_3, N_2O, HNO_3, H_2O,ClO, HCl and OH. Trace gases like O_3, NO_2, BrO, and OClO compounds are observed by the GASCOD-A (Gas Absorption Spectrometer Correlating Optical Differences-Airborne), a differential optical absorption spectrometer, operating in the ultraviolet and visible spectral regions.

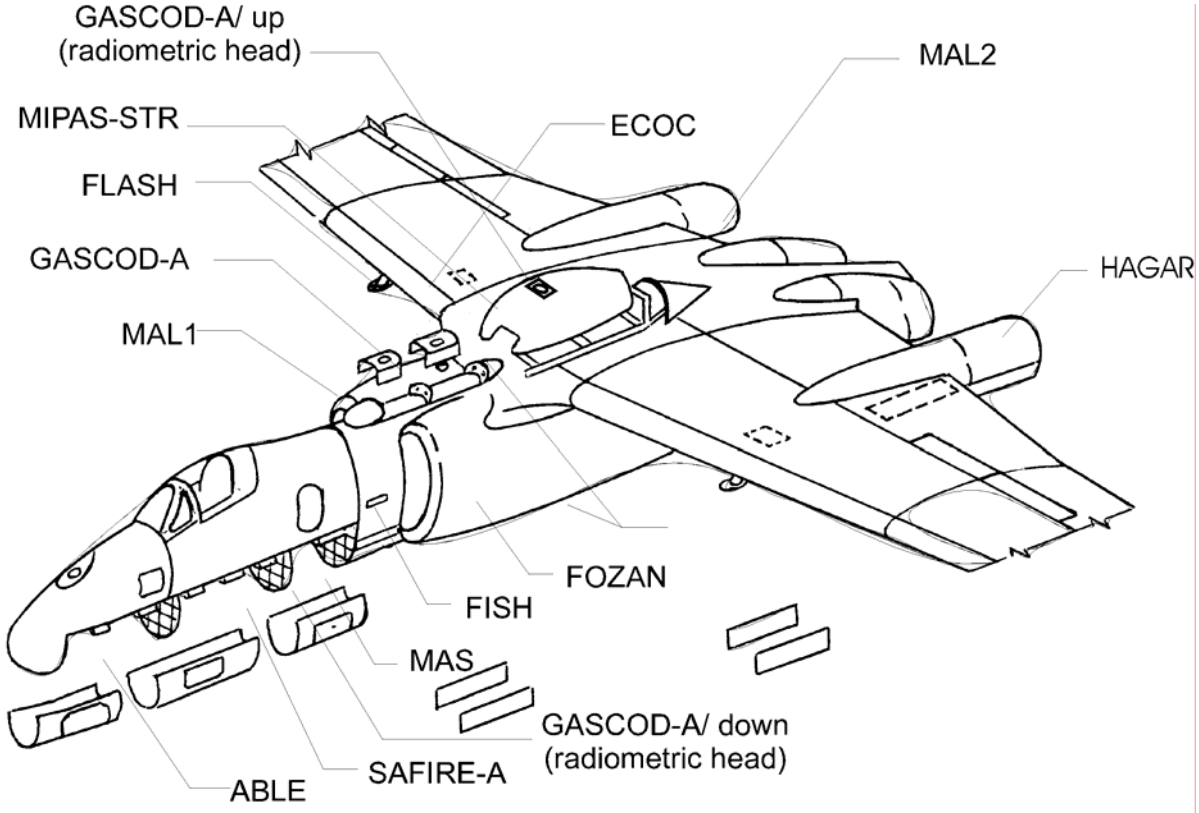

Figure 3.2: Schematic of M55 showing instrument location on the aircraft during APE-GAIA campaign.

In situ measurements of ozone are provided by ECOC (ElectroChemical Ozone Cell) an electrochemical ozonometer, and by FOZAN (Fast OZone ANalyzer) that utilizes the chemiluminescent reaction between ozone and a solid state dye sensor.
Fast In-Situ Stratospheric Hygrometer (FISH), FLuorescent Airborne Stratospheric Hygrometer (FLASH) and Aircraft Condensation Hygrometer (ACH) are instruments for water vapour measurement. Other tracers like N_2O and CO_2 are provided by High Altitude Gas chromatograph for Atmospheric Research (HAGAR). Chemical conversion resonance fluorescence sensor HALogen OXide Monitor (HALOX) provides in-situ measurements of BrO, ClO, Cl_2O_2, $ClONO_2$. Furthermore, the higher spatial resolution, and the possibility provided by these sensors of measuring the horizontal variability of the atmospheric composition, will provide an important synergy with the limb sounding observations.
Finally, another important feature of the M55 scientific payload is the possibility of studying heterogeneous chemistry by combining the composition measurements from the chemical sensors with the measurements of aerosols and polar stratospheric cloud particles obtained by in situ devices (Forward Scattering Spectrometer Probe (FSSP-300), Multi-wavelength Aerosol Spectrometer (MAS), and COndensation PArticle System (mini-COPAS)) and lidars (AirBorne Lidar Experiment (ABLE) and Microjoule Airborne Lidar (MAL)).

3.2.2 Technological tests on the instrumentation

All scientific instruments had to meet design specifications agreed between the scientists and MDB, the designers of the aircraft. These design specifications defined all the tests that mock-

ups and instruments had to undergo in order to be mounted on the aircraft. The tests were subdivided into various phases:

- vibration and shock tests on the mock-ups;
- mock-up test flights;
- Electro Magnetic Interference (EMI) tests on the instruments;
- baroclimatic tests on the instruments;
- instrument test flights.

The mock-ups of ABLE, SAFIRE-A, GASCOD-A, MAS, and FSSP-300 were flown in three different flights during the second part of August 1996. During the mock-up flights, temperatures and vibrations were measured in critical points of each instrument. EMI tests (phase 3) started on May 1996 at Ente per le Nuove Technologie, l'Energia e l'Ambiente (ENEA), and continued until the end of September 1996. In September, baroclimatic tests were carried out at the military airport of Pratica di Mare.
Three instrument test flights, at Pratica di Mare (Italy), of approximately 3 hours each, were performed. On 23 December 1996, the temperature sensors on board the Geophysica were compared with those on board the Falcon. The intercomparison occurred during a period of approximately 15 min at 10600 to 10900 m altitude, over northern Sweden, with temperatures ranging between -54° and -56°C. The aircraft were in sight of each other during the intercomparison period. The difference in the recorded temperatures was smaller than one degree. This intercomparison could be performed only at the Falcon's maximum altitude, of course, and did not guarantee that the Geophysica's sensors were reliable at higher altitudes and much lower temperatures. Their performance at high altitude was tested during the mock-up flights in August 1996 in Moscow, when several radiosondes were launched close to the airport. Good agreement was obtained at stratospheric levels between the aircraft temperature sensors and the radiosondes data [12].

3.2.3 Flight planning

Conflicting measurement constraints arose between different instruments: MAL and MAS could operate only during night time, while GASCOD-A required sunlight to make measurements. To measure photochemical radical species, measurements by SAFIRE-A were best performed during the day. Moreover, MAS, MAL, FOZAN, ECOC, ACH, and FLASH will benefit from slow ascents and descents, in order to maximize vertical profile resolution, while the remote sensing instruments will benefit from rapid ascents that would maximize time at cruise altitudes. The orientation of the flight path, with respect to the prevailing stratospheric flow, was also an important consideration. The maximum gradients in long-lived tracer fields occur across the flow, particularly across the polar vortex edge (appendix C). Therefore, in order to sample the greatest range of latitudes, flights across the flow are preferred. However, the most useful information in aerosol microphysics is the one recorded as closely to Lagrangian as possible, that is, along the direction of the mean flow. This is particularly important when the size of the aerosol perturbation (a PSC) is smaller than the aircraft's range, so that both onset and end of the episode can be sampled. Mountain-induced waves are the most important example of such perturbations. Two possible flight paths were investigated: along the wind, or perpendicularly to the wind, turning back in such a way as to cross the same air parcel several times. In the first case stationary conditions can be assumed along the wind pattern, since the aircraft was flying at much higher speed than the wind itself, and hence could not follow physically an air parcel. The second case requires rapid calculation of air mass trajectories and assumes that changes occur on time scales close to that of the frequency of the encounter. For mountain-wave clouds, changes have been observed on a much smaller scale than could be sampled using this second technique [12].

3.3 APE Campaigns

The campaigns performed by the M55-Geophysica aircraft in the frame of APE project are:

- **APE-POLECAT**: The fist APE mission. This arctic campaign took place from December 1996 to January 1997 from Rovaniemi (Lapland - Finland). Seven missions were planned, the first three flights were mainly devoted to study stratospheric transport and mixing processes, the others to investigate the presence of PSCs in the arctic stratosphere [13].
- **APE-THESEO**: This project was mainly funded by the European Commission and by the Italian Space Agency and the European Science Foundation. The campaign has been carried out from the International Airport of Mahé (Seychelles) in the period 15 February – 15 March 1999. Two aircraft were involved in the campaign execution: the DLR Falcon and the M55-Geophysica.
- **APE-GAIA**: (Airborne Polar Experiment-Geophysica Aircraft in Antarctica) Antarctic Campaign (September - October 1999, Ushuaia, Argentina); APE-GAIA aimed at studying the physical and chemical processes responsible for the depletion of the Antarctic stratospheric ozone layer (see section 3.3.1).
- **ENVISAT** Satellite Validation Mid-Latitude and Arctic Campaigns (July 2002 - March 2003, from Forli' (Italy) and from Kiruna (Sweden)), see section 3.3.2.
- **APE-Infra**: The Airborne Platform for Earth observation Infrastructure (October 2002 - January 2004)
- **EuPLEx**: European Polar Stratospheric Cloud and Lee Wave Experiment (February - March 2003).

Since its first flight in 1996, SAFIRE-A took part in several of these APE campaigns. The results presented in this thesis were obtained during three particular Campaigns: APE-GAIA Campaign, ENVISAT Mid-Latitude Validation campaign and ENVISAT Arctic Validation Campaign (ENVISAT AVC).

3.3.1 APE-GAIA Campaign (September – October 1999, Ushuaia, Argentina)

The need for new experimental data, related to chemistry and transport issues, is particularly strong for the middle and high latitudes of the southern hemisphere. The altitudes of the low stratosphere are barely accessible with ground-based and satellite observations and, compared to the Arctic region, the southern hemisphere has been less sampled by the most recent measurement campaigns.

The objectives of the APE-GAIA campaign have been identified in the light of these considerations. The priority assigned in this mission to the study of chemistry, together with the observation capabilities offered by remote sensing measurement techniques, have identified the beginning of the southern spring as the optimum period for observations. This transition period between the ozone depletion phase (August-September) and the ozone recovery phase (October-November) is preferable, compared to the May-July period, which is more suitable for microphysical observations (because of the higher probability of formation of PSCs). In the ozone depletion phase, key aspects are both the study of the most important catalytic cycles involved in ozone chemistry, as a function of latitude and altitude, and the possibility of extending the measurements to those compounds for which the observation database is very limited (for example, HBr and HOBr in the bromine family). Similar interest exists for observations conducted at the beginning of the recovery phase, because the processes involved in the reconversion processes of the active chlorine species into the reservoir compounds $ClONO_2$ and HCl can be analysed.

MIPAS STR (Michelson Interferometer for Passive Atmospheric Sounding/STRatospheric aircraft)	Profiles and vertical column of the atmospheric constituents	Remote sensing chemistry
SAFIRE-A A (Spectroscopy of the Atmosphere using Far InfraRed Emission/Airborne)	Profiles and vertical column of the atmospheric constituents	Remote sensing chemistry
GASCOD A (Gas Absorption Spectrometer Correlating Optical Differences/Airborne)	Profiles and vertical column of the atmospheric constituents	Remote sensing chemistry
ACH (Airborne Condensation Hygrometer)	Water vapour (from 0 to 8 km)	In situ chemistry
ECOC (ElectroChemical Ozone Cell)	Ozone	In situ chemistry
FISH (Fast In-Situ Stratospheric Hygrometer)	Water vapour (total content)	In situ chemistry
FLASH (FLuorescent Aircraft Stratospheric Hygrometer)	Water vapour (from 8 to 20 km, gas phase content)	In situ chemistry
FOZAN (Fast OZone Analyser)	Ozone	In situ chemistry
HAGAR (High Altitude Gas chromatograph for Atmospheric Research)	CFC-11, CFC-12, N_2O and SF_6	In situ chemistry
FSSP-300 (Forward Scattering Spectrometer Probe)	Particle dimensions (23-0.4 mm)	In situ microphysics
MAS (Multi-wavelength Aerosol Spectrometer)	Density and optical properties of the particles	In situ microphysics
mini-COPAS (COndensation Particle System)	Density of small particles (<0.4 mm)	In situ microphysics
ABLE (AirBorne Lidar Experiment)	Density and optical properties of the particles (2-15 km from the plane)	Remote sensing microphysics
MAL (Microjoule Airborne Lidar)	Particle density (0-2 km from the aircraft)	Remote sensing microphysics

Table 3.2: Instruments onboard Geophysica Aircraft during APE-GAIA campaign.

Finally, another aim of the observations was to clarify the extent and altitude region of the mixing of polar air masses with middle latitude, in order to determine how much of the ozone losses in middle latitudes are due to transport or dilution effects of the vortex.

The Antarctic campaign took place from the operative base of Ushuaia in Tierra del Fuego (Argentina) from 15th September to 14th October 1999. Observations were also carried out during the return transfer flight of the aircraft from South America to Europe.

The choice of the site was determined in the first place by its favourable geographic location: Ushuaia (-54.8° latitude, -68.3° longitude) is the southernmost airport in the world able to accommodate the M55-Geophysica, and thus the nearest to the Antarctic continent.

Considering that the polar vortex generally extends to a latitude between 60° and 70° S, and that the operative radius of the M55 is about 15° latitude, departing from Ushuaia the aircraft was able to reach the vortex, explore its edges, and penetrate its interior. In order to forecast the exact location of the polar vortex and the conditions of the stratosphere, and thus to work out the best routes for the M55, the flight missions were planned with the support of meteorological analyses and computer simulations.

A total of 30 hours of flight were scheduled, distributed over 5 missions (Figure 3.3). The flight profiles of the M55-Geophysica mainly responded to the optimum requirements for remote sensing observations: they were, as far as possible, flight profiles at maximum (20 km) and constant altitude. Occasionally dives were made to the troposphere, in order to allow in situ measurements. During the campaign, about 70 scientists were based in the Argentine town to take care of the different aspects of the mission. This involved a team of Russian technicians, responsible for the management of the aircraft, a group in charge of scientific and

logistic co-ordination, experimental groups responsible for the scientific instruments, and the theoretical groups in charge of modelling and data analysis [14].
In parallel with M55-Geophysica flights, a series of ground based and balloon measurements were made from Ushuaia, Punta Arenas, and several bases located in the Antarctic Peninsula, in order to validate the measurements conducted during the APE-GAIA campaign.

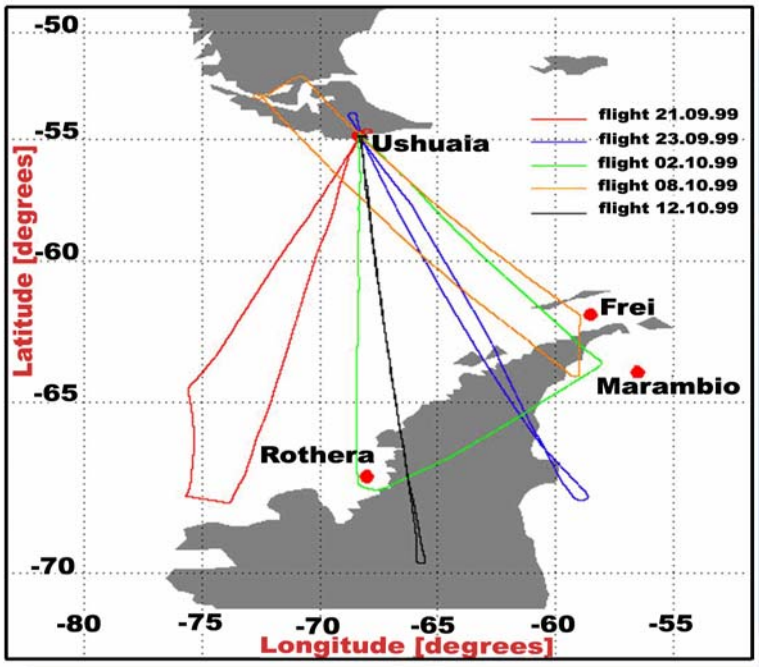

Figure 3.3: APE-GAIA campaign flight routes.

3.3.2 ENVISAT Mid-Latitude and Arctic Validation Campaigns (October 2002, Forlì, Italy and February-March 2003, Kiruna, Sweden)

ENVISAT (ENVIronmental SATellite) is an advanced Earth observing satellite designed to provide measurements of the atmosphere, ocean, land and ice over a five years period. As the successor to the highly successful ERS-1 and ERS-2 satellites it will provide continuity of measurement with most ERS instruments, thereby extending to more than 10 years the long term data sets critical for global environmental monitoring, and furthering many operational and commercial applications.
For the validation of the ENVISAT geophysical products the European Space Agency (ESA) has to verify the algorithms which are used to generate ENVISAT data products, monitor the quality of these products and provide a database of collocation data to the members of the ESA expert teams responsible for geophysical validation and algorithm development.
The validation programme includes the ENVISAT Stratospheric Aircraft and Balloon Campaign (ESABC), which provided additional data for validation of atmospheric chemistry products [15].
The first of the ESABC Campaigns was the Mid Latitude Campaign occurred in autumn 2002 (October 2002). The campaign was scheduled from Forlì (44.2° latitude, 20.25° longitude) with 24 flight hours. Because of the unavailability of MIPAS in the beginning, the three flights of the Geophysica chemistry payload were delayed to the last week of the campaign. Part of the campaign was dedicated to aerosol and part to chemistry. Most of the instruments flew during all flights and were able to collect measurements. The main difference between aerosol and chemical validation was relative to the flight pattern: collocation was different when dealing with remote sensing scanning instruments and when dealing with in situ instruments. The aerosol instruments fall essentially in the in situ category, as even the high power lidar produced data about clouds in the vicinity of the aircraft. Therefore for the aerosol

package it was necessary to fly inside the footprint of the ENVISAT instruments, giving maximum priority to the GOMOS, and MERIS instruments, while during the flights dedicated to chemistry the aircraft could fly outside the footprint of the ENVISAT instruments, but the instruments on board the aircraft and ENVISAT had to look at the same air volume.

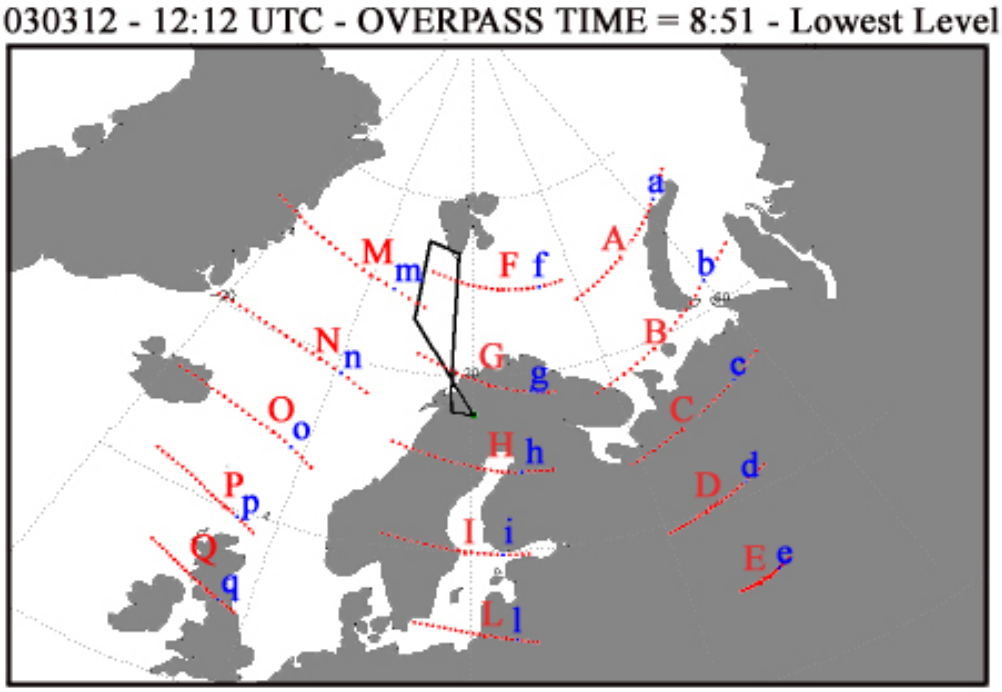

Figure 3.4: Location of the MIPAS tangent points at 15 km altitude of 3 orbits (upper case letters) and relative air mass trajectories (red dots) and positions at selected time (12:12 UTC, lower case letters), together with the track of the March 12th 2003 Geophysica flight.

The second ESABC campaign, the Arctic campaign, took place from the operative base of Kiruna (67.49° latitude, 20.25° longitude) in Sweden from January to 16th of March 2003. The campaign was composed of two branches: the first in January 2003 (in synergy with the project EUPLEX), the second in late February, early March 2003. All flights relative to the aerosol validation occurred in early January while all the flights related to the chemistry occurred in the second part of the campaign. Correlative measurements of the ENVISAT standard products in the Arctic region and validation of the chemistry instruments in presence of strong horizontal gradients across the edge of the polar vortex have been the primary goals of the high latitude flights executed by the M55-Geophysica aircraft. One test flight and four validation flights have been performed with the Geophysica chemistry payload during this Arctic campaign. All the information and tools needed for the preparation of the flight plan (i.e. the Excel sheets for the exact location of the MIPAS scans, along with the support from the modelling for meteorological data and trajectory calculations) were available during the campaign.

The Geophysica flight were optimised according to the requirements of the limb-sounding instruments, with several legs at constant high altitude. The flights were tuned to spatially match several MIPAS scans. To obtain the best temporal coincidence, some of the MIPAS scans were matched exactly whereas other scans were reached within one-two hour from the respective overpasses times (scan belonging to different orbits as in Figure 3.4). Moreover, during one flight, an excellent time and space matching was also obtained for the observations of the Geophysica limb sounders with limb measurements made by SCIAMACHY [16].

MIPAS STR (Michelson Interferometer for Passive Atmospheric Sounding/STRatospheric aircraft)	Profiles and vertical column of the atmospheric constituents	Remote sensing chemistry
SAFIRE-A A (Spectroscopy of the Atmosphere using Far InfraRed Emission/Airborne)	Profiles and vertical column of the atmospheric constituents	Remote sensing chemistry
GASCOD A (Gas Absorption Spectrometer Correlating Optical Differences/Airborne)	Profiles and vertical column of the atmospheric constituents	Remote sensing chemistry
ECOC (ElectroChemical Ozone Cell)	Ozone	In situ chemistry
FISH (Fast In-Situ Stratospheric Hygrometer)	Water vapour (total content)	In situ chemistry
FLASH (FLuorescent Aircraft Stratospheric Hygrometer)	Water vapour (from 8 to 20 km, gas phase content)	In situ chemistry
FOZAN (Fast OZone Analyser)	Ozone	In situ chemistry
HAGAR (High Altitude Gas chromatograph for Atmospheric Research)	CFC-11, CFC-12, N_2O and SF_6	In situ chemistry
HALOX (Chemical Conversion Resonance Fluorescence sensor)	BrO, ClO, Cl_2O_2, $ClONO_2$	In situ chemistry
TDC (Thermo Dynamic Complex)	Temperature and pressure	In situ
SIOUX (Chemioluminescence NO/NO_y sonde)	NO/NO_y	In situ chemistry
FSSP-300 (Forward Scattering Spectrometer Probe)	Particle dimensions (23-0.4 mm)	In situ microphysics
MAS (Multi-wavelength Aerosol Spectrometer)	Density and optical properties of the particles	In situ microphysics
COPAS (COndensation Particle System)	Density of small particles (<0.4 mm)	In situ microphysics
MTP (Microwave radiometer)	Temperature profile	Remote sensing
ABLE (AirBorne Lidar Experiment)	Density and optical properties of the particles (2-15 km from the plane)	Remote sensing microphysics
MAL (Microjoule Airborne Lidar)	Particle density (0-2 km from the aircraft)	Remote sensing microphysics

Table 3.3: Instruments onboard Geophysica Aircraft during ESABC Arctic campaign.

Chapter 4: Inverse Method

In the case of SAFIRE-A experiment the composition of the atmosphere is analysed indirectly by measuring the atmospheric emission in the far infrared spectral region. Indirect measurements are used whenever direct measurements are difficult or expensive to perform and the measurement of the atmospheric composition can be considered a typical case. Unfortunately complex problems of interpretation may arise from the analysis of indirect measurements since usually the relationship between the measured and the required quantities is rather complicated. In this chapter, the mathematics behind the inversion procedure that enables to obtain the wanted parameters from the real data will be described (the notation and concepts introduced here are the ones first introduced by Rodgers [17]).

4.1 The Problem

The target of the analysis of indirect measurements is the *state of the atmosphere* and it is usually denoted by x, while y are the quantities measured by the instrument. The *forward problem* (F) is the procedure that maps the state of the atmosphere to the quantities that we are able to measure. In our case F is represented by the physical theory which links the electromagnetic emission of the atmosphere to its characteristics of temperature/pressure and composition. The measurements (y) are inevitably affected by some measurement error: in fact they are a corrupted version of the error-free data obtained from the state of the atmosphere through the forward process. The *measurement noise* (ε) may then be defined as the difference between the error-free data and the measurements; thus the mapping from the state of the atmosphere to the measured data may be described by the following equation:

$$y = F(x) + \varepsilon \tag{4.1}$$

The inverse problem is then the one of finding the best representation of the required atmospheric parameters x given the measured data y, the forward problem F and the noise ε.
There are several classifications of the forward problem depending on whether the state of the atmosphere and the measured data are functions of continuous or discrete variables, i.e. whether they have infinite or finite dimensions. In most inverse problems the quantities to be retrieved are often functions of continuous variables such as time and space, so the dimension of the state space is infinite; on the other hand, only a limited number of data can be measured, so the dimension of the data space is always finite. Thus most inverse problems are formally *ill-posed*. The error-free inverse problem $F(x) = y$ is *ill-posed* if it meets one or more of the following conditions:

- the inverse of the forward operator F does not exist;
- the inverse is not *unique*;
- an arbitrary *small* change in the measured data can cause an arbitrary *large* change in the retrieved quantities.

On the contrary, if the problem is well-posed, the relative error propagation of the solution is controlled by the condition number *cond(F)*:

$$\frac{\|\Delta x\|}{\|x\|} \leq cond\,(F)\,\frac{\|\Delta y\|}{\|y\|} \tag{4.2}$$

where Δy is the variation of the measurements y and Δx the corresponding variation of the parameters x.
Since the fractional error in the retrieved parameters depends on the condition number multiplied by the fractional error in the measurements, small values of the conditional number

are desirable. If *cond(F)* is close to unity, the problem is said to be *well-conditioned* and the solution is stable with respect to small variations of the measurements. Otherwise the problem is said to be *ill-conditioned*. The separation between well-conditioned and ill-conditioned problems is not very sharp and the concept of "well-conditioned" problem is vaguer than the concept of "well-posed".

4.2 Formalization of the Inverse Problem

As discussed previously, there are problems where the dimension of the state space is infinite; this means that there are infinite solutions which may satisfy the data. It is then convenient to express the continuous function in terms of a finite number of parameters. Given the *state vector* $\boldsymbol{x}$ with n elements, the *measurement vector* $\boldsymbol{y}$ with m elements and the error vector $\boldsymbol{\varepsilon}$, the inverse problem may be written as:

$$\boldsymbol{y} = \boldsymbol{F}\left(\boldsymbol{x}\right) + \varepsilon \tag{4.3}$$

where the **bold** characters identify the vector quantities. $\boldsymbol{F}(\boldsymbol{x})$ is the *forward model* which comprises our understanding of the physics behind the measurements and the way the measurement device works.

A first step toward the solution of the inverse problem is the linearisation of the forward model about some reference state $\mathbf{x}_0$, if the non-linearities are not significant, this is often an adequate approximation:

$$\boldsymbol{y} - \boldsymbol{F}\left(\boldsymbol{x_0}\right) = \frac{\partial \boldsymbol{F}\left(\boldsymbol{x}\right)}{\partial \boldsymbol{x}}\left(\boldsymbol{x} - \boldsymbol{x}_0\right) + \varepsilon = \boldsymbol{K}\left(\boldsymbol{x} - \boldsymbol{x}_0\right) + \varepsilon \tag{4.4}$$

The eq.(4.4) defines the $m \times n$ weighting function matrix **K**, not necessarily square, where each element is the partial derivative of the forward model element i with respect to a state vector element j, i.e.:

$$Kij = \frac{\partial F_i(\boldsymbol{x})}{\partial x_j} \tag{4.5}$$

The term *weighting function* is peculiar to the atmospheric remote sounding. Matrix $\boldsymbol{K}$ may also be called *Jacobian,* since it is a matrix of derivatives, or the *kernel* of the problem (hence $\boldsymbol{K}$).

4.2 Linear Inverse Problems

Let us consider first a *linear* problem without measurement errors. This is an unrealistic situation but it is useful to introduce some concepts. In this case the problem reduces to the solution of the set of m linear equations:

$$\mathbf{y} = \mathbf{K}\,\mathbf{x}$$

This set of equations can have one, infinite, or no solutions. The m weighting function vectors $\mathbf{k}_j = (K_{1j},.....,K_{nj})$ will span some subspace of the state space whose dimension won't be greater than m and may be less than m if the vectors are not linearly independent. The dimension of this subspace, called the row space of $\boldsymbol{K}$, is known as the *rank* of the matrix **K** and it is denoted by p ($p \leq min(n,m)$). P is equal to the number of linearly independent rows (or columns) of $\boldsymbol{K}$; it means that the measurements represented by $\boldsymbol{K}$ cannot provide more than

p independent pieces of information to describe the state. Four different types of inverse problems can exist:

Case *1*: $m = n = p$
The number of unknowns is equal to the number of measurements and they are all independent. $\boldsymbol{K}$ is a square matrix; there's a unique solution which is called the *exact solution*:

$$\boldsymbol{x}_e = \boldsymbol{K}^{-1}\boldsymbol{y} \tag{4.6}$$

Case *2*: $p < m = n$
The number of unknowns is equal to the number of measurements, but the measurements are not independent, so they could be inconsistent; the number of independent pieces of information is less than the unknowns since the rank of **K** (p) is less than n: only the components of the state vector in the row space contribute to the measurement vector; all the components outside, which are orthogonal to it, give no contribution to the measurements, i.e. they are unmeasurable. So a part of the state space, called null space of **K,** is not determined. If a retrieved state has components in the null space as in this case, their values cannot be obtained from the measurements: they can take any value, so the solution of the inverse problem is not unique.

Cases *3*: $m < n$
The number of unknowns exceeds the number of simultaneous equations so that the parameters cannot be determined from the measurements. The number of unknowns must be reduced to a number lower than or equal to m: the other previously discussed cases can then be obtained.

Cases *4*: $m > n$
The number of measurements exceeds the number of unknowns, so the rank of $\boldsymbol{K}$ cannot be greater than n ($p \leq n$). If $p = n$, the unknowns are all in the row space: there's information about all of them. If $p < n$, a null space exists (see case *2*): the data have no information about the components of the state vector in the null space.

4.3 Least Squares Method

In the case there is not a unique solution that can fit all the measurements, some criterion must be used to select an acceptable one; the Least Squares Method (LSM) is one of the possible approaches. The LSM is appropriate when the number of measurements is considerably higher than the number of unknowns and when the algebraic form of the solution is someway known from reasonable physical assumptions. So we define:

- the residuals as the differences between the measurements and the forward model calculations made using the solution
- the residual norm or χ^2 as the sum of the squares of the residuals

The goal of LSM is to find a solution that minimizes the χ^2 which can be written as follows:

$$\chi^2 = \left(\boldsymbol{y} - \boldsymbol{K}\boldsymbol{x}\right)^T \left(\boldsymbol{y} - \boldsymbol{K}\boldsymbol{x}\right) \tag{4.7}$$

The minimization requires to equate the derivative of χ^2 with respect to $\boldsymbol{x}$ to zero:

$$\frac{\partial}{\partial \boldsymbol{x}}\chi^2 = 0 \Rightarrow \frac{\partial}{\partial \boldsymbol{x}}\left(\boldsymbol{y} - \boldsymbol{K}\boldsymbol{x}\right)^T \left(\boldsymbol{y} - \boldsymbol{K}\boldsymbol{x}\right) = 0 \Rightarrow 2\boldsymbol{K}^T \left(\boldsymbol{y} - \boldsymbol{K}\boldsymbol{x}\right) = 0 \tag{4.8}$$

$$\boldsymbol{K}^T \boldsymbol{y} = \boldsymbol{K}^T \boldsymbol{K}\boldsymbol{x}$$

Equation (4.8) is known as the "normal equation" of the Least Squares problem.
If $p = n$, $\mathbf{K}^T\mathbf{K}$ is invertible since it is an $n \times n$ matrix of independent rows and a unique solution is possible; then the best fit parameters $\hat{\mathbf{x}}$ can be expressed as:

$$\hat{\mathbf{x}} = (\mathbf{K}^T\mathbf{K})^{-1}\mathbf{K}^T\mathbf{y}. \tag{4.9}$$

The matrix $(\mathbf{K}^T\mathbf{K})^{-1}\mathbf{K}^T$ is also known as the *Moore-Penrose inverse* of $\mathbf{K}$. If $p < n$, there's an infinite number of exact solutions, all minimizing the χ^2*;* in this case a different kind of *s*olution should be developed.

4.3.1 Measurement Error

All real measurements are subject to experimental error or noise, so that any practical retrieval must allow for this. For a proper treatment of the experimental error we need a formalism which expresses both the uncertainty in the measurements and the resulting uncertainty in the retrievals. Moreover the search for a solution of the inverse problem must ensure that the uncertainty in the retrieved values is as small as possible. In the case of a scalar measurement $\bar{y}$ and an error σ, the *p*robability *d*ensity *f*unction *(pdf) P(y)* is a good description of our knowledge of its true value; usually *P(y)* is approximated by the *Gaussian* or *normal distribution* which fits well the experimental error in most cases:

$$P(y) = \frac{1}{\sigma\sqrt{2\pi}} \exp\left\{-\frac{(y-\bar{y})^2}{2\sigma^2}\right\} \tag{4.10}$$

When the measured quantity is a vector, as in our case, the probability density function can still be defined over the measurement space as:

$$P(\boldsymbol{y}) = \frac{1}{\sqrt{|\boldsymbol{S}_y|}\,(2\pi)^{n/2}} \exp\left\{-\frac{1}{2}\left(\boldsymbol{y}-\bar{\boldsymbol{y}}\right)^{\boldsymbol{T}} \boldsymbol{S}_y^{-1}\left(\boldsymbol{y}-\bar{\boldsymbol{y}}\right)\right\} \tag{4.11}$$

$\boldsymbol{S}_y$ is the *variance-covariance matrix* (VCM) of the measurements whose diagonal elements are the individual variances of each component of $\boldsymbol{y}$ and the off-diagonal elements are the covariances, i.e. the possible correlations between different components of the vector $\boldsymbol{y}$. VCM elements are defined as follows:

$$S_{ij} = \varepsilon\left\{(y_i - \bar{y}_i)(y_j - \bar{y}_j)\right\}$$

where ε is the expected value operator; clearly $\mathbf{S}_y$ must be non singular.
Let us suppose that the noise is gaussian-distributed with zero mean and covariance matrix $\mathbf{S}_\varepsilon$; then eq.(4.7) can be generalized to account for the measurements uncertainties; in this case a weighted χ^2 has to be minimized (*weighted least squares method*):

$$\chi^2 = \left(\boldsymbol{y} - \boldsymbol{K}\boldsymbol{x}\right)^T \boldsymbol{S}_\varepsilon^{-1}\left(\boldsymbol{y} - \boldsymbol{K}\boldsymbol{x}\right) \tag{4.12}$$

Deriving eq.(4.12) with respect to $\boldsymbol{x}$ and equating it to zero, the result is:

$$\hat{\mathbf{x}} = (\mathbf{K}^T \mathbf{S}_\varepsilon^{-1} \mathbf{K})^{-1} \mathbf{K}^T \mathbf{S}_\varepsilon^{-1} \mathbf{y}. \tag{4.13}$$

4.3.2 χ^2-test

Since the expectation value of the eq. (4.12) is $m - n$, a reduced χ^2 may be defined:

$$\chi^2_{red} = \frac{\chi^2}{m-n} \tag{4.14}$$

whose expectation value is now equal to 1. This reduced χ^2 provides a good estimate of the agreement between the forward model and the observations *(χ^2-test*): if it deviates too much from unity, it means that some incorrect assumptions have been made in the retrieval procedure or that systematic errors not included in the forward model are present; very small values are equally unacceptable: they may imply some misunderstanding of the experiment.

4.3.3 Bayesian Approach

Because of the ill-conditioned nature of the inverse problems, the mathematical solution often gives results that are unacceptable in the sense that they do not agree with our understanding and with our preliminary knowledge of the measured quantity. If this is the case, rather than looking for a measurement of the true state we must look for an *estimate* of the true state which is acceptably accurate in some statistical sense. In literature there are many statistical methods or probability techniques for combining the measurements with other information in order to select the best solution among all the possible ones. A very powerful tool in probability theory is the *Bayesian approach* [18] which in short permits to know how the measurement *pdf* maps into the state *pdf* and how it combines with prior expectations and notions. So the Bayes' theorem expresses the relationship between the conditional probability of **y** given $\boldsymbol{x}$ (P(**y**|**x**)), or alternatively the conditional probability of $\boldsymbol{x}$ given $\boldsymbol{y}$ (P(**x**|**y**)). For the vector case it states that:

$$P(\boldsymbol{x}|\boldsymbol{y}) = \frac{P(\boldsymbol{y}|\boldsymbol{x})P(\boldsymbol{x})}{P(\boldsymbol{y})} \tag{4.15}$$

Where:
P($\boldsymbol{x}$) is the a priori *pdf* of the state $\boldsymbol{x}$, i.e. our quantitative knowledge of $\boldsymbol{x}$ before the measurement is made
P($\boldsymbol{y}$) is the a priori *pdf* of the measurement $\boldsymbol{y}$, i.e. the *pdf* before the measurement is made.
In the left-hand side of the equation P(**x**|**y**) represents the posterior *pdf* of the state when the measurement is made: it is the quantity that we obtain when we update the a priori knowledge P(**x**) of the state with the measurement **y**. P(**y**|**x**) requires the knowledge of the forward model and the statistical description of the measurement error. The denominator, P(**y**), can be determined as a normalization term. It can be noted that the Bayesian view is quite general: given a measurement together with its error statistics, a forward model describing the relation between the measurement and the unknown state and any a priori information that might be available, it enables to identify the *class* of possible states that are consistent with the available information, and to assign them a probability density. It is very important to underline that the Bayes' theorem does not produce a solution but an estimate of the possible solutions; so more work is needed to find out which is the result of the inverse problem.

4.3.4 Example of Bayes' Theorem: the linear problem with gaussian statistics

Let's analyse a simple example of the Bayesian approach where the following assumptions are made:

- the problem is linear with a linear solution. We expect the linear solution to be in the general form

$$\hat{\mathbf{x}} = \mathbf{x}_0 + \mathbf{G}\mathbf{y} \tag{4.16}$$

  where $\mathbf{x}_0$ is some constant offset and $\mathbf{G}$ is the $n \times m$ retrieval gain matrix that in its general form is given by:

$$\boldsymbol{G} = \left(\boldsymbol{K}^T \boldsymbol{S}^{-1} \boldsymbol{K}\right)^{-1} \boldsymbol{K}^T \boldsymbol{S}^{-1} \tag{4.17}$$

  $\mathbf{G}$ has various names: in atmospheric literature it is often called *contribution function* matrix. If there is an error ε in the measurement, then there will obviously be a corresponding error $\mathbf{G}_\varepsilon$ in the solution; thus the size of the gain provided by the matrix $\mathbf{G}$ quantifies the ill-conditioning nature of the solution.

- all *pdf*s are gaussian (eq.(4.11)). It must be noted that for the measurement error the gaussian distribution is usually a good approximation but for the a priori knowledge of the state it is less realistic.

The maximum probability value for $\mathbf{x}$ is equal to its expected value, because the *pdf* beeing a gaussian distribution is symmetric about it.
For simplicity, instead of using $P(\mathbf{y}|\mathbf{x})$ the Bayes' theorem will be expressed through the scalar quantity J:

$$J = -ln\left[P\left(\boldsymbol{x}|\boldsymbol{y}\right)\right] + constant \tag{4.18}$$

which will be referred to as the *cost function* hereafter.
Since all *pdf*s are gaussian, the following expressions can be written for the a priori knowledge of $\boldsymbol{x}$ (eq.(4.20)), using equation:

$$P(\boldsymbol{x}) = \frac{1}{(2\pi)^{N/2}\left|\boldsymbol{S}_a\right|^{1/2}} \exp\left\{-\frac{1}{2}\left(\boldsymbol{x}-\boldsymbol{x}^a\right)^T (\boldsymbol{S}_a)^{-1}\left(\boldsymbol{x}-\boldsymbol{x}^a\right)\right\} \tag{4.19}$$

We can obtain:

$$\ln P(\boldsymbol{x}) = \ln\left(\frac{1}{(2\pi)^{N/2}\left|\boldsymbol{S}_a\right|^{1/2}}\right) - \frac{1}{2}\left(\boldsymbol{x}-\boldsymbol{x}^a\right)^T (\boldsymbol{S}_a)^{-1}\left(\boldsymbol{x}-\boldsymbol{x}^a\right)$$

And thus,

$$
\begin{aligned}
-2\ln P(\boldsymbol{x}) &= -2\ln\left(\frac{1}{(2\pi)^{N/2}\left|\boldsymbol{S}_a\right|^{1/2}}\right)+\left(\boldsymbol{x}-\boldsymbol{x}^a\right)^T(\boldsymbol{S}_a)^{-1}\left(\boldsymbol{x}-\boldsymbol{x}^a\right) \\
&= \left(\boldsymbol{x}-\boldsymbol{x}^a\right)^T(\boldsymbol{S}_a)^{-1}\left(\boldsymbol{x}-\boldsymbol{x}^a\right)+c_2
\end{aligned}
\tag{4.20}
$$

In the same way, for the measurements conditional probability, using equation

$$
P(\boldsymbol{y}|\boldsymbol{x}) = \frac{1}{(2\pi)^{N/2}\left|\boldsymbol{S}_\varepsilon\right|^{1/2}}\exp\left\{-\frac{1}{2}(\boldsymbol{y}-\boldsymbol{K}\boldsymbol{x})^T(\boldsymbol{S}_\varepsilon)^{-1}(\boldsymbol{y}-\boldsymbol{K}\boldsymbol{x})\right\} \tag{4.21}
$$

we can obtain:

$$
-2\ln P(\mathbf{y}\mid\mathbf{x}) = (\mathbf{y}-\mathbf{K}\mathbf{x})^T\mathbf{S}_\varepsilon^{-1}(\mathbf{y}-\mathbf{K}\mathbf{x})+c_1, \tag{4.22}
$$

where c_1 and c_2 are constants, $\mathbf{S}_\varepsilon$ is the measurement error VCM, $\boldsymbol{x}_a$ the a priori value of $\mathbf{x}$ and $\mathbf{S}_a$ is the associated VCM. Eq.(4.20) and eq.(4.22) into the Bayes' theorem result in the a posteriori *pdf* of $\boldsymbol{x}$:

$$
-2\ln P(\mathbf{x}\mid\mathbf{y}) = (\mathbf{y}-\mathbf{K}\mathbf{x})^T\mathbf{S}_\varepsilon^{-1}(\mathbf{y}-\mathbf{K}\mathbf{x})+(\mathbf{x}-\mathbf{x}_a)^T\mathbf{S}_a^{-1}(\mathbf{x}-\mathbf{x}_a)+c_3, \tag{4.23}
$$

where c_3 is a constant that includes the *cost function* of the measurements (ln P($\mathbf{y}$)).
Since P($\mathbf{x}$|$\mathbf{y}$) is also a gaussian distribution with expected value $\hat{\mathbf{x}}$ and covariance $\hat{\mathbf{S}}$, it is a quadratic form in $\boldsymbol{x}$ as the previous *pdf*s:

$$
-2\ln P(\mathbf{x}\mid\mathbf{y}) = (\mathbf{x}-\hat{\mathbf{x}})^T\hat{\mathbf{S}}^{-1}(\mathbf{x}-\hat{\mathbf{x}})+c_4. \tag{4.24}
$$

Equating the quadratic terms in $\boldsymbol{x}$ in Eqs. (4.23) and (4.24), one obtains:

$$
\begin{aligned}
\mathbf{x}^T\mathbf{K}^T\mathbf{S}_\varepsilon^{-1}\mathbf{K}\mathbf{x}+\mathbf{x}^T\mathbf{S}_a^{-1}\mathbf{x} &= \mathbf{x}^T\hat{\mathbf{S}}^{-1}\mathbf{x} \\
\hat{\mathbf{S}}^{-1} &= \mathbf{K}^\mathbf{T}\mathbf{S}_\boldsymbol{\varepsilon}^{-\mathbf{1}}\mathbf{K}+\mathbf{S}_a^{-1}
\end{aligned}
\tag{4.25}
$$

Likewise, equating the linear terms in $\mathbf{x}^T$, one obtains:

$$
\left(-\mathbf{K}\mathbf{x}\right)^\mathbf{T}\mathbf{S}_\varepsilon^{-1}\left(\mathbf{y}\right)+\mathbf{x}^\mathbf{T}\mathbf{S}_a^{-1}\left(-\mathbf{x}_a\right) = \mathbf{x}^\mathbf{T}\hat{\mathbf{S}}^{-1}\left(-\hat{\mathbf{x}}\right) \tag{4.26}
$$

Substituting $\hat{\mathbf{S}}^{-1}$ with eq.
(4.25), the expression becomes:

$$
\mathbf{K}^T\mathbf{S}_\varepsilon^{-1}\mathbf{y}+\mathbf{S}_a^{-1}\mathbf{x}_a = (\mathbf{K}^T\mathbf{S}_\varepsilon^{-1}\mathbf{K}+\mathbf{S}_a^{-1})\hat{\mathbf{x}} \tag{4.27}
$$

and hence:

$$
\hat{\mathbf{x}} = (\mathbf{K}^T\mathbf{S}_\varepsilon^{-1}\mathbf{K}+\mathbf{S}_a^{-1})^{-1}(\mathbf{K}^T\mathbf{S}_\varepsilon^{-1}\mathbf{y}+\mathbf{S}_a^{-1}\mathbf{x}_a). \tag{4.28}
$$

$\hat{\mathbf{x}}$ is the expected value of the solution of the Bayes' theorem, i.e. the a posteriori *pdf* of the state vector. Note that if we assume that the a priori knowledge of $\boldsymbol{x}$ is uniform, i.e. P($\mathbf{x}$)=*C*

where C is a constant, $\mathbf{S}_a^{-1}$ is equal to zero and the expected value $\hat{\mathbf{x}}$ and the corresponding covariance $\hat{\mathbf{S}}$ become:

$$\hat{\mathbf{x}} = (\mathbf{K}^T\mathbf{S}_\varepsilon^{-1}\mathbf{K})^{-1}\mathbf{K}^T\mathbf{S}_\varepsilon^{-1}\mathbf{y} \quad \text{and} \quad \hat{\mathbf{S}}^{-1} = \mathbf{K}^T\mathbf{S}_\varepsilon^{-1}\mathbf{K}.$$

This is the solution of the weighted *LSM*, expressed by the eq. (4.13). For the well-posed problem, an exact solution is possible, such that a matrix $\mathbf{G}$ exists so $\mathbf{KG} = \mathbf{I}_m$, the identity matrix (e.g. we could choose $\mathbf{G} = \mathbf{K}^T (\mathbf{K}\mathbf{K}^T)^{-1}$). If we insert $\mathbf{KG}$ before $\mathbf{y}$ in Eq. (4.28), we obtain:

$$\hat{\mathbf{x}} = (\mathbf{K}^T\mathbf{S}_\varepsilon^{-1}\mathbf{K} + \mathbf{S}_a^{-1})^{-1}(\mathbf{K}^T\mathbf{S}_\varepsilon^{-1}\mathbf{K}(\mathbf{G}\mathbf{y}) + \mathbf{S}_a^{-1}\mathbf{x}_a). \tag{4.29}$$

This represents a weighted mean of the *a priori* $\boldsymbol{x}_a$ and *any* exact retrieval $\mathbf{x}_e = \mathbf{G}\mathbf{y}$ with matrix weights $\mathbf{S}_a^{-1}$ and $\mathbf{K}^T\mathbf{S}_\varepsilon^{-1}\mathbf{K}$ respectively.

4.3.5 Optimal Linear Inverse Methods

The Bayesian approach provides a framework within which we can understand the inverse problem: it allows to find a group of possible states given the available information. However, in most cases it is desirable to have "the solution", instead of a bunch of possible states; it is then necessary to specify an objective selection criterion to obtain that. The most straightforward and logical approach is to choose the solution that optimizes something; there's a range of possible quantities that may be used, for example:

- the solution can be either the expected value or the most likely state ("maximum a posteriori solution") according to the posterior pdf of the state vector; the error estimate is provided by some measure of the width of the pdf. If the pdfs are gaussian, these two approaches lead to the same result since the normal distribution is symmetric.
- any term that contributes to the error analysis is a quantity that might be minimised in a solution

4.4 Non-linear Inverse Problems

It might be believed that the source of non-linearity in an inversion problem may come just from the non-linearity of the forward model; in practice this definition turns out to be a bit too oversimplified. An inversion problem does not contain just the information coming from the forward model; there may be various kinds of prior information which contribute: they can introduce non-linear terms even when the forward model is linear; for example any non-gaussian *pdf* as a prior information would lead to a non-linear problem.
It is possible to make a qualitative classification of the degree of linearity of inverse problems as follows:

- *Linear*: when the forward model can be put in the form $\mathbf{y} = \mathbf{K}\mathbf{x}$ and any a priori is gaussian; very few practical problems are truly linear.
- *Nearly linear*: problems which are non-linear, but for which a linearisation about some a priori state is adequate to find a solution.
- *Moderately non-linear*: problems where linearisation is adequate for the error analysis, but not for finding a solution. Since many problems are of this kind, this is the case which will be analysed.

- *Grossly non-linear*: problem which are non-linear even within the range of the errors.

Much of what has been described so far for linear problems applies directly to moderately non-linear problems when they are appropriately linearised. The main difference is that there is no general explicit expression for optimal solutions in the moderately non-linear case, as there is for linear and nearly linear problems.
Now we assume that the forward model is a non-linear mapping from the state space into the measurement space. The inverse mapping from the measurement space into the state space will map the *pdf* of the measurement error into a *pdf* in the state space: if the problem is no worse than moderately non-linear and the measurement error is gaussian, then the retrieval error will be gaussian and the linear error analysis will apply.
The primary task of a linear retrieval method is to select a state satisfying some criterion of optimality from an ensemble of states which agree with the measurement within the experimental error; finding the set of possible states is straightforward .
In the non-linear case it may no longer be possible to write down an explicit solution; it must be found numerically or iteratively. For non-linear problems we can consider either the maximum *a posteriori* approach or the equivalent least squares method.
In case the forward model is a general function of the state and the measurement error is gaussian, the Bayesian solution for the linear problem (eq. (4.23)) can be modified into the following equations, respectively with and without the a priori information:

$$\begin{aligned} J_{with\_a} &= \left[\mathbf{y}-\mathbf{F}(\mathbf{x})\right]^T \mathbf{S}_\varepsilon^{-1}\left[\mathbf{y}-\mathbf{F}(\mathbf{x})\right]+\left[\mathbf{x}-\mathbf{x}_a\right]^T \mathbf{S}_a^{-1}\left[\mathbf{x}-\mathbf{x}_a\right]+c \\ J_{without\_a} &= \left[\mathbf{y}-\mathbf{F}(\mathbf{x})\right]^T \mathbf{S}_\varepsilon^{-1}\left[\mathbf{y}-\mathbf{F}(\mathbf{x})\right]+c \end{aligned} \tag{4.30}$$

Like the linear case, the goal is to find the best estimate $\hat{\mathbf{x}}$ and its *pdf*. The solution comes from the minimization of the cost function *J*; so the derivative of *J* with respect to $\boldsymbol{x}$ must be set to zero; the resulting expressions are:

$$\begin{aligned} \nabla_x J_{with\_a} &= -\left[\boldsymbol{K}(\boldsymbol{x})\right]^T \boldsymbol{S}^{-1}{}_\varepsilon \left[\boldsymbol{y}-\boldsymbol{F}(\boldsymbol{x})\right]+\boldsymbol{S}^{-1}{}_a\left[\boldsymbol{x}-\boldsymbol{x}_a\right]=0 \\ \nabla_x J_{without\_a} &= -\left[\boldsymbol{K}(\boldsymbol{x})\right]^T \boldsymbol{S}^{-1}{}_\varepsilon \left[\boldsymbol{y}-\boldsymbol{F}(\boldsymbol{x})\right]=0 \end{aligned} \tag{4.31}$$

where $\boldsymbol{K}(\boldsymbol{x})=\nabla \boldsymbol{F}(\boldsymbol{x})$. In this case the solution of eqs.(4.31) is not that straightforward since they must be solved numerically; the difficulty is mainly due to the non-linearity of the forward model $\boldsymbol{F}(\boldsymbol{x})$.

4.4.1 Newton and Gauss-Newton methods

If the non-linearity is not so significant, the zero of the gradient of the cost function *J* can be calculated numerically using the Newtonian iteration method. For a general *vector equation* $\boldsymbol{g}(\boldsymbol{x})=0$, the Newton's iteration can be written similarly to the scalar case as:

$$\mathbf{x}_{i+1} = \mathbf{x}_i - \left[\nabla_x \mathbf{g}(\mathbf{x}_i)\right]^{-1} \mathbf{g}(\mathbf{x}_i), \tag{4.32}$$

In our case $\boldsymbol{g}(\boldsymbol{x})$ is the first derivative of the cost function *J* (eqs.(4.31)):

$$\boldsymbol{g}(\boldsymbol{x}) = \nabla_x \boldsymbol{J} \tag{4.33}$$

so the first derivative of $\boldsymbol{g}(\boldsymbol{x})$ corresponds to the second derivative of J, and it is known as the *Hessian*:

$$\begin{aligned}\nabla_x \boldsymbol{g}(\boldsymbol{x}) &= \nabla^2{}_x J_{with\_a} = \boldsymbol{S}^{-1}{}_a + \boldsymbol{K}^T \boldsymbol{S}^{-1}{}_\varepsilon \boldsymbol{K} - \left[\nabla_x \boldsymbol{K}^T\right] \boldsymbol{S}^{-1}{}_\varepsilon \left[\boldsymbol{y} - \boldsymbol{F}(\boldsymbol{x})\right] \\ \nabla_x \boldsymbol{g}(\boldsymbol{x}) &= \nabla^2{}_x J_{without\_a} = \boldsymbol{K}^T \boldsymbol{S}^{-1}{}_\varepsilon \boldsymbol{K} - \left[\nabla_x \boldsymbol{K}^T\right] \boldsymbol{S}^{-1}{}_\varepsilon \left[\boldsymbol{y} - \boldsymbol{F}(\boldsymbol{x})\right]\end{aligned} \tag{4.34}$$

The *Hessian* comprises both the first and the second derivatives of the forward model, i.e. the Jacobian $\boldsymbol{K}$ and $\nabla_x \boldsymbol{K}^T$ respectively. $\nabla_x \boldsymbol{K}^T$ is quite a complicated object but in the moderately linear problems the part of the eqs.(4.34) which contains it is usually negligible; so we will ignore it. Consequently, the omission of this term and the combination of the equations (4.31), (4.32) and (4.34) give the Gauss-Newton method:

$$\begin{gathered}\mathbf{x}_{i+1} = \mathbf{x}_i + (\mathbf{S}_a^{-1} + \mathbf{K}_i^T \mathbf{S}_\varepsilon^{-1} \mathbf{K}_i)^{-1} [\mathbf{K}_i^T \mathbf{S}_\varepsilon^{-1} (\mathbf{y} - \mathbf{F}(\mathbf{x}_i)) - \mathbf{S}_a^{-1} (\mathbf{x}_i - \mathbf{x}_a)] \\ \textit{or} \\ \mathbf{x}_{i+1} = \mathbf{x}_i + (\mathbf{K}_i^T \mathbf{S}_\varepsilon^{-1} \mathbf{K}_i)^{-1} \mathbf{K}_i^T \mathbf{S}_\varepsilon^{-1} [\mathbf{y} - \mathbf{F}(\mathbf{x}_i)]\end{gathered} \tag{4.35}$$

where $\mathbf{K}_i = \mathbf{K}(\mathbf{x})|_{\mathbf{x}_i}$; equations (4.35) represent the iterative solution in a non-linear problem with and without the a priori information.
When does the iteration procedure stop? *Convergence criteria* are needed in order to establish when the minimum of J is close enough to stop the procedure; obviously the main task of the convergence test must be to check whether the difference between the solution and the maximum probability state is negligible in comparison with the solution error. There are different kinds of criteria which may be chosen such as, for example, checking for the smallness of the reduction of the cost function in the subsequent iterations or of the gradient of the cost function. Once the iteration has converged, it is quite important to examine if the solution is the *correct answer*; the cost function may have multiple minima so it might happen to find a spurious minimum. For this purpose the χ^2-test can be used (see sect. 4.3.2).
In case some a priori information is available eq.(4.35) shows the way it can be combined with the solution of the previous iteration (it is also called *optimal estimation formula*). However it is also possible to decide to use the a priori vector $\boldsymbol{x_a}$ after the convergence is reached:

$$\boldsymbol{x\_new} = \boldsymbol{x} + \left[\boldsymbol{S_a}^{-1} + \boldsymbol{K}^T \boldsymbol{S_\varepsilon}^{-1} \boldsymbol{K}\right]^{-1} \left[\boldsymbol{K}^T \boldsymbol{S_\varepsilon}^{-1} \left(\boldsymbol{y} - \boldsymbol{F(x)}\right) - \boldsymbol{S_a}^{-1} \left(\boldsymbol{x} - \boldsymbol{x_a}\right)\right] \tag{4.36}$$

The best choice is specific of the type of a priori information available.

4.4.2 Levenberg-Marquardt method

If the cost function J is exactly quadratic in $\boldsymbol{x}$ as in the linear case (its gradient is linear=one minimum), both the Newton and the Gauss-Newton methods will reach the minimum in one step; if J is nearly quadratic, the two approaches will get close to it but for moderately linear problems it may also be seriously non-quadratic so that the solution is quite far away from the minimum. These approaches can then give bad results, far from the true minimum if the true solution is sufficiently distant from the iteration result. In these cases, the χ^2 may even increase rather than decrease during the iterations.
To avoid the latter case, for the non-linear least squares problem, Levenberg [19] proposed the following iterative solution:

$$\boldsymbol{x}_{i+1} = \boldsymbol{x}_i + \left(\boldsymbol{K}_i^T \boldsymbol{S}_\varepsilon^{-1} \boldsymbol{K}_i + \lambda_i \boldsymbol{I}\right)^{-1} \boldsymbol{K}_i^T \boldsymbol{S}_\varepsilon^{-1} \left[\boldsymbol{y} - \boldsymbol{F}(\boldsymbol{x}_i)\right] \tag{4.37}$$

where λ_i is chosen at each step to maximally reduce the cost function; it can be seen that for $\lambda_i \to 0$ the iteration coincides with the Gauss-Newton one. Selecting the optimal value of λ_i requires a significant computational effort; so Marquardt [20] simplified the choice of λ_i by not searching for the best λ_i at each iteration, but by starting a new iteration step as soon as a value is found for which the cost function is reduced. An initially arbitrary value of λ is then updated at each iteration.
A simplified version of Marquardt's method is given by Press and al. [21]:

- if χ^2 increases as a result of a step, increase λ, do not update $\mathbf{x}_i$ and try again
- if χ^2 decreases as a result of a step, update $\mathbf{x}_i$ and decrease λ for the next step

The factor by which λ is increased or decreased is usually empirically determined.

4.5Regularization methods

The a priori knowledge sometimes is not provided by the measurement of the unknown but by some general understanding of its shape and behaviour.
We may regard solving the inverse problem as a competition between two conflicting desires:

- the desire to minimize the residual
- the desire for the solution to have a small sum-square norm or to be smooth or similar to what we believe the answer should be.

One way of selecting a solution from several feasible reconstructions is to introduce a second function $\Omega(\mathbf{x})$ representing our version of a particular reconstruction. For example, we can decide that the solution of minimum norm should be selected from the feasible set; this can be done by choosing $\Omega(\mathbf{x}) = \|\mathbf{x}\|^2$. Sometimes, we have a preference for reconstructions that are close to some default solution or a priori knowledge $\mathbf{x}^\infty$. This may be appropriate if we have historical information about the quantity. This can be done by choosing $\Omega(\mathbf{x}) = \|\mathbf{x} - \mathbf{x}^\infty\|^2$.
More generally, it may not be the norm of $\mathbf{x} - \mathbf{x}^\infty$ which needs to be small, but some linear operator acting on this difference. Introducing the operator $\mathbf{L}$ for this purpose, we can set:

$$\Omega(\mathbf{x}) = \left\|L(\mathbf{x} - \mathbf{x}^\infty)\right\|^2 = (\mathbf{x} - \mathbf{x}^\infty)^T L^T L(\mathbf{x} - \mathbf{x}^\infty). \tag{4.38}$$

$\mathbf{L}$ is a $p \times n$ matrix, where $p \le n$ (n: dimension of unknown space, p: rank of $\mathbf{K}$). Typically, $\mathbf{L}$ is the identity matrix or a banded matrix approximation to the $(n - p)^{\text{th}}$ derivative. There are many ways of balancing the conflicting requirements of minimizing the residual and the $\Omega(\mathbf{x})$ function and these lead to a variety of regularization methods.

4.5.1 Twomey-Tikhonov regularization

The first two methods applied to the retrieval problem, in which error sensitivity and constraints were considered, were published at about the same time by Twomey [22] and by Tikhonov [23].
Both methods consider the minimization of the following function R:

$$R = \left(\boldsymbol{y} - \boldsymbol{K}\boldsymbol{x}\right)^T \left(\boldsymbol{y} - \boldsymbol{K}\boldsymbol{x}\right) + \gamma^2 \left(\boldsymbol{x} - \boldsymbol{x}_a\right)^T \boldsymbol{L}^T \boldsymbol{L} \left(\boldsymbol{x} - \boldsymbol{x}_a\right) \tag{4.39}$$

where

$(\boldsymbol{y}-\boldsymbol{Kx})^T(\boldsymbol{y}-\boldsymbol{Kx})$ is the square of the residual norm, and
$(\boldsymbol{x}-\boldsymbol{x}_a)^T\boldsymbol{L}^T\boldsymbol{L}(\boldsymbol{x}-\boldsymbol{x}_a)$ is the square of the difference of the solution from some a priori x_a

A whole family of solutions is parameterized by the weighting factor γ^2; γ is the *regularization parameter*. A formal solution to the problem may be found by minimizing the function *R*:

$$\hat{\boldsymbol{x}}=\left(\boldsymbol{K}^T\boldsymbol{K}+\gamma^2\boldsymbol{L}\boldsymbol{L}^T\right)^{-1}\left(\boldsymbol{K}^T\boldsymbol{y}+\gamma^2\boldsymbol{L}^T\boldsymbol{L}\boldsymbol{x}_a\right) \tag{4.40}$$

If γ is very large, the solution is usually smoother; it is closer to the a priori solution and less affected by the noise on the data because they are effectively ignored. Whereas for small values of γ, the solution can be very sensitive to noise as it is primarily determined by the requirement of minimizing the residual. Of course, if γ is reduced to zero, the problem reduces to the least-squares case considered earlier.
Perhaps the most convenient graphical tool for setting the regularization parameter γ is the "L-curve" (Figure 4.1): plotting $\log\|\boldsymbol{y}-\boldsymbol{K}\boldsymbol{x}_\gamma\|$ versus $\log\|\boldsymbol{x}_\gamma-\boldsymbol{x}_a\|$ generates the characteristic L-shaped curve with a corner separating the vertical and horizontal parts of the curve. The regularization is a trade-off between the residual norm $\|\mathbf{y}-\mathbf{K}\mathbf{x}\|$ and the solution semi-norm $\mathbf{L}\|\mathbf{x}-\mathbf{x}_a\|$.

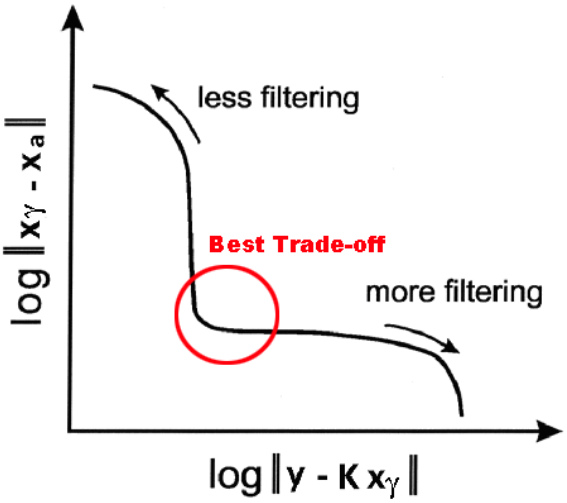

Figure 4.1:The generic form of the L-curve. "more filtering" = higher γ.

In the vertical part of the curve the solution semi-norm is a very sensitive function of the regularization parameter because the solution is undergoing large changes with γ in an attempt to fit better the data. On the horizontal part, the solution is not changing very much as γ changes; however, the residuals are sharply increasing with increasing γ. So it is desirable to choose a solution which lies not too far from the corner.

4.6 Quality of the retrievals

In our case, the inverse problem is the search for the vertical distribution (profile) of the concentration of some atmospheric gas that minimizes the difference between the simulated and the measured spectra. The quality of the solution of the inverse problem is then determined by the vertical resolution and the accuracy of the retrieved profiles. The averaging kernel provides a rigorous tool for the characterisation of the vertical resolution. The accuracy

of the retrieval depends on several considerations. A general mathematical description of the different errors that can affect the retrieval is discussed by Rodgers [17].

4.6.1 Averaging Kernels

The Averaging Kernel Matrix (A_{AKM}) is the derivative of the retrieved profiles with respect to the true profiles performed in a particular state of the atmosphere (linearisation point [17]) and indicates the way in which the observing system smoothes the profile.

$$A_{AKM} = \left.\frac{d\hat{x}}{dx}\right|_{\tilde{x}} \tag{4.41}$$

In an ideal inverse method, A_{AKM} would be a unit matrix. In reality the rows of A_{AKM} are in general functions peaking at the appropriate level and with a finite half-width that is a measure of the spatial resolution of the observing system. The A_{AKM} provides information on the vertical resolution of the measurement and its knowledge is indispensable in inter-comparison and assimilation problems. The analytical expression of A_{AKM} is obtained considering the expression of the forward and the retrieval models expanded up to the first order:

$$\begin{aligned} \boldsymbol{y} - \tilde{\boldsymbol{y}} &= \boldsymbol{K}(\boldsymbol{x} - \tilde{\boldsymbol{x}}) + \boldsymbol{\varepsilon} \\ \hat{\boldsymbol{x}} - \tilde{\boldsymbol{x}} &= \boldsymbol{G}(\boldsymbol{y} - \tilde{\boldsymbol{y}}) \end{aligned} \tag{4.42}$$

where $\boldsymbol{y}$ is the measurement vector related to the state $\boldsymbol{x}$, $\tilde{\boldsymbol{y}}$ is the measurement vector related to the true state $\tilde{\boldsymbol{x}}$, $\boldsymbol{K}$ is the Jacobian matrix calculated in the fine vertical grid of the true profile, $\hat{\boldsymbol{x}}$ is the retrieved state when the measurement is y, and $\mathbf{G}$ is the gain matrix representing the mapping of the measurement variations into the coarse vertical grid of the retrieval variations. From equations (4.42) in the case of negligible measurement errors ε we have

$$\hat{\boldsymbol{x}} - \tilde{\boldsymbol{x}} = \boldsymbol{KG}(\boldsymbol{x} - \tilde{\boldsymbol{x}}) \tag{4.43}$$

From the eq. (4.41), we obtain the analytical expression for A_{AKM}:

$$\boldsymbol{A}_{\boldsymbol{AKM}} = \boldsymbol{GK} \tag{4.44}$$

with the gain matrix G:

$$\boldsymbol{G} = \left(\boldsymbol{K}^{\boldsymbol{T}}\boldsymbol{S}^{-1}\boldsymbol{K} + \boldsymbol{P}\right)^{-1}\boldsymbol{K}^{\boldsymbol{T}}\boldsymbol{S}^{-1} \tag{4.45}$$

where the term $\boldsymbol{P}$ is a perturbation term that in the case of Optimal Estimation is the inverse of the covariance matrix related to the a priori profile ($\mathbf{P} = \mathbf{S}_a^{-1}$) or accounts for all the regularisation procedures; in the case of Tikhonov regularization: $\mathbf{P} = \gamma\mathbf{L}^{\mathbf{T}}\mathbf{L}$; in the case of Levenberg Marquardt solution $\mathbf{P} = \lambda\mathbf{I}$. Therefore equation (4.44) becomes:

$$\boldsymbol{A}_{\boldsymbol{AKM}} = \left(\boldsymbol{K}^{\boldsymbol{T}}\boldsymbol{S}^{-1}\boldsymbol{K} + \boldsymbol{P}\right)^{-1}\boldsymbol{K}^{\boldsymbol{T}}\boldsymbol{S}^{-1}\boldsymbol{K} \tag{4.46}$$

The A_{AKM} can be calculated analytically using equation (4.46) or numerically using a perturbation method.

The analytical calculation can in principle be performed together with the retrieval operation. The calculation with the perturbation method is a time consuming operation, but it can be performed off-line without interfering with the retrieval process. Furthermore, this off-line calculation can be limited to a few test cases that correspond to typical measurement conditions.

4.6.2 Averaging Kernels integral and Full Width Half Maximum

The range of altitudes over which the observing system is sensitive to the profile is indicated by the range of retrieval altitudes for which the area of the relative averaging kernel (the sum of its elements) is of the order of unity. Outside this range the area will tend toward zero.
If x describes an altitude profile of some quantity, the l-th row of A can be regarded to as a smoothing function for the altitude corresponding to l-th element of the vector x. This smoothing function is a peaked function, whose width, the Full Width at Half Maximum (FWHM) of the Averaging Kernel, qualitatively describes the vertical resolution of the retrieval.

4.6.3 Trace of the Averaging Kernel matrix and Information Content

Other useful parameters in assessing the quality of the retrieval are the trace of the Averaging Kernel Matrix and the information content.
The trace of AKM gives information about the degrees of freedom of the retrieval and is related to the rank of matrix $\boldsymbol{K}$ (sect. 4.2).
The information content, H, of the measurement and its degrees of freedom are closely related. They both characterize the change in the knowledge of the state as a result of making a measurement. The information content describes the reduction in the entropy given by the difference between the knowledge after and before a measurement.
The information content of a measurement depends on the entropies of the probability density function (pdf) before and after the measurement. In general terms, if the pdf $P_A(x)$ describes the knowledge before a measurement and $P(x)$ describes it afterwards, then the information content of the measurement is the reduction in its entropy (ε is the expected value operator):

$$H = \varepsilon(P_A) - \varepsilon(P) \tag{4.47}$$

where $\varepsilon(P)$ is the entropy of the continuous pdf defined by:

$$\varepsilon(P) = -\int P(x) \log_2 P(x) dx \tag{4.48}$$

The entropy of a multivariate Gaussian distribution for a vector with m elements is:

$$\varepsilon(P(x)) = m \ln(2\pi e)^{1/2} + \frac{1}{2} \ln|S_x| \tag{4.49}$$

The information content of a measurement when the prior covariance is S_a and the posterior covariance is S^x can be written as:

$$H = \frac{1}{2} \ln|S_a| - \frac{1}{2} \ln|S^x| \tag{4.50}$$

It is important to notice that the evaluation of the information content of a measurement can be performed both in the state space *Hs* and in the measurement space *Hm*. In the state space

the measurement depends on the entropy of the pdf of the state before the measurement and on the *posterior-pdf* after the measurement, according to the following:

$$H = \varepsilon(P(x)) - \varepsilon(P(x)|y) \tag{4.51}$$

Where $\varepsilon(P(x)|y)$ is the conditional entropy of the state given the measure y, that is the uncertainty on x when y is known. Trivially, if the estimation is perfect this term is null. In the case of the use of optimal estimation by assuming gaussian distribution the knowledge of the state before the measurement is given by equation (4.19) and its entropy (using natural logarithm for algebraic convenience) is:

$$\varepsilon(P_a) = N \ln(2\pi e)^{1/2} + \frac{1}{2}\ln|S_a| \tag{4.52}$$

where the symbol |…| denotes the determinant of the matrix. After the measurement the knowledge of the state is given by equation (4.21) and its entropy:

$$\varepsilon(P) = N \ln(2\pi e)^{1/2} + \frac{1}{2}\ln|S^x| \tag{4.53}$$

With, in case of optimal estimation:

$$\boldsymbol{S}^x = \left(\boldsymbol{K}^T \boldsymbol{S}^{-1} \boldsymbol{K} + (\boldsymbol{S}_a)^{-1}\right)^{-1} \tag{4.54}$$

According to the previous formulas we obtain the information content of the measurement in the state space:

$$\boldsymbol{H} = \frac{1}{2}\boldsymbol{ln}|\boldsymbol{S}_a| - \frac{1}{2}\boldsymbol{ln}|\boldsymbol{S}^x| = \frac{1}{2}\boldsymbol{ln}\left|\left(\boldsymbol{S}^x\right)^{-1}\boldsymbol{S}_a\right| \tag{4.55}$$

That is

$$\boldsymbol{H} = \frac{1}{2}\boldsymbol{ln}\left|(\boldsymbol{K}^T \boldsymbol{S}^{-1} \boldsymbol{K} + (\boldsymbol{S}_a)^{-1})\boldsymbol{S}_a\right| \tag{4.56}$$

This formula is used to estimate the gain of information on the vector x due to a measurement. We can also relate the information content with the averaging kernel matrix. Therefore, according to equation (4.46) one can find:

$$\boldsymbol{I} - \boldsymbol{A}_{AKM} = \boldsymbol{I} - \left(\boldsymbol{K}^T \boldsymbol{S}^{-1} \boldsymbol{K} + \boldsymbol{S}_a^{-1}\right)^{-1} \boldsymbol{K}^T \boldsymbol{S}^{-1} \boldsymbol{K} \tag{4.57}$$

But the unit matrix I can be written as :

$$\boldsymbol{I} = \left(\boldsymbol{K}^T \boldsymbol{S}^{-1} \boldsymbol{K} + \boldsymbol{S}_a^{-1}\right)^{-1} (\boldsymbol{K}^T \boldsymbol{S}^{-1} \boldsymbol{K} + \boldsymbol{S}_a^{-1}) \tag{4.58}$$

And thus:

$$\begin{aligned} \boldsymbol{I}-\boldsymbol{A}_{AKM} &= \left(\boldsymbol{K}^T\boldsymbol{S}^{-1}\boldsymbol{K}+\boldsymbol{S}_a^{-1}\right)^{-1}\left(\boldsymbol{K}^T\boldsymbol{S}^{-1}\boldsymbol{K}+\boldsymbol{S}_a^{-1}\right)-\left(\boldsymbol{K}^T\boldsymbol{S}^{-1}\boldsymbol{K}+\boldsymbol{S}_a^{-1}\right)^{-1}\boldsymbol{K}^T\boldsymbol{S}^{-1}\boldsymbol{K} \\ \boldsymbol{I}-\boldsymbol{A}_{AKM} &= \left(\boldsymbol{K}^T\boldsymbol{S}^{-1}\boldsymbol{K}+\boldsymbol{S}_a^{-1}\right)^{-1}\left[\left(\boldsymbol{K}^T\boldsymbol{S}^{-1}\boldsymbol{K}+\boldsymbol{S}_a^{-1}\right)-\boldsymbol{K}^T\boldsymbol{S}^{-1}\boldsymbol{K}\right] \\ \boldsymbol{I}-\boldsymbol{A}_{AKM} &= \left(\boldsymbol{K}^T\boldsymbol{S}^{-1}\boldsymbol{K}+\boldsymbol{S}_a^{-1}\right)^{-1}\boldsymbol{S}_a^{-1} \end{aligned} \tag{4.59}$$

And so:

$$\left(\boldsymbol{I}-\boldsymbol{A}_{AKM}\right)^{-1} = \left(\boldsymbol{K}^T\boldsymbol{S}^{-1}\boldsymbol{K}+\boldsymbol{S}_a^{-1}\right)\boldsymbol{S}_a \tag{4.60}$$

Using equations (4.56) and (4.60):

$$H = \frac{1}{2}\ln\left|\left(\boldsymbol{I}-\boldsymbol{A}_{AKM}\right)^{-1}\right| \tag{4.61}$$

Finally:

$$H = -\frac{1}{2}\ln\left|\boldsymbol{I}-\boldsymbol{A}_{AKM}\right| \tag{4.62}$$

A similar procedure can be used to compare the gain of information from two different measurements.

As seen for information content, also the number of independent pieces of information in a measurement can be related to the averaging kernel matrix. If we consider the simplest case with one degrees of freedom let us consider making a single direct measurement of a scalar, with noise:

$$y = x + \varepsilon \tag{4.63}$$

where *x* has prior variance σ_a^2 and ε has σ_ε^2. The prior variance of y will be $\sigma_y^2 = \sigma_a^2 + \sigma_\varepsilon^2$.

The best estimate of x will be:

$$\hat{x} = \frac{\sigma_\varepsilon^{-2}x + \sigma_a^{-2}x_a}{\sigma_\varepsilon^{-2} + \sigma_a^{-2}} = \frac{\sigma_a^2 x + \sigma_\varepsilon^2 x_a}{\sigma_\varepsilon^2 + \sigma_a^2} \tag{4.64}$$

If $\sigma_a^2 >> \sigma_\varepsilon^2$ then y will be providing information about x, but if $\sigma_a^2 << \sigma_\varepsilon^2$ then it will provide information about ε. In the first case we can say that the measurement provides a 'degree of freedom for signal', and in the second case a 'degree of freedom for noise'.

Now consider the general case of measuring a vector y with m degrees of freedom. The most probable state in the Gaussian linear case is the one which minimises

$$\chi^2 = \left(\boldsymbol{x}-\boldsymbol{x}_a\right)^T\boldsymbol{S}_a^{-1}\left(\boldsymbol{x}-\boldsymbol{x}_a\right) + \boldsymbol{\varepsilon}^T\boldsymbol{S}_\varepsilon^{-1}\varepsilon \tag{4.65}$$

where $\varepsilon = y - Kx$. As we have seen, the minimum is at

$$\hat{\boldsymbol{x}} - \boldsymbol{x}_a = \boldsymbol{G}\left(\boldsymbol{y} - \boldsymbol{K}\boldsymbol{x}_a\right) = \boldsymbol{G}\left[\boldsymbol{K}\left(\boldsymbol{x} - \boldsymbol{x}_a\right) + \boldsymbol{\varepsilon}\right] \tag{4.66}$$

with G:

$$\boldsymbol{G} = \left(\boldsymbol{K}^T \boldsymbol{S}^{-1} \boldsymbol{K} + \boldsymbol{S}_a^{-1}\right)^{-1} \boldsymbol{K}^T \boldsymbol{S}^{-1} = \boldsymbol{S}_a \boldsymbol{K}^T \left(\boldsymbol{K}\boldsymbol{S}_a \boldsymbol{K}^T + \boldsymbol{S}_\varepsilon\right)^{-1} \tag{4.67}$$

At the minimum the expected value of χ^2 is equal to the number of degrees of freedom, or the number of measurements, m. This can be divided into two parts, corresponding to the two terms ($\boldsymbol{\varepsilon}$ is the expected value operator):

$$d_{signal} = \boldsymbol{\varepsilon}\left\{\left(\hat{\boldsymbol{x}} - \boldsymbol{x}_a\right)^T \boldsymbol{S}_a^{-1} \left(\hat{\boldsymbol{x}} - \boldsymbol{x}_a\right)\right\} \tag{4.68}$$

$$d_{noise} = \boldsymbol{\varepsilon}\left\{\hat{\boldsymbol{\varepsilon}}^T \boldsymbol{S}_\varepsilon^{-1} \hat{\boldsymbol{\varepsilon}}\right\} \tag{4.69}$$

The first term measures the part of χ^2 attributable to the signal, the second to the noise. They may therefore be described as the number of 'degree of freedom for signal', and in the second case a 'degree of freedom for noise'. Thus d_{signal} describes the number of useful independent quantities that there are in a measurement, and hence is a measure of information that is not necessarily an integer.
We can find explicit expression for d_{signal} as follows. In the derivation we use the relation for the trace of a product of two matrices tr(CD)=tr(DC) where C and D are rectangular matrices such that C^T and D are the same size. It is clear that

$$\begin{aligned} d_{signal} &= \boldsymbol{\varepsilon}\left\{\left(\hat{\boldsymbol{x}} - \boldsymbol{x}_a\right)^T \boldsymbol{S}_a^{-1} \left(\hat{\boldsymbol{x}} - \boldsymbol{x}_a\right)\right\} = \\ &= \boldsymbol{\varepsilon}\left\{tr\left[\left(\hat{\boldsymbol{x}} - \boldsymbol{x}_a\right)\left(\hat{\boldsymbol{x}} - \boldsymbol{x}_a\right)^T \boldsymbol{S}_a^{-1}\right]\right\} = \\ &= tr\left(\boldsymbol{S}_{\hat{x}} \boldsymbol{S}_a^{-1}\right) \end{aligned} \tag{4.70}$$

where, from equations (4.67) and (4.68)

$$\begin{aligned} \boldsymbol{S}_{\hat{x}} &= \boldsymbol{\varepsilon}\left\{\left(\hat{\boldsymbol{x}} - \boldsymbol{x}_a\right)\left(\hat{\boldsymbol{x}} - \boldsymbol{x}_a\right)^T\right\} = \\ &= \boldsymbol{G}\left(\boldsymbol{K}\boldsymbol{S}_a \boldsymbol{K}^T + \boldsymbol{S}_\varepsilon\right)\boldsymbol{G}^T = \\ &= \boldsymbol{S}_a \boldsymbol{K}^T \left(\boldsymbol{K}\boldsymbol{S}_a \boldsymbol{K}^T + \boldsymbol{S}_\varepsilon\right)^{-1} \boldsymbol{K}\boldsymbol{S}_a \end{aligned} \tag{4.71}$$

Therefore

$$\begin{aligned} d_{signal} &= tr\left(\boldsymbol{S}_a \boldsymbol{K}^T \left[\boldsymbol{K}\boldsymbol{S}_a \boldsymbol{K}^T + \boldsymbol{S}_\varepsilon\right]^{-1} \boldsymbol{K}\right) = \\ &= tr\left(\boldsymbol{K}\boldsymbol{S}_a \boldsymbol{K}^T \left[\boldsymbol{K}\boldsymbol{S}_a \boldsymbol{K}^T + \boldsymbol{S}_\varepsilon\right]^{-1}\right) \end{aligned} \tag{4.72}$$

using equation in (4.67) we also obtain

$$d_{signal} = tr\left(\left[\boldsymbol{K}^T \boldsymbol{S}_\varepsilon^{-1} \boldsymbol{K} + \boldsymbol{S}_a^{-1}\right]^{-1} \boldsymbol{K}^T \boldsymbol{S}_\varepsilon^{-1} \boldsymbol{K}\right) \tag{4.73}$$

and finally using equation (4.46):

$$d_{signal} = tr\left(\boldsymbol{A}_{\boldsymbol{AKM}}\right) \tag{4.74}$$

4.6.4 Ratio between Biased and Unbiased error

The ratio between the biased and unbiased error quantifies the influence of the a-priori information on the retrieval results. The ratio can assume values from 0 to 1. When the ratio is one, the information about the retrieved parameter comes from the measurements only, when the ratio approaches zero the information is mainly coming from the a-priori knowledge.

Chapter 5: Forward and Retrieval Models

The problem of retrieving the altitude distribution of a physical or chemical quantity from remote sensing observations of the atmosphere made with the limb-scanning technique, falls within the general class of inverse problems that do not have a direct solution and require a retrieval procedure based on the fitting of the experimental observations with a forward model of the observations.
The forward model reproduces the observations using a set of physical and chemical parameters and the retrieval procedure consists in the search of the values of the parameters that produce the "best" simulation of the observations. The most common criterion adopted to assess which is the “best” simulation is the minimisation of the χ^2 function (defined as the weighted squared summation of the differences between observations and simulations) with respect to the value of the parameters. This criterion is generally referred to as Least Squares Fit (LSF). When the forward model does not depend linearly on the unknown parameters the problem cannot be solved directly, and an iterative procedure must be used (called Non-linear Least Squares Fit (NLSF), see Chapter 4).
The algorithm for the analysis of the atmospheric spectra observed by SAFIRE-A that will be discussed in this chapter has been developed by the group I am working with and with my collaboration.

5.1 RAS General features

RAS (Retrieval Algorithm for SAFIRE) is the scientific code which has been developed to perform the retrieval of Volume Mixing Ratio (VMR) profiles of H_2O, O_3, HNO_3, N_2O, ClO, HCl, OH in the SAFIRE-A spectral regions. Some of the algorithm general features are summarised in the following sections.
RAS works with the assumption that the atmosphere is horizontally uniform (perfectly stratified atmosphere). In this case all the calculations are more simple: the atmosphere can be modelled as a function of a single variable, the radiative transfer can be efficiently calculated, and fewer unknowns must be retrieved. Moreover, the assumption of a stratified atmosphere is well verified in the stratosphere.
The VMR profiles of the target molecules are retrieved one by one. If some reciprocal spectral interference exists the VMRs are retrieved sequentially according to the degree of interference. RAS simultaneously retrieves the VMR profiles of the target species, the atmospheric continuum, the offset correction to the spectrum and the instrumental line shape parameter.
The measured spectra are analysed only in narrow spectral intervals called microwindows (mws). The use of these mws aims at optimizing the analysis of the measured spectra: it allows to work just with those spectral ranges where the “best” information on the target parameters can be found, and to avoid the analysis of regions where little information on the target is present or affected by systematic errors.
Limb measurements are in general affected by the observation geometry, in particular by the pressure at tangent altitudes, so the correct interpretation of the retrieval results requires a good estimate of the pressure profile. Far infrared emission spectra are not too sensitive to the temperature (see Figure 1.7) so temperature profiles coming from external sources can be used in the analysis. In SAFIRE-A retrievals temperature and pressure profiles are obtained from ECMWF (European Centre for Medium-Range Weather Forecasts) or NCEP (National Centers for Environmental Predictions) data (see section 5.7).

5.2 Retrieval scheme

The signal that reaches the spectrometer can be modelled, through of the radiative transfer equation (described in sect. 5.3.A), as a function S = S(**b**, x(z)) of the observation parameters **b** and of the distribution profile x(z) of the atmospheric quantity which is to be retrieved. The observation parameters are all the parameters that characterise the observation both in its dimensions (for instance spectral frequency bands and channels and direction of observation) and in its modelling (for instance spectroscopic parameters and atmospheric description). Several observations with different observation parameters may be available. Since usually the radiative transfer is not a linear transformation, the problem of deriving the distribution x(z) from the observed values (y) of S cannot be solved through the analytical inversion of the radiative transfer equation. The problem of retrieving the vertical distribution of a physical or chemical quantity from a limb scanning observation is a typical non-linear inverse problem (Chapter 4). In the case of SAFIRE-A the retrieval algorithm scheme can be represented as in Figure 5.1:

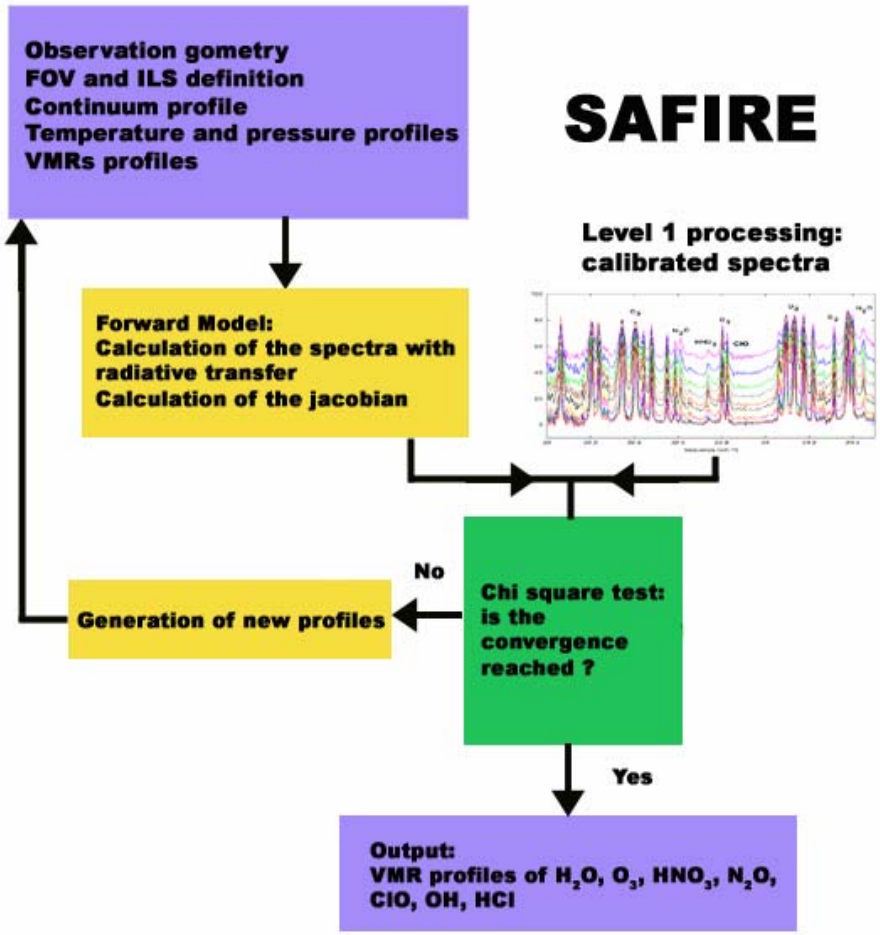

Figure 5.1: SAFIRE-A retrieval scheme.

The forward model (sect.5.3) computes the simulated spectra starting from the atmospheric physical and chemical description, from some first-guess values of the unknown parameters and using data on the observation geometry and the instrumental parameters.
The simulated spectra are then compared with the measured spectra provided by SAFIRE-A level 1 processing that converts the interferograms into fully calibrated radiance spectra.

The quadratic summation of the differences between the simulated and the measured spectra gives the value of the χ^2 function to be minimized; the χ^2 is described by the following equation:

$$\chi^2 = \boldsymbol{n}^T \boldsymbol{S}_n^{-1} \boldsymbol{n} \tag{5.1}$$

where $\boldsymbol{n}$ is the difference between the observations and the simulations and $\boldsymbol{S}_n$ the Variance Covariance matrix associated with the vector $\boldsymbol{n}$.
The χ^2 minimization "solution" is described by the Levenberg formula (sect.4.4.2) which allows to generate a new profile by modifying the first initial guess with the correction provided by equation (4.37).
Convergence criteria are applied in order to assess whether the minimum of the χ^2 function has been reached: if the convergence criteria are fulfilled, the procedure stops; if the convergence is not reached, the improved profile is used as a new initial guess for generating simulated spectra that are again compared with the measured ones.

5.2.1 Different type of geophysical retrieval

The complexity of the retrieval problem has caused over the years the development of retrievals characterised by different state vectors. Early retrievals were limited in computing capabilities and adopted the "onion peeling" techniques [25]. In the onion peeling technique the vertical profile of one geophysical parameter is determined starting from observations with the highest tangent altitude with a sequence of "small" retrievals, each retrieving the value of the target at a single altitude using a single limb scanning measurement. In this case the vertical profile is retrieved at a number of points equal to the number of limb scanning angles and the error affecting each point propagates into the subsequent ones.
With the global-fit retrieval, introduced by [24], the whole altitude profile is retrieved from the simultaneous analysis of all the limb-scanning measurements. Compared with the onion peeling method, the global fit approach avoids the error propagation on the retrieved amounts of gas and allows the use of retrieved altitudes that are no longer strictly connected with the geometry of the observed spectra. For these reasons the global-fit approach is the one implemented into RAS.
In all cases the retrievals operation requires the calculation of the following ingredients:
1) Forward Model, i.e. the simulation of the observations in the case of the assumed state vector.
This operation is discussed in Sect 5.3.
2) The Jacobian matrix, i.e. the matrix needed for the calculation of solution matrix. This operation is discussed in Sect 5.4.

5.3 Forward Model

The Forward Model simulates the spectra measured by the instrument for a given atmospheric composition and instrumental properties. The measured signal is equal to the atmospheric radiance that reaches the interferometer, modified by the instrumental effects due to the finite spectral resolution and the finite Field Of View (FOV) of the instrument. The atmospheric radiance reaching the instrument is computed through the radiative transfer equation. The instrumental effects are taken into account by convolving the atmospheric limb radiance computed at high spectral resolution with the Instrument Line Shape (ILS) and with the instrument Field Of View in order to simulate the spectrum measured by the real instrument.
It is assumed that the effects of the FOV and of the ILS can be modelled as two linear and independent averaging processes.

A. The Radiative Transfer model

The atmospheric radiance that reaches the instrument for each limb geometry is expressed by the radiative transfer equation (the Lambert-Beer law for a non-homogeneous medium):

$$S(\sigma,\theta,h)=\int_{\tau^b}^{1} J(\sigma,x)\,d\tau(\sigma,x) \tag{5.2}$$

where the integration is between the observer location x_0 ($\tau(x_0)=1$) and the farthest point along the optical path that contributes to the signal observed by the instrument (x^b in which we have trasmissivity τ^b); the meaning of the quantities in eq.(5.2) is summarized in the following table:

σ	Wavenumber
Θ	Direction of the line of sight (limb angle)
h	Altitude of the observer
x	Co-ordinate along the optical path, described by the geometrical quantities θ and h
$S(\sigma,\theta,h)$	Observed atmospheric spectral intensity
$J(\sigma,x)$	Source function
$\tau(\sigma,x)$	Transmittance of the atmosphere located between the point x and the observer (located at $x=0$). This quantity depends on the atmospheric composition, pressure and temperature through the co-ordinate x .

Under the local thermal equilibrium assumption, the source function $J(\sigma,x)$ coincides with the Planck function (APPENDIX B):

$$B(\sigma,T)=\frac{2hc^2\sigma^3}{\exp\left[\frac{hc\sigma}{k_B T}\right]-1} \tag{5.3}$$

with h = Plank's constant
c = velocity of the light
k_b = Boltzmann's constant
T = Kinetic temperature
σ = frequency (in cm^{-1})

The transmission τ can be expressed as a function of x as:

$$\tau(\sigma,x)=\exp\left[-\int_{x^0}^{x}\left(\overline{k(\sigma,x')}\eta(x')\right)dx'\right] \tag{5.4}$$

$$\eta(x)=\frac{p(x)}{k^B T(x)} \tag{5.5}$$

$$\overline{k(\sigma,x)}=\sum_{m=1}^{molec} k_m(\sigma,x)X_m(x) \tag{5.6}$$

where $\eta(x)$ is the number density of the air, $p(x)$ the pressure and $\overline{k(\sigma,x)}$ the weighted absorption cross section. In eq.(5.6) *molec* represents the number of different absorbers in the

spectral region under consideration, $X_m(x)$ the volume mixing ratio of the species m at the point x and $k_m(\sigma,x)$ the absorption cross sections of the species m.
Eq.(5.2) can be then written as:

$$S(\sigma,\theta,h)=\int_{x^0}^{x^b} B(\sigma,T(x))\frac{d\tau(\sigma,x)}{dx}dx=\int_{x^0}^{x^b} B(\sigma,T(x))\eta(x)\tau(\sigma,x)\overline{k(\sigma,x)}dx \qquad (5.7)$$

The calculation of this integral requires two basic steps:
1) the ray tracing, i.e. the determination of the optical path x and, consequently, the temperature $T(x)$, the pressure $p(x)$ and the volume mixing ratio $X_m(x)$ along the optical path, and the calculation of the absorption cross sections. The optical path in the atmosphere is given by the viewing direction of the instrument and the propagation properties of the atmosphere (Earth curvature and refractive index). In turn the refractive index $n(p(x),T(x))$ can be expressed as a function of pressure and temperature.
2) The calculation of the *absorption cross sections* $k_m(\sigma, x)$ for each gas:

$$k(\sigma,T,p)=\sum_{l=1}^{lines} L_{m,l}(T)A_{m,l}(\sigma-\sigma_{m,l},T,p) \qquad (5.8)$$

where $L_{m,l}(T)$ is the line strength of line l of species m, $\sigma_{m,l}$ the central wavenumber of line l of species m, $A_{m,l}(\sigma-\sigma_{m,l},T,p)$ the line profile (lineshape). In turn the line strength and the line shape depend on the physical conditions of pressure and temperature encountered along the optical path.
The computation of equation (5.7) requires many operations that must be repeated for many variables. One of the objectives of the code is to reduce the computing time optimizing the computation of the Radiative Transfer equation avoiding the repetition of the same calculation while achieving a good accuracy.

B. Frequency grid

Limb radiance spectra contain spectral features varying from the narrow, isolated, Doppler-broadened lines at high altitudes, to wide, overlapping, pressure-broadened lines at low altitudes. So to correctly simulate the atmospheric spectra a suitable frequency grid has to be chosen. The simplest procedure to resolve the sharp lines at high altitudes is to choose a frequency grid fine enough so that the narrowest lines are adequately sampled. The choice of a fine grid can be optimized in order to reduce either the computing time and the memory requirements. In case of SAFIRE-A we choose to use a fine grid with a step of 1/30 of the measurement resolution (fine step of the order of 0.0001 cm^{-1}).

C. Instrumental effects

The measured spectrum is the atmospheric spectrum perturbed by the instrument. This perturbation can be expressed by the convolution products between $S(\sigma,\theta,h)$ (eq.(5.7)) and the instrumental functions (ILS and FOV).The ILS term accounts for the finite spectral resolution of the instrument and the distortion of the original line-shape by the instrument (see APPENDIX A); while the FOV term deals with the finite FOV of the instrument.
The two convolutions can be performed in any order. Therefore, even if the logic of the process suggests the operation first of the effect of the FOV and then of the effect of the ILS, from the computational point of view a different order is to be preferred. As a matter of fact, the spectrum is computed over a finer frequency grid than the measured one; so the convolution with the ILS maps the computed spectrum over the measurement frequency grid reducing the number of spectral points on which the FOV convolution is carried out:

$$S^{ILS}(\sigma,\theta,h) = \int S(\sigma',\theta,h)\cdot ILS(\sigma-\sigma')d\sigma'$$
$$S^{Fin}(\sigma,\theta^t,h) = \int S^{ILS}(\sigma,\theta,h)\cdot FOV(\theta-\theta^t)d\theta \quad (5.9)$$

D. Ray tracing, Refractive Index and Atmospheric layering

The radiative transfer integral (eq.(5.7)) is a path integral along the line of sight in the atmosphere. The line of sight is determined by the viewing direction of the instrument; because of refraction it is not a straight line but it bends towards the Earth.
Refractive index is a function of pressure, and temperature: this dependence can be defined using the Clausius-Mossotti (or Lorentz-Lorenz) formula [26]:

$$\frac{n^2-1}{n^2+2} = const\cdot\rho \quad (5.10)$$

where n is the refractive index, ρ the air density.
Since n-1<<1 , we can write:

$$n = 1+\alpha\cdot\rho(p,T) \quad (5.11)$$

Where α is a factor dependent on the empirical model chosen for the refractive index.
Starting from the instrument position (r_0, equal to the summation of the local radius, of curvature of the Earth and the altitude of the considered point referred to the Earth surface), an iterative procedure is applied to an atmosphere stratified with a fine step; from the generic intersection position P_{i-1} (r_{i-1}) and the related limb angle (α_{i-1}) of the incident ray path, the new limb angle (α_i) of the ray path outgoing from the point P_{i-1} and the new intersection P_i (r_i) with the lower layer.

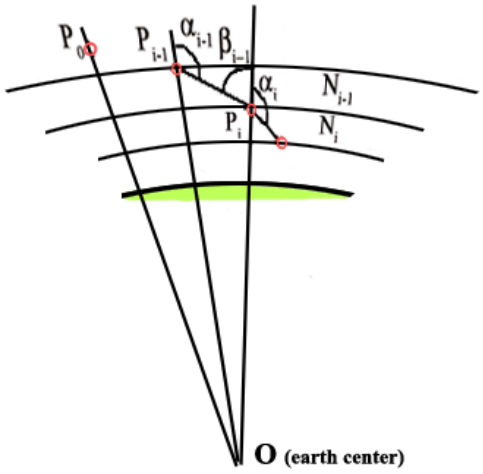

Figure 5.2: Deduction of Snell's law for media with spherical symmetry.

In fact, according to the Snell's law in point P_i we can find:

$$n(r_i)\sin(\pi-\alpha_i) = n(r_{i-1})\sin(\beta_{i-1}) \quad (5.12)$$

From the 'sine' theorem applied to triangle P_{i-1},P_i,O in Figure 5.2, we obtain:

$$\frac{\sin(\pi-\beta_{i-1})}{r_{i-1}}=\frac{\sin(\pi-\alpha_{i-1})}{r_i} \tag{5.13}$$

and thus combining the two equations (5.12) and (5.13):

$$r_i n(r_i)\sin(\alpha_i)=r_{i-1}n(r_{i-1})\sin(\alpha_{i-1}) \tag{5.14}$$

where r is the summation of R, local radius of curvature of the Earth at sea level, and the altitude from sea level of the considered point.
Equation (5.14) states that the quantity $r_i n(r_i)\sin(\alpha_i)$ is constant along the line of sight. In this way at tangent altitude it reduces to $r(t_a)\cdot n(r(t_a))$, because at tangent altitude α_i=90.
The atmosphere is divided into sub-layers. In this way the calculation of the Radiative Transfer Integral becomes a summation over the layers. So the boundaries of these layers should be chosen in such a way that the gas may be considered homogeneous in them and can be well represented by appropriate Curtis-Godson [27] parameters for pressure and temperature**.** The Curtis-Godson pressure and temperature (or "equivalent" pressure and temperature) are obtained by means of weighting the pressure and the temperature along the ray-path with the local number density of each absorbing gas. Curtis-Godson quantities have in principle to be computed for each gas, each layer and each limb view.
Since the transmittance weighting functions for limb geometries peak near the tangent point, it is important that a fine layer structure is used.

E. Absorption Cross Sections

The computation of cross sections is a very time consuming part of the forward model, due to the large number of spectral lines to be considered, the high spectral resolution required and the number of *p,T* combinations for which they have to be computed. In the code we use the explicit line-by-line (LBL) method which performs the computation for every line from a pre-selected spectroscopic database (see APPENDIX B) at every frequency fine grid point.
In order to calculate the cross section of a molecular species on each frequency point, it is necessary to compute the contribution coming from all the transitions of this species present in the considered spectral range (microwindow). Besides, also the transitions lying outside the microwindow can contribute, with their wings, to the cross-sections at the frequencies inside the microwindow. Of course, the required computing time is proportional to the number of the transitions. For this reason outside the considered MW it is useful to consider only the most intense transitions and to neglect those that bring negligible contribution.

F. Continuum Cross Sections

There are two different kinds of effects which contribute to the spectral intensity of a microwindow as continuum (in addiction to the instrumental continuum): the near and the far continuum.
The near continuum is caused by nearby atmospheric lines; therefore, the simulation of this effect has to be performed during the calculation of the absorption cross sections. This simulation is performed by taking into account transitions located in a spectral interval broader than the simulated spectral interval. Two different approach can be used, one consists in calculating this contribution at each fine-grid point inside the band (option 1), the other is to calculate the wings of the lines only at three grid points inside the microwindow and to apply polynomial interpolation in between (option 2). In our case the nearby continuum is simulated according to option 1.
The far continuum includes the line wings of far lines of H_2O, the pressure broadened bands of O_2 and N_2. Water vapour continuum represents by far the most important source of

continuum absorption in the troposphere and is proportional, to first order, to the variable amount of water vapour present in the atmosphere. The far continuum is taken into account in RAS by using an externally provided cross section profile. So the forward model implemented into the retrieval code does not have to simulate any far continuum effects. These are included into a single atmospheric continuum for each microwindow which is fitted like an additional absorption cross section. This leads to one cross section at each atmospheric layer for each microwindow. Since SAFIRE-A spectra are recorded on narrow bands, it is also possible to fit only one continuum cross section for each limb view valid for all the used microwindows.

G. Instrument Line Shape Convolution

The Instrument Line Shape (ILS) function is the response of the instrument to a Dirac delta signal. ILS accounts for the finite spectral resolution of the instrument and distortion of the line-shape by the instrument.
The ILS is equal to the convolution of the *sinc* function associated with the finite spectral resolution of the instrument with a term due to the finite angular aperture; if the angular aperture is circular, this term is equal to a *rectangular* function shifted in wavenumber, whose width varies linearly with the wavelength [29].
In a real instrument alignment errors and irregular angular aperture lead to a more elaborated ILS.
The distortion of the ILS of the SAFIRE–A spectrometer from a pure sinc is described in RAS by a linear combination of a sinc and a $sinc^2$ functions (see Chapter 2, Figure 2.4). The ILS is assumed to be independent from the tangent altitude. Into the RAS code, the value of the contribution of the $sinc^2$ to the ILS can be fitted during the retrieval procedure. The high resolution spectrum computed with the radiative transfer model is convoluted with the ILS function according to equation (5.9).

H. Instrument Field of View Convolution

The atmospheric spectral intensity can be considered to be uniform over the pupil of the instrument. However, this intensity varies significantly as a function of the limb angle and the averaging effect of the instrument FOV must be taken into account. In general, the FOV is the two dimensional angular distribution of the instrument sensitivity.
Nevertheless, since within the finite angular aperture of the instrument the atmosphere has a negligible variability in the horizontal direction, in practice, we are only interested in the vertical dependence of the FOV. Therefore, for our purposes, the FOV distribution of the instrument is a function of the vertical angle.
Into the RAS code the FOV can be represented with a trapezium, with user defined values of the two basis, or read from tabulated values from a file. The FOV spread in the angular domain (FOV(θ)) is measured experimentally and tabulated in a FOV pattern distribution, then used in the convolution product with the spectrum; so the convolution requires the forward model calculation for a number of lines of sight that span the vertical range of the FOV around the central direction. The number of pencil beams used to simulate the FOV is an user defined parameter. This value is tuned in order to obtain the best compromise between simulation accuracy and number of geometry to be simulated (and so computing time).

5.4Jacobian Calculation

An important part of the retrieval code is the fast determination of the derivatives of the radiance with respect to the retrieved parameters. The Jacobian is the matrix of the derivatives of the simulated measurements with respect to all the retrieved quantities (Chapter 4):

$$K_{ij} = \frac{\partial F_i(\boldsymbol{x})}{\partial x_j} \tag{5.16}$$

Jacobian calculation is the most time consuming task of the retrieval code. It is important that an efficient calculation strategy is adopted. In most circumstances it is preferable to evaluate eq.(5.16) in an algebraic way rather than calculating the perturbation of the forward model for each element of the state vector and re-computing the forward model several times. In the RAS code, whenever possible, derivatives are computed analytically, in the sense that analytical formulae of the derivatives are implemented into the code.

5.5Regularization

Contiguous values of the retrieved profiles often turn out to be anti-correlated and as a consequence, the profile assumes oscillating values that do not correspond to a real atmospheric behaviour. The physical expectation of a smooth profile can be injected in the retrieval through a regularisation procedure.

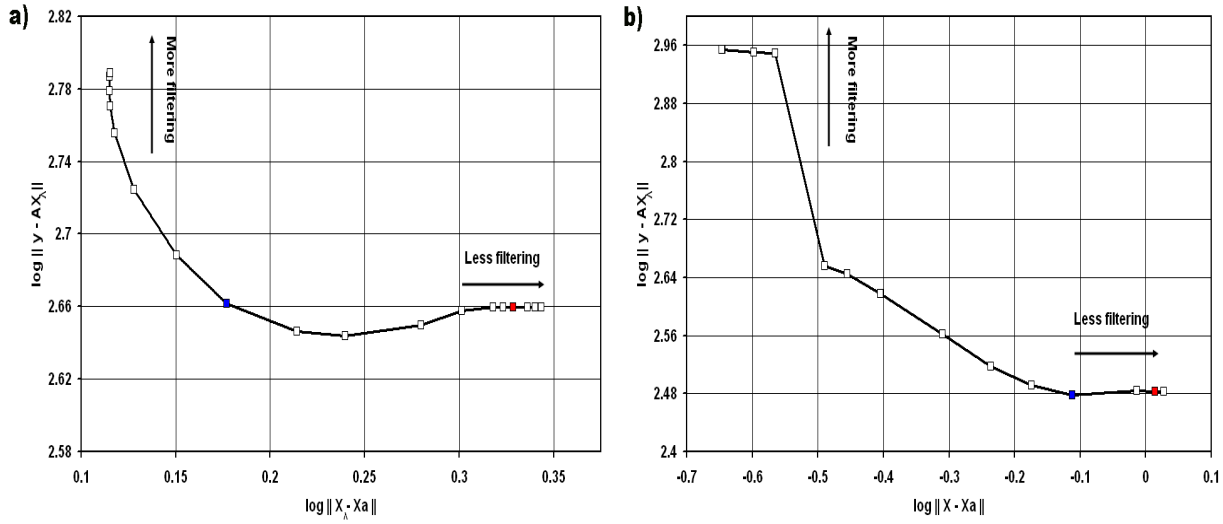

Figure 5.3: L-curve for SAFIRE-A sequence(a) 35 flight 12 October 1999 and for (b) sequence 20 2nd March 2003.

Into RAS, an option for the use of the Tikhonov regularization (see Chapter 4) exist. The strength of the used regularization is an user defined parameter. As reported in chapter 3, an evaluation method used to infer the most suitable value for this parameter is the L-curve method. In Figure 5.3 is reported, as an example, the case of L-curve calculation for sequence 35 recorded during the flight performed on the 12th October 1999 (Figure 5.3.a) and for sequence number 20 (Figure 5.3.b) of 2nd March 2003 Geophysica arctic flight. The value in blue represents the best trade-off between the two residual norm. In general, in SAFIRE-A retrieval we are inclined to use a value of the regularization parameter that provides a small contribution of the regularization (red point on the graph) to the retrieval.

5.6Convergence criteria

We review here some criteria that can be considered for evaluating if the convergence has been reached avoiding unneeded computation.
In RAS the convergence is established by these conditions:

- The relative variation of the χ^2 function obtained in the present iteration with respect to the previous iteration is less than a fixed threshold (t_1)

$$\left|\frac{\chi^2(q^{iter-1}) - \chi^2(q^{iter})}{\chi^2(q^{iter})}\right| < t_1 \tag{5.17}$$

where *iter* is the current iteration index.

- At the current iteration the relative difference between the actual χ^2 and its expected value in the linear approximation (χ^2_{LIN}) must be less than a fixed threshold (t_3) (condition of linearity).

$$\left|\frac{\chi^2(q^{iter}) - \chi_{LIN}{}^2(q^{iter})}{\chi^2(q^{iter})}\right| < t_3 \tag{5.18}$$

- That the maximum number of iterations must be less than a given threshold (condition on computing time).

The convergence criterion is obtained as a suitable combination of the above conditions. In RAS the default choice is that convergence is reached if condition in (5.17) or in (5.18) is satisfied. In some case the convergence criteria can be satisfied also when the iterative process is still far from reaching convergence. If only the condition on computing time is satisfied, the retrieval is considered unsuccessful.

5.7 Inputs

As shown in Figure 5.1, the inputs needed by the retrieval algorithm, apart from the measured spectra, are the instrumental parameters, described in the following subsection, and the atmospheric and continuum parameters.
Pressure and Temperature profiles were obtained by ECMWF data processed at University of L'Aquila. Temperature and geopotential height values at different pressure levels (from 1 to 1000 mbar) on a latitude-longitude grid (latitude step 1.125°, longitude step 1.125°) are provided every 6 hours (at 00, 06, 12 and 18).
ECMWF data are, in general, available 6-7 days after the flight. In order to provide the first results during the campaign, NCEP data were sometimes preferred. These data, that are available in 1 day, are provided every 6 hours (at 00, 06, 12 and 18) at 26 pressure levels (from 10 to 1000 mbar) on a latitude-longitude grid (latitude step 1°, longitude step 1°).
In order to produce pressure and temperature profiles, in an external program, ECMWF (or NCEP) values for temperature and geopotential height were linearly interpolated in latitude and in time on a given altitude grid, in order to make use of the most suitable values for each sequence.
VMR profiles coming from a standard mid-latitude and polar atmospheric model were used either as initial guess of the retrieval and to model interfering gases. These profiles are sequences independent.

5.8 Error budget

The main error sources which contribute to the total retrieval error are the noise error and the systematic error.
The noise error is due to the mapping of radiometric noise in the retrieved profiles. In SAFIRE-A retrieval we calculate both the biased and the unbiased error where the **unbiased error** is the expression of the Variance-Covariance Matrix (VCM) of the errors associated with the retrieved quantities in the case of the pure Gauss Newton method. This VCM determines how the measurement errors map onto the retrieved quantities when no auxiliary information is used. When auxiliary information is used (either in the form of Marquardt

technique, or Tikhonov regularization) the error propagation leads to a rather complex expression: the **biased error** (see Chapter 4). By comparing the unbiased retrieval error given by the diagonal of the inverse of the Gauss Newton VCM with the actual retrieval error (biased retrieval error) we can deduce the perturbation/added information introduced by the retrieval technique in the result.

Chapter 6: Software Validation, Update and Development

6.1 Performances and validation

Several tests have been performed to verify the baselines adopted in the models and their performance.

The retrieval accuracy of the RAS (Retrieval Algorithm for SAFIRE-A) code was validated by performing retrievals from simulated spectra generated by FAS (Forward Algorithm for SAFIRE-A). Simulated observations allow for the retrieval process to be started with an initial guess of the parameters perturbed by a known amount with respect to the reference values used to produce the synthetic spectra; the amplitude of this perturbation can be used to test the capability of the retrieval system to converge also in presence of a poor initial guess. Results indicate that both forward model error, i.e. error due to imperfect modelling of the atmosphere, and convergence error, i.e. error due to the fact that the inversion procedure does not find the real minimum of the chi-square function, are much smaller than the measurement error due to the radiometric noise.

RAS has also been used to validate MARSCHALS (Millimetre-wave Airborne Receivers for Spectroscopic CHaracterisation in Atmospheric Limb Sounding), forward model.

6.1.1 Internal Validation Tests

The first step in the internal validation procedure of the RAS code, was the retrieval of VMRs profiles starting from simulated spectra. These spectra were produced with the self standing forward model, named FAS. Starting from mid-latitude VMRs and temperature profiles and realistic instrumental noise, all the spectra composing a limb scanning sequence were produced (simulated observations). In the retrieval algorithm, the simulated observations were analysed using as initial guess for the target species, the profiles employed in the simulations perturbed by a known quantity. If the retrieval procedure is correct, the difference between the retrieved profiles and the profiles used in the simulations (named reference profiles) has to be close to 0 and inside the error bar. An example of a retrieval test for ozone is reported in Figure 6.1. Similar tests have been done for all the target quantities of SAFIRE-A instrument in order to assess the performance and the robustness of RAS code. The results of these tests indicate that RAS is able to retrieve all the targets with good precision.

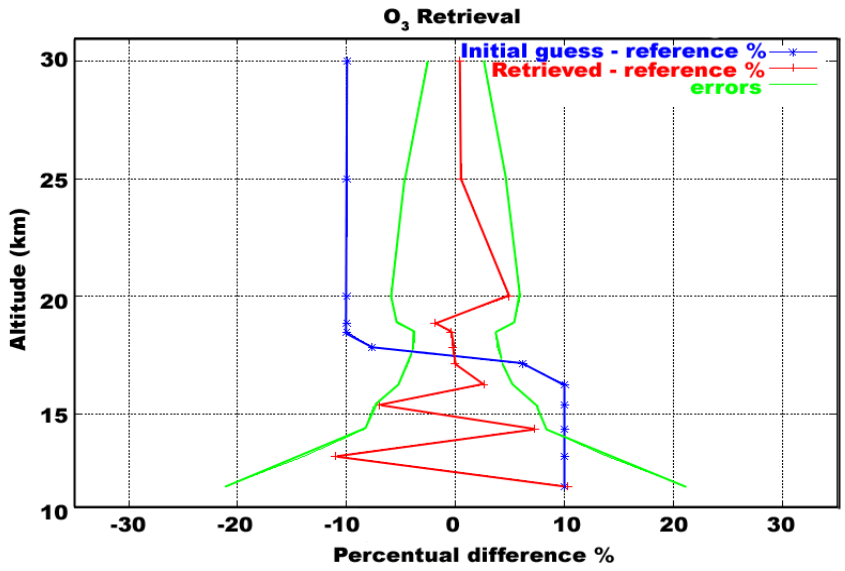

Figure 6.1: O_3 retrieval, internal test.

6.1.2 Validating MARSCHALS Forward Model

MARSCHALS (Millimetre-wave Airborne Receivers for Spectroscopic CHaracterisation in Atmospheric Limb Sounding, see subsection 6.1.2.1 for details), is a new instrument that will fly onboard the M55-Geophysica and will measure VMR profiles of different species. The group I'm working with, collaborates at the development of a retrieval code for the analysis of MARSCHALS measurements. In the frame of this project, it was necessary to validate the forward model used into MARC (MArschals Retrieval Code): MFM (MARC Forward Model) algorithm. FAS code was chosen for a first comparison. In the subsequent sessions, along with a description of the MARSCHALS experiment, a detailed description of the modification applied to FAS in order to perform this test and the results obtained can be found.

6.1.2.1 MARSCHALS Instrument

MARSCHALS (Millimetre-wave Airborne Receivers for Spectroscopic CHaracterisation in Atmospheric Limb Sounding), is an heterodyne spectrometer for the measurement of high resolution spectra of the atmospheric emission in the millimetre and submillimetre region with limb sounding geometry. MARSCHALS has been developed by an European consortium led by RAL (Rutherford and Appleton Laboratories) under an ESA (European Space Agency) contract and will fly on board of the M-55 Geophysica up to an altitude of 21 km. The major objective of MARSCHALS is verify the extent of millimetre-wave advantages and to validate the spectro-radiometric requirements of MASTER (Millimetre-wave Acquisition for Stratosphere-Troposphere Exchange Research) millimetre-wave heterodyne spectrometer onboard the ACECHEM (Atmospheric Composition Explorer for CHEMistry and climate) ESA mission.

Incoming radiation is distributed into a number of discrete spectral bands, each of which is down converted and amplified. Spectrometers measure the spectral power density across each band. For reasons of cost, the design of MARSCHALS does not permit instantaneous coverage of all five MASTER bands and only three bands (MASTER bands B, C and D) are time multiplexed. The main features of the MARSCHALS instrument are summarised in Table 6.1, that is taken from the reference [30], where further information on this instrument can be found.

Species that are expected to be detected in the bands of MARSCHALS are: H_2O, CO, O_3, HNO_3 , N_2O and O_2 . Since the concentration of molecular oxygen in the atmosphere is well known, the measurement of this species can be used for pointing and temperature determination. Other species could be present with weak signals.

Instrument Type	Total Power Single Sideband Radiometer
Bands	Band B 294 – 305.5 GHz Band C 316.5 – 325.5 GHz Band D 342.2 – 348.8 GHz
Instantaneous bandwidth	12 GHz
Spectral resolution	200 MHz (with provision for addition of high resolution 2MHz spectrometer with 4-12 GHz bandwidth)
Beam pointing	<<0.0025 deg. rms pointing knowledge during scan, bias excepted
Scan range	Tangent heights from –2km to platform altitude (21km on aircraft) in 1 km steps with +20 deg. "space view"
Mass	330 kg
Dimension	1.55 x 0.76 x 0.56m

Table 6.1: MARSCHALS main characteristic.

6.1.1.2 Simulation Assumptions

In order to perform a comparison between the two forward models some general assumptions were necessary. Since MARC and RAS use a different parametrization of the atmospheric continuum it was not included in both forward models. No spectral noise was added to the

synthetic spectra. Since FAS cannot cope with horizontal disomogeneities in the atmosphere, the atmosphere was considered uniform. No clouds were included in the simulations (clear sky condition).
The comparison was performed using:

- Mid-Latitude atmosphere
- 200 MHz resolution
- Bands as in Table 6.1
- MASTER spectroscopic database
- Instrumental Line Shape is a boxcar function
- The FOV was the one relative to the SAFIRE-A instrument.

The flight altitude was set to 20 km, constant for all the limb scanning angles while the limb scanning sequence was composed by the angles: 90.0 90.5 91.0 91.5 92.0 92.5 93.0 93.5 94.0.
Furthermore, the fact that MARSCHALS operates into the microwave region and SAFIRE-A in the far infrared, required some changes in the FAS code for the spectroscopic parameters as well as for the calculations of the refraction index.
All these changes are briefly described in the sequent sections.

6.1.1.3 Updates for RAS code

A. MARSCHALS Refraction Index

As we have seen in chapter 5, refractive index is a function of pressure, temperature and water vapour content and can be expressed by the formula:

$$n = 1 + \alpha \cdot \rho(p, T) \tag{5.11}$$

Where α is a factor dependent on the empirical model chosen for the refractive index.
In SAFIRE-A code we have used, as a model for the refraction index, the simplified version of Barrel-Sears formula (6.1.a), commonly used in infrared region:

$$(n-1)\cdot 10^{6} \approx \frac{p}{T}\cdot\left(77.48 + \frac{0.44}{\lambda^2} + \frac{0.007}{\lambda^4}\right) - \left(12.79 - \frac{0.14}{\lambda^2}\right)\cdot\frac{p_{H_2O}}{T} \tag{6.1.a}$$

where T is the temperature in °K, p is the atmospheric pressure in mm Hg, λ is the wavelength in μm, and p_{H_2O} is the partial pressure of water vapour in mm Hg. Its simplified empirical version is reported in equation (6.1.b):

$$n = 1 + \alpha^{0}\frac{\rho}{\rho_0} \tag{6.1.b}$$

with $\frac{\rho}{\rho_0} = \frac{p}{T}\frac{T^0}{p^0}$, p^0 =1013.25 hPa, T^0 =288.16 K and $\alpha^0 = 0.000272632$.

In the microwave region close to the MARSCHALS bands, the refractive index is usually computed using a simplified version of the formula of Essen and Froome [31]:

$$(n-1)\cdot 10^{6} = \frac{103.49}{T}\left(p - p_{H_2O}\right) + \frac{86.26}{T}\left(1 + \frac{5748}{T}\right)\cdot p_{H_2O} \qquad (6.2)$$

where T is the temperature in °K, p is the atmospheric pressure in mm Hg, and p_{H_2O} is the partial pressure of water vapour in mm Hg. The coefficients of this formula have been determined with measurements performed at 24 GHz, and the formula is typically used in applications up to 40 GHz. In the case of this equation the contribution of the water vapour to the refractive index is only 1.7 % at the height of 5 km. In the millimeter region no specific measurement of the refractive index exists and Eq. (6.2) appeared to be the most appropriate expression and was implemented into the MARSCHALS code.
In order to compare MARSCHALS and SAFIRE-A ray tracing strategy, we have to use the same formula for the refractive index.
Since in FAS we could not include the water vapour dependency of the refraction index into the existing code, it was decided to use the formula (6.1.b) computing a new value for α^0 to produce a refraction index close to the one expressed in (6.2). Using the equation (6.2) and the (6.1.b), we can obtain:

$$\alpha^0 \cong 10^{-6}\left(\frac{103.49}{T}\left(p' - p_{H_2O}\right) + \frac{86.26}{T}\left(1 + \frac{5748}{T}\right)\cdot p_{H_2O}\right)\cdot\frac{p^0 T}{p T^0} \qquad (6.3)$$

Where p' and p_{H_2O} are expressed in mm Hg while p and p^0 in hPa:

$$p' = 0.7507\ p \quad \text{and} \quad p_{H_2O} = 10^{-6}\cdot VMR_{H_2O}\cdot p' \qquad (6.4)$$

Using equations (6.3) and (6.4) with selected mid latitude profiles for temperature, pressure and water vapour, α^0 at different altitudes can be calculated. The results of the computation are reported in Table 6.2. An average α^0 value can be evaluated from the values reported in the table: the mean α^0 value is 0.000273386.

Altitude [km]	VMR H_2O [ppmv]	Pressure [hPa]	T [K]	Pressure [mm Hg]	Partial Pressure H_2O [mm Hg]	Refraction index	P^0 [hPa]	T^0 [K]	α^0
20	3.77	5.34E+01	214.4319	40.10014	0.000151178	1.000019355	1013.25	288.16	0.0002732
17	2.63	8.62E+01	209.2875	64.70283	0.000170168	1.000031997	1013.25	288.16	0.0002732
15	1.95	1.20E+02	207.1787	89.70865	0.000174932	1.000044813	1013.25	288.16	0.00027319
14	1.97	1.41E+02	207.3198	105.6986	0.000208226	1.000052765	1013.25	288.16	0.00027319
13	2.31	1.66E+02	209.4902	124.391	0.000287343	1.000061453	1013.25	288.16	0.00027319
12	2.77	1.95E+02	214.7195	146.0862	0.000404659	1.000070415	1013.25	288.16	0.0002732
11	3.29	2.28E+02	219.9488	170.7843	0.00056188	1.000080363	1013.25	288.16	0.0002732
10	3.81	2.65E+02	225.1781	199.0856	0.000758516	1.000091505	1013.25	288.16	0.0002732
9	7.25	3.08E+02	230.0111	231.2156	0.001676313	1.000104048	1013.25	288.16	0.00027322
8	11.3	3.56E+02	236.3149	267.5495	0.003023309	1.000117195	1013.25	288.16	0.00027324
7	17.3	4.11E+02	242.969	308.4626	0.005336403	1.000131431	1013.25	288.16	0.00027327
6	25.5	4.72E+02	250.3536	354.1803	0.009031597	1.00014648	1013.25	288.16	0.00027331
5	36.8	5.40E+02	256.7075	405.1528	0.014909623	1.000163446	1013.25	288.16	0.00027337
4	51.9	6.15E+02	263.4016	461.9808	0.023976802	1.000181681	1013.25	288.16	0.00027343
3	71.9	7.00E+02	268.4647	525.1897	0.037761141	1.000202712	1013.25	288.16	0.00027353
2	110	7.93E+02	274.0781	595.6054	0.065516592	1.000225325	1013.25	288.16	0.0002737
1	161	8.98E+02	279.5114	673.8283	0.10848636	1.000250169	1013.25	288.16	0.00027393
0	266	1.01E+03	285.315	760.4591	0.202282121	1.000277055	1013.25	288.16	0.00027439

Table 6.2: Calculation of α^0.

In order to prove the reliability of the approximation provided by this calculation in Figure 6.2 is reported the comparison between the refraction index obtained using the Essen Froome formula in (6.2) and the formula in (6.1.b) with α^0 value equal to 0.000273386.
The difference between the two calculation can be hardly seen and its maximum percentual value is = 0.0001 % (see Figure 6.2.b). Therefore the new value α^0 of was introduced in FAS for the comparison with MARSCHALS forward model.

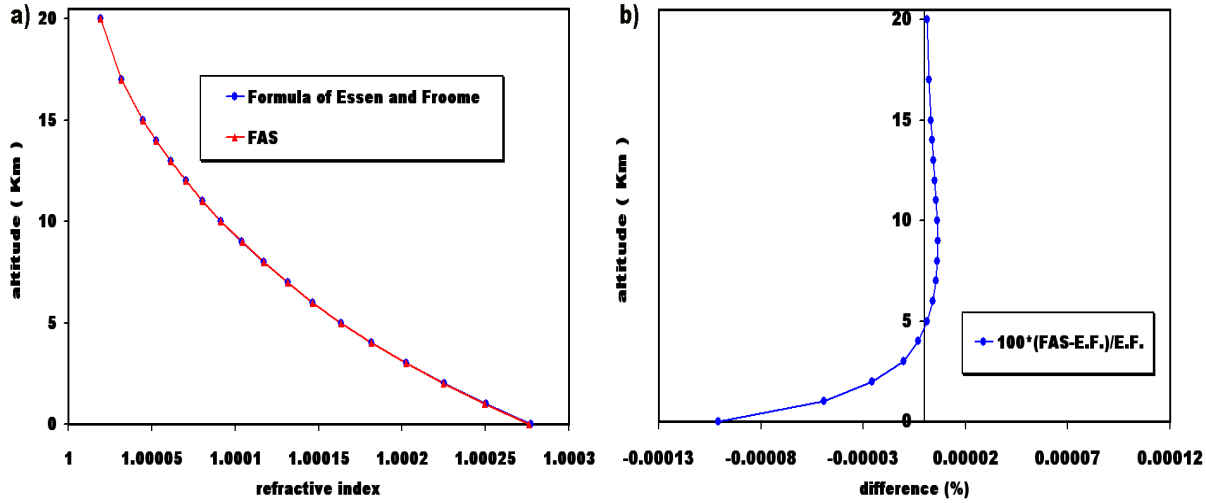

Figure 6.2: a) Comparison between refraction index calculated with Essen Froome formula and FAS approximation, b) Percentual difference between refraction index calculated with Essen Froome formula and FAS approximation.

Considering that SAFIRE-A channel one is located at 22-24 cm^{-1}, very near to MARSCHALS bands (about 11 cm^{-1}) where the Essen Froome formula has to be preferred, it was decided to implement the approximated Essen-Froome formula (6.1.b) also in RAS code for the channel one. Since the other two SAFIRE-A channels are quite far from the MARSCHALS bands, the approximated Barrel-Sears formula in (6.1.b) with α^0 equal to 0.000272632 has to be preferred for these channels (see Table 6.3).
Since the water vapour content in the atmosphere has a large variability, the value of α^0 has been evaluated for different atmospheric scenario that could be observed during different measurements campaigns (different water vapour profiles). The calculations reported in Table 6.2 were performed for different atmospheres: Mid-latitude, North Pole, South Pole and finally an atmosphere without water vapour. In Figure 6.3.a and in Figure 6.3.b, a comparison of the values of refraction index calculated with (6.2) for these atmospheres is reported. As can be seen in the figure, these values differ only at low altitudes, below the lowest SAFIRE-A tangent point. Inside the SAFIRE-A operational altitude range it seems that the α^0 value does not depend very much on the atmospheric scenario; for this reason a mean (over different atmospheres) α^0 value could be used for SAFIRE-A channel one (see Table 6.3).

	SAFIRE-A Channel 1(22-24 cm^{-1})	SAFIRE-A Channel 2 (centered at 118 cm^{-1}) and 3 (centred at 125 cm^{-1})
α^0	0.000273699	0.000272632

Table 6.3: α^0 values for different SAFIRE-A channels.

Finally, in order to appreciate the improvement apported by this update a calculation of the difference in tangent altitude obtained with equation (6.1.b) with α^0 value equal to 0.000273386 instead of 0.000272632 was performed: the maximum observed difference

was of the order of 22 meters at 11 Km. So, we can conclude that the correction given by the use of equation (6.1.b) with α^0 value equal to 0.000273386 instead of α^0 value equal to 0.000272632 is small.

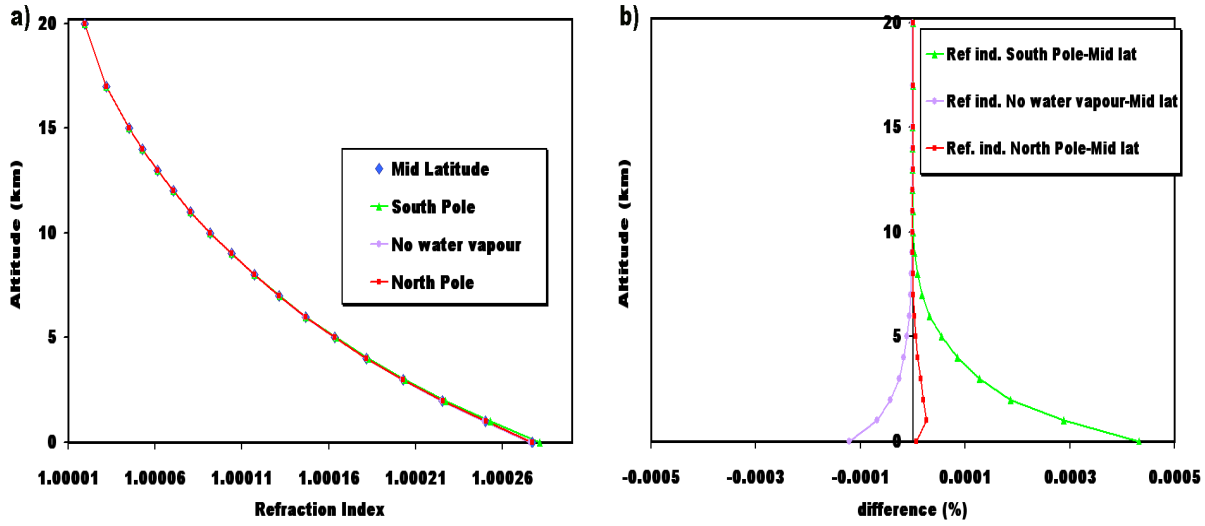

Figure 6.3: a) Comparison between refraction index calculated with Essen Froome formula in different atmospheric scenarios, b) Percentual difference between refraction index calculated with Essen Froome formula in different atmospheric scenarios and the Mid Latitude case.

B. MARSCHALS Partition Function

In Chapter 5 we have seen that the atmospheric cross section is a linear combination of the cross sections of the individual species each weighted by their concentration (Eq (5.7)). The absorption cross section of one molecular species *m* is a function of temperature and pressure and is given by the following sum over all lines of the species:

$$k(\sigma, T, p) = \sum_{l=1}^{lines} L_{m,l}(T) A_{m,l}(\sigma - \sigma_{m,l}, T.p) \tag{5.8}$$

where $L_{m,l}(T)$ is the line strength of line l of species m,
$\sigma_{m,l}$ the central wavenumber of line l of species m,
$A_{m,l}(\sigma\text{-}\sigma_{m,l}, T, p)$ the line profile (lineshape).
The line strength value depends only on the temperature according to the following expression:

$$L_{m,l}(T) = \frac{const}{Q_m(T)} \left\{ \exp\left[-\frac{hcE''_{m,l}}{k^B T} \right] \cdot \exp\left[+\frac{hcE'_{m,l}}{k^B T} \right] \right\} \tag{6.6}$$

$L_{m,l}(T)$ = line strength at reference temperature T
$Q_m(T)$ = total internal partition function of the species m at temperature T
$E'_{m,l}$ = upper state energy of the transition
$E''_{m,l}$ = lower state energy of the transition
h = Plank constant
And:

$$E'_{m,l} = E''_{m,l} + \sigma_{m,l} \tag{6.7}$$

Into the spectroscopic databases, the line strength is usually tabulated at a reference temperature T_0 (generally 296 °K). From the tabulated value it is possible to find the line strength for a generic temperature using the expression:

$$L_{m,l}(T) = L_{m,l}(T^0)\frac{Q_m(T^0)}{Q_m(T)} \cdot \frac{\exp\left[-\frac{hcE''_{m,l}}{k^B T}\right]}{\exp\left[-\frac{hcE''_{m,l}}{k^B T^0}\right]} \cdot \frac{1-\exp\left[-\frac{hc\sigma_{m,l}}{k^B T}\right]}{1-\exp\left[-\frac{hc\sigma_{m,l}}{k^B T^0}\right]} \tag{6.8}$$

Information on L, E and σ are provided in the spectroscopic database.
In expression (6.8), the value of the total internal partition function at different temperatures plays a very important role.
In MARSCHALS and SAFIRE-A codes an evaluation of the partition sum for every isotopic species is performed (subroutine fparts.f), in order to calculate the lines intensity.
Before the release of the HITRAN 2000 database (see APPENDIX B), partition functions were computed using the Gamache's procedure, according to which the partition sum versus the temperature is given by [32]:

$$Q(T) = A + BT + CT^2 + DT^3 \tag{6.9}$$

And the values of A, B, C, D are tabulated for each isotope.
In the HITRAN 2000 database, the values of the partition sums (TIPS = Total Internal Partition Sum) for every isotope are tabulated with respect to the temperature with a step of 1°K and also the partition function at a reference temperature 296 K is given for every isotope.
Considering that reading a file for every isotope is not practical, it is preferable to fit the tabulated TIPS with a 3rd degree polynomial as in (6.9), and replace the new coefficients in the program.
In order to perform this fit the IDL 5.1 function POLY_FIT (http://www.astro.washington.edu/deutsch-bin/getpro/library07.html/POLY_FIT) was used.
The function performs a least square polynomial fit with error estimate (output: A, B, C, D, Q(296), error on Q(296)).
The calculated coefficients and the corresponding partition functions at 296 °K are listed in the tables below, (values computed in a temperature range between 70 and 500 °K).
For some isotopes of HNO_3, C_2H_6, SF_6 and $ClONO_2$ the fit was performed over a restricted temperature range (from 150 to 300 °K) in order to improve the accuracy, since the temperatures outside this range can not be found in the atmospheric region considered.

Isotope	A	B	C	D	Q(296) coeff
H2O_161	-7.9787e+00	3.1496e-01	1.0998e-03	-3.1407e-07	1.73464e+02
H2O_181	-8.0819e+00	3.1795e-01	1.1077e-03	-3.1563e-07	1.74898e+02
H2O_171	-4.7834e+01	1.8741e+00	6.8496e-03	-2.2372e-06	1.04901e+03
H2O_162	-4.3173e+01	1.5796e+00	5.3053e-03	-1.1589e-06	8.59162e+02
H2O_182	-3.8802e+01	1.6192e+00	5.2746e-03	-1.0949e-06	8.74225e+02
H2O_172	-2.3398e+02	9.6899e+00	3.1346e-02	-6.4340e-06	5.21378e+03

Isotope	A	B	C	D	Q(296) coeff
CO2_626	1.2829e-01	9.2710e-01	-5.9991e-04	2.5116e-06	2.87125e+02

CO2_636	1.2138e+00	1.8385e+00	-1.1609e-03	5.2072e-06	5.78742e+02
CO2_628	3.5181e-01	1.9640e+00	-1.2811e-03	5.4126e-06	6.09823e+02
CO2_627	7.3981e-01	1.1478e+01	-7.5035e-03	3.1411e-05	3.55542e+03
CO2_638	2.5258e+00	3.8991e+00	-2.4980e-03	1.1264e-05	1.22992e+03
CO2_637	1.8317e+01	2.2701e+01	-1.4298e-02	6.4901e-05	7.16824e+03
CO2_828	1.5171e-01	1.0431e+00	-6.8732e-04	2.9229e-06	3.24493e+02
CO2_728	2.8975e+00	1.2147e+01	-7.9386e-03	3.3759e-05	3.77838e+03

Isotope	A	B	C	D	Q(296) coeff
O3_666	-2.8415e+02	8.7675e+00	2.5026e-03	3.6467e-05	3.47605e+03
O3_668	-6.1111e+02	1.8839e+01	4.2749e-03	8.1404e-05	7.45094e+03
O3_686	-3.0145e+02	9.2716e+00	1.6900e-03	4.0458e-05	3.64027e+03
O3_667	-3.5270e+03	1.0902e+02	2.8543e-02	4.6254e-04	4.32394e+04
O3_676	-1.7468e+03	5.4012e+01	1.3149e-02	2.3026e-04	2.13645e+04

Isotope	A	B	C	D	Q(296) coeff
N2O_446	3.6067e+01	1.4975e+01	-8.5862e-03	4.9662e-05	5.00433e+03
N2O_456	2.8412e+01	9.9045e+00	-5.4406e-03	3.3981e-05	3.36474e+03
N2O_546	2.5739e+01	1.0320e+01	-5.9339e-03	3.4693e-05	3.46029e+03
N2O_448	3.8830e+01	1.5863e+01	-9.2863e-03	5.3886e-05	5.31815e+03
N2O_447	2.2547e+02	9.2566e+01	-5.3593e-02	3.1082e-04	3.09903e+04

Isotope	A	B	C	D	Q(296) coeff
CO_26	9.9366e-02	3.6361e-01	-1.4379e-05	2.3947e-08	1.07089e+02
CO_36	1.3833e-01	7.6133e-01	-3.3045e-05	5.5406e-08	2.24034e+02
CO_28	3.8049e-02	3.8259e-01	-1.8250e-05	2.9700e-08	1.12456e+02
CO_27	5.6313e-01	2.2388e+00	-9.0548e-05	1.5311e-07	6.59285e+02
CO_38	1.1757e-02	8.0294e-01	-4.2148e-05	6.8207e-08	2.35758e+02
CO_37	9.0530e-01	4.6893e+00	-1.8864e-04	3.1300e-07	1.38053e+03

Isotope	A	B	C	D	Q(296) coeff
CH4_211	-4.9338e+01	1.4963e+00	1.3189e-03	3.0595e-06	5.88470e+02
CH4_311	-9.9433e+01	3.0032e+00	2.5946e-03	6.1638e-06	1.17670e+03
CH4_212	-4.0207e+02	1.2109e+01	1.0658e-02	2.4799e-05	4.75915e+03

Isotope	A	B	C	D	Q(296) coeff
O2_66	-3.5749e-01	7.4514e-01	-1.0159e-04	1.7073e-07	2.15731e+02
O2_68	-5.4882e+00	1.5796e+00	-2.2823e-04	3.8886e-07	4.52162e+02
O2_67	-3.1812e+01	9.2162e+00	-1.2900e-03	2.1804e-06	2.63971e+03

Isotope	A	B	C	D	Q(296) coeff
NO_46	-5.6207e+01	3.1339e+00	4.0078e-03	-3.1711e-06	1.14033e+03
NO_56	-3.9335e+01	2.1725e+00	2.7379e-03	-2.1466e-06	7.87938e+02
NO_48	-6.0408e+01	3.3204e+00	4.1553e-03	-3.2434e-06	1.20239e+03

Isotope	A	B	C	D	Q(296) coeff
SO2_626	-3.7900e+02	1.3232e+01	1.3302e-02	6.2786e-05	6.33145e+03
SO2_646	-3.8113e+02	1.3300e+01	1.3335e-02	6.3085e-05	6.36010e+03

Isotope	A	B	C	D	Q(296) coeff
NO2_646	-8.9493e+02	3.0040e+01	4.1125e-02	7.5458e-05	1.35571e+04

Isotope	A	B	C	D	Q(296) coeff
NH3_4111	-1.0642e+02	3.7339e+00	6.8001e-03	4.9229e-06	1.72228e+03
NH3_5111	-7.1378e+01	2.4976e+00	4.5276e-03	3.3031e-06	1.15027e+03

Isotope	A	B	C	D	Q(296) coeff

HNO3_146	-4.0963e+04	8.8476e+02	-2.8347e+00	9.2646e-03	2.12832e+05

Isotope	A	B	C	D	Q(296) coeff
OH_61	6.8092e+00	1.8795e-01	2.7193e-04	-2.3245e-07	8.02394e+01
OH_81	6.7297e+00	1.9012e-01	2.7072e-04	-2.2987e-07	8.07631e+01
OH_62	5.7189e+00	5.0410e-01	7.8644e-04	-6.5269e-07	2.06910e+02

Isotope	A	B	C	D	Q(296) coeff
HF_19	1.4811e+00	1.3443e-01	2.5157e-06	-1.1159e-09	4.14639e+01

Isotope	A	B	C	D	Q(296) coeff
HCl_15	2.6114e+00	5.3476e-01	-7.2902e-06	1.4446e-08	1.60636e+02
HCl_17	2.6188e+00	5.3550e-01	-6.9386e-06	1.3958e-08	1.60881e+02

Isotope	A	B	C	D	Q(296) coeff
HBr_19	2.3727e+00	6.7136e-01	-2.1141e-05	3.4987e-08	2.00150e+02
HBr_11	2.4502e+00	6.7059e-01	-1.7223e-05	3.0474e-08	2.00226e+02

Isotope	A	B	C	D	Q(296) coeff
HI_17	3.0090e+00	1.3151e+00	-7.5220e-05	1.2401e-07	3.88904e+02

Isotope	A	B	C	D	Q(296) coeff
ClO_56	1.1609e+02	6.6925e+00	1.3364e-02	9.0501e-07	3.29144e+03
ClO_76	1.1733e+02	6.8155e+00	1.3544e-02	1.0584e-06	3.34884e+03

Isotope	A	B	C	D	Q(296) coeff
OCS_622	6.8454e+00	3.4907e+00	-2.9442e-03	1.6950e-05	1.22172e+03
OCS_624	7.3429e+00	3.5737e+00	-2.9948e-03	1.7354e-05	1.25283e+03
OCS_632	1.5482e+01	6.9750e+00	-5.9404e-03	3.5634e-05	2.48375e+03
OCS_623	2.7090e+01	1.4157e+01	-1.2042e-02	6.9010e-05	4.95222e+03
OCS_822	7.6176e+00	3.7152e+00	-3.1648e-03	1.8675e-05	1.31435e+03

Isotope	A	B	C	D	Q(296) coeff
H2CO_126	-2.1409e+02	6.7014e+00	8.9802e-03	1.0867e-05	2.83816e+03
H2CO_136	-4.3919e+02	1.3743e+01	1.8422e-02	2.2269e-05	5.82033e+03
H2CO_128	-2.1409e+02	6.7014e+00	8.9802e-03	1.0867e-05	2.83816e+03

Isotope	A	B	C	D	Q(296) coeff
HOCl_165	-1.1563e+03	4.0708e+01	6.5568e-02	1.0079e-04	1.92520e+04
HOCl_167	-1.1858e+03	4.1551e+01	6.6246e-02	1.0312e-04	1.95919e+04

Isotope	A	B	C	D	Q(296) coeff
N2_44	7.4967e-01	1.5772e+00	-3.9795e-05	7.0159e-08	4.65934e+02

Isotope	A	B	C	D	Q(296) coeff
HCN_124	4.4269e+00	2.8817e+00	-1.4256e-03	6.3151e-06	8.96283e+02
HCN_134	9.0315e+00	5.9135e+00	-2.9316e-03	1.3092e-05	1.84210e+03
HCN_125	3.4545e+00	1.9876e+00	-9.6876e-04	4.4373e-06	6.21984e+02

Isotope	A	B	C	D	Q(296) coeff
CH3Cl_215	-1.4073e+04	3.7518e+02	-3.6070e-01	1.9238e-03	1.15270e+05
CH3Cl_217	-1.4324e+04	3.8158e+02	-3.6791e-01	1.9561e-03	1.17119e+05

Isotope	A	B	C	D	Q(296) coeff
H2O2_1661	-5.2844e+02	1.5924e+01	2.2217e-02	1.4161e-04	9.80419e+03

Isotope	A	B	C	D	Q(296) coeff
C2H2_1221	-1.1308e+01	1.4917e+00	-2.7518e-03	8.6648e-06	4.13849e+02
C2H2_1231	-4.4273e+01	5.9536e+00	-1.0957e-02	3.4601e-05	1.65534e+03

Isotope	A	B	C	D	Q(296) coeff
C2H6_1221	-9.4630e+03	2.1567e+02	-4.6107e-01	2.2277e-03	7.17521e+04

Isotope	A	B	C	D	Q(296) coeff
PH3_1111	-2.7209e+02	8.3133e+00	5.0251e-03	2.3555e-05	3.23981e+03

Isotope	A	B	C	D	Q(296) coeff
COF2_269	-1.1157e+04	2.7739e+02	-7.0437e-01	2.3269e-03	6.95830e+04

Isotope	A	B	C	D	Q(296) coeff
SF6_29	-1.7727e+06	2.9936e+04	-1.6257e+02	3.3901e-01	1.63662e+06

Isotope	A	B	C	D	Q(296) coeff
H2S_121	-2.4759e+01	9.7178e-01	2.7914e-03	-1.9320e-07	5.02449e+02
H2S_131	-9.9980e+01	3.9019e+00	1.1140e-02	-7.2422e-07	2.01224e+03
H2S_141	-2.5067e+01	9.7739e-01	2.7860e-03	-1.7944e-07	5.03685e+02

Isotope	A	B	C	D	Q(296) coeff
HCOOH_126	-6.0930e+03	1.5146e+02	-3.3044e-01	1.1208e-03	3.88545e+04

Isotope	A	B	C	D	Q(296) coeff
HO2_166	-2.6109e+02	9.0268e+00	1.9523e-02	6.6030e-06	4.29261e+03

Isotope	A	B	C	D	Q(296) coeff
NO+_46	4.4633e-01	1.0574e+00	-3.5385e-05	4.9600e-08	3.11623e+02

Isotope	A	B	C	D	Q(296) coeff
HOBr_169	-1.5772e+03	5.7573e+01	8.9781e-02	1.9199e-04	2.83098e+04
HOBr_161	-1.5743e+03	5.7391e+01	8.9280e-02	1.9189e-04	2.82123e+04

Isotope	A	B	C	D	Q(296) coeff
ClONO2_5646	-2.2080e+06	3.8667e+04	-2.0983e+02	5.3628e-01	4.76103e+06
ClONO2_7646	-2.2440e+06	3.9203e+04	-2.1324e+02	5.4914e-01	4.91843e+06

Table 6.4: Coefficients and Q(296) for isotopes in HITRAN 2000 database.

In the HITRAN 2000 database there are no data for BrO. However, this gas is present in the MARSCHALS spectral range.
For linear molecules the TIPS value is proportional to the square of the temperature so the ratio $Q(T_0)/Q(T)$ can be expressed as:

$$Q(T_0)/Q(T) \propto \left(T_0/T\right)^2 \tag{6.10}$$

so the formula in (6.10) has been applied to the two BrO isotopes, that are not present in the HITRAN database.
These partition functions have been implemented into FAS and used until May 2003, when Robert Gamache provided a new version of his subroutine. In this update the total internal partition functions are tabulated every 25K from 60 to 3010 K and the subroutine

BD_TIPS_2003.f calculates the Partition function at the requested temperature by a 4-point Lagrange interpolation. Before implementing the new expression in both codes, a comparison of these new partition functions with the previous ones has been performed. The partition sums seem to be quite similar for all the molecules; some very small (max. 1.59%) differences are present in ^{16}OD, $^{35}Cl^{16}O$, $^{37}Cl^{16}O$, $^{1}H_2{}^{16}O$ (see Figure 6.4), H_2CO cases.

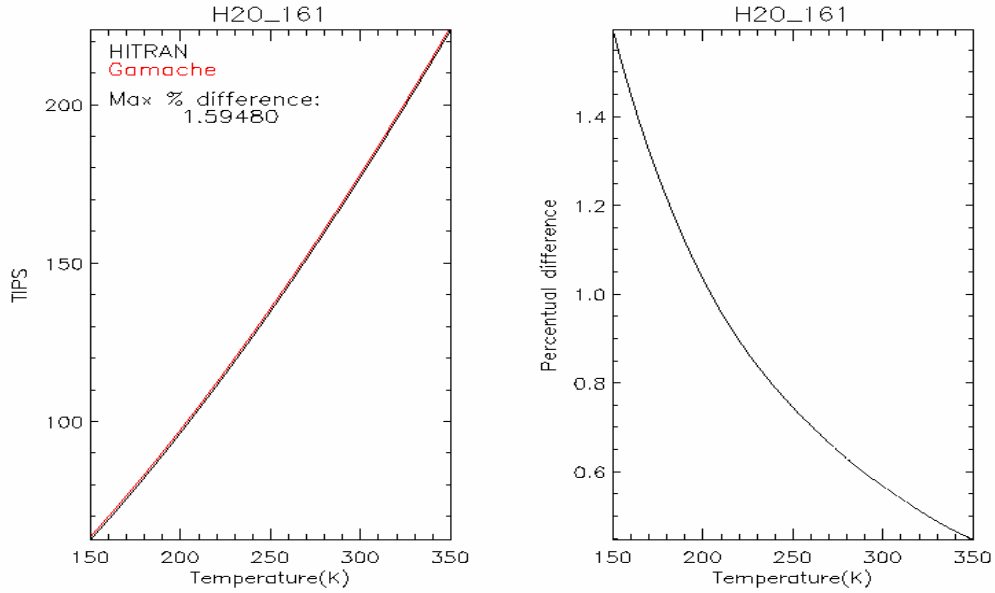

Figure 6.4: Comparison between TIPS for $^{1}H_2{}^{16}O$ isotope in HITRAN 2003 and Bob Gamache calculation.

6.1.1.4 Validation Results

The first step of the validation activity was the comparison of the results produced by the ray tracing procedure of the two forward models. For this purpose, a comparison between tangent altitudes computed by FAS (Forward Algorithm for SAFIRE) and the ones generated by MFM (MARSCHALS Forward Model) was carried out. Both SAFIRE-A forward model and MARSCHALS forward model codes have been run to generate spectra in the same atmospheric and spectroscopic conditions (temperature, pressure, VMRs, latitude and Earth radius); the set of pointing angles reported in section 6.1.1.2 have been chosen to perform the simulation. The result of the ray tracing procedure performed by the two codes is reported in Table 6.5. In general we can observe a very good agreement between the tangent altitudes calculated by FAS and MFM with differences of the order of few meters for almost all altitudes and with maximum value of 17 m on 7 km (see Table 6.5).

Pointing Angle [deg]	Geometrical [Km]	Refractive FAS [Km]	Refractive MFM-0.7 [Km]	Difference [Km]
90.00	20.000	20.000	20	0
90.50	19.756	19.75075	19.75582	0.00507
91.00	19.024	19.00085	19.00778	0.00693
91.50	17.805	17.74555	17.7527	0.00715
92.00	16.097	15.97335	15.9831	0.00975
92.50	13.902	13.66405	13.67588	0.01183
93.00	11.220	10.80665	10.81156	0.00491
93.50	8.150	7.35355	7.37038	0.01683
94.00	4.393	3.23845	3.23134	-0.00711

Table 6.5: Comparison of tangent altitudes obtained with FAS and MFM.

The second step of the validation was the comparison of the simulated spectra obtained by FAS and MFM. Since the more representative part of the forward model is the simulation of atmospheric spectra on the high resolution frequency grid, we decided to compare the spectra before the convolution with ILS and FOV. The comparison was carried on over all the three MARSCHALS bands. Some results of this comparison are reported in Figure 6.5, Figure 6.6, Figure 6.7 for spectra simulated at limb angles of 90 and 92 degrees. From these examples it can be seen that FAS and MFM spectra are very similar and the observed differences are negligible.

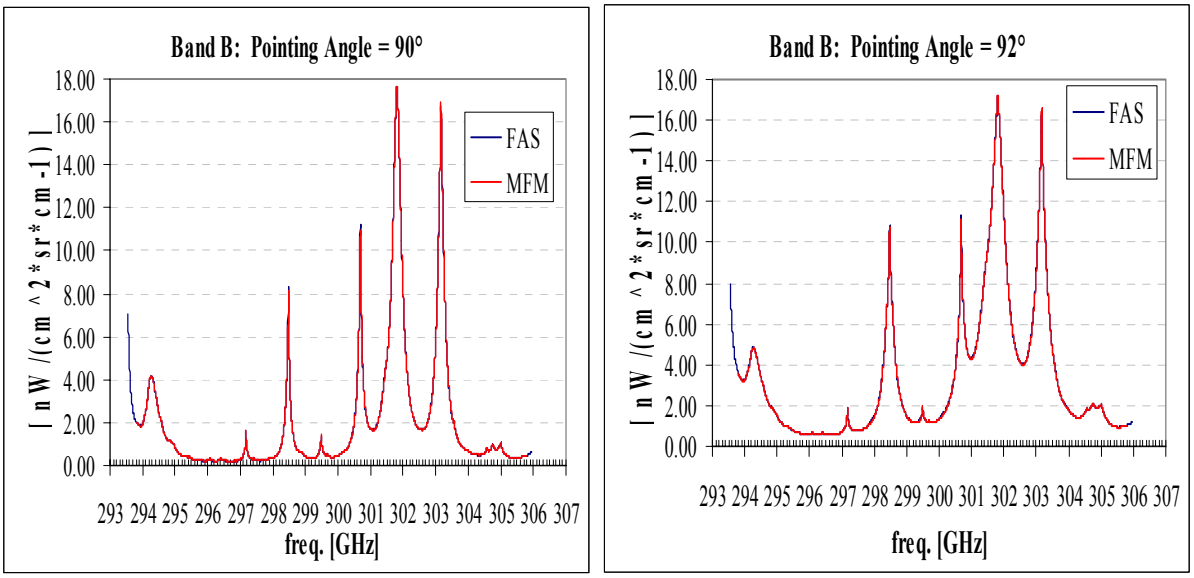

Figure 6.5: Comparison of spectra simulated with SAFIRE-A and MARSCHALS forward models (respectively named FAS and MFM). Atmosphere 1D, at mid-latitude. Spectral Band B. Pointing angles: 90°, 92°.

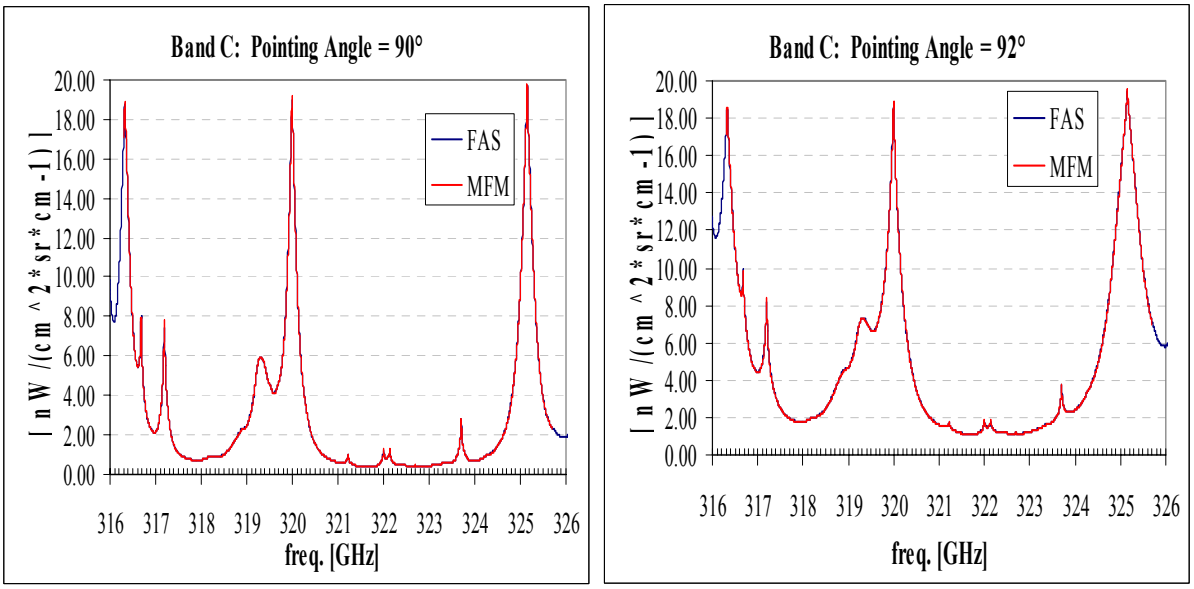

Figure 6.6: Comparison of spectra simulated with SAFIRE-A and MARSCHALS forward models (respectively named FAS and MFM). Atmosphere 1D, at mid-latitude. Spectral Band C. Pointing angles: 90°, 92°.

The obtained results were used to validate MARSCHALS forward model in the case of an uniform atmosphere. An other validation procedure was carried on between MFM and a Reference Forward Model (RFM, Oxford University). Also this procedure produced good results, assessing the reliability of MARSCHALS forward model. Since MFM has been

validated, the comparisons reported in this section can then be used to claim that SAFIRE-A forward model has been validated.

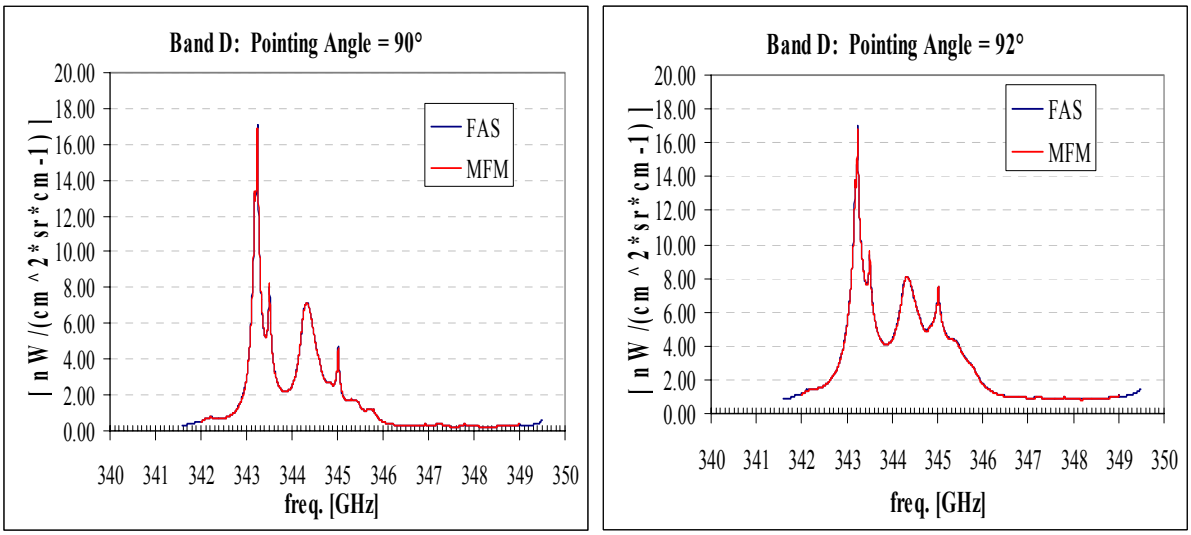

Figure 6.7: Comparison of spectra simulated with SAFIRE-A and MARSCHALS forward models (respectively named FAS and MFM). Atmosphere 1D, at mid-latitude. Spectral Band D. Pointing angles: 90°, 92°.

6.2 Software Development

After assessing the quality of the forward model inside RAS (FAS) (through the MARSCHALS code validation) and of the retrieval procedure (through internal validation tests), I have worked on a further development of the code. Two different features were implemented: the first, presented in section 6.2.1, is the possibility to retrieve the pointing angles values, while the second is the implementation of the algebra for the averaging kernel calculations (section 6.2.2) into the existing code.

6.2.1 Implementation of Pointing Angle Retrieval in RAS code

The exact knowledge of the pointing angle is a crucial element of the retrieval procedure. In RAS the pointing angle is read from the level one files (code input). An error in this value propagates in the retrieved VMR profiles through the wrong computation of the tangent altitude value. So the pointing retrieval procedure could be a very useful code feature. In the following sections a description of the implementation of the pointing angles retrieval in RAS code is reported.

6.2.1.1 Microwindow selection

In order to perform pointing angle retrieval, a gas with well known concentration profile and with spectral features in the SAFIRE-A channels is needed.

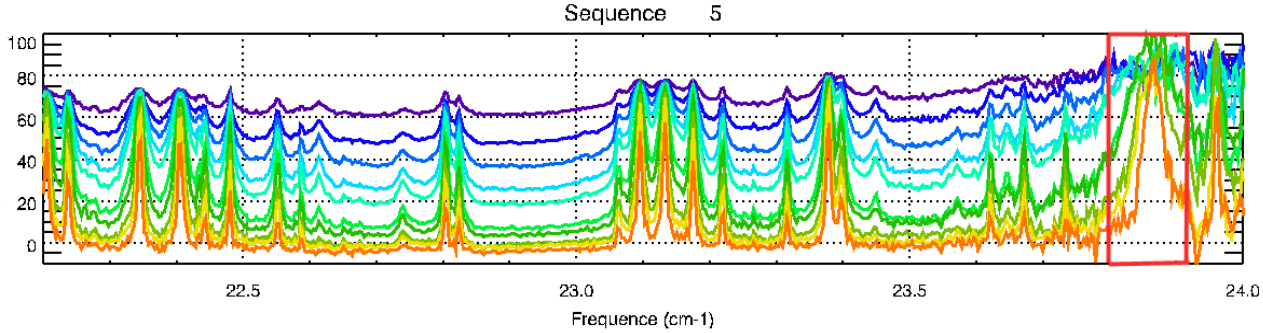

Figure 6.8: O_2 line position, evidenced by the red square, in SAFIRE-A channel one spectra (sequence 5 of 2nd March 2003).

Since O_2 VMR profile is well known, as well as its broadening coefficient (see APPENDIX B), it is the most suitable molecule to be used to determine the location of a measurement, and so the exact pointing angle. Looking at the spectra in SAFIRE-A channel one (22-24 cm^{-1}), one can notice that an O_2 line centred at 23.862946 cm^{-1} is present (Figure 6.8). The line is located at the edge of the channel, where the filter function degrades, this causes a not very good quality of the O_2 line(enhanced noise). In Table 6.6 and in Figure 6.9, the chosen microwindow for pointing retrieval is reported.

Center Wave Number (cm^{-1})	MW (cm^{-1})	Chemical Specie
23.862946	23.7999-23.9402	O_2

Table 6.6: MW used in RAS code for pointing angle retrieval.

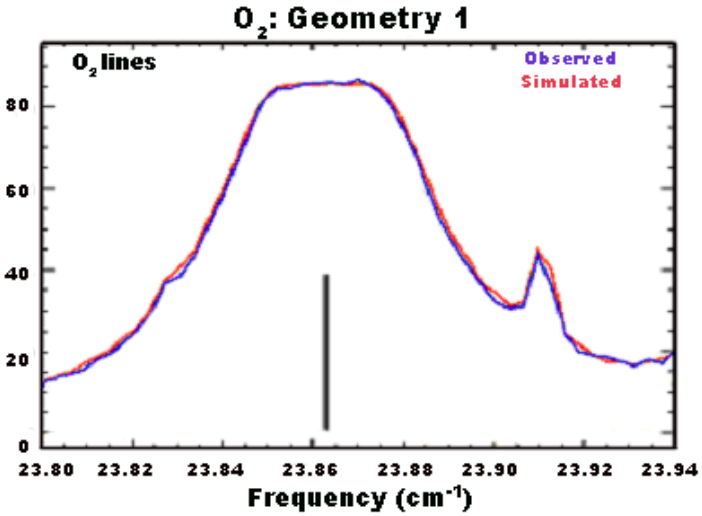

Figure 6.9: MW used in RAS code for pointing angle retrieval, and O_2 line position.

6.2.1.2 Jacobian calculation for Pointing angle

As evidenced in chapter 4, the retrieval procedure needs the calculation of the derivatives of the radiance with respect to the retrieved parameters. In the case of the pointing angle retrieval, the derivative of the spectrum (S) respect to the pointing angle θ is needed:

$$\frac{dS(\sigma,\theta,h)}{d\theta} \tag{6.11}$$

For the calculation of this derivative a numerical approach is preferred:

$$\frac{dS(\sigma,\theta,h)}{d\theta} = \frac{S(\sigma,\theta+\delta\theta,h) - S(\sigma,\theta,\mathrm{h})}{\delta\theta} \tag{6.12}$$

The spectrum at an angle $\theta+\delta\theta$ can be evaluated by simply apply a displacement $\delta\theta$ to the field of view. If we consider a given pointing angle θ_0 , the equation (6.12) becomes:

$$\frac{dS(\sigma,\theta_0,h)}{d\theta} = \frac{S(\sigma,\theta_0+\delta\theta,h) - S(\sigma,\theta_0,\mathrm{h})}{\delta\theta} \tag{6.12}$$

where from equation (5.9) we obtain:

$$S(\sigma,\theta_0,\mathrm{h}) = \int_{\theta_0-\Delta\theta}^{\theta_0+\Delta\theta} S(\sigma,\theta,\mathrm{h})\cdot FOV(\theta-\theta_0)d\theta \tag{6.13}$$

where $\Delta\theta$ is half of the FOV dimension (0.29°, in SAFIRE-A case), and θ scans all the FOV range (from θ_0 - $\Delta\theta$ to θ_0 + $\Delta\theta$). Now, If we substitute θ_0 with $\theta_0+\delta\theta$ into the (6.13), we can find:

$$S(\sigma,\theta_0+\delta\theta,\mathrm{h}) = \int_{\theta_0-\Delta\theta+\delta\theta}^{\theta_0+\Delta\theta+\delta\theta} S(\sigma,\theta,\mathrm{h})\cdot FOV(\theta-(\theta_0+\delta\theta))d\theta \tag{6.14}$$

Obviously in this case the θ range is from $\theta_0+\delta\theta$ - $\Delta\theta$ to $\theta_0+\delta\theta+\Delta\theta$.
Finally we obtain:

$$\frac{dS(\sigma,\theta_0,\mathrm{h})}{d\theta} = \frac{\int_{\theta_0-\Delta\theta+\delta\theta}^{\theta_0+\Delta\theta+\delta\theta} S(\sigma,\theta,\mathrm{h})\cdot FOV(\theta-(\theta_0+\delta\theta))d\theta - \int_{\theta_0-\Delta\theta}^{\theta_0+\Delta\theta} S(\sigma,\theta,\mathrm{h})\cdot FOV(\theta-\theta_0)d\theta}{d\theta} \tag{6.15}$$

The formula in (6.15) is the one implemented into the retrieval code. Using this approach I can simply calculate the derivative of the spectrum respect to the pointing angle during the FOV convolution. In this way, the pointing angle retrieval does not cause any increment in the retrieval computing time.

6.2.1.3 Retrieval tests of Pointing angles from simulated spectra

A series of different tests were performed in order to check the performance of this new code feature. It is important to stress that, while in a VMR retrieval the ray tracing calculation is performed only at the beginning of the retrieval, in a pointing angle retrieval this calculation has to be performed at every iteration to account for the pointing angles variation.
Some preliminary tests with constant pointing angles perturbation over all angles were performed with successful results. Then some other test with non uniform perturbation were carried on. An example is given in Table 6.7 and in Figure 6.10, where are reported the result of one test where a constant bias of -0.1° was applied to all initial guess pointing angles but the one at 90.0 where a large bias of -0.9° was applied:

Reference Pointing Angle [deg]	Initial guess Pointing Angle [deg]	Retrieved Pointing Angle [deg]
80.00	79.9	78.74 ± 0.243
85.00	84.9	85.48 ± 0.677
87.00	86.9	87.10 ± 0.840
89.00	88.9	88.45 ± 0.413
90.00	89.9	89.98 ± 0.146
90.90	90.0	90.74 ± 0.145
91.35	91.25	91.12 ± 0.104
91.75	91.65	91.77 ± 0.060
92.10	92.00	92.07 ± 0.056
92.40	92.30	92.35 ± 0.023

Table 6.7: result of pointing angle retrieval in case of constant bias -0.1 deg for all angles but the one at 90.9, where the perturbation is -0.9 deg.

The results obtained for this retrieval can be considered quite good. At higher pointing angles, when the instrument looks above the flight altitude (angles < 90 degrees), the retrieval error is

quite large and for these geometries the sensibility to the pointing angles is very small (in accordance with the fact that it is not possible to define a 'tangent' altitude for these angles).

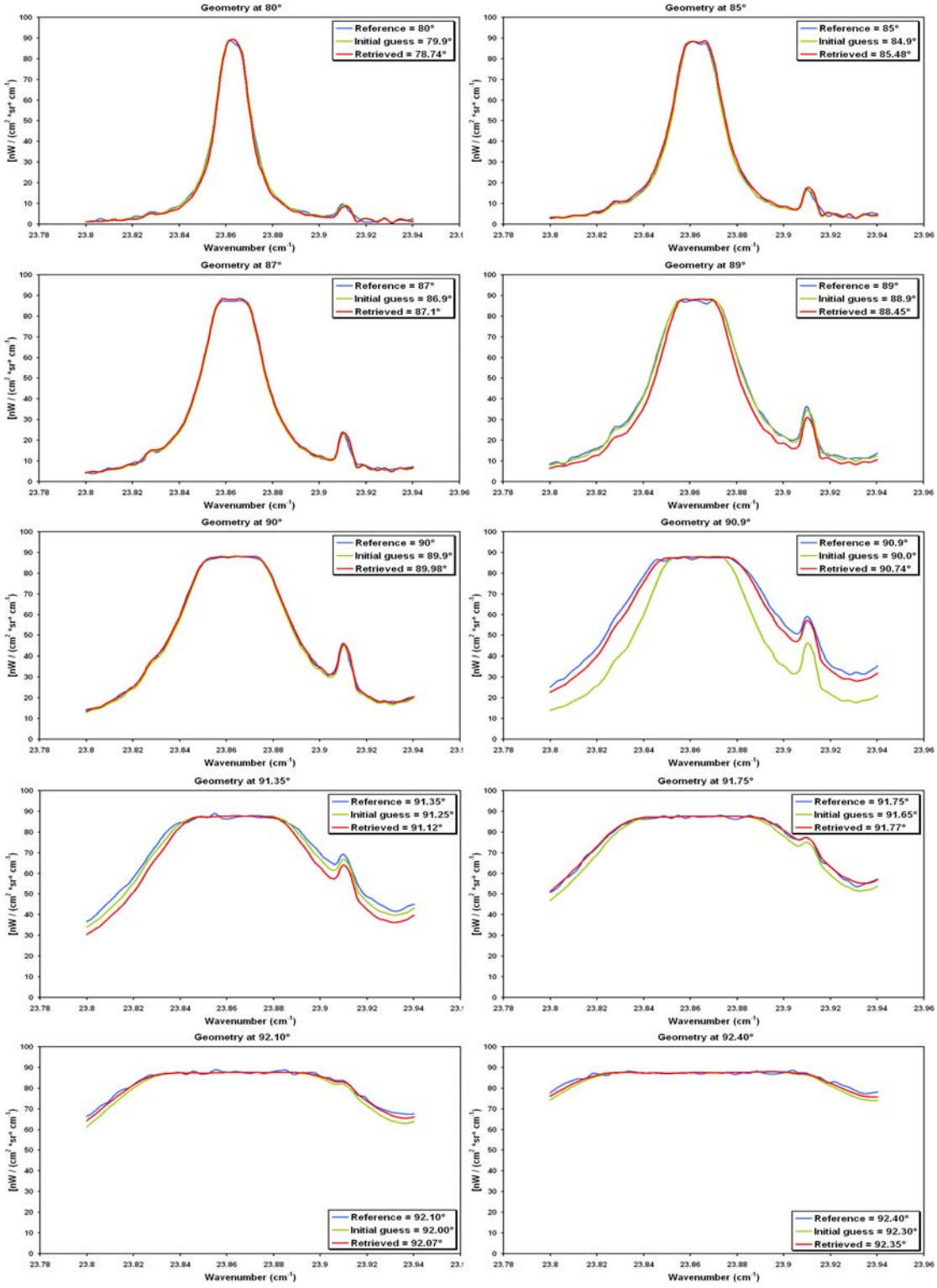

Figure 6.10: Comparison between true, retrieved and initial guess spectra reported in Table 6.7.

For all the "*tangent angles*" (angles > 90 degrees) the retrieved pointing seems to be in quite a good agreement with the reference one, especially for the one at 90.9° where a strong perturbation was applied (see Figure 6.10). This tests is quite significant because two of the initial guess angles (the one at 89.9 and the one at 90 degrees) were set at a very similar value.

Despite of this fact, the algorithm was able to retrieve the two very different reference value (89.98 and 90.74 respectively).
After these first results, other tests with a non uniform perturbation of the angles were performed. In some cases only one or two angles were perturbed, and also in these cases the code was able to retrieve the correct value of the perturbed pointing angle leaving almost unchanged the other ones.

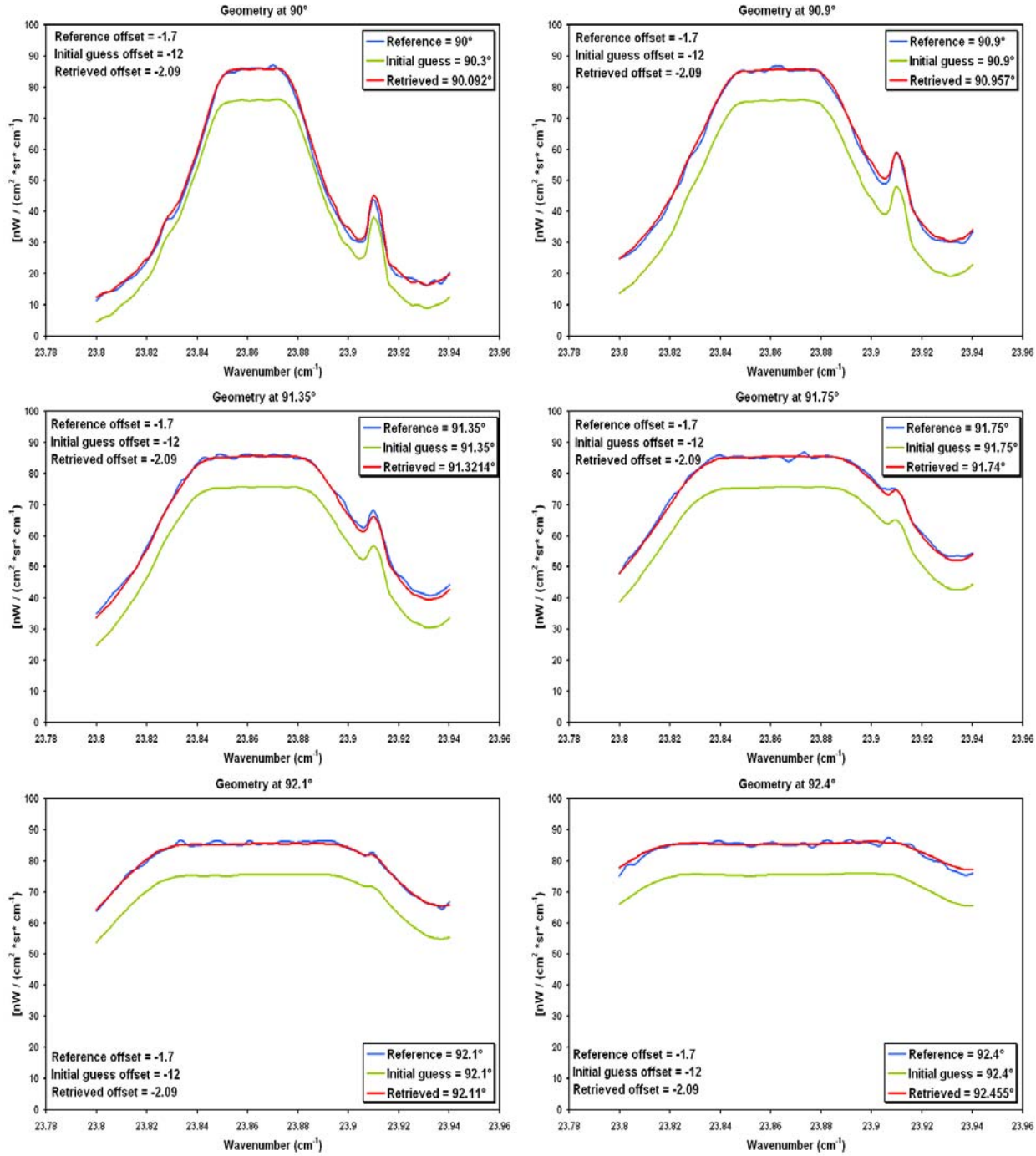

Figure 6.11: Comparison between true, retrieved and initial guess spectra reported in Table 6.8.

Finally, further tests were performed in order to check the existence of cross-correlation between offset and pointing. Two cases were analysed: in the first of the two tests only the offset was perturbed while both the offset and the pointing angles values were retrieved, while in the second only the pointing angles values were perturbed and both the offset and the

pointing were retrieved. The results of these tests show that the code is able to separate an offset effect from a pointing bias effect and no strong correlations exist.
In the last test, where only one pointing angle and the offset were perturbed, RAS has no problem in separate a constant (over the altitude range) offset effect from a single angle perturbation and both the offset and the angle value were well determined (see Table 6.8 and Figure 6.11).

Reference Pointing Angle [deg]	Initial guess Pointing Angle [deg]	Retrieved Pointing Angle [deg]
90.00	90.30	90.0920 ± 0.014678
90.90	90.90	90.9570 ± 0.060270
91.35	91.35	91.3214 ± 0.094950
91.75	91.75	91.7336 ± 0.080624
92.10	92.10	92.1139 ± 0.053537
92.40	92.40	92.4552 ± 0.024303
Offset reference value	**Offset initial guess value**	**Offset Retrieved value**
-1.7	-12	-2.0912 ± 0.085396

Table 6.8: result of pointing angle and offset retrieval in case of only one angle and offset perturbed.

6.2.1.4 Retrieval of Pointing angles from real spectra

The final test for pointing angles retrieval was the application of the algorithm to real data. For this test, the SAFIRE-A sequence number one for the Geophysica flight of 8th March 2003 from Kiruna was chosen. No particular pointing problems were reported during this flight and so it was expected that the retrieved pointing angles should be very similar to the commanded ones. The results of this test (shown in Table 6.9) confirm our expectation.

Initial guess Pointing Angle [deg]	Retrieved Pointing Angle [deg]
85	85.0191 ± 0.086
87	86.9958 ± 0.125
89	88.8570 ± 0.095
90	90.1083 ± 0.102
90.9	90.8863 ± 0.136
91.35	91.3405 ± 0.147
91.75	91.6829 ± 0.073
Offset initial guess value	**Offset Retrieved value**
0	6.522 ± 0.173

Table 6.9: result of pointing angle retrieval for sequence 1 of Geophysica flight on the 8th March 2003.

All the performed tests confirm that the pointing angles can be correctly retrieved by the SAFIRE-A code. It is then desirable that in future campaigns measured spectral ranges will include some molecular oxygen transitions with a better signal-to-noise ratio.

6.2.2 Implementation of the Averaging Kernel Calculation in RAS code

The quality of the retrieved profile is determined by its vertical resolution and its accuracy. The averaging kernels, already discussed in Chapter 4, provide a rigorous tool for the characterisation of the vertical resolution.
In the following sections a brief description of the averaging kernels, the connected quality parameters and their implementation into the code is discussed.
As an example of averaging kernels and quality parameters calculation, the case of the ozone retrieval for sequence 16th of the Geophysica flight on 2nd March 2003 from Kiruna is presented (see Table 6.10 for a description of the limb scanning sequence).

Flight altitude (km)	Limb angle	Tangent altitude(km)
18.16	80	--
18.16	85	--
18.16	87	--
18.16	89	--
18.149	90	18.14900
18.15	90.9	17.33705
18.15	91.35	16.31525
18.15	91.75	15.04995
18.15	92.10	13.67105
18.14	92.40	12.25525
18.14	92.70	10.63445

Table 6.10: Flight altitudes, limb angles and tangent altitudes for sequence 16th of Geophysica flight on 2nd March 2003.

6.2.2.1 Averaging Kernel Matrix

The Averaging Kernel Matrix (A_{AKM}) is the derivative of the retrieved profiles with respect to the true profiles performed in a particular state of the atmosphere and indicates the way in which the observing system smoothes the profile.
As described in Chapter 4, the A_{AKM} can be calculated using the expression (4.46) and reported below:

$$\boldsymbol{A_{AKM}} = \left(\boldsymbol{K^T S^{-1} K} + \boldsymbol{P}\right)^{-1} \boldsymbol{K^T S^{-1} K'} \tag{4.46}$$

AK can be calculated as part of the retrieval procedure or off line. The vertical discretization of the Averaging Kernel is dictated by the vertical grid used in the computation of the ***K'*** matrix. In general, the AAKM matrix has to be evaluated on a fine vertical grid. The retrieval procedure is performed instead on a more coarse grid, thus the evaluation of the high resolution A_{AKM} during the retrieval may result in a longer computing time.
In RAS we prefer to calculate the A_{AKM} matrix during the retrieval procedure, ***K'*** is computed using the retrieval vertical grid (***K'=K***) for an evaluation of the performances of the retrieval, and to calculate, off line and only in a restricted number of cases, an high resolution A_{AKM} matrix where ***K'*** is calculated on a fine vertical grid.

6.2.2.2 Averaging Kernel calculation in SAFIRE-A data analysis

The first test was carried on in order to check if the formula in (4.46) was implemented correctly into RAS. The simplest test we can perform is to neglect the part due to the regularization in the equation (4.46). Therefore, if the Tikhonov regularization as well as the Marquardt lambda were switched off, ***P*** is equal to zero and the formula can then be written as:

$$\boldsymbol{A_{AKM}} = \left(\boldsymbol{K^T S^{-1} K}\right)^{-1} \boldsymbol{K^T S^{-1} K} = \boldsymbol{I} \tag{6.16}$$

Equation (6.16) evidences that, in an ideal case, the averaging kernel matrix would be a unit matrix with all the rows peaking at the corresponding retrieval altitude with value 1 and infinitesimal width.
Once this consistency check was performed, I moved to the calculation of A_{AKM} for SAFIRE-A retrievals of real data (sequence 16 on 2nd March 2003 as in Table 6.10).
In Figure 6.12.a the AK are computed on a coarse vertical grid (retrieval grid, composed of one point at 20 km and the tangent altitudes). As can be seen in the figure every row of the A_{AKM} peaks at the corresponding retrieved altitude and the maximum value is close to 1.

Moreover, the AK relative to the higher tangent altitudes seem have peaks higher than the ones relative to the lower tangent altitudes.
In Figure 6.12.b I report the same averaging kernels computed on a fine vertical grid for the same retrieval grid. The fine grid goes from 0 to 25 km with an altitude step of 250 m. You can notice that also in this case the rows of A_{AKM} peak at the corresponding retrieval altitudes (but for the point at 20 km), even if in this case they are less well shaped and have a maximum value of 0.5 (since the AK are normalized in order to have an integral equal to 1).

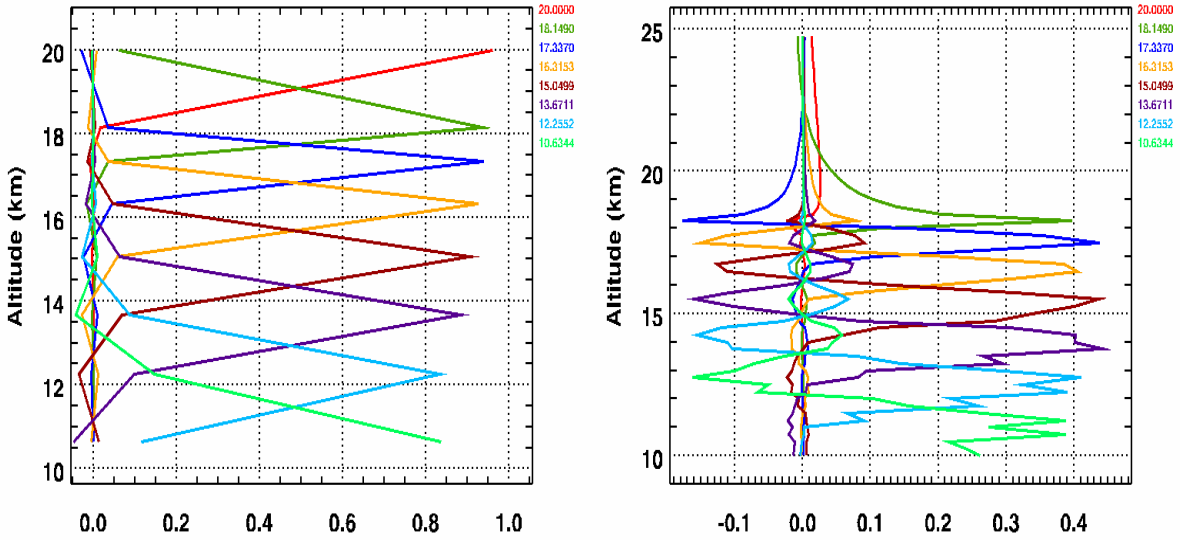

Figure 6.12: a) Averaging kernel calculation for sequence 16 on 2nd March 2003 in case of coarse vertical grid (retrieval grid); b) Averaging kernel calculation for sequence 16 on 2nd March 2003 in case of fine vertical grid (grid step 250 m) in case of Ozone retrieval.

For the retrieved point above the flight altitude (20 km) the averaging kernel shows that the information in the measurements is very poor and homogeneously distributed in the range of altitudes form 25 to 20 km. This behaviour is in accordance with the fact that, when the instrument looks above the flight altitude, the sensibility to the pointing is very small as previously shown in the pointing bias retrieval (Figure 6.10). This behaviour was not evident in the case of the coarse vertical grid calculation in Figure 6.12.a because in this case the highest point includes the contributions coming form all the points above it, enhancing the averaging kernel value.
In the case of the retrieved point at flight altitude (when the instrument looks horizontally) the corresponding averaging kernel seems to be asymmetric. The part below the flight altitude suggest an AK very sharp while the one above is broader. This reflect the fact that the point retrieved at aircraft altitude is influenced by the VMR concentration above the flight altitudes through the instrumental FOV and reflects the fact that above the flight altitudes the AK broadens, as shown in Figure 6.12.b. This behaviour was present also in the case of the coarse grid calculation of Figure 6.12.a.
The AK at tangent altitudes below the flight altitude are well peaked at higher altitudes while they broaden going further down in the atmosphere. This behaviour is due to the fact that the vertical amplitude of the FOV increases when decreasing the tangent altitudes of the measurements so that the vertical resolution of the measurements is inversely proportional to the tangent altitudes. This features was also shown in case of the coarse retrieval grid calculation in Figure 6.12.a.
All these considerations can be used to choose the retrieval grid and will be reported here only in the case of the ozone retrieval (see subsequent section 6.2.3.2).

6.2.2.3 Full Width Half Maximum Calculation

As recalled in Chapter 4, the Full Width Half Maximum (FWHM) of the Averaging Kernel, provides an indication of the vertical resolution of the observing system. Into the RAS code, the FWHM is calculated dividing the averaging kernel into two parts one above and one below where it peaks (see Figure 6.13.a and Figure 6.13.b). The two partial widths (a and b in Figure 6.13.a) can be evaluated using the altitudes corresponding to the half maximum value of the parts; summing them the values of the FWHM (in km) for the averaging kernel can be obtained (for the one in the Figure 6.13.a is 1.41 km). This value indicates the vertical resolution of the VMR retrieved at 18.149 km.

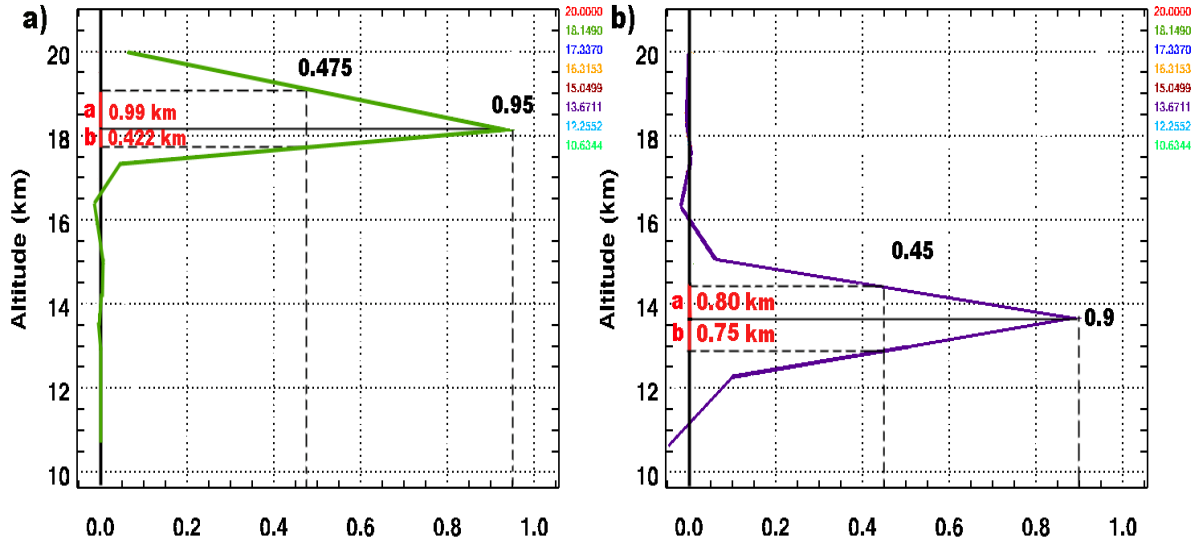

Figure 6.13: a) FWHM calculation for sequence 16 on 2nd March 2003 tangent altitude 18.1649 km; b) FWHM calculation for sequence 16th on 2nd March 2003 tangent altitude 13.6711 km in case of Ozone retrieval.

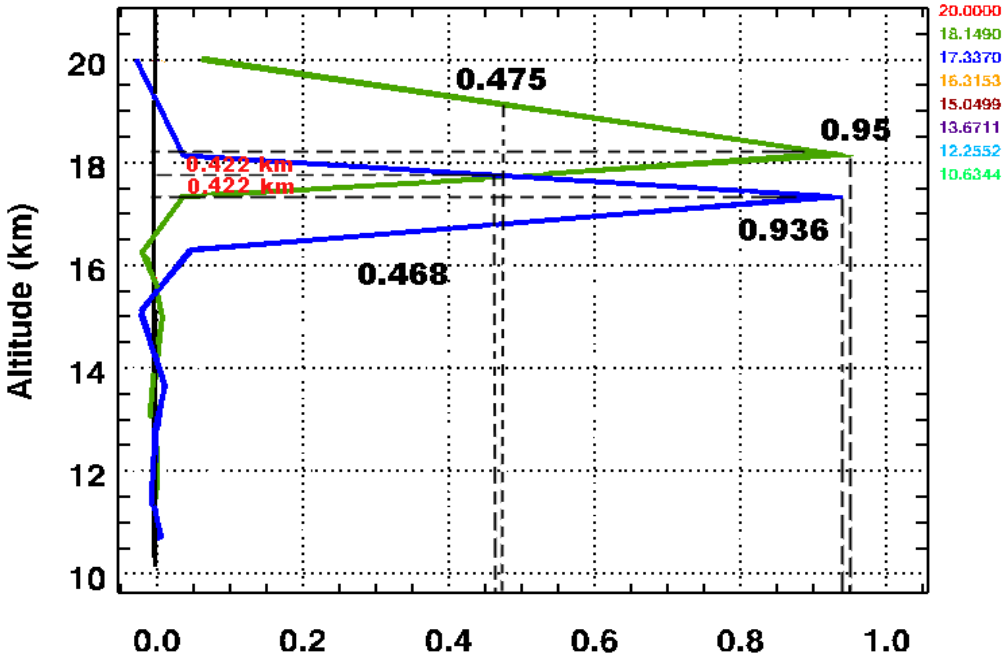

Figure 6.14: FWHM calculation for sequence 16th on 2nd March 2003 tangent altitude 18.1649 km and 17.337 km.

In Figure 6.13.b you can find an example of this calculation for another averaging kernel corresponding to the tangent altitude of 13.6711 km. In this case, the AK is nearly symmetric and, the two values of the partial width at half maximum (reported on the graph) are similar (0.8 and 0.75 km) and the FWHM is 1.55 km.
If we look at the AKs belonging to two contiguous tangent altitudes (as shown in Figure 6.14) and we calculate the partial width at half maximum (inferior partial width for the tangent altitude at 18.149 km and the superior one for tangent altitude at 17.337 km) we can notice that the summation of these two values (about 0.822 km) is similar to the separation between the two tangent altitudes (that is about 0.82 km).
In this case we can say that the two retrieval altitudes are independent. In cases where the summation of the partial width of two contiguous tangent altitudes is sensibly greater than the separation between the two tangent altitudes some over sampling has been performed in the measurement: the VMRs retrieved at the two altitudes are correlated and the retrieved profile may oscillate.
In Table 6.11 I report the comparison between the summation of the partial widths and the separation of two contiguous tangent altitudes. As can be noticed, we have no over sampling at high tangent altitudes while at the lower tangent altitudes some very small correlations between two subsequent points of the retrieval grid exist (but also here the over sampling is very small). This behaviour is in accordance with the fact that the pointing angle step was chosen in order to minimize the oversampling due to the instrumental FOV dimension.

Tangent altitudes (km)	Summation of partial width (km)	Separation between altitudes (km)
18.149 – 17.337	0.822	0.814
17.337 – 16.3153	1.068	1.027
16.3153 – 15.0499	1.34	1.278
15.0499 – 13.6711	1.488	1.379
13.6711 – 12.2552	1.587	1.42
12.2552 - 10.6344	1.92	1.66

Table 6.11:Comparison between the summation of partial width and the separation between the contiguous tangent altitude for sequence 16th on 2nd March 2003.

From this analysis I can conclude that the SAFIRE-A retrieval at tangent points gives uncorrelated results in the case of ozone retrieval.
In Table 6.12 we report the value of the FWHM calculated for all the tangent altitudes. It can be noticed, that for tangent altitudes below the flight altitude the value of the FWHM tends to increase with decreasing altitude and that the mean value (not including the extreme points) is 1.54 km (resolution of the ozone retrieval for this flight), while the average separation between the tangent altitudes is 1.13 km, very close to the vertical resolution.

Tangent altitudes (km)	FWHM (km)
20.00	0.94344*
18.149	1.41318
17.337	0.95898
16.3153	1.20740
15.0499	1.41385
13.6711	1.53897
12.2552	1.73087
10.6344	0.98237*

Table 6.12: FWHM calculation for sequence 16th on 2nd March 2003
*** This value represent only a partial width at half maximum.**

6.2.2.4 Integral Calculation

The range of altitudes over which the observing system is sensitive to the profile is indicated by the range of altitudes for which the area of the averaging kernel (the sum of its elements) is of the order of unity. Outside this range the area will tend toward zero as the retrieval tends toward the initial guess profile plus a measurement error component.
In Figure 6.15 I report the integral of the averaging kernels for the ozone retrieval of the sequence 16th of the 2nd March 2003. This integral is computed for each retrieved altitude, as the summation of the contribution of all the averaging kernels at this altitude. The value of the integral is near one over all the retrieval altitude range and has some oscillations near the lower altitudes. It means that the observing system is sensitive in the whole range with a small loss of sensitivity at lower altitudes where the retrieved VMR seems to be a little bit more influenced by the initial guess profile.

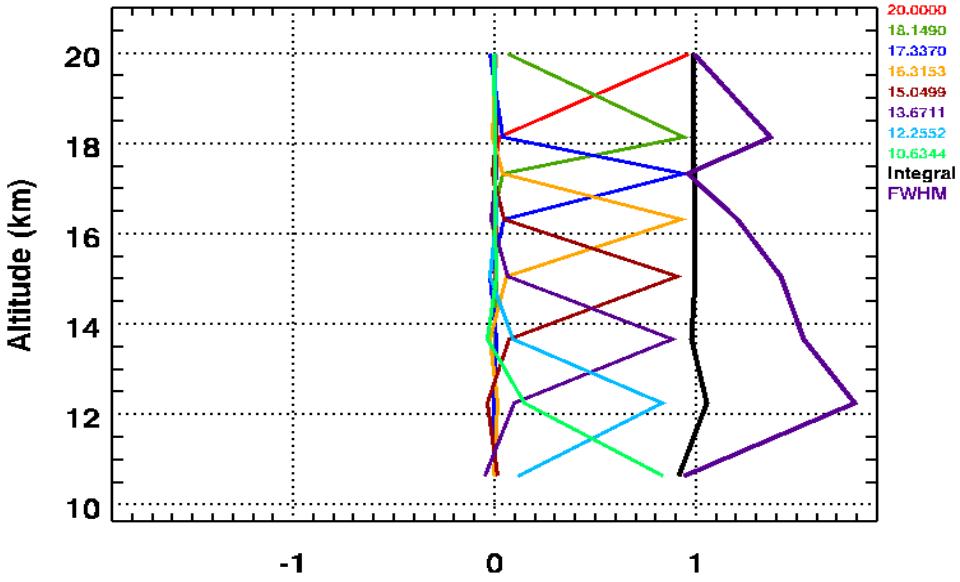

Figure 6.15: Integral and FWHM calculation for sequence 16th on 2nd March 2003.

6.2.2.5 Information Content Calculation

The information content of a measurement depends on the entropies of the probability density function (pdf) before and after the measurement. The formula implemented into the SAFIRE-A code is:

$$H = -\frac{1}{2}\ln\left|\boldsymbol{I} - \boldsymbol{A}_{AKM}\right| \tag{4.62}$$

The information content can be used to compare the gain or loss of information provided by two different measurements or two different grids applied to the same measurement.
In case of ozone retrieval of sequence 16th for the flight of 2nd March 2003, the value of the information content is 41.32.

6.2.2.6 Averaging Kernel Trace Calculation

As seen for the information content, also the number of independent pieces of information in a retrieval can be related to the averaging kernel matrix. Equation (4.74) was implemented into the RAS code.
In the case of the reported retrieval example the value of the trace is 15.29. This is a total value representing both the contribution of the ozone retrieval and of the continuum retrieval (simultaneously retrieved). For the ozone retrieval the trace of the averaging kernel matrix

related to ozone alone is 7.22 while the number of retrieved point is 8, this means that in the retrieval there are some retrieved points where the information is lower. Looking at Figure 6.15 one can notice that these points are the one where the integral is less than ones, so the lower retrieved altitudes.

6.2.2.7 Biased/Unbiased errors

The diagonal elements of the variance-covariance matrix quantify the errors associated with the retrieved quantities in the case of the pure Gauss Newton method. In this case the VCM determines how the measurement errors map onto the retrieved quantities when no auxiliary information is used.

$$\boldsymbol{S} = \left(\boldsymbol{K}^{\boldsymbol{T}}\boldsymbol{S}^{-1}\boldsymbol{K}\right)^{-1} \tag{6.17}$$

The squared root of the diagonal elements of the VCM is the unbiased errors associated with the retrieved parameter. When auxiliary information is used the error propagation leads to a rather complex expression. However, if also the "smoothing error" [17] is taken into account in the retrieval error, a simple expression is again obtained for the VCM of the retrieved quantities. In this case, the expression of the variance-covariance matrix S will be the following:

$$\boldsymbol{S} = \left(\boldsymbol{K}^{\boldsymbol{T}}\boldsymbol{S}^{-1}\boldsymbol{K} + \boldsymbol{P}\right)^{-1} \tag{6.18}$$

Being $\boldsymbol{P}$ related to Marquardt and Tikhonov regularization.
The biased error associated with the retrieved parameter is computed as the root of the diagonal elements of the modified VCM of parameters, taking into account the contribution due to the applied perturbation.
By comparing the unbiased retrieval error given by the diagonal of the inverse of the Gauss Newton VCM with the actual retrieval error (biased retrieval error) we can deduce the perturbation/added information introduced by the retrieval technique in the result. In case of the reported example, the value of the ratio between biased and unbiased error is reported in Figure 6.16.3, together with the integral and the FWHM. It is possible to notice that the biased/unbiased ratio is close to one (the minimum value is 0.75) in accordance with the value of the integral and the trace. The value of the ratio between the two errors seems to show that in this retrieval the VMR values are mainly due to the measurements than to the initial guess.
Moreover it seems that the measurements provide more information at high tangent altitudes than at the lower.

6.2.2.8Visualisation of Retrieval results including Averaging Kernel information

In order to condense in only one graph all the information for a single retrieval, we decided to include all the information in a four panel graph (this approach comes from MARSCHALS study where this form was applied for the first time). Figure 6.16 shows this graph for the test case.
In the title the name of the target molecule of the retrieval is reported; the second row (subtitle) reports the value of the number of independent points (trace of the part of A_{AKM} matrix relating to the retrieved species), the number of the retrieved points for the species (and the grid used for the retrieval), the trace and the information content for the whole retrieval. In the example, where we retrieve the value of ozone VMR and continuum profile simultaneously, the trace is 15.29 that is the summation of the number of independent points retrieved for ozone and continuum (7.22 for ozone and 8.07 for continuum). Then the following plots are reported:

Plot 1 - (Top left) shows the retrieved profile together with the error bars (unbiased error) and the initial guess profile.
Plot 2 - (Top right) shows the biased and unbiased ESD (in percent).
Plot 3 - (Bottom left) shows the ratio between the biased ESD and the unbiased ESD, the Averaging Kernel integral and the FWHM of the AK.
Plot 4 - (Bottom Right) shows the Averaging Kernels.

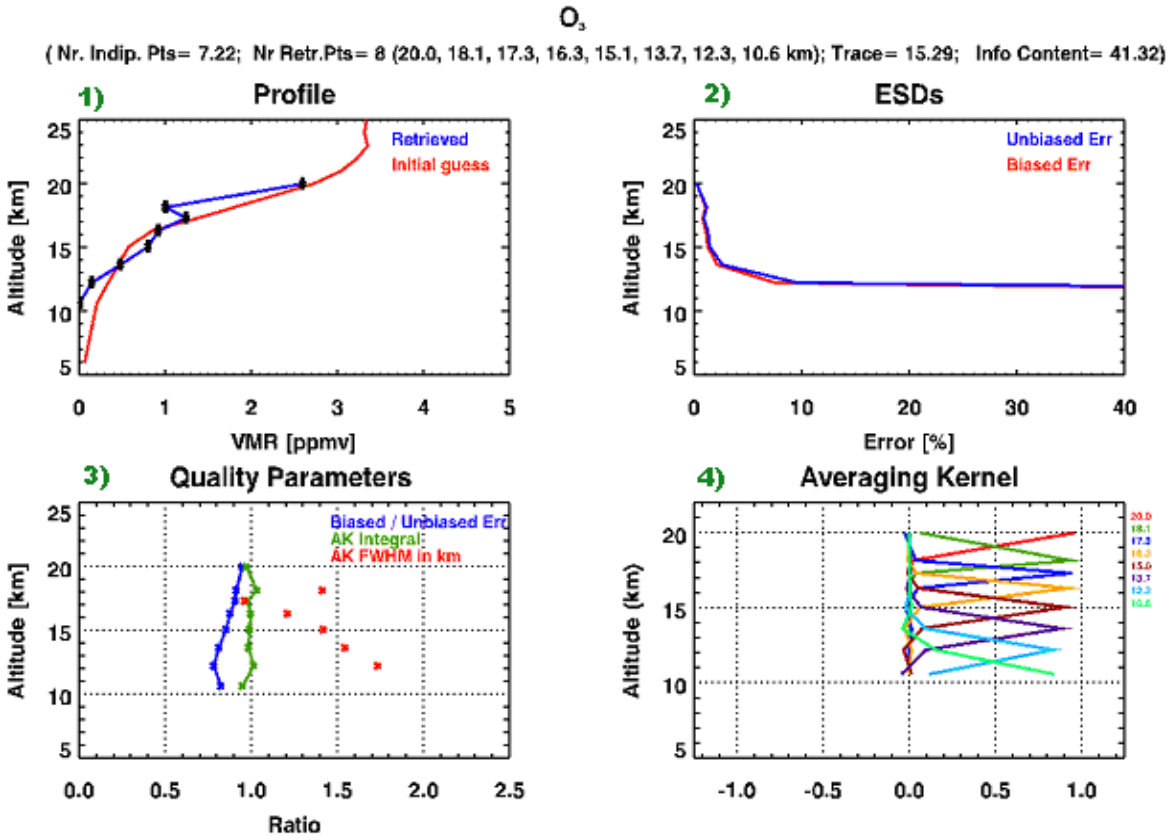

Figure 6.16: Integral, FWHM, Biased/Unbiased error calculation for sequence 16th on 2nd March 2003, ozone retrieval.

6.2.3 Examples of Averaging Kernel applications to SAFIRE-A data analysis

In the two following subsection are reported two applications of averaging kernels calculations. In the first case, the averaging kernel are used to tune the value of the Tikhonov regularization parameters, while in the second case the intent is to find a suitable retrieval grid.

6.2.3.1 Regularization

A good example of the use of averaging kernel matrix and of the quality parameters (trace, information content, biased/unbiased errors, FWHM) is the tuning of the Tikhonov regularization parameter. In the two Figure 6.18 and Figure 6.19 I report the 8 plots resulting from retrievals of ozone VMR plus continuum profile (not reported here) for sequence 20th on the 2nd March 2003 form Kiruna with different γ^2 parameters for ozone profile regularization (no regularization was applied to the continuum profile).
For this sequence, I first tuned the value of γ^2 using the L-curve method (also reported in Figure 5.3, and here in more details in Figure 6.17). In order to do this, I performed the same retrieval with different values of the regularization parameter, then, for each retrieval, I plotted in the graph below the value of the logarithm of the norm of the residual and of the difference between the retrieved and the initial guess profiles.

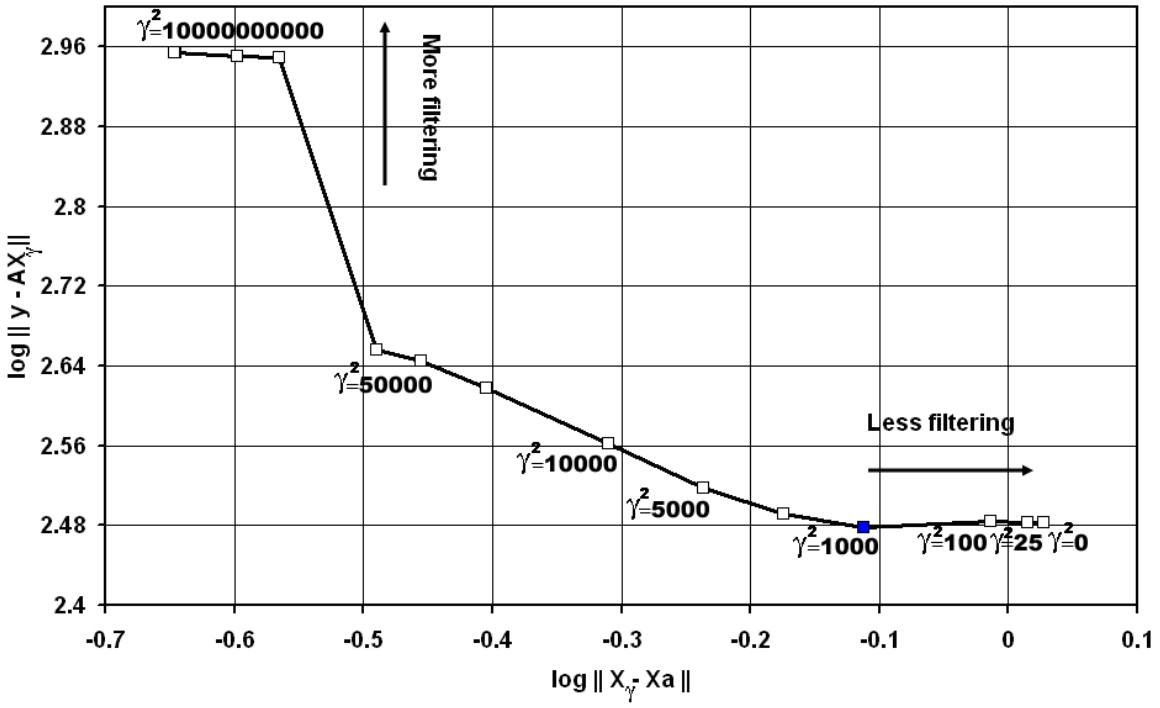

Figure 6.17: L-curve for SAFIRE-A sequence number 20 2nd March 2003, ozone retrieval, with indications of γ^2 value for retrieval cases in figure 5.20 and 5.21.

As can be seen in Figure 6.17, according to the L-curve procedure reported in section 5.4, the value of the regularization parameter which minimizes the χ^2 and which does not introduces too much regularization is the one marked in blue equal to 1000. If everything works well, looking at the retrieval results and at the value of averaging kernels and quality parameters in Figure 6.18 and Figure 6.19, I should be able to find the same value of the regularization parameter found with the L-curve method.

In the first plot of Figure 6.18 the value of the γ^2 is 0 and the only regularization comes from the Marquardt lambda, while in the second and in the third plot the value of γ remains small. For these cases the retrieved ozone profile oscillates a lot, the number of independent point is about 5.5 against 8 retrieved point. The value of the integral is near but below 1 at all altitudes and, according to the fact that the averaging kernels are all peaking at values near but less than one (about 0.9).

In the fourth plot of Figure 6.18 is reported the case of the ozone retrieval with regularization factor equal to 1000. In this case the value of retrieved independent points is 5.30, near to the previous case, but the ozone profile seems to be smoother below flight altitude. Considering the biased/unbiased ratio we can see that the value is very near to 1 for the highest tangent altitudes (more than in the previous cases) while it decreases going further down in the atmosphere, with a minimum value of 0.4 for the altitudes below 15 km. This behaviour is also reflected into the averaging kernels shape. They are sharp at 0.9 near the flight altitude while they tend to decrease the peak value and becomes larger for lower altitudes (the regularization acts mainly at these altitudes also because in RAS the regularization is normalized using the retrieved value at the corresponding altitude).

The integral value is 1 for all the altitude range but for the last retrieved point. Considering the values of the averaging kernels and of the quality parameters, it seems to be the better case for ozone retrieval on this sequence (same result obtained with L-curve method).

In the first and second plot of Figure 6.19 the value of the γ^2 are high (5000 and 10000). These cases are similar to the previous one with the only difference that the number of independent pieces of information is lower (respectively 4.07 and 3.55) than in the previous case (5.30).

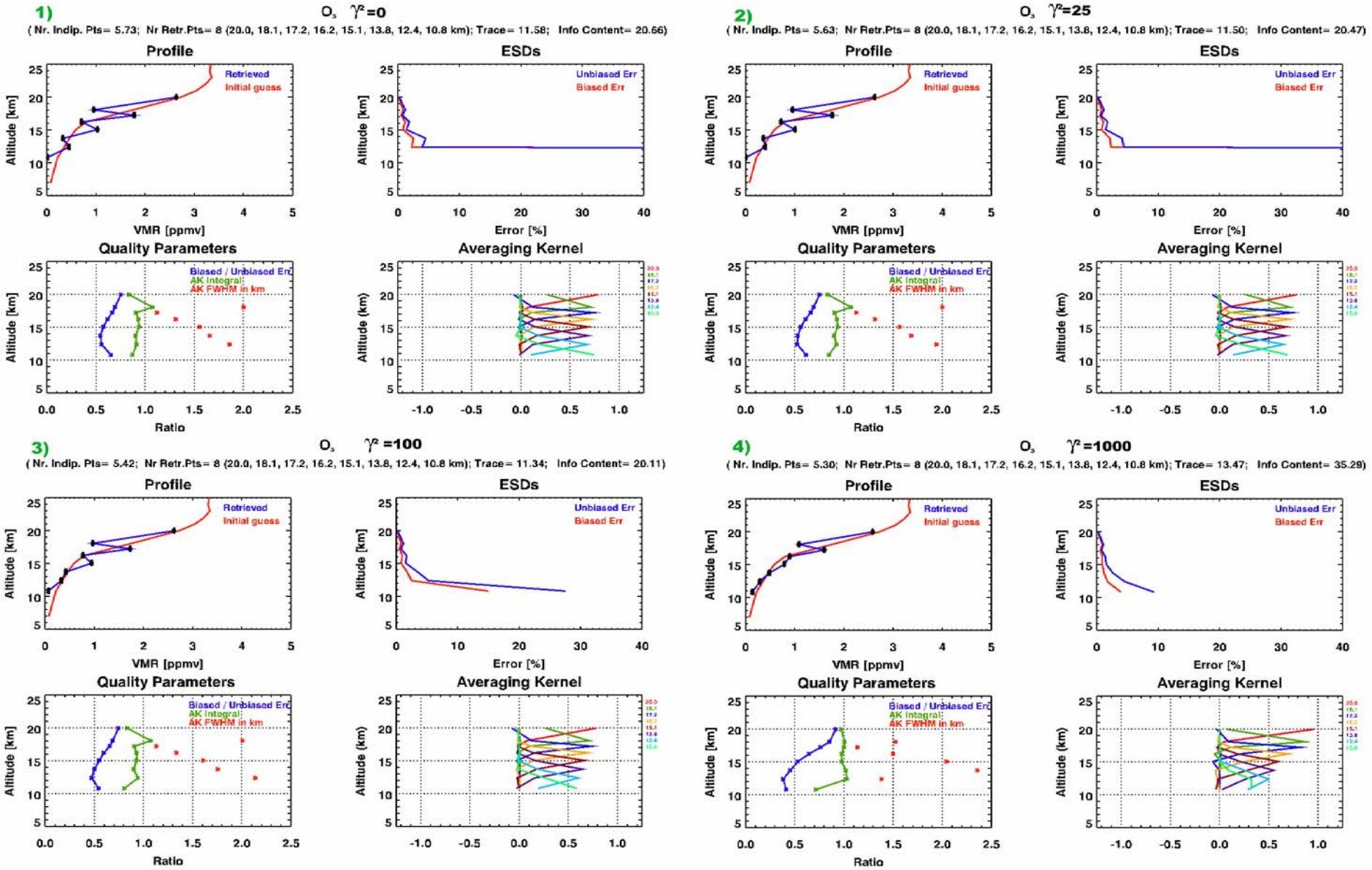

Figure 6.18: Ozone retrievals for sequence number 20 on 2nd March 2003 with different lambda values: 1) 0, 2) 25, 3) 100, 4) 1000.

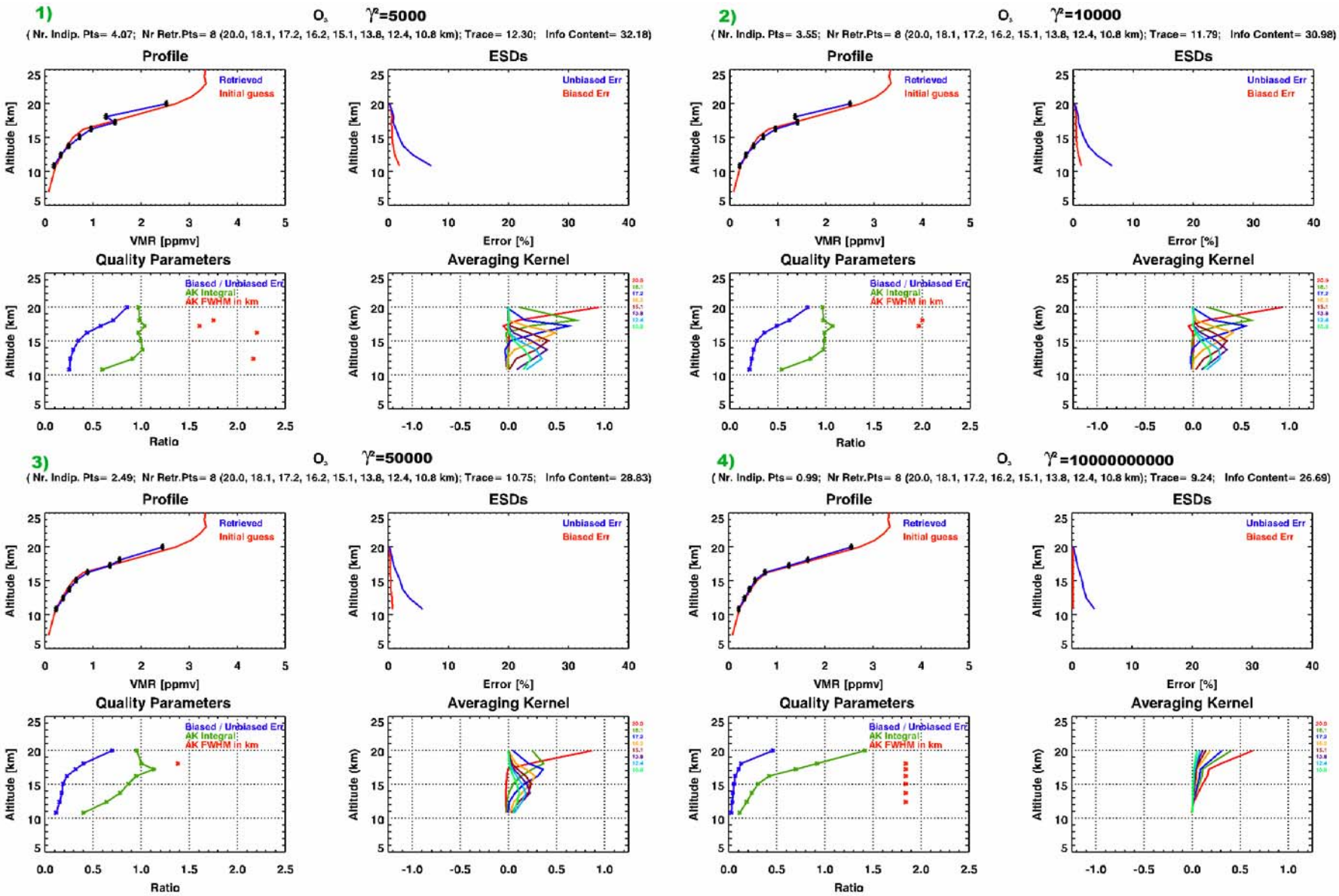

Figure 6.19: Ozone retrievals for sequence number 20 on 2nd March 2003 with different lambda values: 1) 5000, 2) 10000, 3) 50000, 4) 10000000000.

In case of plot 4 of Figure 6.19, the value of γ^2 parameter is huge. The retrieved profile is equal to the initial guess one. The value of the biased error is 0% (in accordance with the fact that the information comes mainly from the initial guess). The value of biased/unbiased errors is near 0 for all altitudes but for the point at 20 km. The averaging kernels broaden, their are all flat and the major contribution comes from the points above the retrieved altitudes.
From these tests, I can conclude that the behaviour of averaging kernels and quality parameters in case of tuning the value of the regularisation parameter is the expected one. When the regularisation effect is small the averaging kernels are well shaped and peaked, the value of the trace is similar to the one obtained with no regularisation and the integral is close to 1. When the value of the regularisation is dominant, the shape of the averaging kernels disappeared, the value of the trace is near 0 as the value of biased/unbiased errors. Moreover, the value of the parameter found with the L-curve method is the same that I have found using the quality parameters of the retrieval.

6.2.3.2 Tuning the Vertical Retrieval Grid

Another example of the utility of the use of the averaging kernel and the quality parameters information is the tuning of the vertical retrieval grid. In Figure 6.20 you can find the retrievals of the ozone VMR for the first sequence of the fourth flight of a test campaign performed in Forli' before the APE-GAIA Campaign in 1999 (see Table 6.13 for limb scanning angles and tangent altitudes). In the figure, I present the results of the retrieval with 6 different retrieval grid.

Flight altitude (km)	Limb angle	Tangent altitude(km)
17	80	--
17.16	85	--
17.33	87	--
17.48	89	--
17.57	90	17.566
17.67	90.6	17.31075
17.78	91.10	16.56225
17.89	91.60	15.30875

Table 6.13: Flight altitudes, limb angles and tangent altitudes for sequence 1 of 4th flight of ETC Campaign.

The grid used into the first test (see Figure 6.20.1) was composed by the reported tangent altitudes and points in between: 17.566, 17.437, 17.31075, 16.9365, 16.56225, 15.9355, 15.30875 km. In this case some oversampling is reported: the value of the ratio of biased/unbiased error is near 0 for all the points but the one at 17.556 km and the number of independent retrieved points is 4.05 and 7 points are retrieved (ratio=0.578). If a retrieval grid composed of tangent altitudes is used (Figure 6.20.2), the value of the independent retrieved points is 3.75 and 4 points are retrieved (ratio=0.9375), all the averaging kernels peak at 1, the value of biased and unbiased errors are very similar and their ratio is very near to 1 (all the information comes from the measurement). These two tests prove that the use of tangent altitudes as retrieval grid, in case of ozone, is a correct choice, since the use of a finer grid do not improve the number of degrees of freedom of the retrieval.
Since four measurements were performed above the flight altitude (Table 6.13), we carried out some tests in order to see if adding some points above the flight altitudes could give some additional information.
In the plot in Figure 6.20.3, one point at 20 km was added. In this case the value of the biased and unbiased errors are very similar and their ratio is very near to 1, as well as the value of the integral.

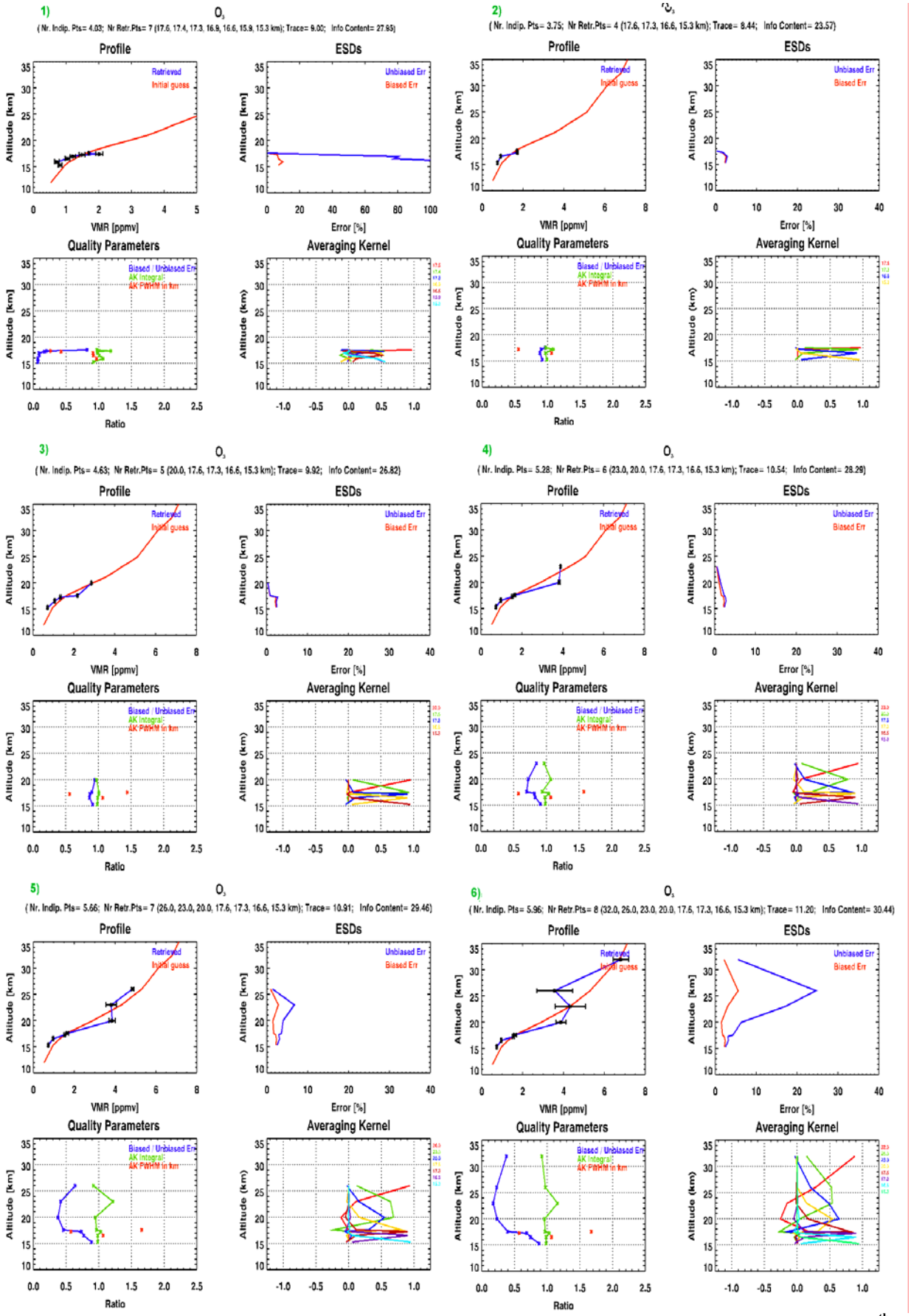

Figure 6.20: SAFIRE-A retrieval for ozone value in sequence number 1 on ETC test campaign in Forli' (4th flight) at different vertical retrieval grids: 1) tangent altitudes and points in between, 2) tangent altitudes 3) 20+ tangent altitudes 4) 23+20+ tangent altitudes, 5) 26+23+20 + tangent altitudes, 6) 32+26+23+20 + tangent altitudes.

The averaging kernels peak at a value near to 1, the value of the independent retrieved points is 4.63 with 5 points retrieved (ratio = 0.926 very similar to the one in Figure 6.20.2). From Figure 6.20.4, 6.20.5, 6.20.6, it seems that adding more than one point above the flight altitude do not improve the retrieval quality: in plot number 4, the retrieval grid is composed by 23, 20 km and tangent altitude. Six points are retrieved, with 5.28 independent points and a ratio of 0.88 sensibly lower than the ones before. In the fifth plot we add another point at 26 km to the vertical grid. Therefore the grid is composed by 7 points with 5.66 independent points retrieved (ratio = 0.808). Both the shape of biased/unbiased ratio and the averaging kernels show that the information above the flight altitude is not well localised. This behaviour is confirmed also in plot 6, where one added point at 32 km is reported. The ratio between biased/unbiased errors is very low above tangent altitudes.
From these tests I can conclude that a suitable retrieval grid seems to be the one composed by the tangent altitudes with an added point above the flight altitude. In some cases also adding 2 altitudes is acceptable but it seems that there is no improved information in adding more altitudes above.

Chapter 7: Data Analysis: APE-GAIA Campaign

7.1 APE-GAIA Campaign

This chapter is dedicated to the discussion of the results of the SAFIRE-A data analysis performed using the measurements collected by the instrument during some of the flights of the APE-GAIA Campaign (see chapter 3.3.1). During this campaign, the scientific planning of the flights was based on relevant scientific objectives [33]. Individual flight plans were then finalised on the field using detailed forecasts. These forecasts included standard output from global numerical weather prediction models, as well as high resolution trajectory/contour advection models, lee wave models and global chemistry transport models. Use was also made of near real-time TOMS (Total Ozone Mapping Spectrometer) and GOME (Global Ozone Monitoring Experiment) (Figure 7.1.b) column O_3 data. During the APE-GAIA campaign five flights were performed toward the Antarctic Peninsula, up to the 70th parallel South. The M-55 flight trajectories were chosen to obtain the best observation conditions for the proposed scientific goals of the various flights, and generally remained in the lower stratospheric altitude range (16-20 km). Some scheduled dives were made down to the troposphere in order to evaluate the vortex depth.

7.2 Flight of the 23rd September 1999

7.2.1 Flight Route and Description

The flight performed on the 23rd September 1999 was the second flight of the APE-GAIA campaign. The results obtained from the first flight (performed on the 21st September) showed a small variation with latitude of the atmospheric composition at 14 km and a strong variation at 18 km in correspondence of the vortex edge. For this reason the second flight was planned to explore the vortex at high altitudes.
For the 23rd of September, high resolution forecast Potential Vorticity maps (PV maps, the potential vorticity is a dynamical tracer of atmospheric motion, Figure 7.1.a), calculated with a Reverse Domain Filling Trajectory (RDFT) approach and based on ECMWF data, showed the Antarctic Peninsula to be well inside the Polar vortex (see APPENDIX C).

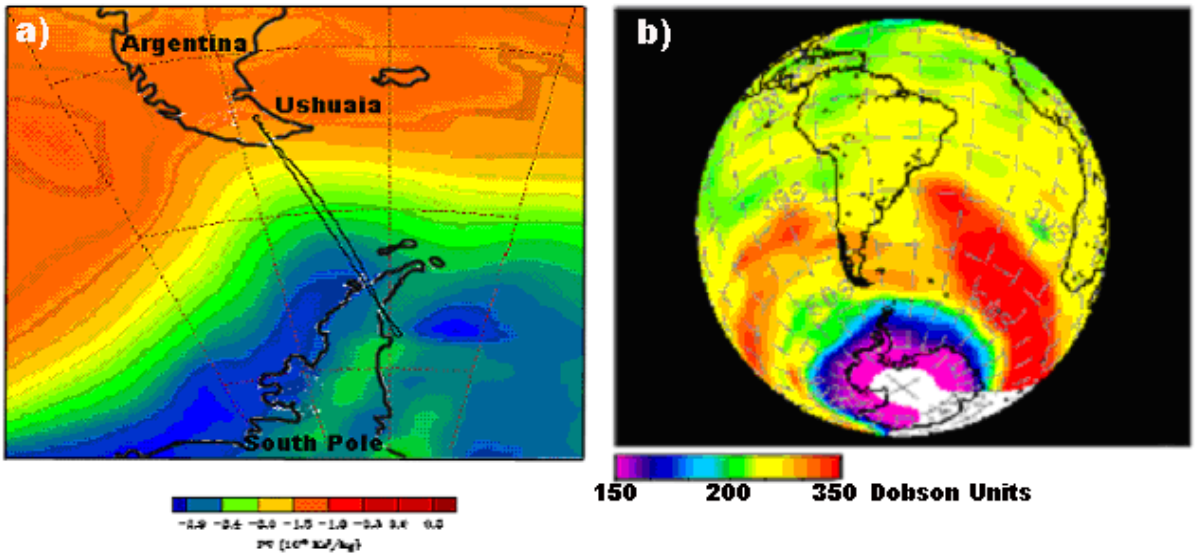

Figure 7.1: a) PV value at 479 K surface together with flight route, b) Total column of O_3 on 23th September 1999 from GOME satellite.

The aircraft took-off at 11 AM local time and the flight lasted 5h and 53 minutes. The flight path followed an almost identical forward and backward trajectory and, with respect to the "turning point" at –68° latitude, the presence of the M-55 inside the vortex was roughly

symmetric (Figure 7.1.a). Potential temperature (θ) is a measure of the entropy and it is calculated from the measured pressure and temperature. In the absence of diabatic processes, parcels tend to move on constant θ surfaces. Because θ increases with altitude, and air movement is stratified somewhat by θ, generally it is used in place of the altitude as the vertical co-ordinate. The aircraft flights were usually performed on surfaces of constant θ (isentropic) and this happened also for this flight [40]. On the forward leg, the aircraft was able to stay on an almost constant isentropic surface with the potential temperature θ equal to 425±3.5 K, while on the backtrack it moved slowly up to the 447±5 K surface, quickly rising to the 479±4 K surface during the final phase of the flight. Shortly before the turning point, the aircraft went into a dive, reaching a θ of 372 K.

The average temperature was about 201 K in the forward leg and about 209 K in the backtrack leg, both of which were well above 196 K, far from favourable levels for PSC formation. Figure 7.2 shows an example of the observations made by the in-situ instruments during the flight of 23rd September 1999 [34]. As shown by the top plot, the altitude was about 17 km in the forward (southbound) leg. While maintaining the southbound direction, a dive was performed down to 14 km. After regaining altitude the reverse (northbound) flight was performed, with two steps at 18 km and at 19 km, in the north direction. Tracers have very similar variations both in the general shape of the curves as well as in some of the small features. The event of a rapid change in concentrations synchronously observed for most species can be considered to identify the crossing of the vortex edge. From Figure 7.2 it is clear that during this particular flight the vortex edge was situated at a latitude of 60°S on the forward leg (17 km altitude), but at 62°S during the return leg (19 km altitude). The different location and gradient of the vortex edge as a function of altitude was also observed during other flights.

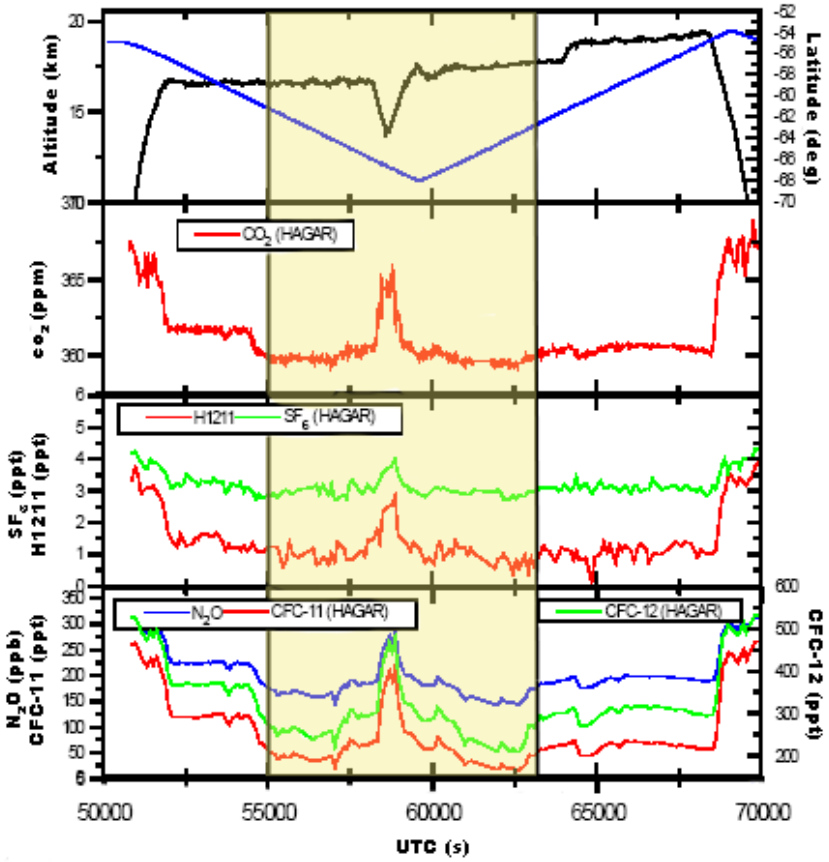

Figure 7.2: Altitude, latitude and in-situ measurements of minor constituents acquired during the flight of 23rd September 1999. (Preliminary data).

7.2.2 SAFIRE-A Measurements

During the flight of the 23rd September 1999, the SAFIRE-A instrument performed 34 limb scanning sequences. In Figure 7.3.a you can find the location of the tangent points of the SAFIRE-A measurements in longitude and latitude for this flight.

The instrument performed 16 limb scanning sequences before the dive. During the dive the instrument did not perform any measurement because of the rapid variation of the flight altitude. After turning back the spectrometer performed 18 limb scanning sequences. In Figure 7.3.b the position of the SAFIRE-A sequences with respect to the flight altitude profile are reported. Since the sequence of pointing angles used during a scan was the same through a whole leg, the first 16th sequences have the maximum tangent altitude at 17 km and the minimum at 10 km. After the dive and the turning point, the M55-Geophysica reached higher altitudes, so that SAFIRE-A limb scanning measurements from 17 to 34 have a maximum tangent altitude of 20 km while the minimum tangent altitude is located at 9 km. During this flight, the selected configuration for the SAFIRE-A measurements was to use the channel at 22-24 cm^{-1} and the channel at 124-126 cm^{-1}. This configuration permits the retrieval of O_3, HNO_3, N_2O, ClO, H_2O and HCl, species that are involved into the ozone hole chemistry (see APPENDIX C). Each limb scanning sequence was composed by two up-looking geometries, one at 80 degrees and one at 89.7 degrees and some down looking geometries. For sequences from 1 to 18 the limb angles for the down looking geometries are 90.3, 90.7, 91, 91.3, 91.6, 91.9, 92.2 and 92.5 degrees, while for sequences from 19 to 34 the limb angles are 90.3, 90.7, 91, 91.3, 91.6, 91.9, 92.2, 92.5 and 92.8 degrees. The overall quality of the recorded spectra was quite good in both the two channels, even if some corrupted spectra were present in sequences 29-30-31 (Table 7.1).

Seq. 29 limb angles	Seq. 29 tangent altitudes	Seq.30 limb angles	Seq.30 tangent altitudes	Seq. 31 limb angles	Seq.31 tangent altitudes
				80	
				89.7	
				90.3	19.08
80				90.7	18.614
89.7		90.3	19.06	91.	18.089
90.3	18.899	91.0	18.10	91.3	17.398
90.7	18.465	92.2	14.12	91.9	15.441
92.5	12.85	92.5	12.07	92.5	12.701

Table 7.1: Available spectra and corresponding tangent altitudes for sequences 29, 30, 31.

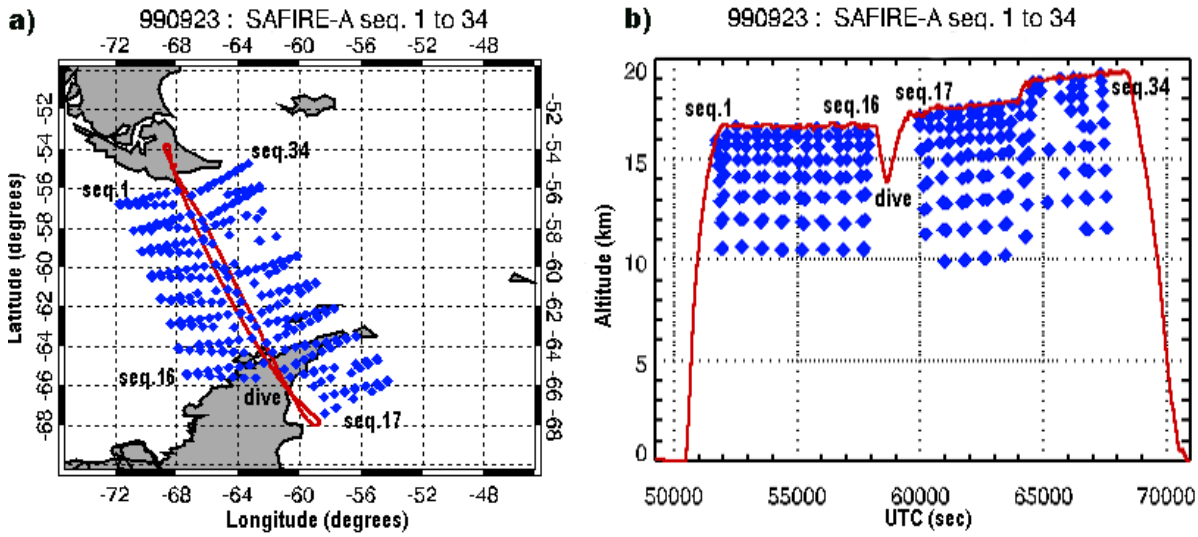

Figure 7.3: a) Location of SAFIRE-A tangent points and sequences in latitude-longitude domain for flight performed on 23rd September 1999, b) Location of SAFIRE-A tangent points and sequences respect to altitude flight profile for 23rd September 1999.

7.2.3 Data Analysis

Due to the good quality of the recorded spectra, it was possible to analyse data in both the two channels. Therefore retrieved profiles for O_3, N_2O, HNO_3, ClO (data analysis for channel one), HCl, H_2O (data analysis for channel 2) could be obtained. The noise in the first channel was about at 0.8 nW/ (cm^2 sr cm^{-1}), while in the second it was 80 nW/ (cm^2 sr cm^{-1}). All the sequences were analysed retrieving at the same time offset, VMR and continuum profile.
Since the implementation of the averaging kernels and of the quality parameters calculation into RAS was performed after the analysis of this data, these tools were not available for choosing the more suitable retrieval grids. A posteriori calculation of the AK is presented for some sequences only as an example and to evaluate the quality of the used grids. In the following subsections is reported a brief description of the pressure and temperature profiles together with the VMR profiles used as starting atmospheric status in the retrieval procedure. Then a description of the microwindows used for the analysis is also given.

7.2.3.1 Pressure, Temperature and VMRs profiles

As seen in Chapter 5, reliable pressure and temperature profiles are needed for the data analysis. Pressure and Temperature profiles were obtained by ECMWF data processed at University of L'Aquila. Temperature and geopotential height values at different pressure levels (from 1 to 1000 mbar) on a latitude-longitude grid (latitude step 1.125°, longitude step 1.125°) are provided every 6 hours (at 00, 06, 12 and 18 for each day). ECMWF values for temperature and geopotential height were linearly interpolated in latitude and in time, in order to make use of the most suitable temperature and pressure values, on a given altitude grid, for each sequence (average time, latitude and longitude for each sequence were used). VMR profiles coming from a standard polar atmospheric model were used either as initial guess of the retrieval and to model the interfering gases (same profiles for the whole flight).

7.2.3.2 Microwindows selection

As in Chapter 5, the measured spectra are analysed only in narrow spectral intervals called MicroWindows (MWs).
In Table 7.2, 7.3, 7.4, 7.5, 7.6 and 7.7 I report the frequency ranges of the used microwindows together with the number of spectral points present in every MW in case of O_3, HNO_3, N_2O, ClO, HCl, H_2O retrievals for this flight while figures from 7.4 to 7.7 show examples of the spectra recorded in the selected MWs.

MW name	MW (cm^{-1})	Number of points
O3_mw01	22.29 – 22.5	70
O3_mw02	22.52 – 22.57	17
O3_mw03	22.77 – 22.88	37
O3_mw04	23.00 – 23.25	83
O3_mw05	23.27 – 23.35	27

Table 7.2: MWs used for ozone retrieval.

MW name	MW (cm^{-1})	Number of points
HNO3_mw01	22.656 – 22.775	40

Table 7.3: MW used for HNO_3 retrieval.

MW name	MW (cm^{-1})	Number of points
N2O_mw01	22.56 – 22.66	34

Table 7.4: MWs used for N_2O retrieval.

MW name	MW (cm^{-1})	Number of points
ClO_mw01	22.86 – 22.92	21

Table 7.5: MWs used for ClO retrieval.

MW name	MW (cm^{-1})	Number of points
HCl_mw01	124.56 – 124.96	132

Table 7.6: MWs used for HCl retrieval.

MW name	MW (cm^{-1})	Number of points
H2O_mw01	124.00 - 124.31	103
H2O_mw02	125.61 – 125.91	99

Table 7.7: MWs used for H_2O retrieval.

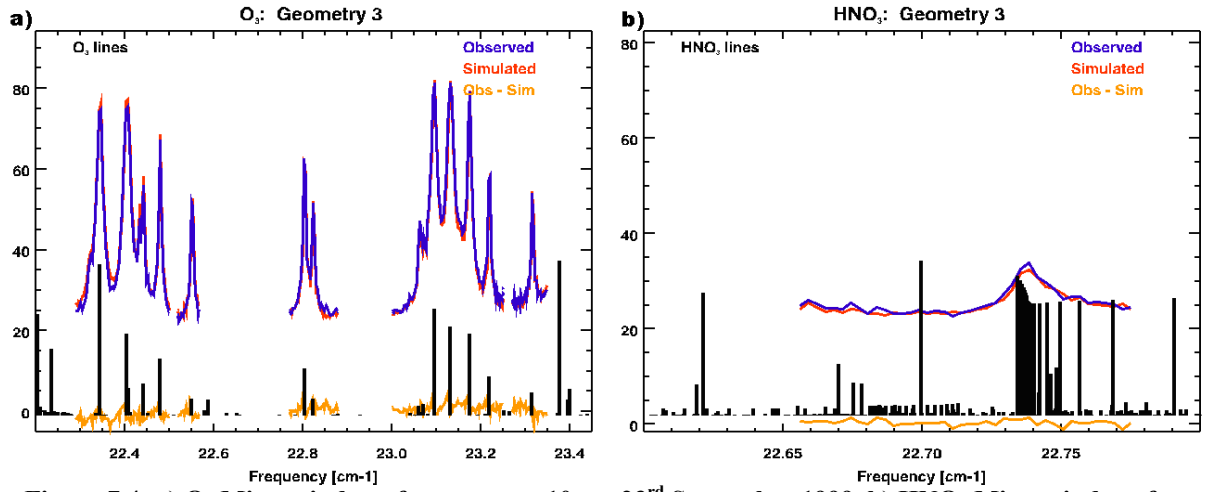

Figure 7.4: a) O_3 Microwindows for sequence 10 on 23rd September 1999, b) HNO_3 Microwindow for sequence 10 on 23rd September 1999.

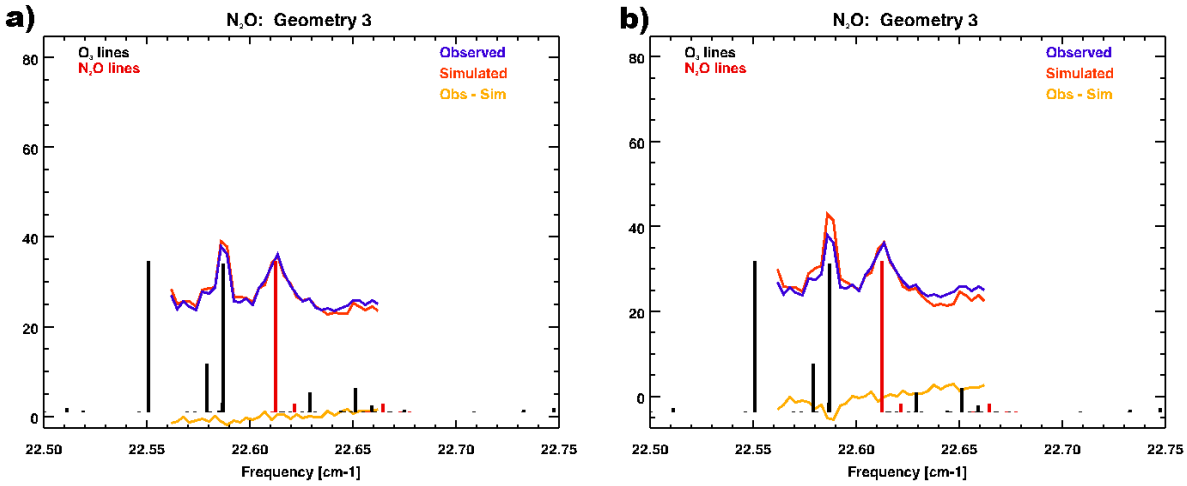

Figure 7.5:a) N_2O Microwindow for sequence 10 on 23rd September 1999 with retrieved ozone profile, b) N_2O Microwindow for sequence 10 on 23rd September 1999 with climatological ozone.

7.2.4 Retrieval results and Comparisons with other instruments onboard the Geophysica

In this section the results of the analysis of the spectra recorded during the flight of 23rd September 1999 are reported. For each target species the results of the retrieval are discussed along with the used retrieval grid. Moreover, the comparison of the VMR profiles measured by in-situ instruments during take off, dive or landing phases and the corresponding SAFIRE-A retrieved profiles provides an internal validation for the retrieval system.

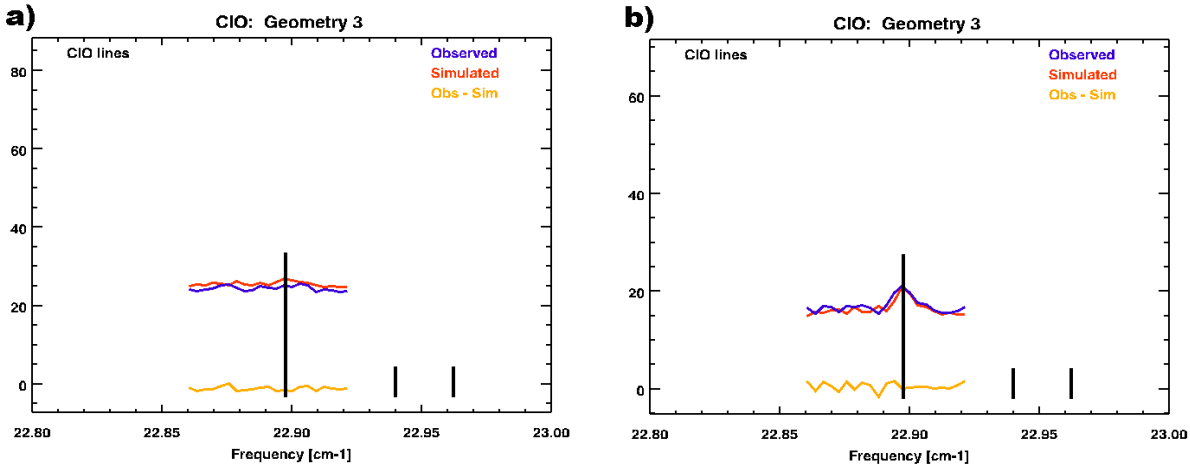

Figure 7.6: a) ClO Microwindow for sequence 10 on 23rd September 1999, and b) for sequence 18 on 23rd September 1999.

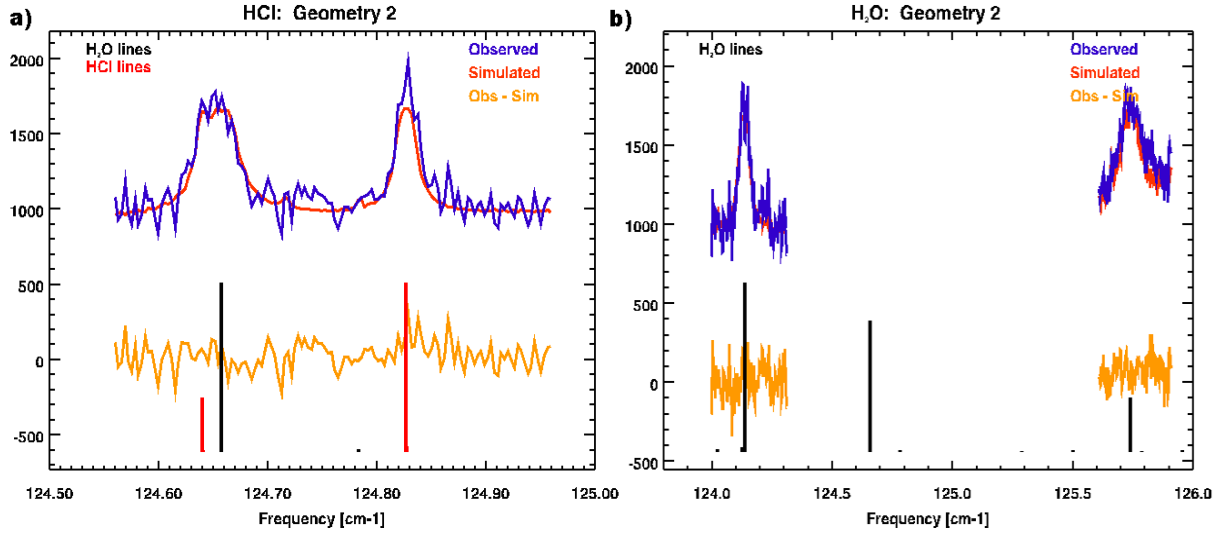

Figure 7.7: a) HCl Microwindows for sequence 10 on 23rd September 1999, b) H_2O Microwindows for sequence 10 on 23rd September 1999.

7.2.4.1 Ozone

In the case of the ozone retrieval the information is contained in 5 MWs, whose spectra are reported as an example in Figure 7.4. For sequence number 10, limb scanning angle at 90.3 deg. the figure shows the position of the O_3 lines, the observed spectra the simulated one, in nW/ (cm^2 sr cm^-1), together with their difference.

The vertical grid used to perform a retrieval is a species dependent choice. In the case of the ozone retrieval the chosen retrieval grid is the one composed by all the tangent altitudes plus one point at altitudes above the flight altitude (see also chapter 6.3.9.2).

For the initial sequences where the aircraft altitude was low (sequences from 1 to 3) one point at 20 km is the only added point, then two points were added, one at 20 and one at 24 km while for the last 7 sequences where the M55 reaches an altitude of about 20 km, only one point at 22 km was added.

As an example, in Figure 7.8.a and Figure 7.8.b the retrieval results for sequences number 7 and 32 are reported together with the averaging kernel and the quality parameters information. In both cases the retrieval grid seems to be correct. At higher tangent altitudes the information comes entirely from the measurements while at the lower altitudes the retrieved values are

partially influenced by the initial guess profile because of the used regularization (also because of the fact that ozone VMR at 10 km is very low). The retrieval grids reported above were applied at the whole flight and the result of the analysis is reported in Figure 7.19.a. The values of the retrieved VMR at tangent altitudes are plotted (retrieved value above flight altitude not included) in a 3D graph according to their latitude-longitude-altitude position, together with the flight path (red line). In Figure 7.19.b you can find the retrieved VMR values plotted versus the time-altitude co-ordinate. The VMRs value are represented using a colour scale (from red for high VMR to purple for the lower one).

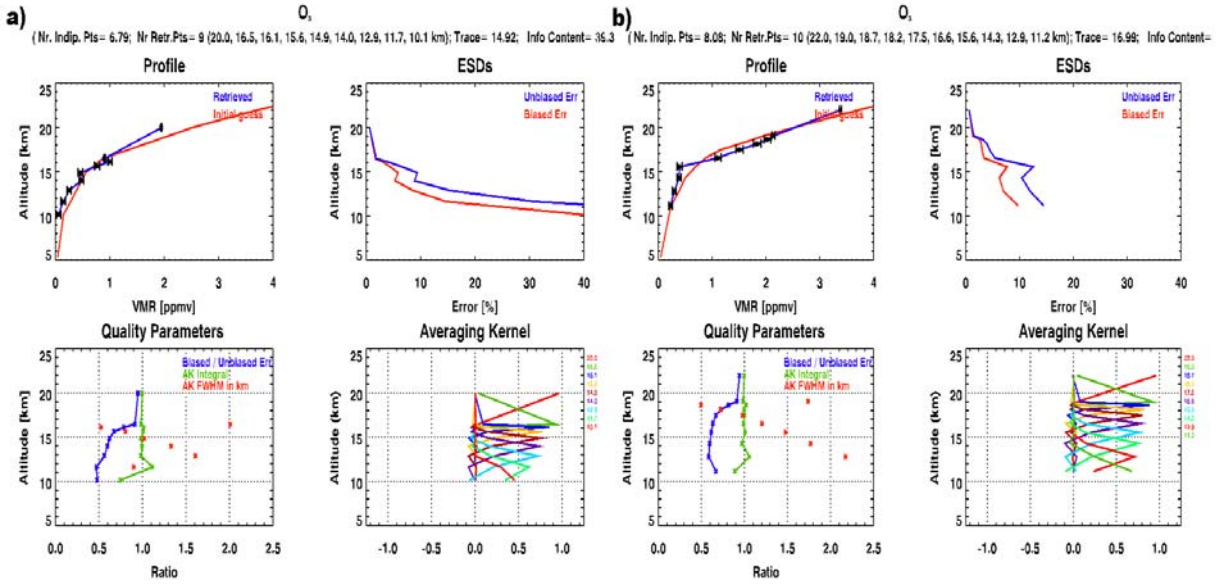

Figure 7.8: a) Ozone retrieval for sequence 7 on 23rd September 1999, b) Ozone retrieval for sequence 32 on 23rd September 1999.

In order to prove the quality of the results for ozone, a comparison with the ozone concentration obtained by in situ instruments on board the Geophysica was performed. As reported in Table 3.2, during the campaign two in-situ instrument for ozone measurement were present onboard the Geophysica. Since in-situ measurements provide data at the location of the airplane only, while SAFIRE-A tangent altitudes were geolocated as in Figure 7.3.a, in-situ data were compared with the data obtained interpolating the SAFIRE-A ozone retrieved profiles at flight altitude. The result of the comparison of SAFIRE-A data with ECOC results is shown in Figure 7.9. As can be seen in the figure, the overall agreement between the two data sets is very good. Both the value of the ozone VMR and the ozone trend along the flight path are in good agreement.

In Figure 7.10.a the comparison with an other in situ instrument, FOZAN, and the remote sensing instrument GASCOD are reported. Also in this case a general good agreement among the different instruments is found, and the ozone trend along the flight path is confirmed. Finally Figure 7.10.b shows the comparison between data recorded by ECOC instrument during the dive and SAFIRE-A data for sequences 16, that is the closest to the dive (Figure 7.3.a and Figure 7.3.b) is reported. The comparison gives very good results for the higher tangent altitudes, where the two data sets are spatially and temporally coincident, while at the lower altitudes the results are a little bit worse, even if the overall trend seems to be the same for the two profiles.

From these comparisons, I can conclude that, in case of the ozone retrieval, the SAFIRE-A retrieved profiles are in good agreement with others measurements and thus, they can be considered a good estimate of the state of the examined atmospheric scenario.

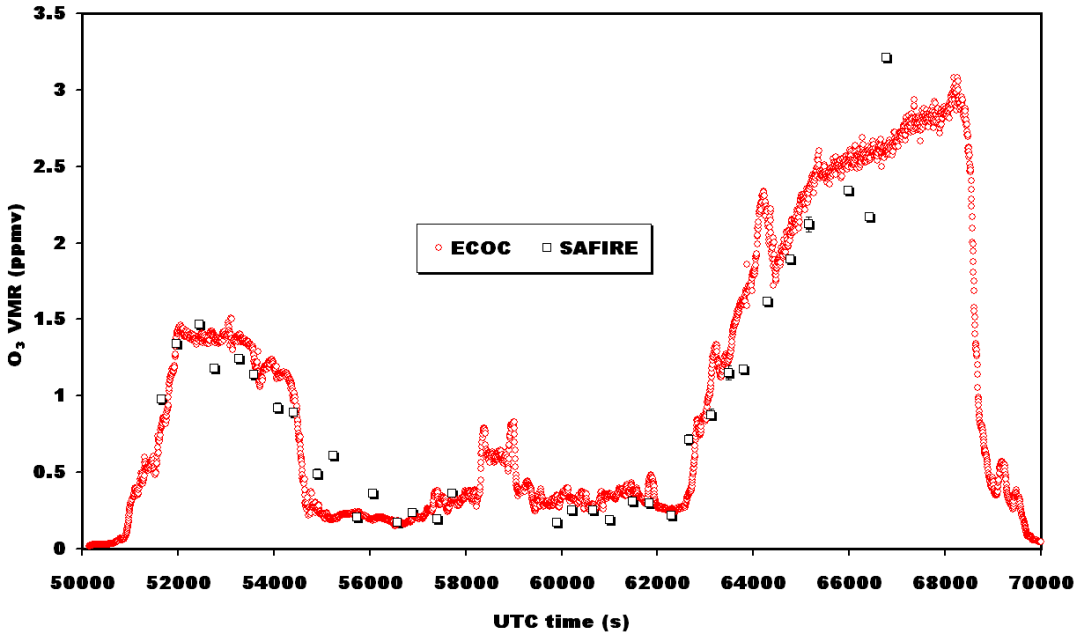

Figure 7.9: Comparison between ozone values at flight altitude along the flight track recorded by ECOC and retrieved by SAFIRE-A on 23rd September 1999.

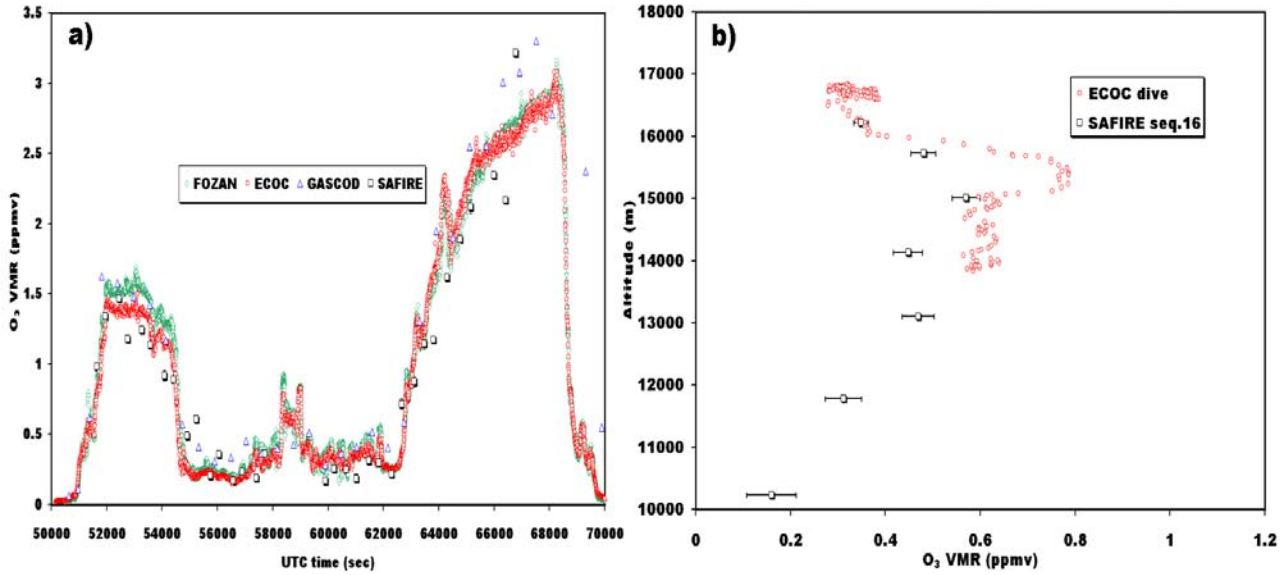

Figure 7.10: a) Ozone values at flight altitude along the flight track recorded by ECOC, FOZAN and retrieved by SAFIRE-A and GASCOD on 23rd September 1999, b) Comparison of ozone values during dive recorded by ECOC and ozone values retrieved by SAFIRE-A for sequence 16 on 23rd September 1999.

7.2.4.2 N_2O

In Figure 7.5.b the spectrum in the microwindow used for the data analysis of N_2O is reported. The N_2O line is centred at 22.61 cm^{-1} and it is indicated by the red line.
In the figure it is also shown (in black) the position of minor O_3 lines. Because of the fact that an O_3 line is present into the microwindow, a good knowledge of this gas during N_2O retrieval is needed. So in the retrieval the ozone retrieved profile for the same sequence was used, instead of the climatological one. As you can see in Figure 7.5.a this approach produces good results in the spectra simulation (in Figure 7.5.b the same spectrum is simulated with the climatological ozone).
The retrieval grid used for N_2O data analysis is the one composed by all the tangent altitudes plus one point above flight altitude (at 20 km).

In Figure 7.11.a the retrieval result for sequence 32 are reported. Looking at the retrieval quantifiers we can conclude that for this sequence it was possibly better to use a coarser retrieval grid in order to reduce the errors (we have 5.66 independent pieces of information against 9 retrieved altitudes), but as already said the averaging kernel and quality parameters calculation were not available at the time of this data analysis. In Figure 7.11.b the retrieval results for sequence number 30 are reported. Although for this sequence only 3 observed spectra were good enough for the data analysis, the retrieval quality is still good (3.13 independent pieces of information against 4 points into the retrieval grid). The N_2O analysis was performed, using the chosen retrieval grid, for all the sequences recorded by SAFIRE-A during this flight, the results are reported in Figure 7.23.a and Figure 7.23.b.
The quality of N_2O retrieval for this flight was assessed using the value of N_2O obtained by the in situ instrument HAGAR. In Figure 7.12.a I report the comparison of N_2O values obtained by SAFIRE-A at flight altitude with the HAGAR ones. As you can notice, the overall trend is the same. SAFIRE-A N_2O mixing ratios at flight altitudes are quite similar to HAGAR value in the first part of the flight (sequences from 1 to 16), while they are a little bit smaller into the second part. A further comparison, between N_2O profile obtained by HAGAR during the descent and SAFIRE-A profile for the last sequence (number 34) is shown in Figure 7.12.b. In this case the profile retrieved by SAFIRE-A seems to be in good agreement with the in situ measurements at all altitudes.

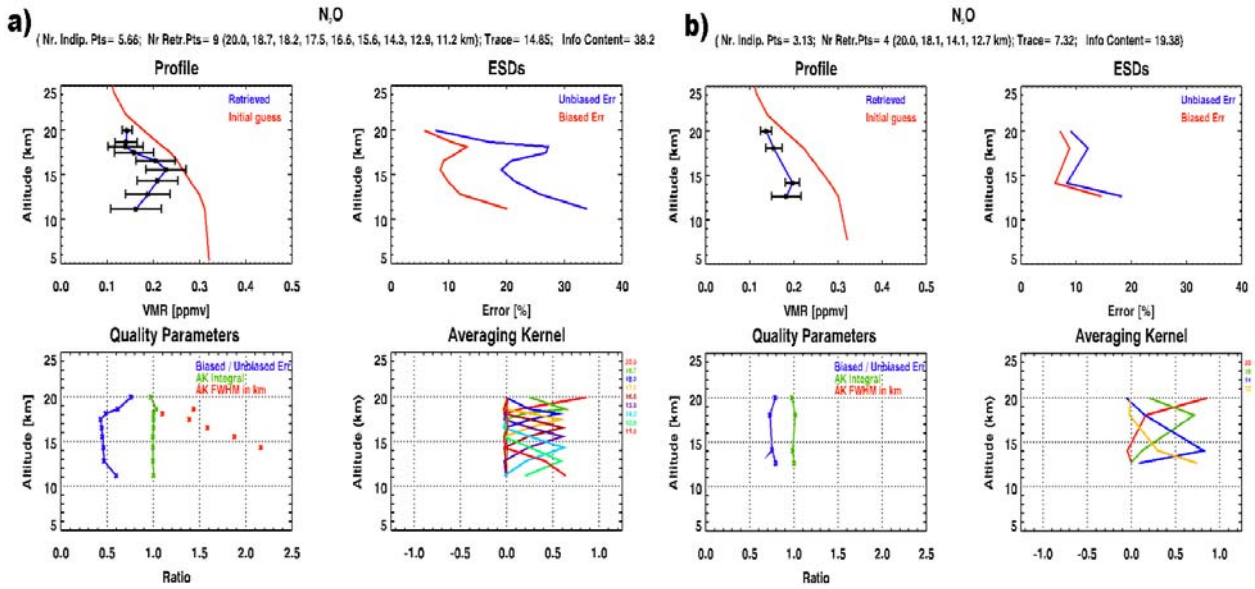

Figure 7.11: a) N_2O retrieval for sequence 30 on 23rd September 1999, b) N_2O retrieval for sequence 32 on 23rd September 1999.

In conclusion, in case of the N_2O retrieval, the results are in quite a good agreement with in situ measurements, even if some deviations can be found at flight level. In general the SAFIRE-A retrieved values can be considered to be reliable, with VMR values that decrease entering the vortex, as identified by the in situ measurements shown in Figure 7.2.

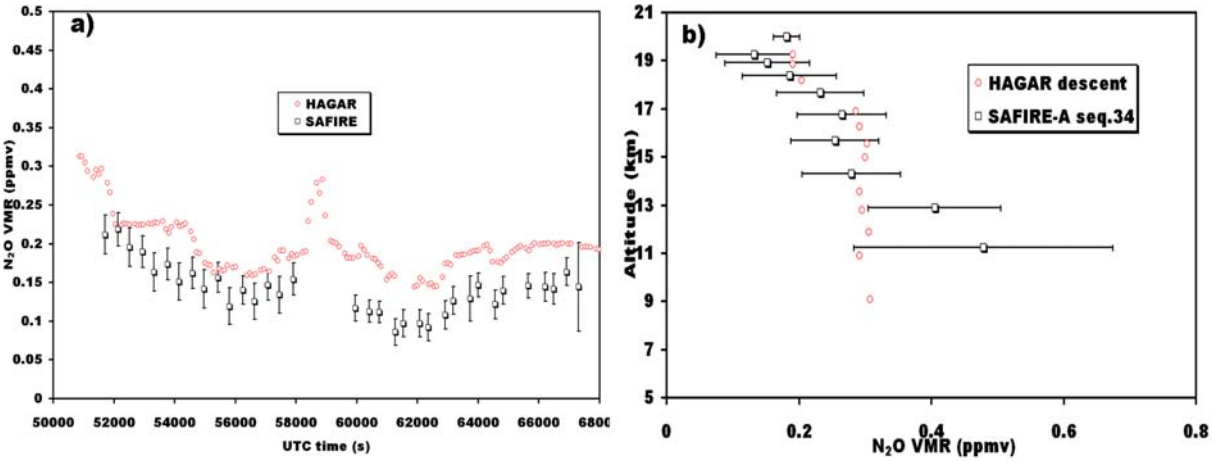

Figure 7.12: a) N_2O values at flight altitude along the flight track recorded by HAGAR and retrieved by SAFIRE-A on 23rd September 1999, b) Comparison of N_2O values during dive recorded by HAGAR and values retrieved by SAFIRE-A for sequence 34 on 23rd September 1999.

7.2.4.3 HNO_3

For HNO_3 retrieval, the information comes from a group of lines at 22.74 cm^{-1} contained in a single MW reported in Figure 7.4.b.

In case of the HNO_3 retrieval the used retrieval grid for the data analysis was the one composed by a part of the tangent altitudes (alternate geometries) and one added point above flight altitude at 20 km. The averaging kernel for sequence 32 are shown in Figure 7.13.a. They are quite broad supporting the choice of the use of a retrieval grid coarser than for the other molecules. Also in this case the retrieval seems to be quite good: the number of independent points is 3.73 and the retrieval grid is composed by 6 altitudes. The HNO_3 retrieval seems to be good at higher altitudes (where the integral of the averaging kernels is near 1) an a little bit worse at lower altitudes (where the integral is about 0.5, and where the value of HNO_3 VMR is very small).

In Figure 7.13.b the retrieval results for sequence number 17 are reported. Also in case of HNO_3 retrieval, the retrieval quality seems to be quite good, even if for this sequence only the spectra relative at 3 tangent altitudes were good enough for the data analysis.

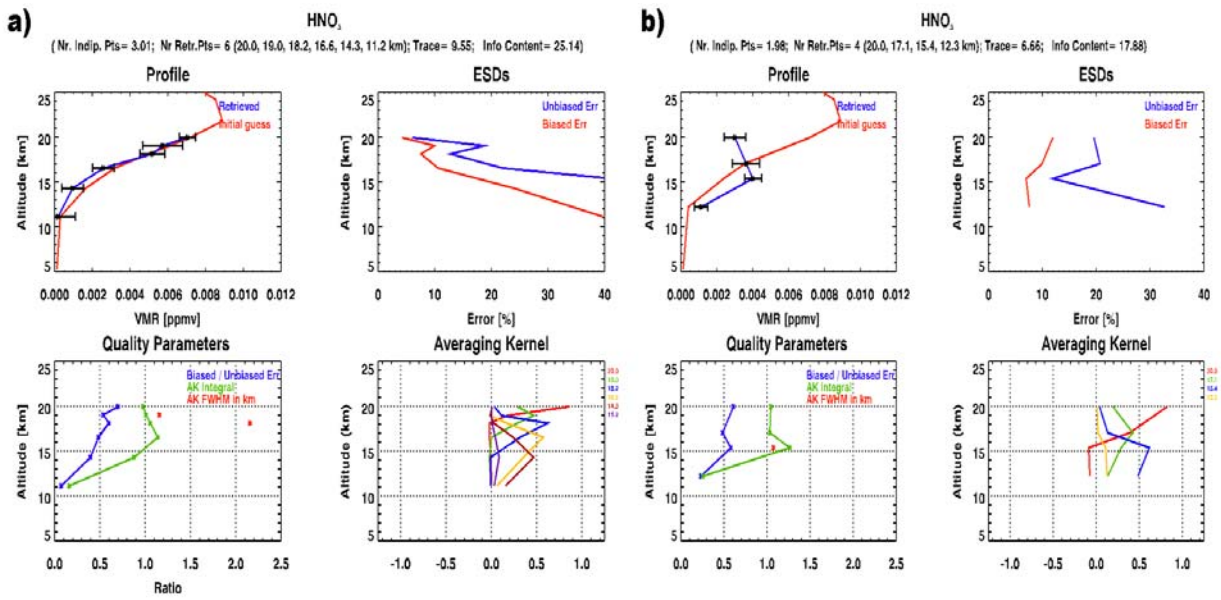

Figure 7.13: a) HNO_3 retrieval for sequence 17 on 23rd September 1999, b) HNO_3 retrieval for sequence 32 on 23rd September 1999.

The described retrieval grid was used for all the flight and an overview of HNO_3 retrieved profiles for SAFIRE-A is given in Figure 7.21.a, where the values of retrieved VMR at all tangent altitudes are plotted (retrieved value above flight altitude not included) in a 3D graph according to their latitude-longitude-altitude position, together with the flight path (red line). In Figure 7.21.b you can find the retrieved VMR values plotted versus the time-altitude co-ordinate.
The validation of HNO_3 profiles could not be performed using an in situ instrument because on board the Geophysica no in situ instruments measure HNO_3. However, this gas is retrieved from the remote-sensing measurements performed by MIPAS-STR (Chapter 3).The measurements performed by this instrument are highly comparable with SAFIRE-A data because both instruments explore the same air masses (both of them have the input optic on the right side of the aircraft) during the flight. In Figure 7.14.a I report the comparison of HNO_3 values obtained by SAFIRE-A at flight altitude with the MIPAS-STR ones.
The two sets of measurements are in good agreement with the difference between the retrieved VMR mostly inside the error bars. In Figure 7.14.b you can also find a comparison of the HNO_3 profile obtained by MIPAS for sequence number 17 and SAFIRE-A sequence 16 (these sequences are spatially and temporally comparable), the two profiles seems to have the same shape and to be in good agreement. Therefore, the result of this comparison seems to proves that the SAFIRE-A HNO_3 retrieved profiles are a reliable estimate of the state of the atmosphere for this flight.

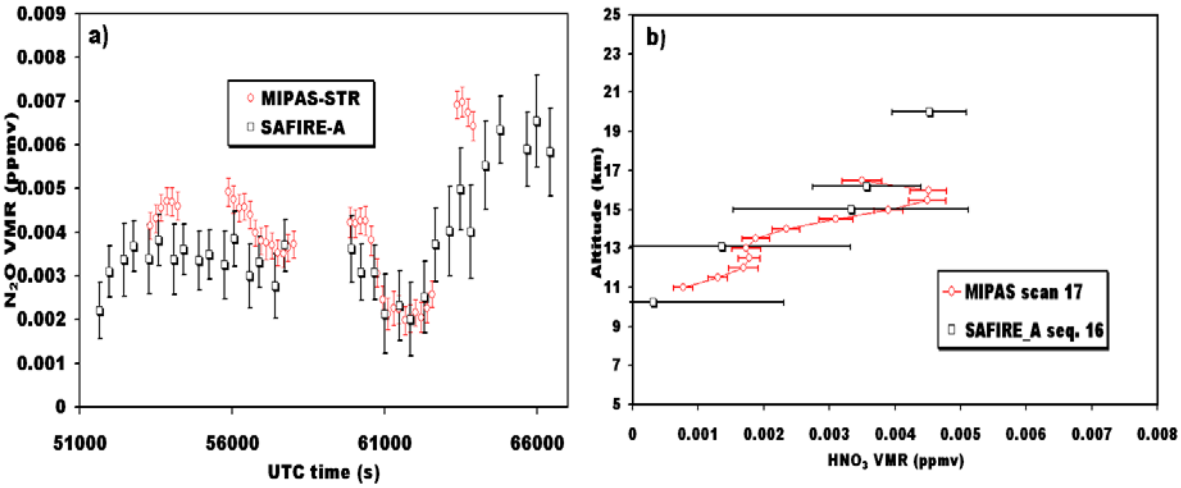

Figure 7.14: a) HNO_3 values at flight altitude along the flight track retrieved by SAFIRE-A and MIPAS-STR on 23rd September 1999, b) Comparison of HNO_3 values retrieved by MIPAS-STR scan 17 and values retrieved by SAFIRE-A for sequence 16 on 23rd September 1999.

7.2.4.4 H_2O

Both the retrieval of H_2O and HCl are performed on the channel centred at 125 cm^{-1}. In Figure 7.7.b the microwindow used for the data analysis in case of H_2O retrieval (sequence number 10 second geometry) is reported. The information in case of H_2O retrieval is contained into two lines, one centred at about 124.1 cm^{-1} and the other at 125.7 cm^{-1}.
In SAFIRE-A channel 2, where the water vapour content is retrieved, the spectra below 14 km are saturated by the water vapour emission and could not be included into the analysis (this is valid also for HCl retrieval).

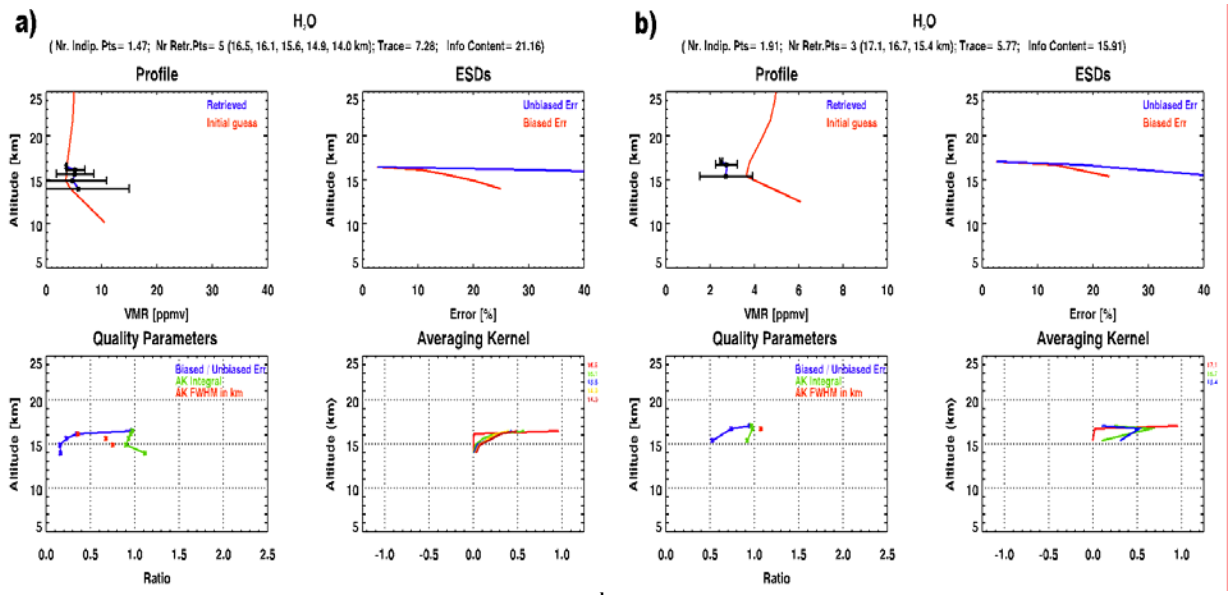

Figure 7.15: a) H_2O retrieval for sequence 7 on 23rd September 1999, b) H_2O retrieval for sequence 17 on 23rd September 1999.

For this reason H_2O profiles are retrieved from flight altitude to about 14 km at all the tangent altitudes (no added points above flight altitude). In Figure 7.15.a and Figure 7.15.b the retrieval results for sequences number 7 and 17 are reported, together with their averaging kernel and the quality parameters information. In both cases the retrieval seems to be sensitive to the measurements at high altitudes while it has some problems at lower altitudes because of poor sensitivity of the spectra to H_2O VMR due to the spectra saturation caused by the very high water vapour content. An overview of H_2O retrieved profiles, using the selected vertical grid, for SAFIRE-A during the whole flight is given in Figure 7.22.a and Figure 7.22.b.
In order to check the quality of the analysis for H_2O profiles, I compared them with the concentrations obtained by in situ instruments on board the Geophysica. During APE-GAIA Campaign, the water vapour content was measured by the in situ instrument FLASH (Chapter 3).

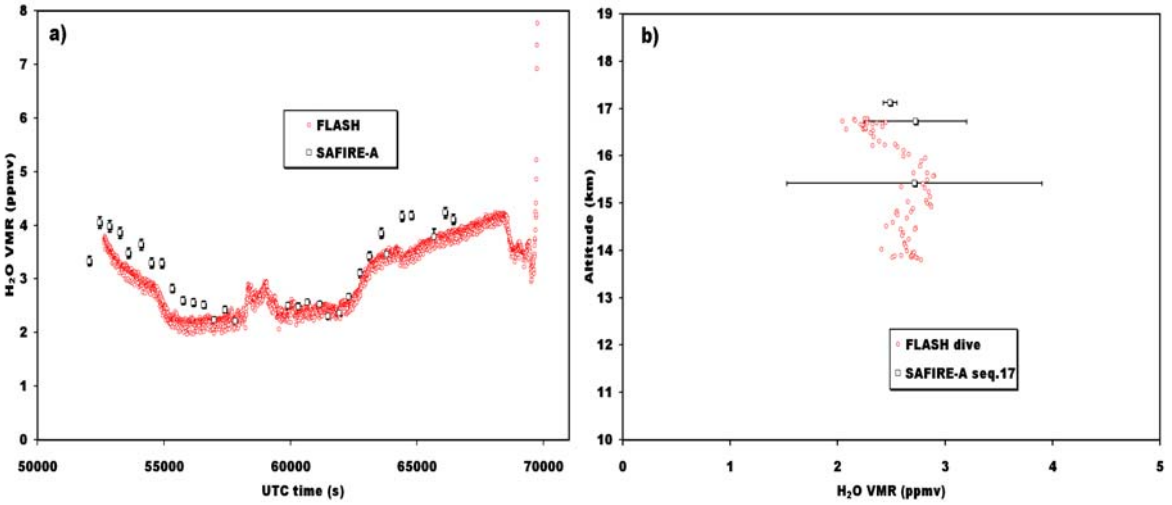

Figure 7.16: a) H_2O values at flight altitude along the flight track recorded by FLASH and retrieved by SAFIRE-A on 23rd September 1999, b) Comparison of H_2O values during dive recorded by FLASH and values retrieved by SAFIRE-A for sequence 17 on 23rd September 1999.

In Figure 7.16.a the comparison of H_2O SAFIRE-A retrieved values at flight altitudes along the flight track with the data obtained by FLASH during the flight is reported. In Figure 7.16.b, a comparison of H_2O profile obtained by FLASH during the dive and SAFIRE-A

sequence 17 is shown. In both cases the overall agreement is quite good, even if SAFIRE-A water vapour profiles are composed only of three points with large error bars at lower altitudes. Therefore, for water vapour retrieval the profiles obtained by SAFIRE-A seems to be a good estimate of the atmospheric water vapour from 18.5 to 15 km for this flight.

7.2.4.5 ClO

The microwindow used in ClO retrieval is shown in Figure 7.6.a and Figure 7.6.b. The ClO line is located at about 22.90 cm^{-1}. In figure 6.6.a is reported the spectra for sequence 10 while in figure 6.6.b the spectra for sequence 18 is shown. As shown in the figure, the ClO line is not visible in the sequence number 10 while it is in sequence number 18. This is due to both the diurnal variability of ClO concentration and to the position of the aircraft respect to the vortex: sequence 10 is located onto the vortex edge (low ClO concentration), while sequence 18 (see Figure 7.1 and Figure 7.3) is located deep into the polar vortex (higher ClO concentration).

Moreover, the information about ClO is very small at low altitudes an a little bit higher at flight altitude and above. For this reason a vertical retrieval grid composed by only 3 points (20, 16, 12 km) was used for all sequences. In Figure 7.17.a and Figure 7.17.b the retrieval results for sequences number 10 and 18 (spectra for the two sequences as in Figure 7.6) are reported, together with averaging kernel and quality parameters information. In both cases the value of the trace is 0.99 and all the information comes from the altitudes above 20 km, because of the ClO profile structure.

The retrieved profile for sequence 32 shows a big increase in the ClO value at 20 km in accordance with the spectral feature in Figure 7.6. An overview of the ClO retrieved profiles interpolated at tangent altitudes, for SAFIRE-A for the whole flight is given in Figure 7.20.a (retrieved value above flight altitude not included) together with the flight path. In Figure 7.20.b the retrieved VMR values plotted versus the time-altitude co-ordinate are reported.

The validation of ClO profiles, obtained from the analysis using data from other instruments onboard the aircraft was not possible because SAFIRE-A was the only instrument measuring ClO during the APE-GAIA campaign.

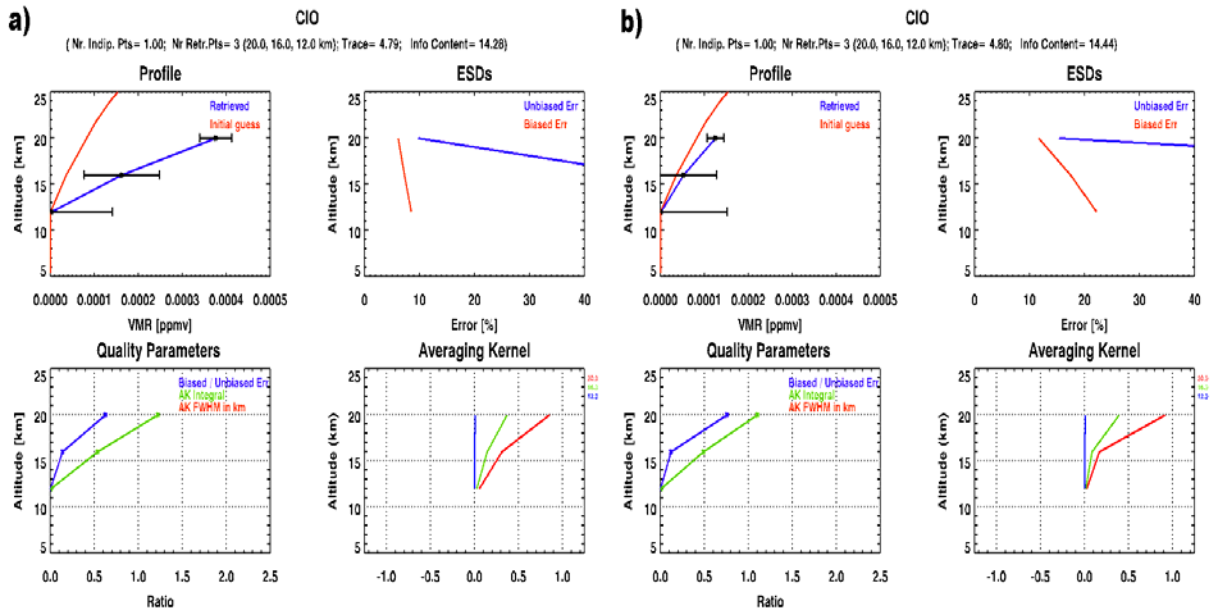

Figure 7.17: a) ClO retrieval for sequence 18 on 23rd September 1999, b) ClO retrieval for sequence 32 on 23rd September 1999.

7.2.4.6 HCl

In Figure 7.7.a the microwindow used for the data analysis in case of HCl retrieval (sequence number 10 second geometry) is reported. In the figure it also shown the position of the HCl and H_2O lines.

As for H_2O, HCl profile were retrieved from flight altitude to about 14 km at all the tangent altitudes and one added points above flight altitude at 20 km.

Results obtained in case of retrievals for sequences 7 and 17 are reported In Figure 7.18.a and Figure 7.18.b. In both cases the retrieval seems to work quite well at high altitudes while it has some problems at lower altitudes, due to the shape of the HCl profile. The results of HCl retrieved profiles for SAFIRE-A during the flight are reported in Figure 7.24.a, Figure 7.24.b and Figure 7.24.c.

As for ClO, the validation of SAFIRE-A profiles was not possible, because no other instrument measured this specie during the flight.

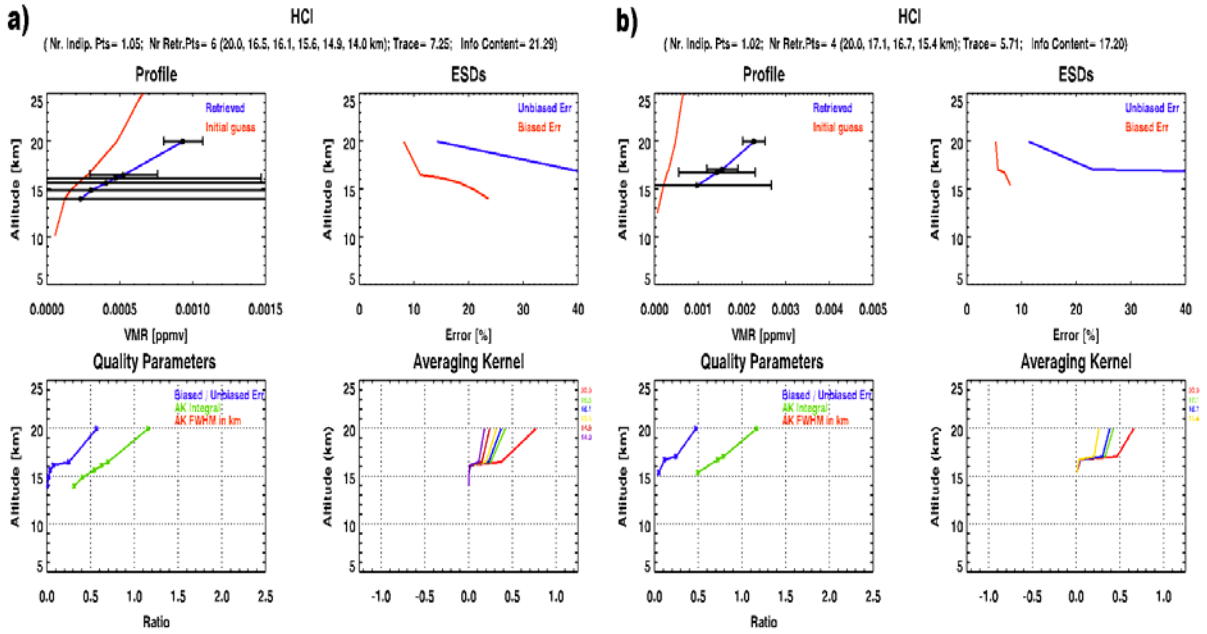

Figure 7.18: a) HCl retrieval for sequence 18 on 23rd September 1999, b) HCl retrieval for sequence 17 on 23rd September 1999.

7.2.5 the Ozone Hole

During the flight SAFIRE-A acquired 34 limb scanning sequences from the tropopause up to flight altitude. The information extracted from individual scans can be combined to reconstruct 2-D distributions of the observed species as a function of altitude along the flight route. The resulting curtain plots are displayed in Figure 7.25. In the figures it is also shown the altitude of the aircraft for each sequence and the position of the vortex edge during the flight (inferred from Figure 7.2) [35],[36].

Looking at ozone values retrieved by SAFIRE-A at flight altitude in Figure 7.9 one can notice that the instruments retrieve small ozone values in correspondence of the polar vortex position (see Figure 7.2 for vortex location along flight track) both during the first and the second part of the flight. During the first leg, the M55 entered the vortex region at -60 degree latitude (corresponding to about 55000 UTC) in correspondence of SAFIRE-A sequence number 9. After the dive and the turning point, the aircraft left the polar vortex at -62 degree latitude (about 63000 UTC) in correspondence of sequence 24. For sequences from 9 to 24 the SAFIRE-A measurements for ozone at flight altitude remained very low (less than 0.5 ppmv), evidencing the latitudinal coverage of the ozone hole phenomenon present on this day.

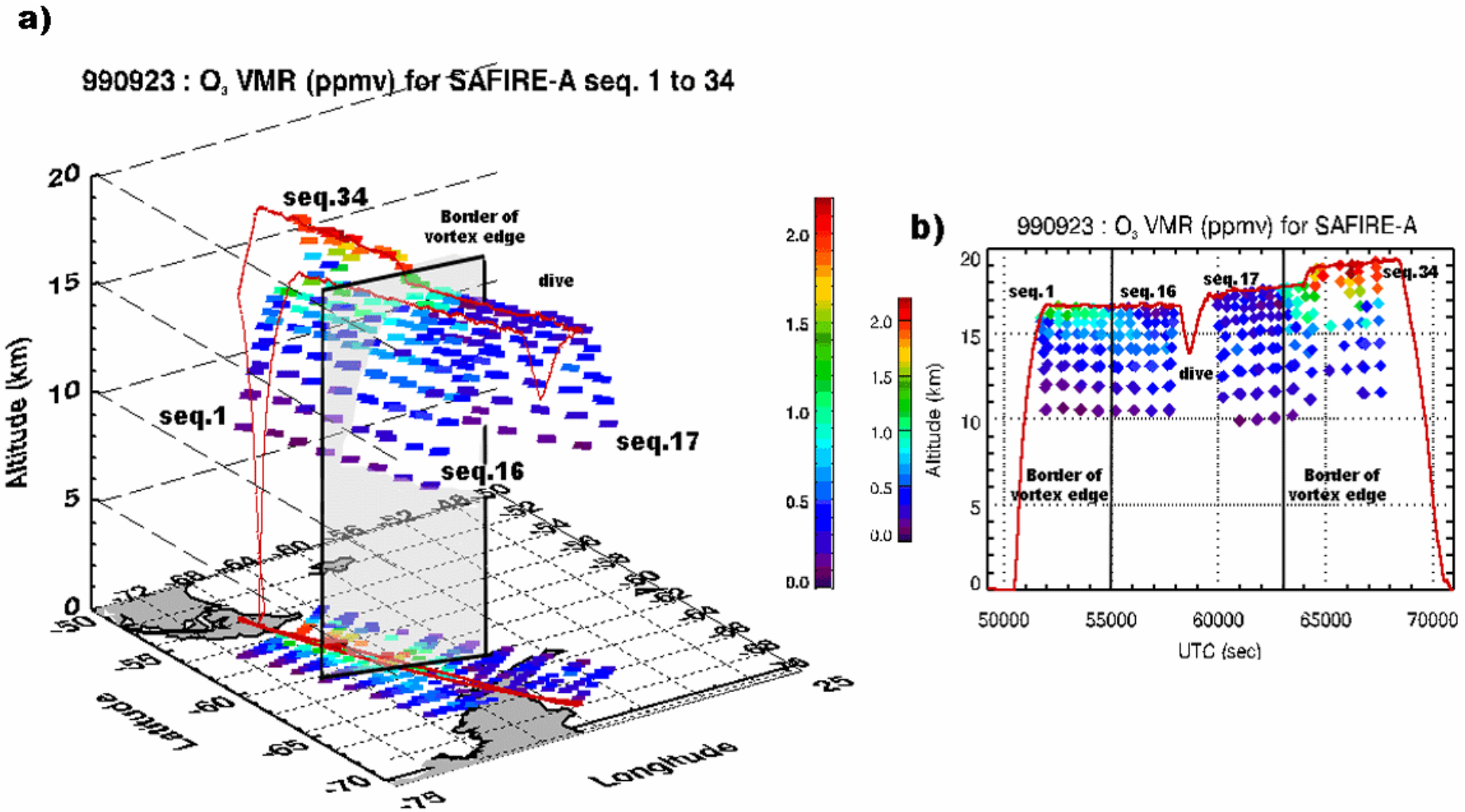

Figure 7.19: a) Ozone values at tangent altitudes recorded by SAFIRE-A on 23rd September 1999 respect to altitude, latitude, longitude, b) Ozone values at tangent altitudes retrieved by SAFIRE-A on 23rd September 1999 respect to altitude and time.

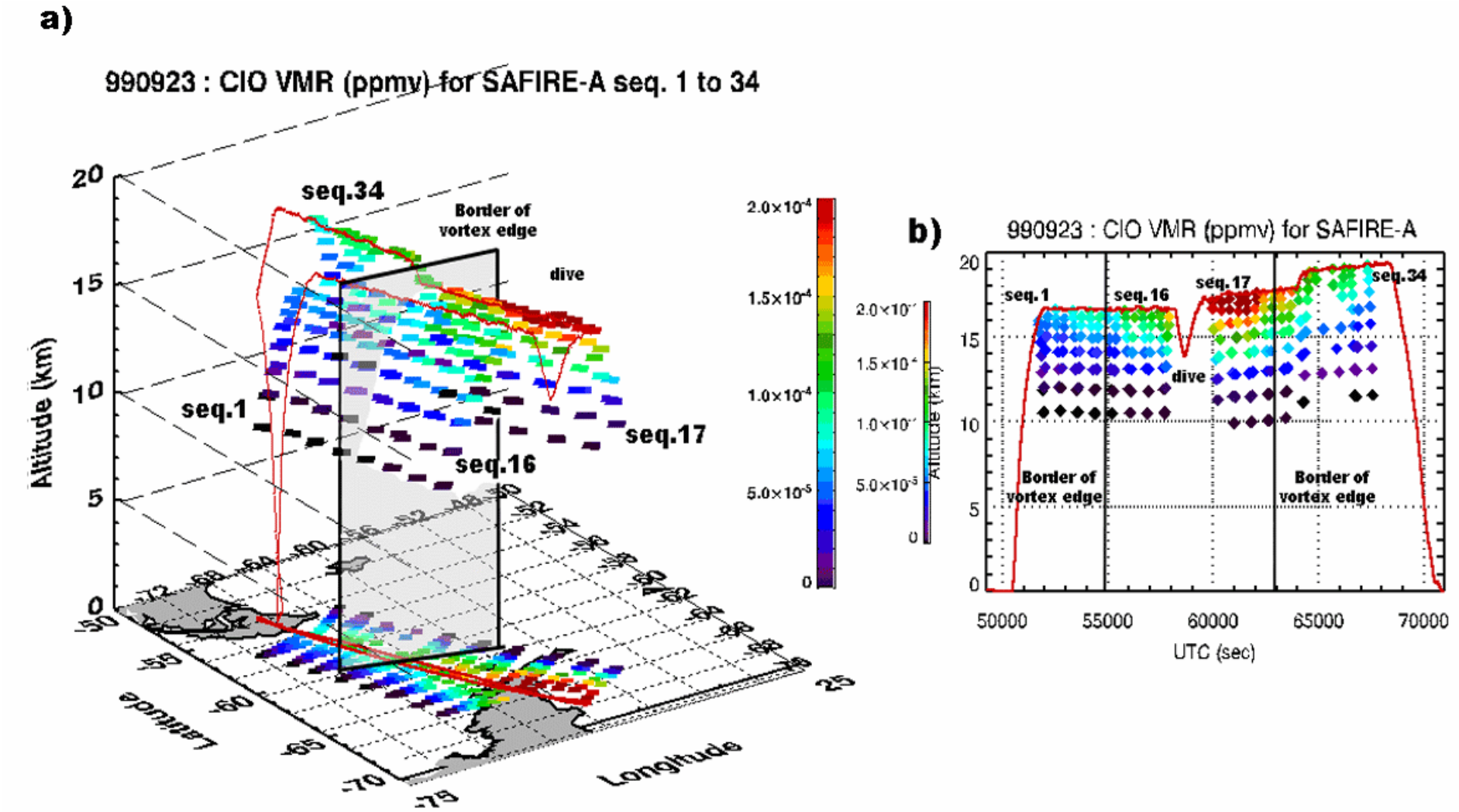

Figure 7.20: a) ClO values at tangent altitudes recorded by SAFIRE-A on 23rd September 1999 respect to altitude, latitude, longitude, b) ClO values at tangent altitudes retrieved by SAFIRE-A on 23rd September 1999 respect to altitude and time.

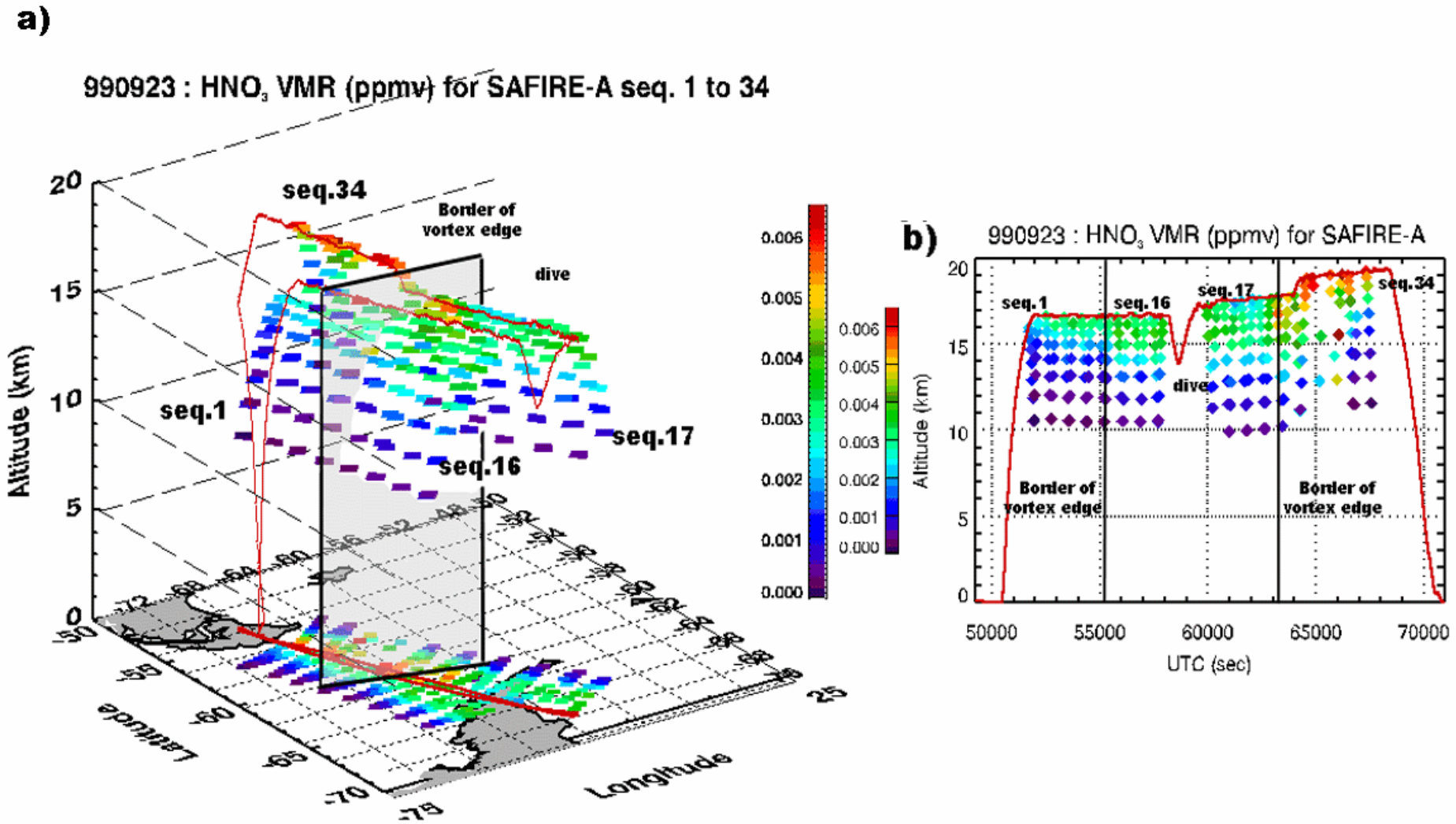

Figure 7.21: a) HNO_3 values at tangent altitudes recorded by SAFIRE-A on 23rd September 1999 respect to altitude, latitude, longitude, b) HNO_3 values at tangent altitudes retrieved by SAFIRE-A on 23rd September 1999 respect to altitude and time.

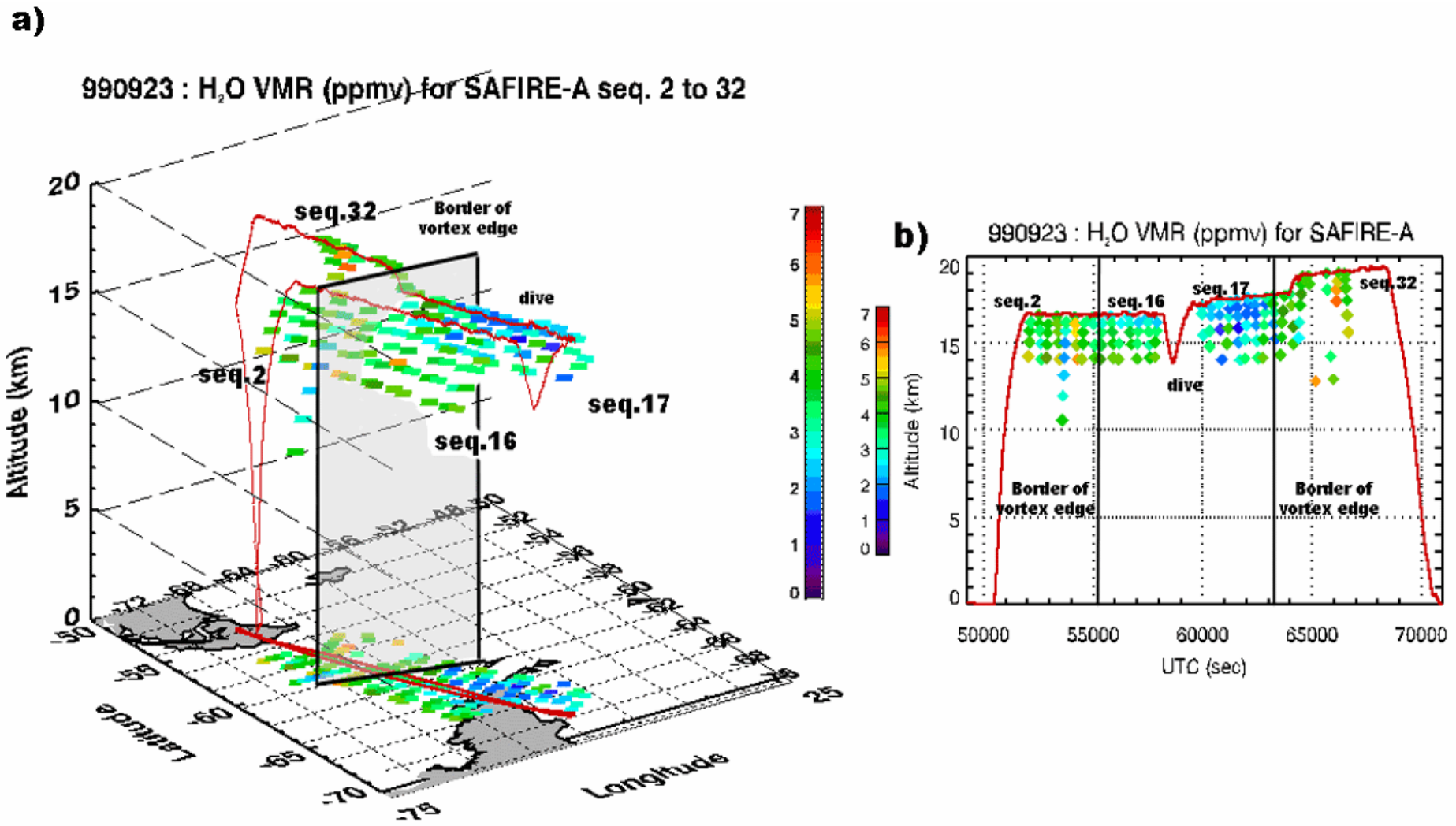

Figure 7.22: a) H_2O values at tangent altitudes recorded by SAFIRE-A on 23rd September 1999 respect to altitude, latitude, longitude, b) H_2O values at tangent altitudes retrieved by SAFIRE-A on 23rd September 1999 respect to altitude and time.

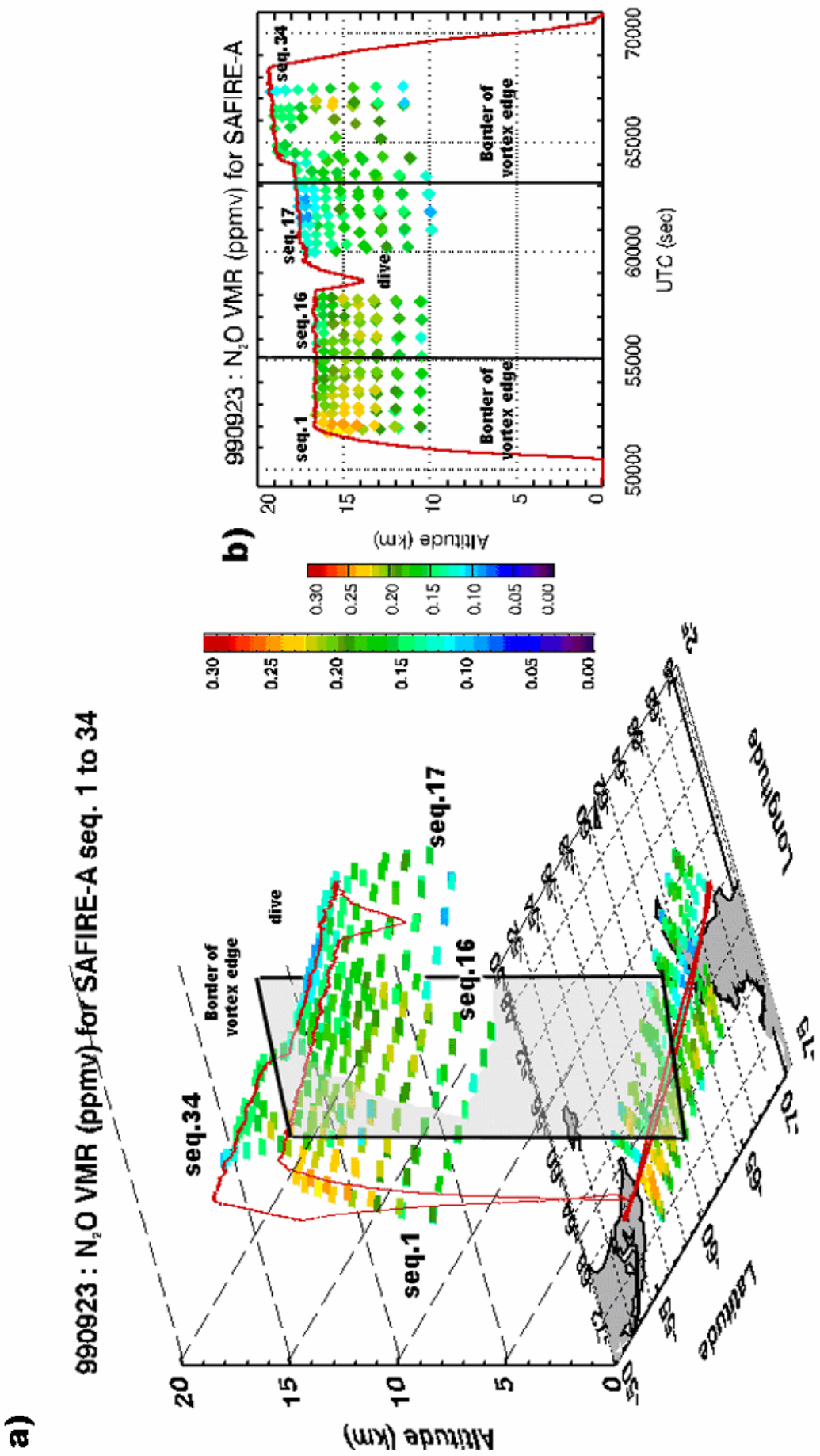

Figure 7.23: a) N_2O values at tangent altitudes recorded by SAFIRE-A on 23rd September 1999 respect to altitude, latitude, longitude, b) N_2O values at tangent altitudes retrieved by SAFIRE-A on 23rd September 1999 respect to altitude and time.

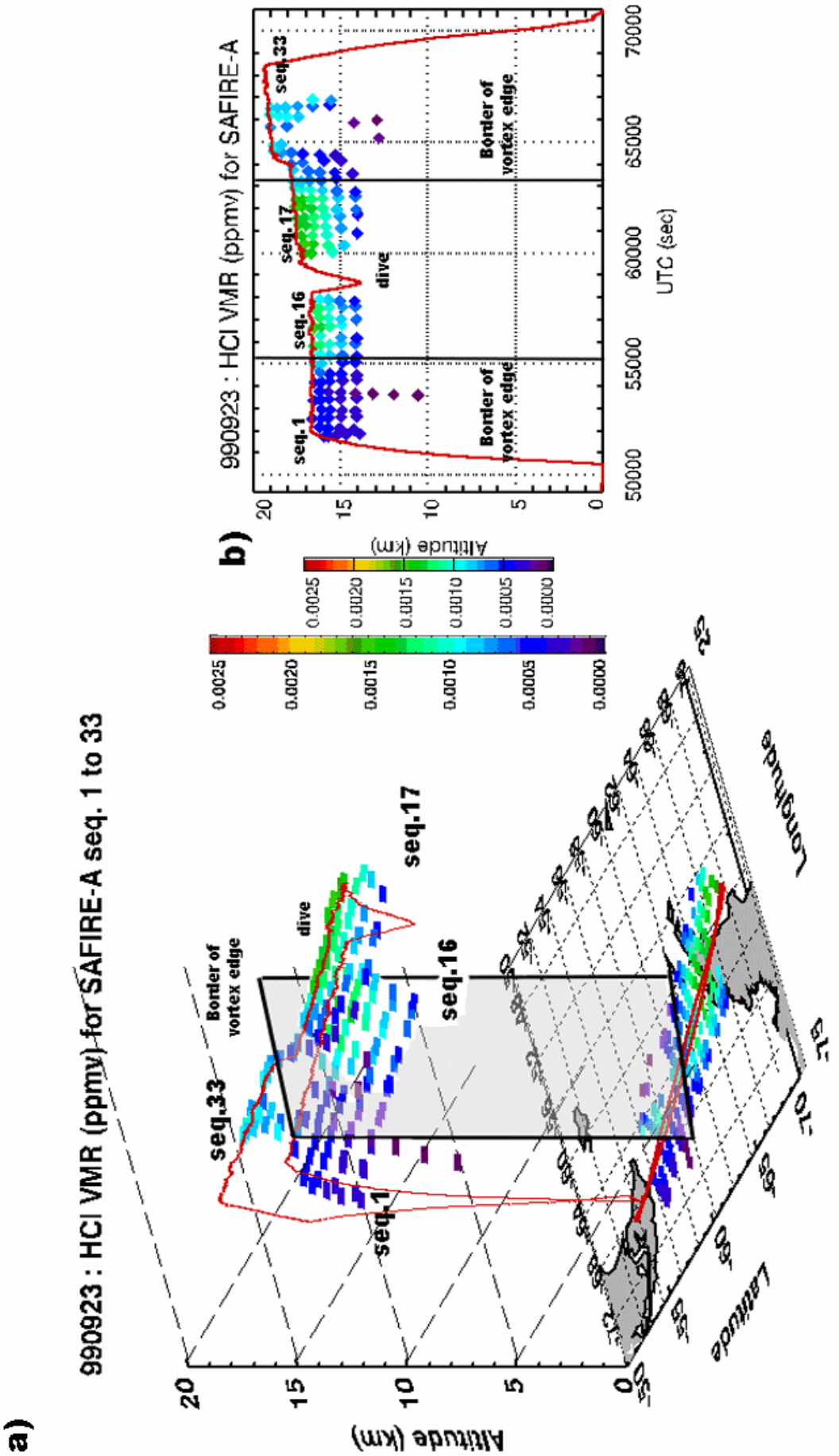

Figure 7.24: a) HCl values at tangent altitudes recorded by SAFIRE-A on 23rd September 1999 respect to altitude, latitude, longitude, b) HCl values at tangent altitudes retrieved by SAFIRE-A on 23rd September 1999 respect to altitude and time.

The results produced by limb sounding instruments (that are able to measure profiles), can be used to infer the vertical extension of the polar vortex. In Figure 7.19 and Figure 7.15.a I report the retrieved values for ozone together with the position of the vortex as indicated by the tracers. As can be noticed from the figure, the ozone depletion inferred from SAFIRE-A data is above 15-14 km.

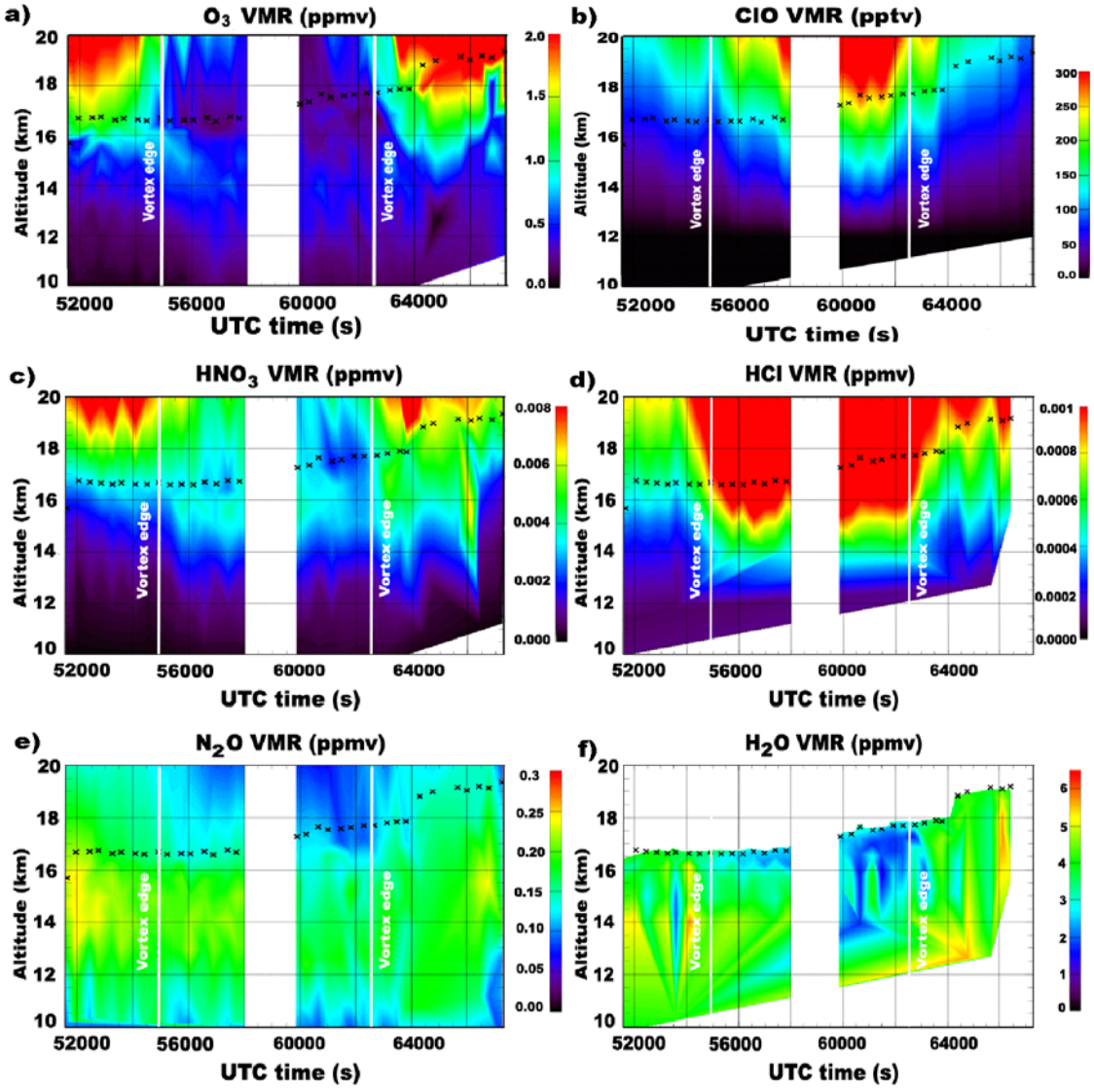

Figure 7.25: Vertical VMR profiles of a) O_3, b) ClO, c) HNO_3, d) HCl, e) N_2O and f) H_2O along flight route (23th September 1999).

The same behaviour observed for ozone can be noticed also in the case of HNO_3. Entering the vortex at 55000 UTC, the values of HNO_3 decreased rapidly, increasing again after sequences 23 (figure 6.21). From Figure 7.21.b and Figure 7.25.c, the denitrification seems to have the same vertical extension of the ozone hole (above 14 km). For N_2O and H_2O values the sequences from 9 to 23 present a decrease in VMR at flight altitude and above (in case of N_2O).

The opposite behaviour is instead observed in the case of ClO VMR (Figure 7.20). During the first leg, for sequences from 11 to 16 the ClO values appeared to be enhanced respect to the previous sequences. Near the dive and the turning point, the ClO values reach their maxima from sequences 16 to 24, then leaving the vortex they decrease again. Also for HCl the VMR values are enhanced into the vortex region (Figure 7.24.a).

These measurements show evidence of the perturbed chemistry occurring in the innermost part of the polar vortex. If no chemistry process acts inside the polar vortex, due to the

descending motion of cold air, the concentrations of O_3 and HNO_3 have to increase. During this flight, clearly this didn't happen: the ozone mixing ratio is strongly reduced entering the vortex, in accordance with GOME satellite data of total ozone column in Figure 7.1 that evidenced the ozone hole extension for this day.
It is also possible to notice clear sign of the anti-correlation existing between O_3 and ClO distributions across the vortex edge. As highlighted in appendix C, ClO is produced by the photodissociation of $ClONO_2$ during the day, and by the destruction of ozone:

$$Cl + O_3 \rightarrow ClO + O_2 \qquad \text{(C.4.1)}$$

Even if the temperature during the flight remains well above the 196 K (threshold temperature for PSC formation), HNO_3 values decrease entering the vortex. This behaviour could be due to a possible sedimentation of PSCs previously to the flight. In fact, since PSCs are composed of hydrated forms of nitric acid, their formation removes NO_x from the gas phase. Should PSC particles become large enough to undergo sedimentation, NO_x is removed entirely. The stratosphere is then denitrified, (see APPENDIX C for PSC formation and Figure 7.26 where NO_y represents the nitrogen reservoir species such as HNO_3).
HCl values increase entering the polar vortex showing the air descending motion in the polar vortex and a small recovery of chlorine species [37],[38]. N_2O values decrease entering the polar vortex as a consequence of descending of cold air into the vortex core and for this reason it is used as a trace species. Also H_2O values show a small decrease into the vortex core. The dehydration of the stratosphere inside the polar vortex is consistent with the expected changes of concentration of some of the species entering the chemically perturbed region [39] as in Figure 7.26.
In conclusion, for the 23rd September 1999, SAFIRE-A measurements show evidence of perturbed chemistry inside the polar vortex: the ozone hole is present, together with enhanced ClO concentration (especially after sunrise) in the inner most part of the vortex. The polar stratosphere seem to be a little dehydrated and denitrified, possibly as a consequence of sedimentation of PSCs previously to the flight.

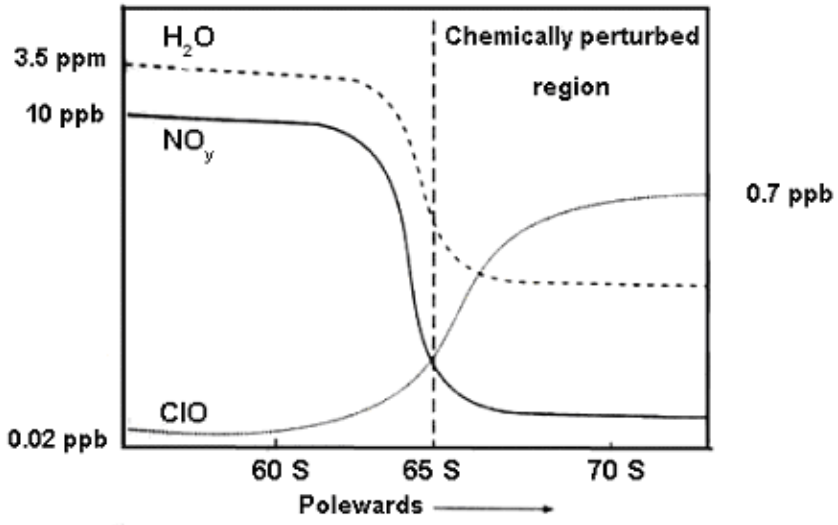

Figure 7.26: Schematic representation of the changes in concentration of some of the species entering the chemically perturbed region.

7.3 Flight of the 8th October 1999

7.3.1 Flight Route and Description

From high resolution RDFT fields, a filament was forecasted for the 8th of October 1999, between Argentina and the Antarctic Peninsula. The signature of the filament was already clearly present in the RDFT forecasted products since 96 hours in advance. In order to verify and study the occurrence of this structure a flight was planned, with a four legs track on two isentropic surfaces: 390K and 450K. As forecasted, while flying quasi isentropically at 450 K, the aircraft has observed an intense and localised variation of the measured tracers, that is supposedly related with the sampling of the vortex filament structures along the flight track. Also, high resolution RDFT products (not shown here) picture a three-dimensional filament with a strong horizontal gradient, a deep vertical shape and a high resolution internal structure that seems to correspond well with the preliminary analysis of the time series of experimental data. The filament is seen straight after the aircraft take off at 14 km (low values of CO_2 and N_2O) and the filamentary structure is seen again in tracer measurements after the dive at 18 km (low CO_2, low N_2O, high O_3) [40].

The flight duration was 5 hours and 53 minutes, the M55 took off at 06:32 UTC and landed at 12:09 UTC, the maximum altitude reached by the aircraft was 18.7 km. The first horizontal leg was carried out at the altitude of 14.3 km. The descending was made with the vertical speed at 10 m/sec over Antarctica. Then, during climbing over Antarctica at the altitude of 18 km without any visible reasons under absolutely clear sky there began heavy turbulence. After reaching the altitude of 18.5 km and turning at the direction of the point with co-ordinates 53°00'S 72°30'W the pilot saw, owing to the illumination arising from the sun at the horizon, that the aircraft flied in washed away clouds that looked like as dense haze.

The flight in the area of this turbulence continued for 8 min, after that (because the top of the cloud went down) the aircraft left it. At the flight altitude the temperatures were approximately standard (about - 55°C), only in the area of turbulence they went down to - 65°C.

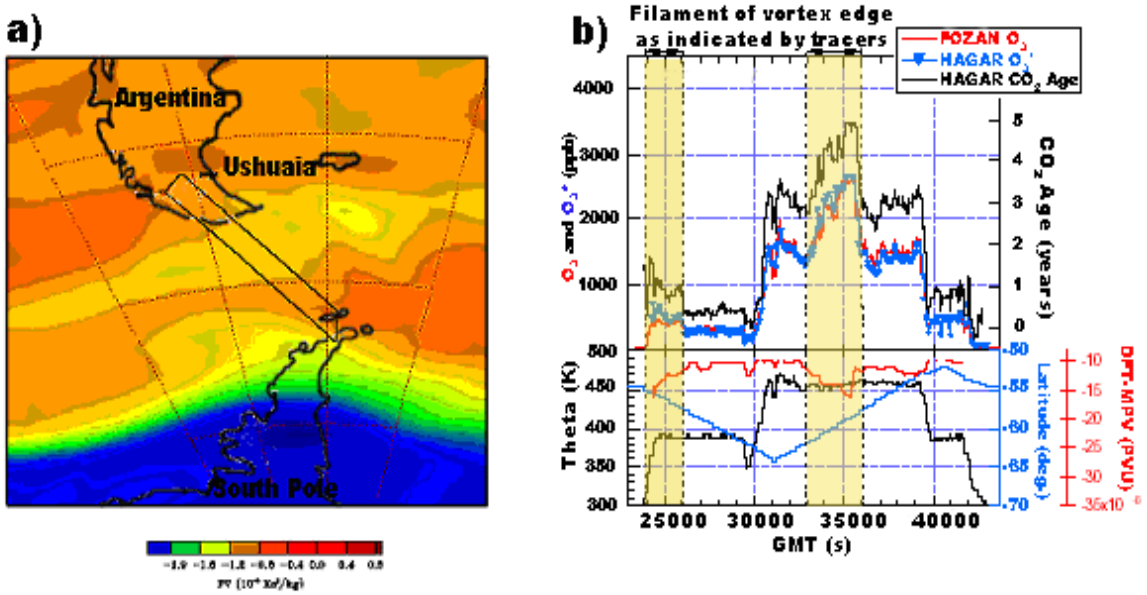

Figure 7.27: a) PV value at 390 K surface together with flight route, b) O_3, O_3* and CO_2 age measurement during flight evidencing the position of polar vortex filament.

Further analyses, involving the set of tracers data available from onboard instrumentation evidenced a sharply increase in values of O_3, O_3*, and CO_2-derived age [41] within the filament. Following Proffitt et al. [42] in [43] they define unperturbed ozone, O_3*, from the linear correlation with N_2O outside the vortex:

$$O_3^* \text{ [ppbv]} = \alpha - \beta * N_2O \text{[ppbv]} \quad (7.1)$$

Where α and β are empirically determined. Despite the fact that the filament originated from the outer vortex edge region, O_3 equals O_3^* throughout the whole flight (Figure 7.27.b), evidencing that no ozone loss is observed within the filament.
From values in Figure 7.27.b it can be inferred that the predicted filament was encountered first during ascent and the beginning of the southbound isentropic flight leg at 390 K. The filament was crossed again on the isentropic northbound return leg at 450 K. The calculated PV along the flight path reproduces the filament at the correct meridional location at both levels (Figure 7.27.a).

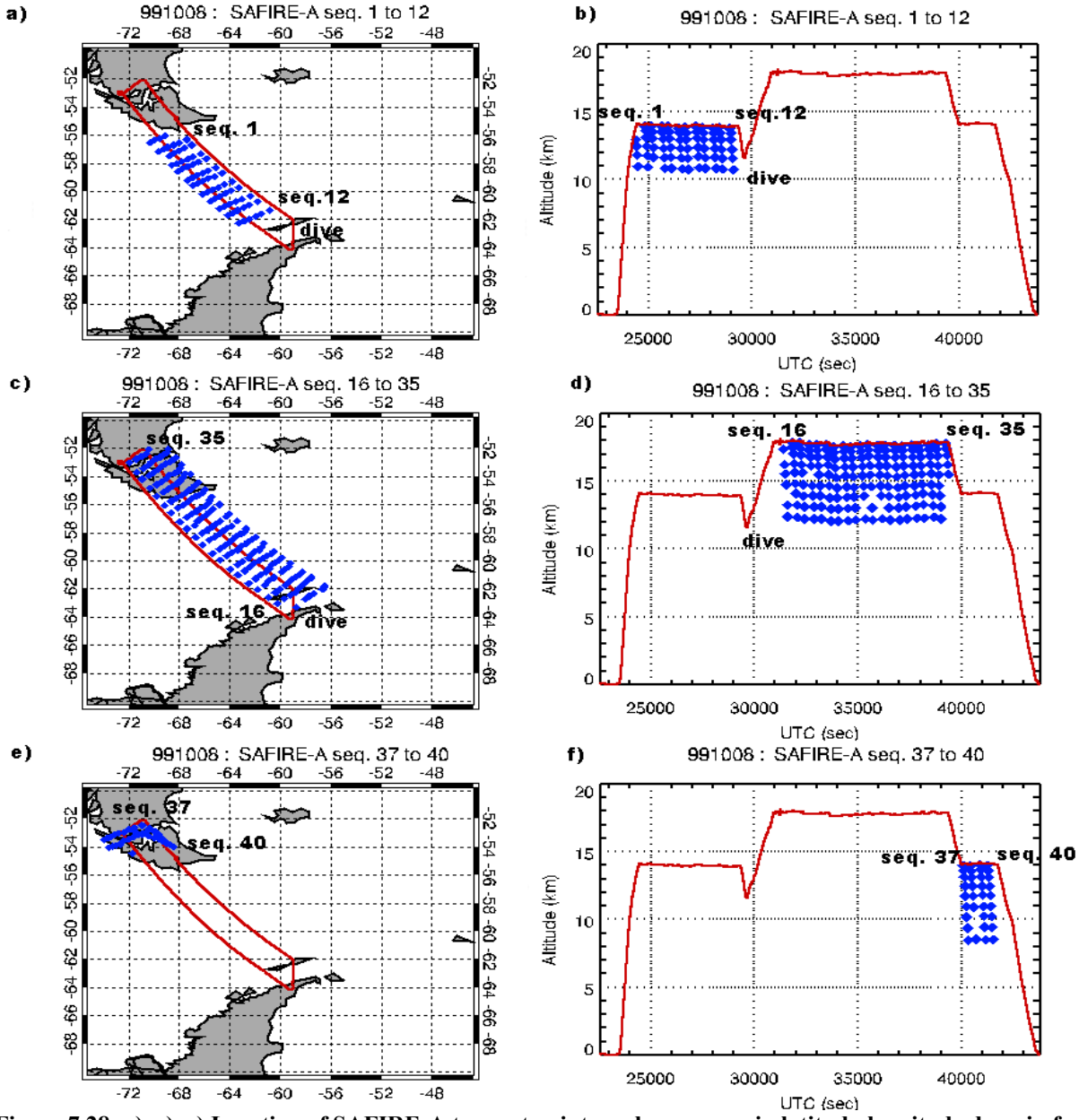

Figure 7.28: a), c), e) Location of SAFIRE-A tangent points and sequences in latitude-longitude domain for flight performed on 8th October 1999, b), d), f) Location of SAFIRE-A tangent points and sequences respect to altitude flight profile for 8th October 1999.

7.3.2 SAFIRE-A Measurements

During the flight of 8th October 1999, the SAFIRE-A instrument performed 40 limb scanning sequences. In Figure 7.28.a, Figure 7.28.c, Figure 7.28.e you can find the location of the SAFIRE-A sequences in longitude and latitude for this flight.
The instrument did not perform any measurement during the rapid variation of the flight altitude. In total SAFIRE-A performed 12 limb scanning sequences before the dive, then, after turning back the instrument performed 19 limb scanning measurements. Then, in the final part of the flight, SAFIRE-A performed 4 limb scanning measurement reaching Ushuaia. From the above mentioned figures, it is possible to notice that during this flight SAFIRE-A measurements explored the same air masses into the first and the second part of the flight (even if with some time delay).
In figures Figure 7.28.b, Figure 7.28.d, Figure 7.28.f I report the position of the SAFIRE-A sequences respect to the flight altitude profile. The first 12th sequences have the maximum tangent altitude at 14.3 km and the minimum at 11 km. After the dive and the turning point, the M55-Geophysica reached higher altitudes, for this reason the SAFIRE-a limb scanning measurements from 16 to 35 have a maximum tangent altitude of 18.5 km while the minimum tangent altitude is located at 12 km.
During this flight, the selected configuration for SAFIRE-a measurements was to use the channel 22-24 cm^{-1} and the channel at 122-124 cm^{-1}. This configuration permits the retrieval of O_3, HNO_3, N_2O, ClO, H_2O and HCl, as in the 23rd September flight. Each limb scanning sequence was composed by some up-looking geometries and some down looking geometries. For sequences from 1 to 12 the limb scanning angles are 80, 85, 83, 89.7, 90.3, 90.7, 91, 91.3, 91.55, 91.8 while for sequences from 16 to 40 the limb scanning angles are 80, 89.7, 90.3, 91, 91.3, 91.55, 91.8, 92, 92.2, 92.4. The overall quality of the recorded spectra was good.

7.3.3 Data Analysis

Also for this flight, it was possible to analyse data in all the two channels. Therefore retrieved profiles for O_3, N_2O, HNO_3, ClO (data analysis for channel one), HCl, H_2O (data analysis for channel centred at 125 cm^{-1}) could be obtained.
The noise in the first channel was at 1.2 nW/ (cm^2 sr cm^{-1}), while in the second it was 305 nW/ (cm^2 sr cm^{-1}), a little bit higher than in the previous flight. All the sequences were analysed retrieving at the same time offset, VMR and continuum profile.
Also for the flight of 8th October 1999, pressure and temperature profiles were obtained by ECMWF data processed at University of L'Aquila. ECMWF values for temperature and geopotential height were linearly interpolated in latitude and in time, in order to make use of the most suitable temperature and pressure values. For each sequence VMR profiles (one profile for the whole flight) coming from a standard polar atmospheric model were used either as initial guess and to model interfering gases. The used microwindows for retrieved VMR profiles during this flight are the same used for the flight of 23rd September 1999.

7.3.4 Retrieval results and Comparisons with other instruments onboard the Geophysica

The results obtained from the analysis of this flight and the retrieval grids used are reported in the following sections. Moreover a comparison with measurements obtained from other instruments onboard the aircraft was carried on in order to validate SAFIRE-A results.

7.3.4.1 Ozone

In case of ozone retrieval the chosen retrieval grid is the one composed by all the tangent altitudes and two points added above flight altitude (18 and 16 for sequences from 1 to 12 and 22 and 20 km for sequences from 16 to 35). In Figure 7.30.a the retrieval results for sequence number 18 are reported, together with averaging kernel and quality parameters information. In

this case 11 points were used in the retrieval and 8.38 are the independent pieces of information.
At higher tangent altitudes the information comes mostly from the measurements while at the lower altitudes the retrieved values are partially influenced by the regularization. The total result of the analysis is shown in Figure 7.34.a, Figure 7.34.b, where the values of the retrieved VMRs at tangent altitudes are plotted (retrieved value above flight altitude not included) in a 3D graph according to their latitude-longitude-altitude position, together with the flight path.
In Figure 7.29.a you can find a comparison of the data recorded by ECOC along the flight track with the data coming from SAFIRE-A ozone retrieved profiles at flight altitude. As you can notice, the overall agreement between the two data sets is good. In Figure 7.34.e and Figure 7.34.f you can find the retrieved VMR values plotted versus their latitude-longitude position and in Figure 7.34.c and Figure 7.34.d versus the time-altitude co-ordinate.
Both the value of the ozone VMR and the ozone trend along the flight path are in good agreement. In Figure 7.29.b you can find the comparison between data recorded by ECOC instrument during the dive and SAFIRE-A data for sequences 16, that is near the dive (Figure 7.28.c and Figure 7.28.d). As you can see the comparison gives very good results in the whole altitude range and the overall trend seems to be the same for the two profiles. In case of the ozone retrieval I can conclude that the retrieved profiles are in good agreement with other measurements, and can be considered a reliable estimate for the O_3 values on this day.

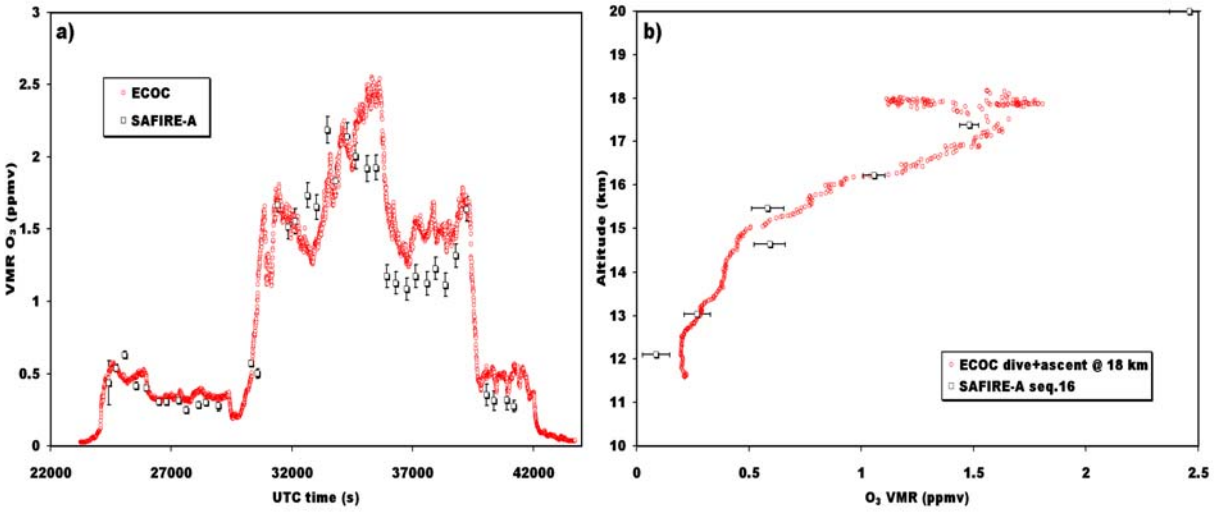

Figure 7.29: a) Ozone values at flight altitude along the flight track recorded by ECOC and retrieved by SAFIRE-A on 8th October 1999, b) Comparison of ozone values during dive recorded by ECOC and ozone value retrieved by SAFIRE-A for sequence 16 on 8th October 1999.

7.3.4.2 N_2O

The used retrieval grid for N_2O data analysis is the one composed by alternate tangent altitudes and one added point above flight altitude (22 km). In Figure 7.30.b you can find the result of the retrieval of sequence number 18 on 8th October. In the figure you can also find the values of the quality parameters and the averaging kernel. The retrieval results seems to be quite good, the number of independent pieces of information is 4.30 against 6 retrieved points.

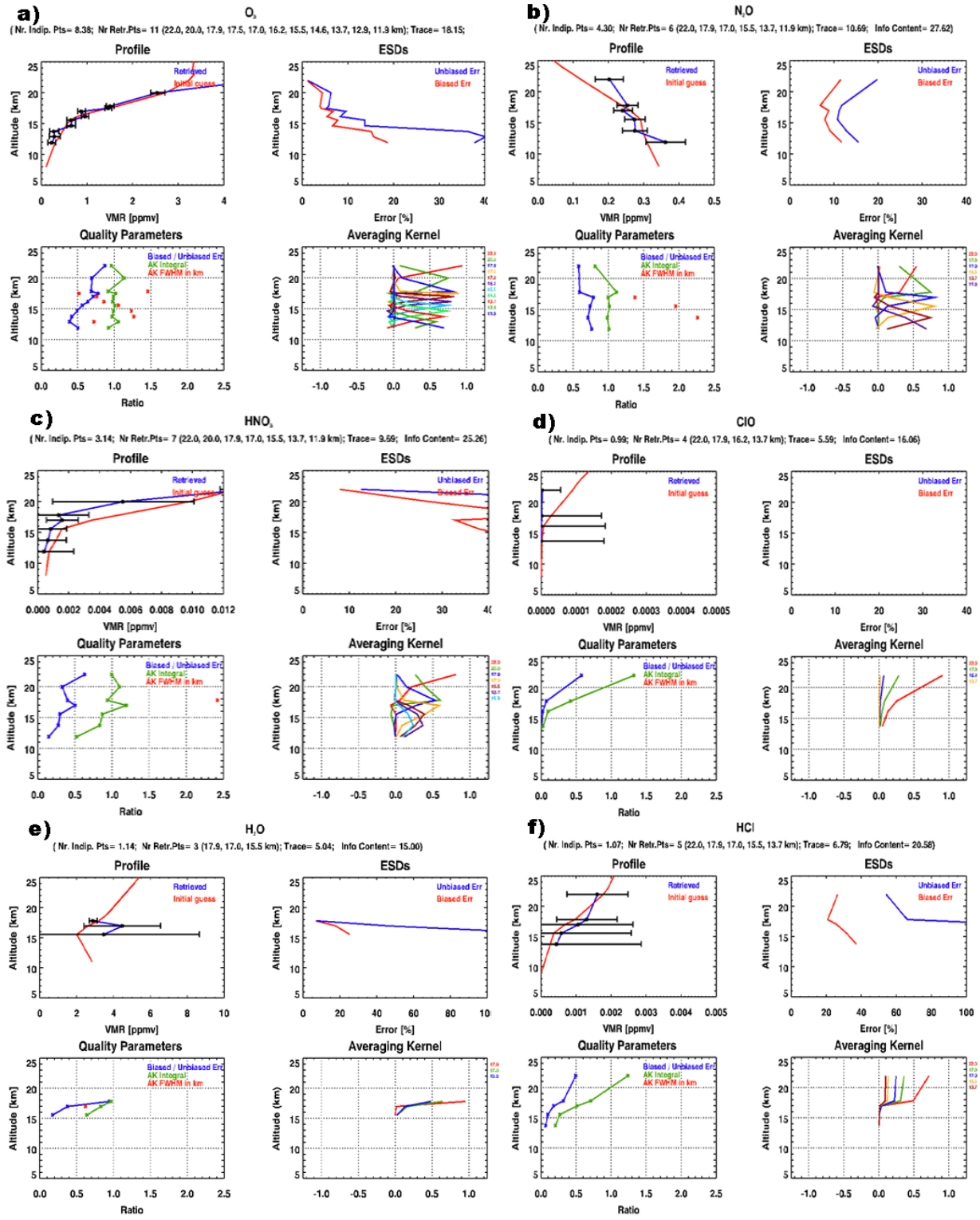

Figure 7.30: a) O_3 retrieval for sequence 18 on 8th October 1999, b) N_2O retrieval for sequence 18 on 8th October 1999, c) HNO_3 retrieval for sequence 18 on 8th October 1999, d) ClO retrieval for sequence 18 on 8th October 1999 e) H_2O retrieval for sequence 18 on 8th October 1999. f) HCl retrieval for sequence 18 on 8th October 1999.

The retrieved profile is sensible to the measurements at all tangent altitudes while it is influenced by the initial guess profile at 22 km (also because the N_2O mixing ratio decreases with altitude). The N_2O analysis was performed, using the chosen retrieval grid, for all the sequences recorded by SAFIRE-A during this flight, the results are reported in Figure 7.36.a, Figure 7.36.b, where the values of the retrieved VMR at tangent altitudes are plotted in a 3D

graph. In Figure 7.36.e and Figure 7.36.f you can find the retrieved VMR values plotted versus their latitude-longitude position and in Figure 7.36.c and Figure 7.36.d versus the time-altitude co-ordinate.
To validate the of N_2O profiles coming from this flight we only had a graph with HAGAR results for N_2O VMR at flight altitude. So we can only compare the SAFIRE-A N_2O retrieved data at flight altitude. In Figure 7.31 is shown the result of this procedure. A part from some points at the beginning of the flight where the SAFIRE-A values are a little bit lower, the agreement between the two data sets is good.

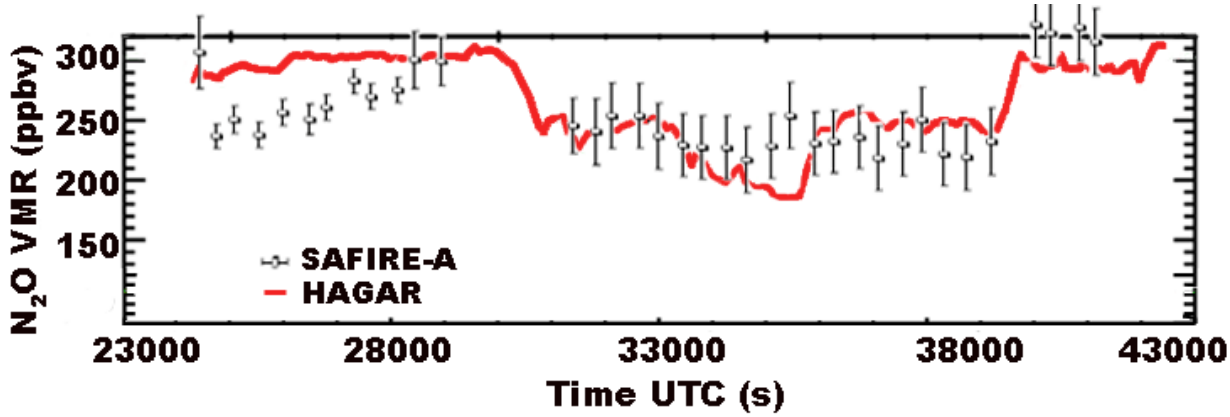

Figure 7.31: N_2O values at flight altitude along the flight track recorded by HAGAR and retrieved by SAFIRE-A on 8th October 1999.

7.3.4.3 HNO_3

As for the previous flight, in case of HNO_3 data analysis, the used retrieval grid is the one composed by alternate tangent altitudes. Two points were added above flight altitude (22 and 20 km). In Figure 7.30.c you can find the result of retrieval of sequence number 18 on 8th October. The retrieval results seem to be quite good (the number of independent pieces of information is 4.13 against 7 retrieved points), even if possibly the used retrieval grid is still too fine.
In Figure 7.35.a and Figure 7.35.b you can find an overview of HNO_3 retrieved profiles for SAFIRE-A where the values of retrieved VMR at tangent altitudes are plotted (retrieved value above flight altitude not included) in a 3D graph.
The quality of SAFIRE-A HNO3 profiles could not be tested, in fact for the flight of 8th October 1999 there were no MIPAS-STR data for HNO_3, thus it was not possible to compare our results with any other instrument.

7.3.4.4 H_2O

In the second channel, the spectra below 14 km are saturated by the high water vapour content at low altitudes and could not be included into the analysis. For this reason, in case of the water vapour retrieval the chosen retrieval grid is the one composed by all the tangent altitudes (from flight altitude to about 15 km) and no added points above flight altitude, as for the flight of 23rd September. In Figure 7.30.e the retrieval results for sequence number 18 are reported.
In this case, the retrieval seems to work well at high altitudes while it has few information content, due to the spectra saturation caused by the increasing water vapour content at lower altitude(the number of pieces of information is 1.14 while the number of retrieved point is 3).
The same retrieval grid was used to analyse the whole flight. Results are reported in Figure 7.32.a.

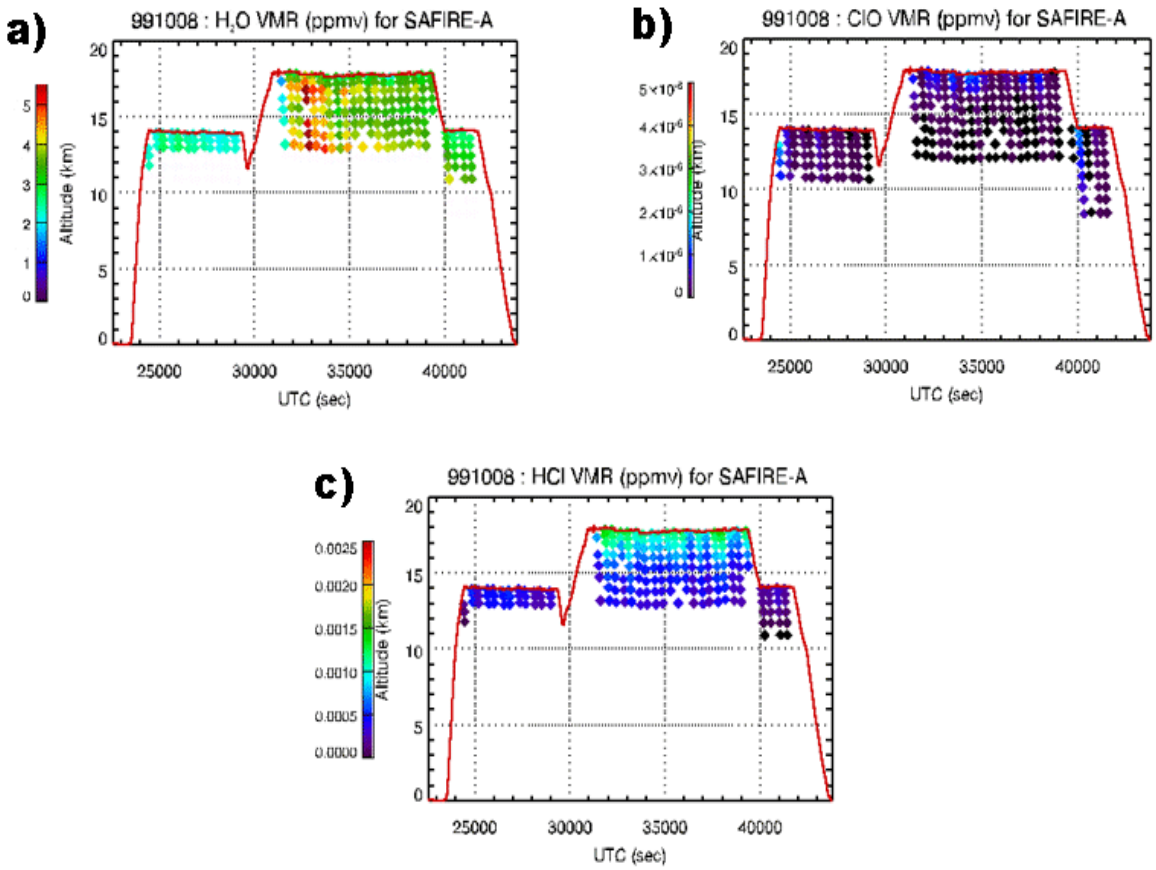

Figure 7.32: a) H_2O values at tangent altitudes altitude retrieved by SAFIRE-A on 8th October 1999; b) ClO values at tangent altitudes altitude retrieved by SAFIRE-A on 8th October 1999; c) HCl values at tangent altitudes altitude retrieved by SAFIRE-A on 8th October 1999.

An internal validation of H_2O profiles was possible since for this flight data for H_2O VMR form the in situ instrument FLASH were available. In Figure 7.33.a one can find the comparison of H_2O SAFIRE-A retrieved values at flight altitudes along the flight track with data obtained by FLASH during the flight.

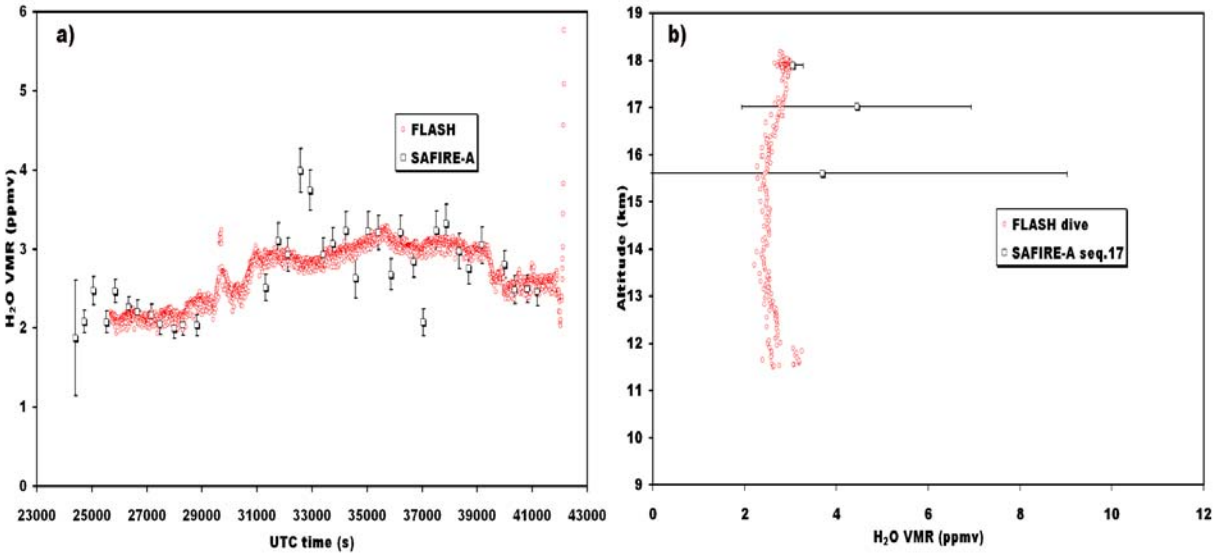

Figure 7.33: a) H_2O values at flight altitude along the flight track recorded by FLASH and retrieved by SAFIRE-A on 8th October 1999, b) Comparison of H_2O values during dive recorded by FLASH and value retrieved by SAFIRE-A for sequence 17 on 8th October 1999.

In Figure 7.33.b, a comparison of H_2O profile obtained by FLASH during the dive and SAFIRE-A sequence 17 is shown. In both cases the overall agreement is good, and the obtained profiles can be considered a good representation of the atmosphere along the flight track.

7.3.4.5 ClO

In case of ClO data analysis, the used retrieval grid is the one composed by some tangent altitudes and one added point above flight altitude (22 km). In Figure 7.30.d you can find the result of retrieval of sequence number 18 on 8th October. For this flight the value of ClO were very low (consider also that the flight was performed outside the vortex and during night time for almost all flight (take off at 3:30 AM local time, landing at 9 AM local time), for this reason the retrieved profile is close to 0 at all the retrieved altitudes.
The small ClO values could be seen also from Figure 7.32.a where an overview of ClO retrieved profiles for SAFIRE-A can be found. The values of retrieved VMR at interpolated at all tangent altitudes are plotted (retrieved value above flight altitude not included) in a graph (Figure 7.32.b) versus the time-altitude co-ordinate.

7.3.4.6 HCl

In the case of HCl retrieval the chosen retrieval grid is the one composed by alternate tangent altitudes (from flight altitude to about 14 km) and one added point (at 22 km) above flight altitude. The retrieval seems to work quite well (see Figure 7.30.f where the retrieval results for sequences number 18 are reported) at high altitudes even if the HCl profile is retrieved over a too fine grid. An overview of HCl retrieved profiles for SAFIRE-A is given in Figure 7.32.c.

7.3.5 Polar Vortex Filament

The measurements collected by SAFIRE-A during the flight of 8th October 1999 show evidence of the presence of a filament of polar vortex air, forecasted from high resolution RDFT fields.
Looking at the ozone value retrieved by SAFIRE-A at flight altitude in Figure 7.29.a and in the Figure 7.27.b (in which the position of the filament, evidenced by tracers and ozone value from in situ instruments, is reported), one can see that the instrument retrieves higher ozone values in correspondence of the stream of polar vortex air (both during the first and the second leg of the flight). The capability of limb sounding technique of measuring profiles can be used in this case to infer the vertical extension of the filament. In Figure 7.34 I report the retrieved values for ozone together with the position of the filament as indicated by the tracers, for the first (Figure 7.34.a, Figure 7.34.c) and the second leg (Figure 7.34.b, Figure 7.34.d) of the flight.
During the first part of the flight, the aircraft crosses the filament at the very beginning, from 23000 to 26000 seconds UTC as in Figure 7.27.b, in correspondence of SAFIRE-A sequences from 1 to 5. The retrieved ozone mixing ratio for these sequences show increased value at the highest tangent altitudes (about 14 km). During the second leg of the flight, the M55 entered the filament at 33000 UTC seconds and went out at 36000 seconds (UTC). This time interval corresponds to SAFIRE-A sequences from 21 to 25. For those sequences the ozone mixing ratio seems to be higher than for the surrounding sequences at tangent altitudes from flight level to 15-14 km.

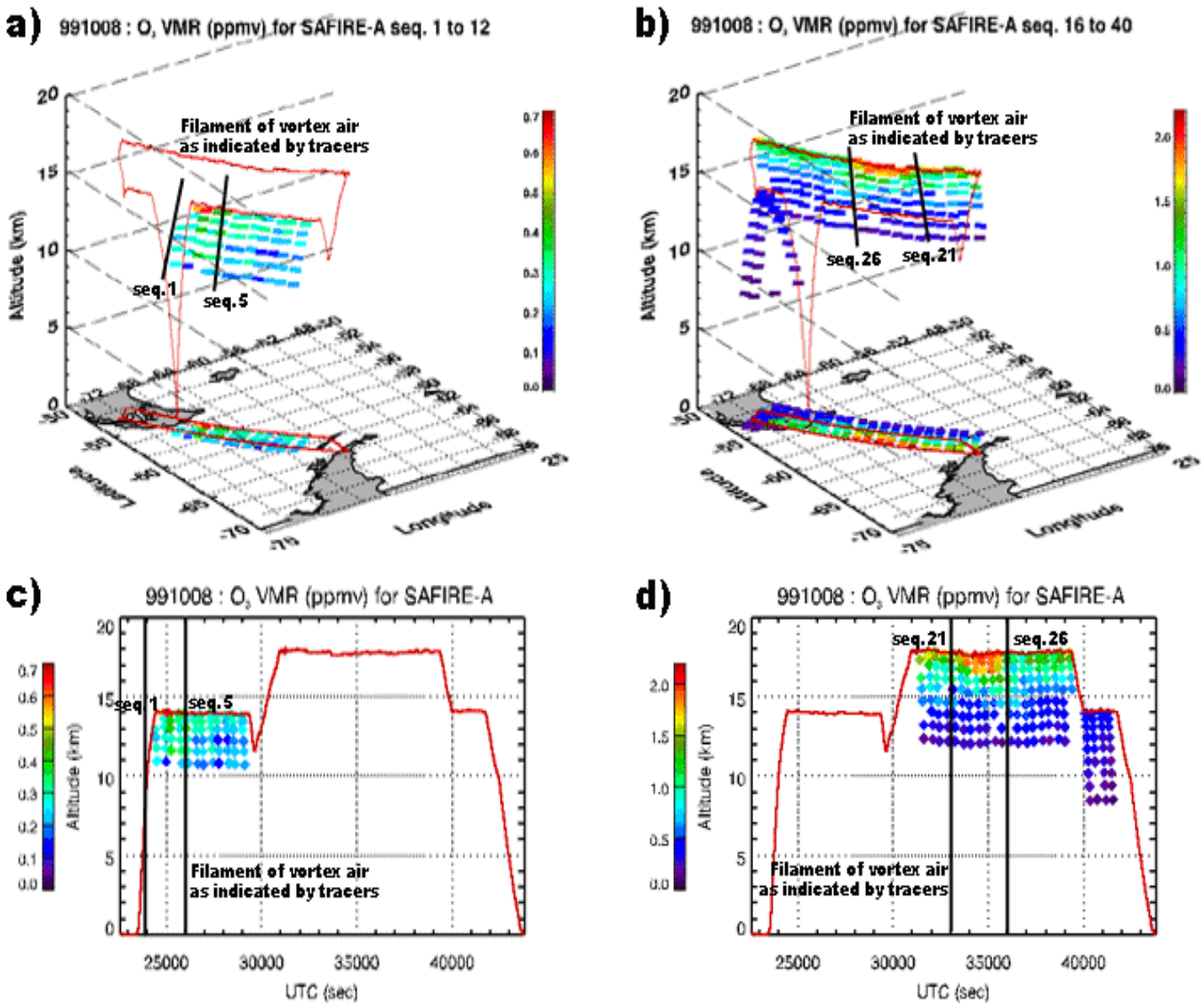

Figure 7.34: O_3 values at tangent altitudes recorded by SAFIRE-A on 8th October 1999 respect to altitude, latitude, longitude for the first (a) and the second leg (b), O_3 values at tangent altitudes retrieved by SAFIRE-A on 8th October 1999 respect to altitude and time for the first (c) and the second leg (d). In each graph the position of vortex filament as indicated by tracers in figure 6.27.b is also shown.

From this figure I can infer that the vertical extension of the filament of polar vortex air is from 18.5 to about 14 km.

The same behaviour is observed also in the case of HNO_3 retrievals. In Figure 7.35.a, Figure 7.35.c and the values of HNO_3 for the first flight leg show a little increase in concentration, while a major increase from flight altitude to 15 km is localised in time co-ordinate from 33000 and 36000 seconds UTC due to the presence of polar vortex air (Figure 7.35.b, Figure 7.35.d).

Also from N_2O retrieved values (Figure 7.36) is possible to recognise the presence of the filament, even if in this case the variation in the gas concentration is less evident than in case of O_3 and HNO_3. the filament is less evident especially for the first part of the flight (Figure 7.36.a, Figure 7.36.c) while for the second (Figure 7.36.b, Figure 7.36.d) this structure is more clear, also because of the range of altitudes covered by the sequences from 16 to 35. ClO values (Figure 7.32.2) remained extremely low for all the flight, in accordance with the fact that the flight route was outside the vortex edge.

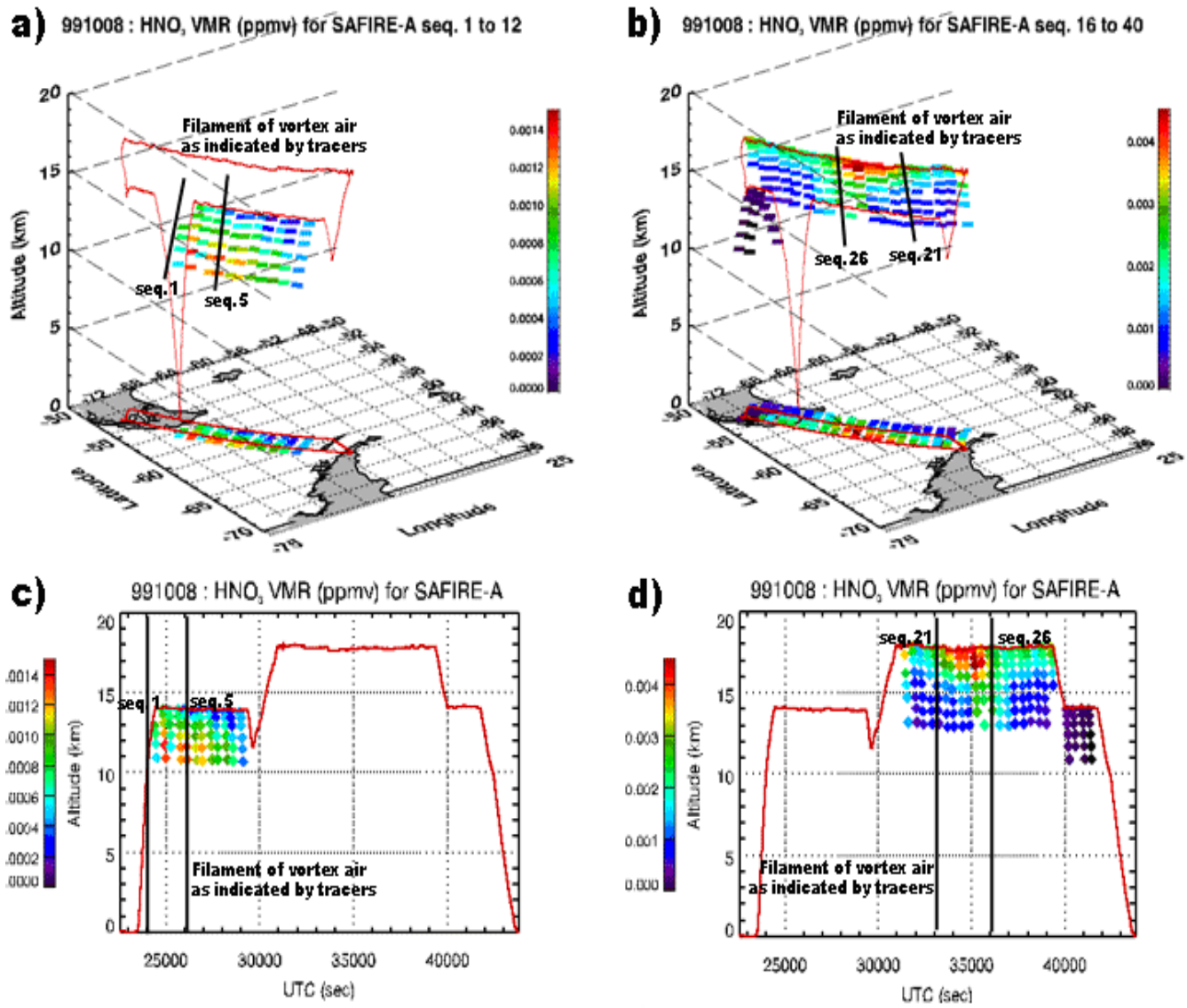

Figure 7.35: HNO_3 values at tangent altitudes recorded by SAFIRE-A on 8th October 1999 respect to altitude, latitude, longitude for the first (a) and the second leg (b), HNO_3 values at tangent altitudes retrieved by SAFIRE-A on 8th October 1999 respect to altitude and time for the first (c) and the second leg (d). In each graph the position of vortex filament as indicated by tracers in figure 6.27.b is also shown.

In conclusion, for the 8th October 1999, SAFIRE-A measurements show evidence of the presence of a filament of the polar vortex air: the ozone values are higher, from flight altitude (about 18.5 km) to 15-14 km, in the region of the filament identified by the tracers than outside.

This happens both during the first and the second part of the flight. The HNO_3 values have the same behaviour but with a more evident increase in the values for the second part of the flight respect to the first. Also in this case the filament extension is from 18.5 to 15 km. Finally, the N_2O values decrease entering the polar vortex air, in accordance with the fact that the filament air has higher PV respect to the surrounding air masses (see tracers in Figure 7.27.b).

From SAFIRE-A measurements I can also infer that, despite the fact that the filament originated from the vortex edge region, no ozone loss or HNO_3 loss is observed within the filament (as shown in [40] and in Figure 7.27.b).

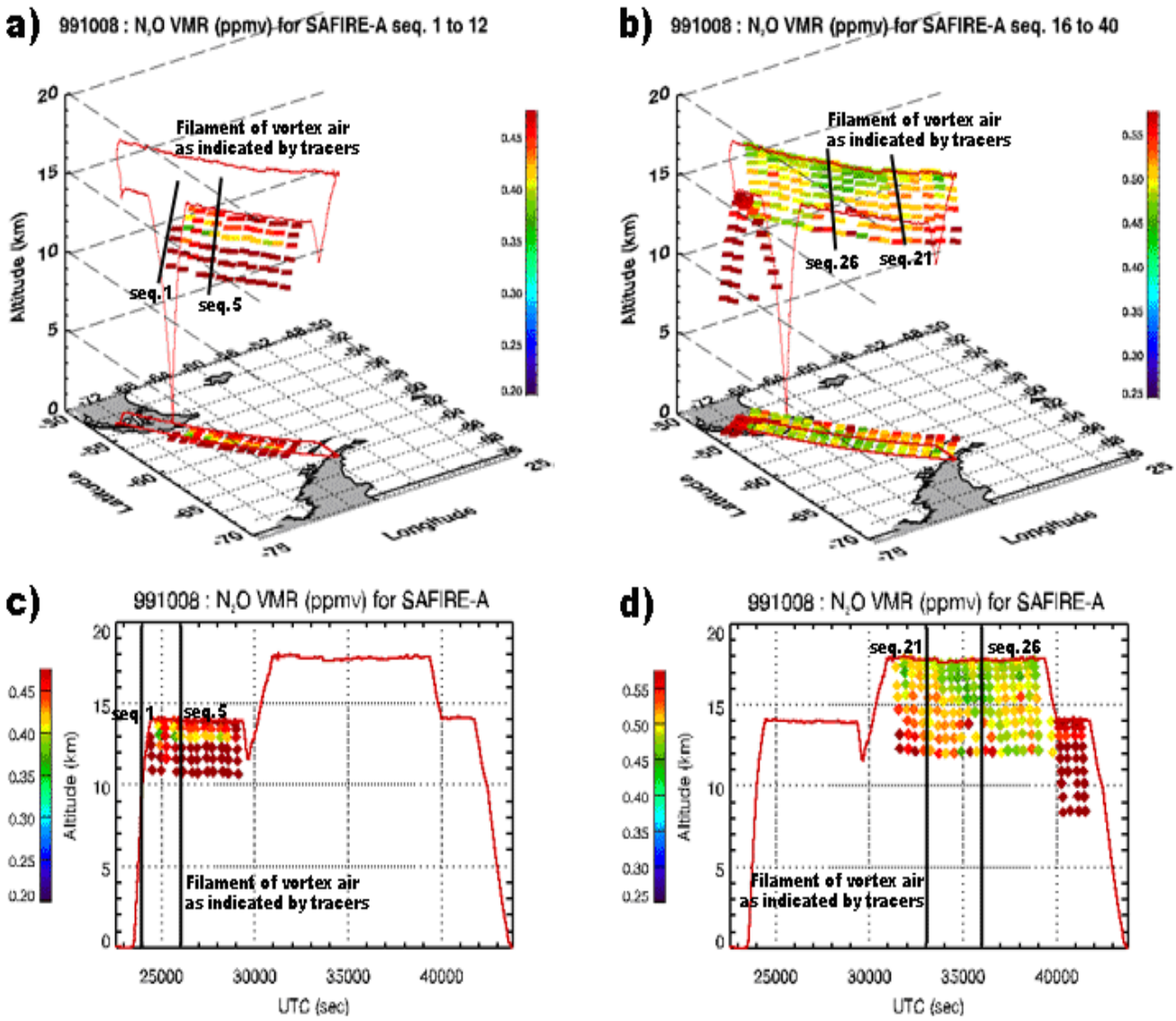

Figure 7.36: N_2O values at tangent altitudes recorded by SAFIRE-A on 8th October 1999 respect to altitude, latitude, longitude for the first (a) and the second leg (b), N_2O values at tangent altitudes retrieved by SAFIRE-A on 8th October 1999 respect to altitude and time for the first (c) and the second leg (d), N_2O values at tangent altitudes retrieved by SAFIRE-A on 8th October 1999 respect to latitude and longitude for the first (e) and the second leg (f). In each graph the position of vortex filament as indicated by tracers in figure 6.27.b is also shown.

7.4APE-GAIA Campaign: Conclusions

During APE-GAIA campaign, SAFIRE-A performed measurements of O_3, HNO_3, N_2O, ClO, HCl, H_2O. The results obtained during the data analysis of the two presented flights show evidence of the quality of recorded measurements and of the reliability of the retrieval procedure. The obtained profiles were used to give an interpretation of the atmospheric scenario (polar vortex and ozone hole event) explored by the M55 Geophysica during this campaign.

Chapter 8: Data Analysis: ENVISAT Validation Campaign

8.1 ENVISAT ESABC

Three ENVISAT validation campaigns with the stratospheric aircraft M55 Geophysica have been conducted: two from Forlì, Italy (Lat. 44°N, Lon. 12°E) in July and October 2002 and one from Kiruna, Sweden (Lat. 68°N, Lon. 20°E) in February-March 2003, as part of the ESABC (ENVISAT Stratospheric Aircraft and Balloon Campaigns) activities. The SAFIRE-A spectrometer was involved in both the mid-latitude and Arctic flights performed with the chemistry payload of the Geophysica aircraft. During the first Mid-latitude campaign, SAFIRE-A had instrumental problems, so no data were available for the analysis. In the other two campaigns the problems were solved and measurements were successfully performed. As a part of the work for this thesis, I participated to all the validation campaigns providing a first diagnostical analysis of the recorded data. The results obtained during one flight at mid latitude and one arctic flight are presented in this chapter.

8.1.1 Flight 24th October 2002: Mid Latitude Campaign

On 24th October 2002, the M-55 Geophysica carried out a night-time flight from Forlì, Italy, in coincidence with an overpass of the ENVISAT satellite (orbit 3403) along a route that had been studied to optimize the overlapping between the air masses observed by the airborne limb-sounders and in-situ sensors and those covered by MIPAS-ENVISAT scans 14, 15 and 16. The aircraft flight track together with the position of MIPAS-ENVISAT and SAFIRE-A scans are shown in Figure 8.1 [44],[45].

SAFIRE–A:

Scan #	Mean time
1	19:07
2	19:14
3	19:23
4	19:30
5	19:39
6	19:46
7	19:55
8	20:19
9	20:28
10	20:35
11	20:45
12	20:51
13	21:01
14	21:07
15	21:17
16	21:24
17	21:33
18	21:41
19	21:50
20	21:57

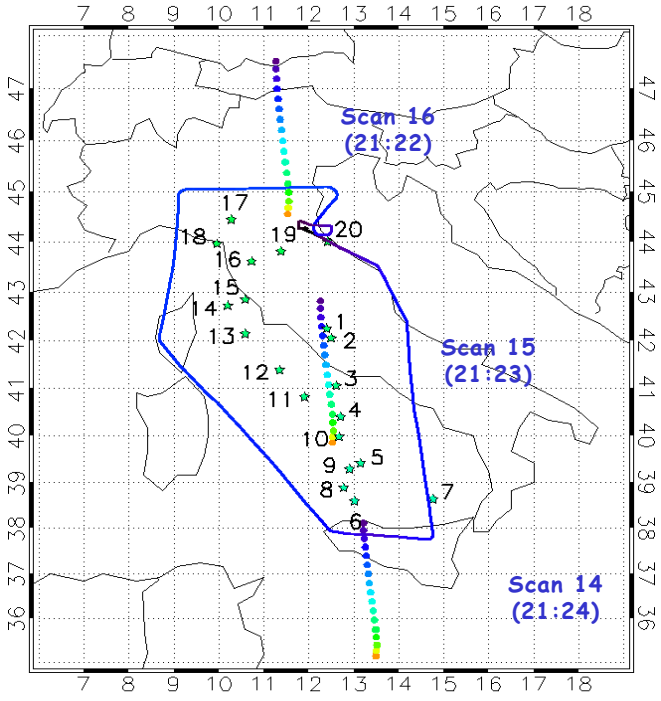

Figure 8.1: M-55 Geophysica flight track on 24th October, 2002.

8.1.1.1 SAFIRE-A Measurements and Coincidence with MIPAS-ENVISAT scans

During the flight the SAFIRE-A spectrometer acquired 20 limb scanning sequences, obtaining several profiles of the target species at approximately the same time and location of MIPAS-ENVISAT measurements [46].

In Figure 8.2.a and Figure 8.2.b you can find the latitude-longitude position of each SAFIRE-A sequences during the first and second flight leg, while in Figure 8.2.c and Figure 8.2.d the sequences are reported with respect to altitude and time. During the first part of the flight only 5 limb scanning sequences where performed, reaching a maximum altitude of 17 km. Then, after the dive, the instrument performed 13 limb sequences, from 8 to 20, and with altitude range from 20 to 11 km.

An estimate of the quality of the spatial and temporal overlapping of aircraft and satellite profiles can be attained by looking at Figure 8.1, where the geolocation of MIPAS tangent points for three scans of the selected overpass is indicated, along with the mean latitude and longitude of the tangent points for each of the limb sequences recorded by SAFIRE-A in the time period 19:05 – 21:55 UT. As can be seen in the figure, the best overlapping was obtained with the MIPAS scan at 21:23 UT (scan 15), whose tangent points in the altitude range 10-20 km correspond to the latitude and longitude region covered by SAFIRE-A observations during both the North-South and the South-North leg of the flight.

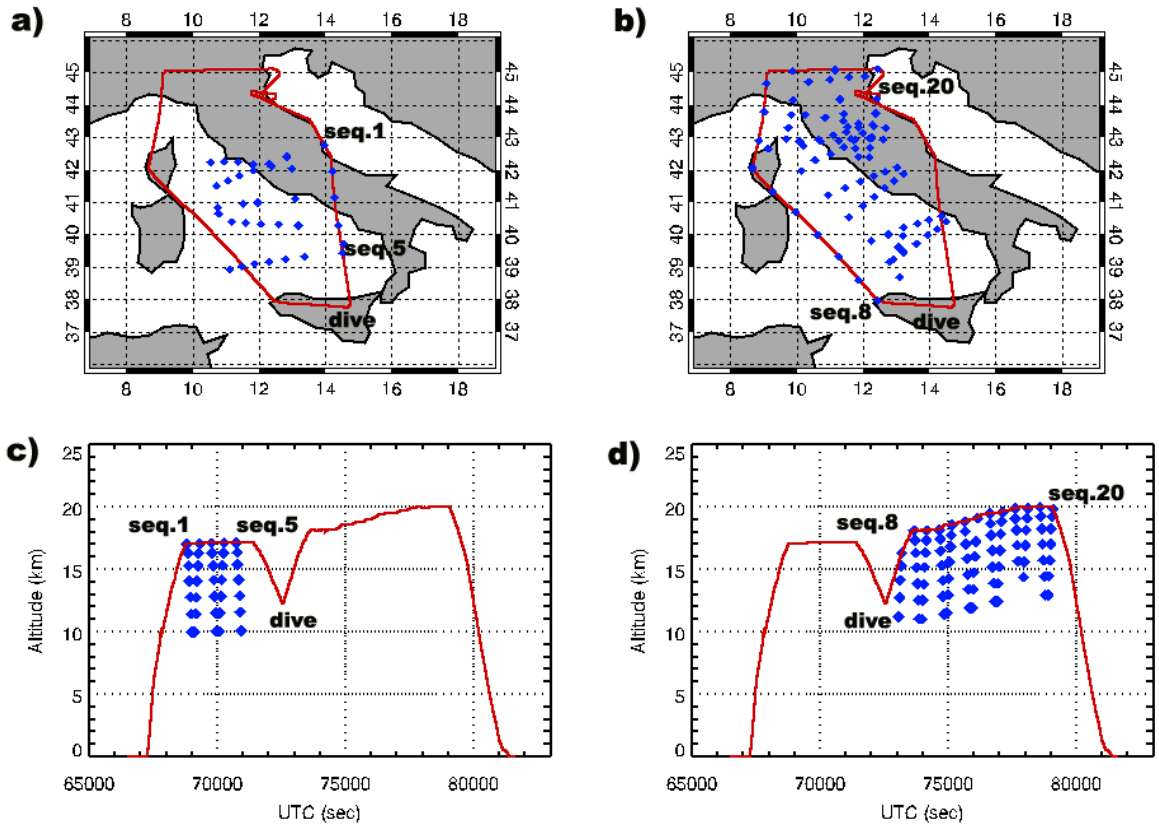

Figure 8.2: Location of SAFIRE-A tangent points and sequences in latitude-longitude domain for flight performed on 24th October 2002 for the first (a) and second (b) part of the flight. Location of SAFIRE-A tangent points and sequences respect to altitude flight profile 24th October 2002 for the first (c) and second (d) part of the flight.

The analysis carried out for validation purposes focused, therefore, on the intercomparison with MIPAS-ENVISAT level-2 products from scan 15 (Lat. 42°N, Lon. 12°E) and particularly on O_3 and HNO_3, for which most of SAFIRE-A scans provided useful results [47],[48]. The choice of the profiles to be used in the intercomparison was made by evaluating the distance between the average location of MIPAS-ENVISAT tangent points in

the range 10-25 km and the one of each SAFIRE-A sequence and by calculating the time difference between the corresponding acquisition times [49]. Table 8.1 summarizes the results of this estimate, whilst a detailed plot reporting latitude and longitudes of individual tangent points of both MIPAS scan 15 and closest SAFIRE-A sequences is shown in Figure 8.3. As can be noticed from the table, the selected sequences for the comparison can be divided into two groups. One group with distances from the MIPAS-ENVISAT scan 15 of maximum 183 km and time delay between 16 minutes to 2 hours and 16 minutes (SAFIRE-A sequences 1, 2, 3, 11, 12, 13, 14, 19, 20) and a smaller group of sequences with time delay of maximum 6 minutes and less than 170 km (sequences 15 and 16) of distance from the same MIPAS-ENVISAT scan. For this second group we can say that very good spatial and temporal coincidence of measurements has been achieved.

SAFIRE-A Sequences Number	Distance(km)	Time difference (SAFIRE-MIPAS)
1	99	-2 h 16 min
2	100	-2 h 09 min
3	183	-2 h 00 min
4	251	-1 h 53 min
5	368	-1 h 44 min
6	No Data	No Data
7	452	-1 h 32 min
8	392	-1 h 04 min
9	339	-0 h 55 min
10	282	-0 h 48 min
11	179	-0 h 38 min
12	139	-0 h 32 min
13	137	-0 h 22 min
14	157	-0 h 16 min
15	130	-0 h 06 min
16	168	+0 h 01 min
17	283	+0 h 10 min
18	248	+0 h 18 min
19	151	+0 h 27 min
20	135	+0 h 34 min

Table 8.1: SAFIRE-A scans distance and time delay from MIPAS-ENVISAT scan 15.

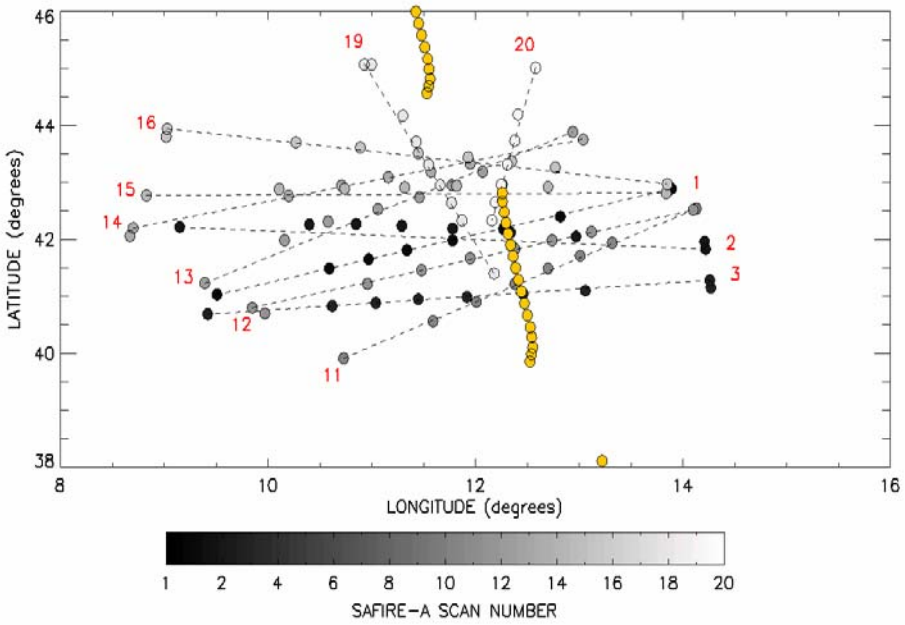

Figure 8.3: Co-location of SAFIRE scans (black/white dots) and MIPAS scan 15 (yellow dots). SAFIRE scan numbers are placed approximately at the instrument location during the scan and the dashed line represents the line of sight.

8.1.1.2 Data Analysis

The results shown here are coming from the limb sounding observations of the atmospheric emission over the frequency interval 22 - 24 cm^{-1} where spectral features of O_3, ClO, N_2O, and HNO_3 are present. The limb-scanning sequence spans the atmosphere with angles ranging from 10° above to 2.7° below the aircraft plane; the result is a sequence of 11 emission spectra (limb scanning angles: 80, 85, 87, 89, 90, 90.9, 91.35, 91.75, 92.1, 92.4, 92.7) with a vertical resolution of about 1.5 Km.

Pressure and temperature profiles, used into the retrieval procedure, were obtained by ECMWF data processed at University of L'Aquila. For each sequence, VMR profiles coming from a standard mid-latitude atmospheric model were used either as initial guess and to model interfering gases. Since the altitude of the tropopause in the adopted atmospheric model was different from the real one, the VMR profiles were vertically shifted in order to match the real atmospheric behaviour. The microwindows used to retrieve the VMR profiles are the same used for the APE-GAIA data analysis.

8.1.1.3 SAFIRE-A Ozone and HNO_3 retrievals

Ozone and HNO_3 retrieval were performed at all the tangent altitudes of the measurements. In order to exploit at their best the information coming from the measurements looking above the aircraft, one altitudes level (22 km), located well above the aircraft flight altitude, was added in the retrieval grid. In Figure 8.4 the result of the retrievals for sequence 15 (in exact coincidence with MIPAS scan 15) for O_3 and HNO_3, with their Averaging Kernels (AK) and their quality parameters information is presented. For both the analysed species, the retrieval quality is good.

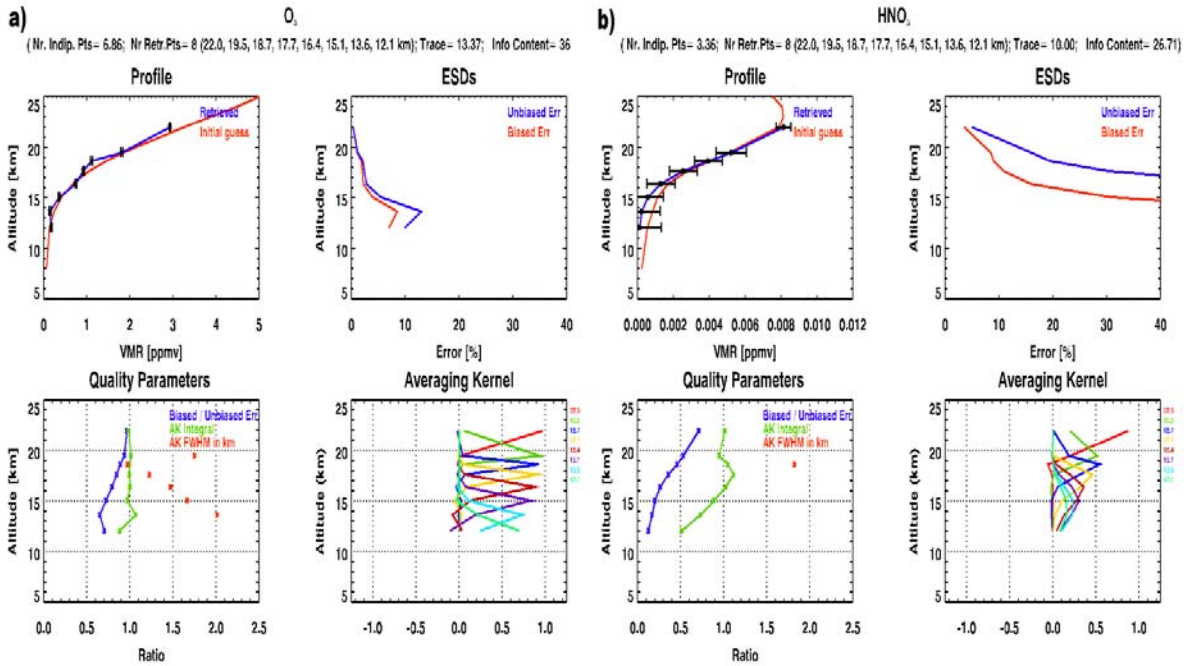

Figure 8.4: a) Ozone retrieval for sequence 15 on 24th October 2002, b) HNO_3 retrieval for sequence 15 on 24th October 2002.

For the ozone retrieval, using a vertical retrieval grid composed of 8 points, 6.87 of them are independent; the value of the biased/unbiased error has minimum value 0.6 - 0.7 at low altitudes while at high tangent altitude it is near 0.9. The value of the AK integral is one for all altitudes but for the lowermost and the averaging kernels peak at a value very close to one for the higher tangent altitudes. The vertical sampling step of the measurements (that is the distance between contiguous tangent altitudes) for the examined sequences is less than 1 km for higher altitudes and 1.5 km for the lower ones. The FWHM of the Ozone retrieved profile

is about 1.5 km for tangent altitudes near the flight level and about 2 km for the lower altitudes. This means that the ozone retrieval is not affected by strong oversampling effects. In the case of HNO_3, the averaging kernels are less well shaped; the FWHM is about 1.8 km for altitudes near the flight level and about 4 km for the lower altitudes. In this case the retrieval performs some oversampling at lower altitudes (3.36 independent points and 8 points used into the retrieval grid).
These retrieval grids were used to analyse all the SAFIRE-A sequences during the whole flight.
For validation purpose, the obtained results for ozone were compared with in situ measurement from the FOZAN instrument on board the Geophysica (no HNO_3 measurements from the Geophysica instrumentation were available for validation). MIPAS-ENVISAT measurements are located at altitudes above or near the flight level. So, in order to validate MIPAS-ENVISAT measurements, an estimate of the quality of SAFIRE-A retrieved data above the highest tangent altitude is needed. For this purpose, in situ data from FOZAN alone could not be sufficient. The selected approach was to use extended profiles obtained from a site that returns a model ozone profile at a user-specified time (every 6 hours: 0, 6, 12, 18 UT) for 158 ground station (in Italy Perugia, San Pietro Capofiume, Ispra, L'Aquila and Rome), based on the ozone fields generated by the TM3-DAM Data Assimilation Model, using GOME (Global Ozone Monitoring Experiment) total column ozone observations produced by the KNMI fast delivery processor. The two stations near Forli' (where the aircraft took off and landed, producing in situ profiles) are Perugia and San Pietro Capofiume. The ozone profiles were available for an altitude range from 0 to 60 km at 18 UT at Perugia and San Pietro Capofiume, and 24 UT only at San Pietro Capofiume.
In Figure 8.4 you can find four graphs where the result of the comparisons between ozone profiles obtained by SAFIRE-A, FOZAN and the ozone assimilated profiles at Perugia and S. Pietro Capofiume are reported. The first plot (Figure 8.5.a) shows the geographical location of SAFIRE-A sequences 1 and 20, and of Forli' (where the aircraft took off and landed), Perugia and S. Pietro Capofiume together with MIPAS-ENVISAT scan 15. As can be seen in the plot SAFIRE-A sequences 1 and 20 are close in space to both Perugia and S. Pietro Capofiume and so the two assimilated profiles can be used for the SAFIRE-A data validation. In Figure 8.5.b, the temporal collocation of SAFIRE-A sequences 1 and 20, MIPAS-ENVISAT scan 15, aircraft ascent and descent, and assimilated data at both stations can be found. SAFIRE sequence 1 is temporally near to Perugia and S. Pietro Capofiume data at 18 UT and, obviously, at FOZAN data recorded during ascent. Sequence 20 is near to S. Pietro Capofiume data at 24. Following this considerations, in Figure 8.5.c you can find a comparison of ozone profiles obtained by SAFIRE-A sequence 1, FOZAN during ascent and assimilated profiles at Perugia and S. Pietro Capofiume at 18 UT; while in Figure 8.5.d a comparison of ozone profiles obtained by SAFIRE-A sequence 20, FOZAN during descent and assimilated profiles at S. Pietro Capofiume at 24 UT. All profiles are plotted against pressure instead of altitude. The results of these comparisons is good. SAFIRE-A profiles agree very well both with the in situ profiles and with the assimilated data for the whole retrieval altitude range. SAFIRE-A profiles are in better agreement with the assimilated data because of the similar resolution (both SAFIRE-A and assimilated profiles cannot reproduce the thin structure at 90 hPa revealed by FOZAN in Figure 8.5.d).
The good results of the comparison can be used to assess the quality of SAFIRE-A retrieved profiles for ozone: the SAFIRE-A ozone profiles reproduce quite well the ozone field (from 10 to 320 hPa) for the 24th October 2002, and therefore can be used to validate MIPAS-ENVISAT data.

8.1.1.4 Comparison with MIPAS-ENVISAT Ozone and HNO_3 profiles

As reported in Table 8.1, the better coincidence between SAFIRE-A and MIPAS-ENVISAT data is between sequences 15 and 16 (for SAFIRE-A) and scan 15 for MIPAS-ENVISAT. In

Figure 8.6.a and Figure 8.6.b you can find a comparison between the geolocation and time overlap of these scans in case of the ozone retrieval. In Figure 8.6.a the position of SAFIRE-A and MIPAS-ENVISAT measurements are reported in a 3D graph respect to longitude, latitude and altitude. During the retrieval procedure, the atmosphere is considered perfectly stratified for the whole limb scanning sequence in both MIPAS-ENVISAT and SAFIRE-A codes. This means that the retrieved values of the VMR are relative not just to the horizontal geolocation of the tangent points but to the whole leg covered by the limb scanning sequence. So, the exact geolocation of the SAFIRE-A retrieved points is not crucial for the validation procedure. In any case for representation purpose, we decided to place the added point at 22 km for SAFIRE-A measurements at the same latitude and longitude of the highest tangent point of each sequence.
As can be noticed from Figure 8.6.a and 8.6.b, the agreement between the SAFIRE-A and MIPAS ozone profiles is good.

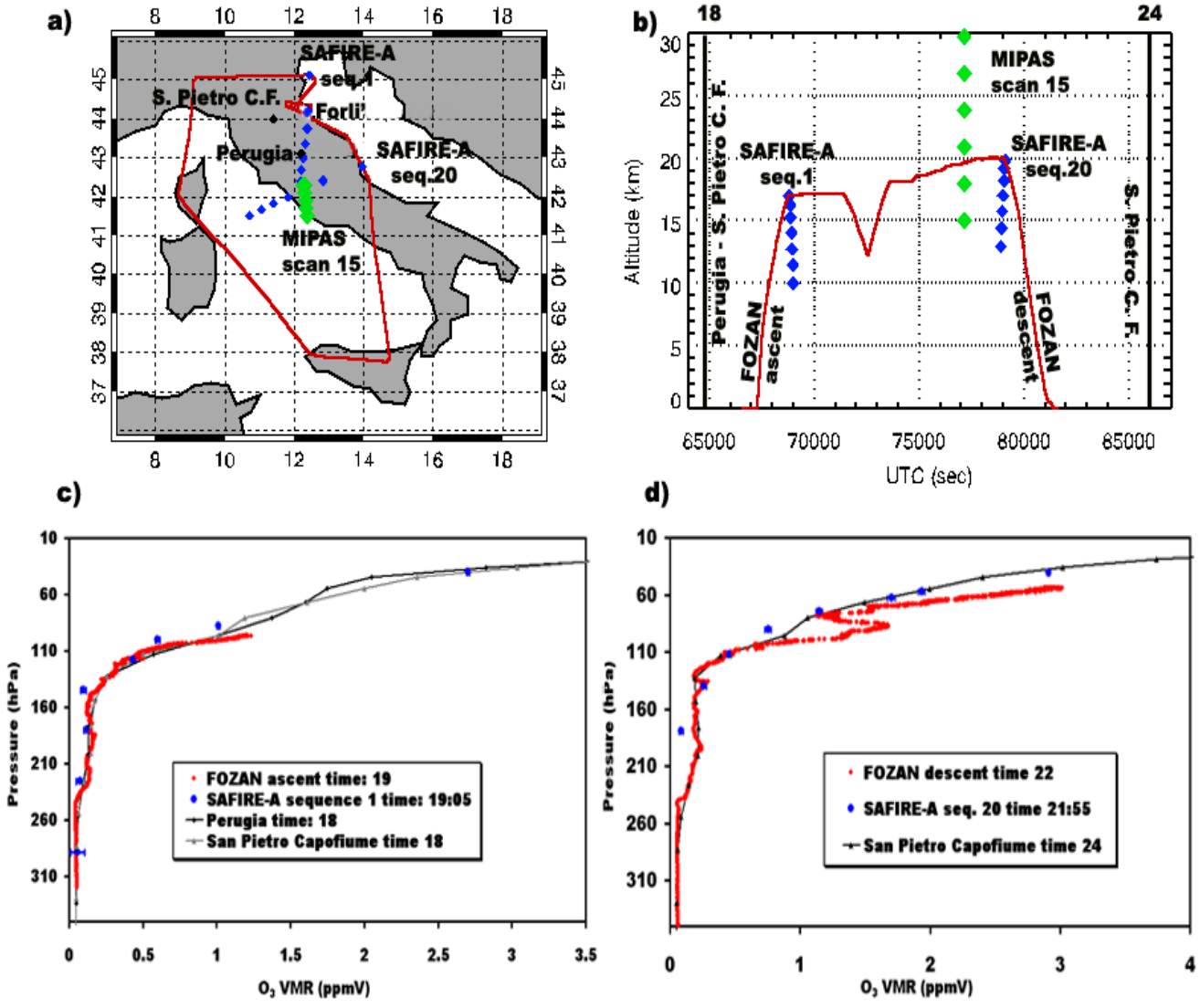

Figure 8.5: a) Location of SAFIRE-A sequences 1 and 20, Forli' (where the aircraft took off and landed), Perugia and S. Pietro Capofiume together with MIPAS-ENVISAT scan 15, b) Temporal collocation of SAFIRE sequences 1 and 20, MIPAS-ENVISAT scan 15, aircraft ascent and descent, and assimilated data at specific stations, c) Comparison of ozone profiles obtained by SAFIRE-A sequence 1, FOZAN during ascent and assimilated profiles at Perugia and S. Pietro Capofiume, d) Comparison of ozone profiles obtained by SAFIRE-A sequence 20, FOZAN during descent and assimilated profiles at S. Pietro Capofiume. All profiles are plotted against pressure instead of altitude.

In MIPAS-ENVISAT products, the value of the tangent altitude of the measurements is computed by retrieving the values of pressure and temperature at tangent points with the hydrostatic equilibrium using the geometrically calculated altitude of the lowermost tangent point as a reference. For this reason, in order to avoid differences arising from a possible altitude error, the profiles of O_3 and HNO_3 are compared in the pressure domain instead than in the altitude domain.

In Figure 8.7.a and Figure 8.7.c, a comparison between the O_3 and HNO_3 profile retrieved by MIPAS-ENVISAT and similar data obtained by SAFIRE-A for the best coincidences of scan 15 and 16 of the airborne instrument are shown, highlighting a substantially good agreement (error bars for both instruments represent just the random errors), with the largest differences corresponding, in the case of O_3, as well as for HNO_3, to MIPAS-ENVISAT lowest tangent pressure.

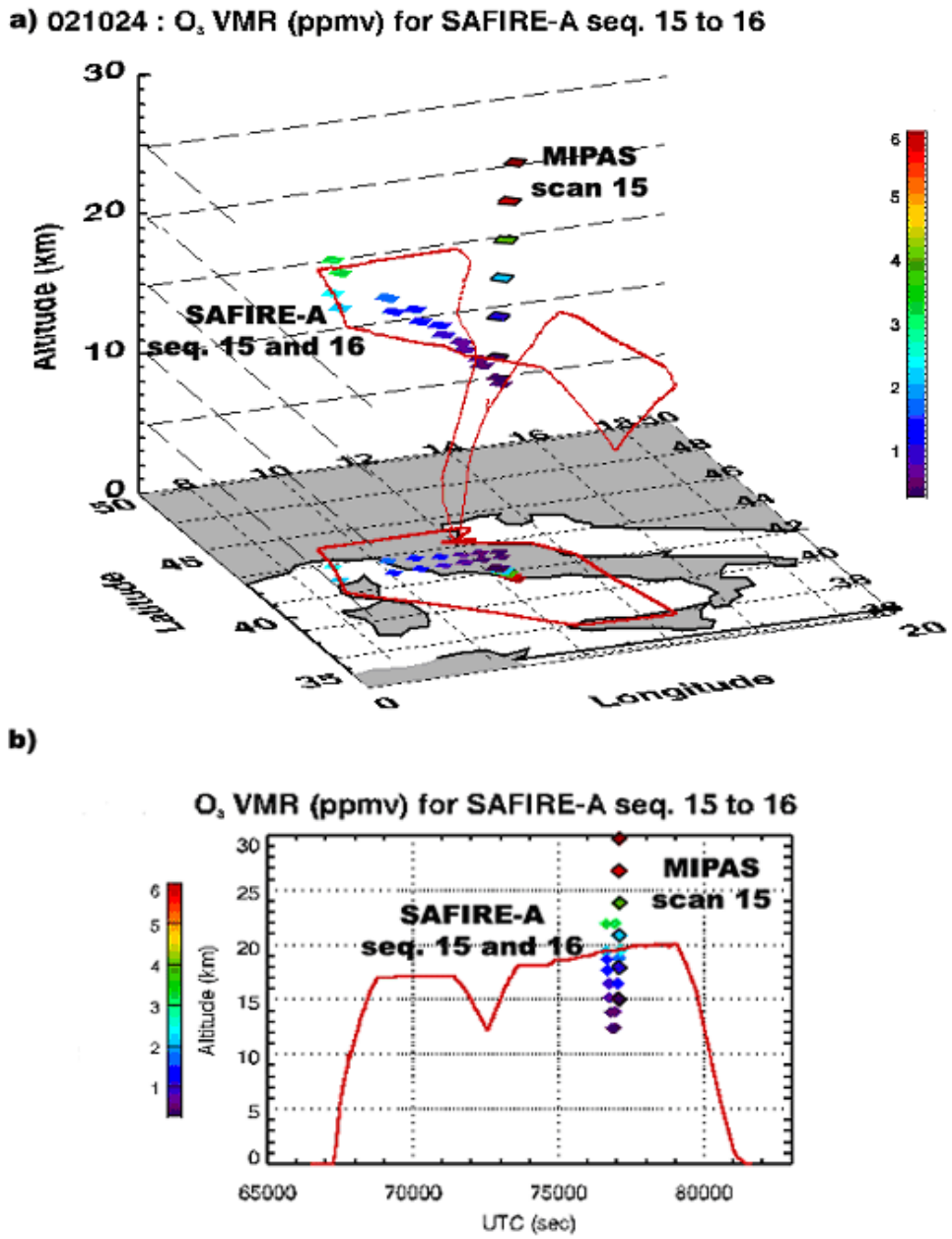

Figure 8.6: a) Location of SAFIRE-A sequences 15 and 16 and MIPAS-ENVISAT scan 15 together with ozone values, b) Temporal collocation of SAFIRE sequences 15 and 16 and MIPAS-ENVISAT scan 15 and ozone retrieved values.

In Figure 8.7.b and Figure 8.7.d, a similar intercomparison is made considering a larger number of SAFIRE-A profiles, as derived from relaxed time-matching requirements (see light yellow rows in Table 8.1). These plots provide an indication of the variability of the VMR vertical distribution measured by SAFIRE-A over a wider region that can still be considered, however, in close proximity to the location of MIPAS measurements.
In addiction, modelling tools can be used to support MIPAS-ENVISAT validation. In particular, the number of MIPAS-ENVISAT and SAFIRE-A data points useful to perform intercomparison can be extended beyond those that are simply co-located in space and time, by using a lagrangian approach. Backward and forward isentropic trajectories, starting from all the available SAFIRE-A tangent points, were calculated at the University of L'Aquila, and used for selecting those air masses sampled by both the satellite and the airborne instrument, even if at different times and locations. Trajectory calculations are based on the United Kingdom Met Office (UKMO) meteorological fields, and performed using the University of L'Aquila Global Trajectory Model (GTM) [50]. The GTM was also routinely operated during the airborne validation campaigns to fine-tune the flight pattern, using forecasts of the direction and intensity of the winds from the NCEP (National Center for Environmental Prediction) Aviation Model and therefore a number of lagrangian correspondences between SAFIRE-A and MIPAS-ENVISAT tangent points are expected to be found.

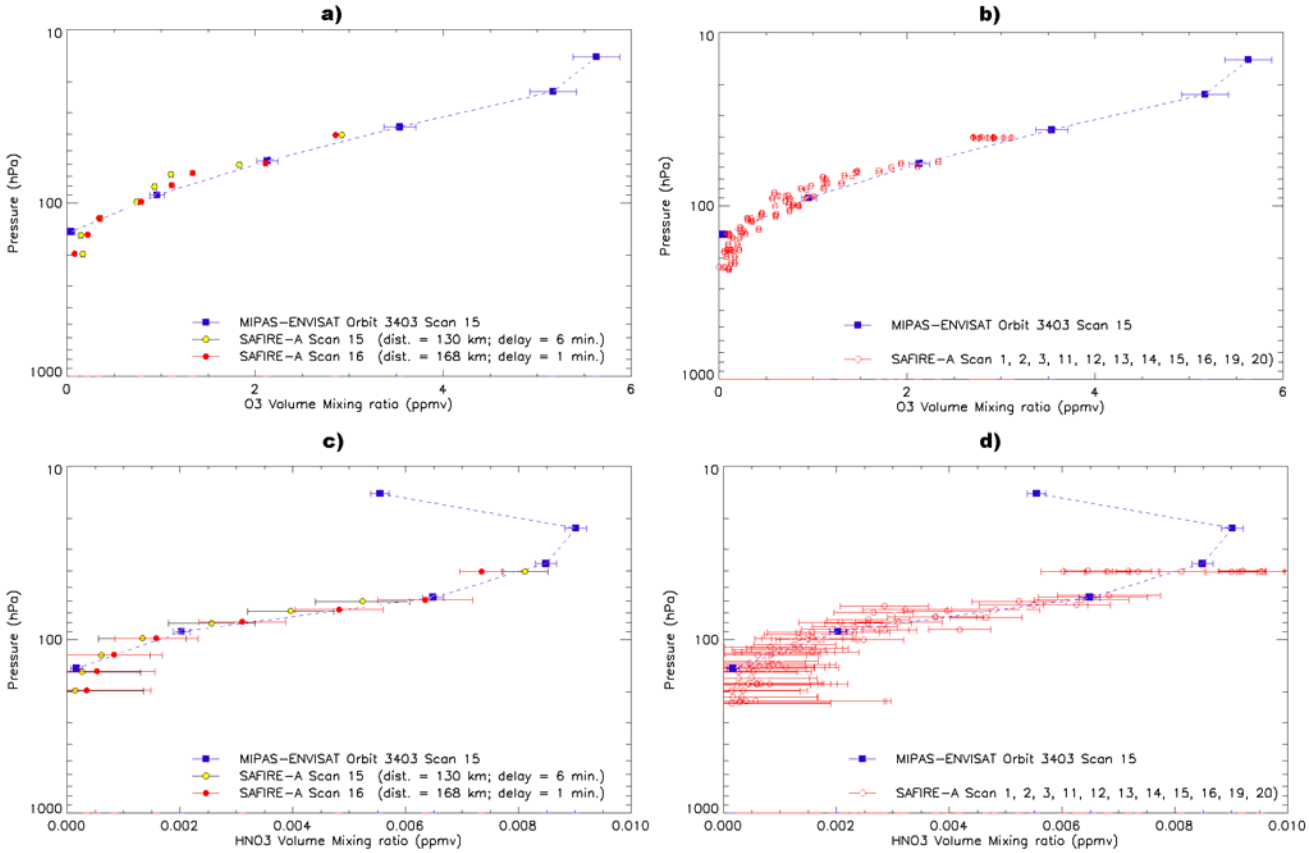

Figure 8.7: Comparison between SAFIRE-A and MIPAS O_3 and HNO_3 VMR profiles:
a) O_3 profiles comparison. Mismatch conditions: distance < 200 km, delay < 10^{min}
b) O_3 profiles comparison. Mismatch conditions: distance < 200 km, delay < 2^h30^{min}
c) HNO_3 profiles comparison. Mismatch conditions: distance < 200 km, delay < 10^{min}
d) HNO_3 profiles comparison. Mismatch conditions: distance < 200 km, delay < 2^h30^{min}.

For the shown comparison, 5 days backward and forward trajectories are launched from the location of SAFIRE-A measurements - i.e. from each of the tangent points of the 20 limb sequences acquired long the flight route - for 24th October, 2002.
Air parcels sampled at least once also from MIPAS-ENVISAT within a prescribed match criterion (Δtime $\leq$ 1h, Δlatitude $\leq$ 1°, Δlongitude $\leq$ 1°, Δaltitude $\leq$ 1km) are then selected and

their O_3 and HNO_3 contents measured from satellite compared to the correspondent SAFIRE-A values at the trajectory starting points.
In Figure 8.8.a and Figure 8.8.b, couples of O_3 and HNO_3 VMR values by MIPAS-ENVISAT (blue triangle) and SAFIRE-A (red triangle) associated to the same air parcel, as defined by the matching criteria and derived by trajectory calculations, are plotted as a function of the retrieval altitude of the SAFIRE-A measurement. In the figures are reported also the values of O_3 and HNO_3 already shown in Figure 8.7.b and Figure 8.7.d (direct coincidences indicated with circles). So, including data from both direct coincidences and trajectory matching calculation, is it possible to enlarge the number of useful matches for MIPAS-ENVISAT validation [51].

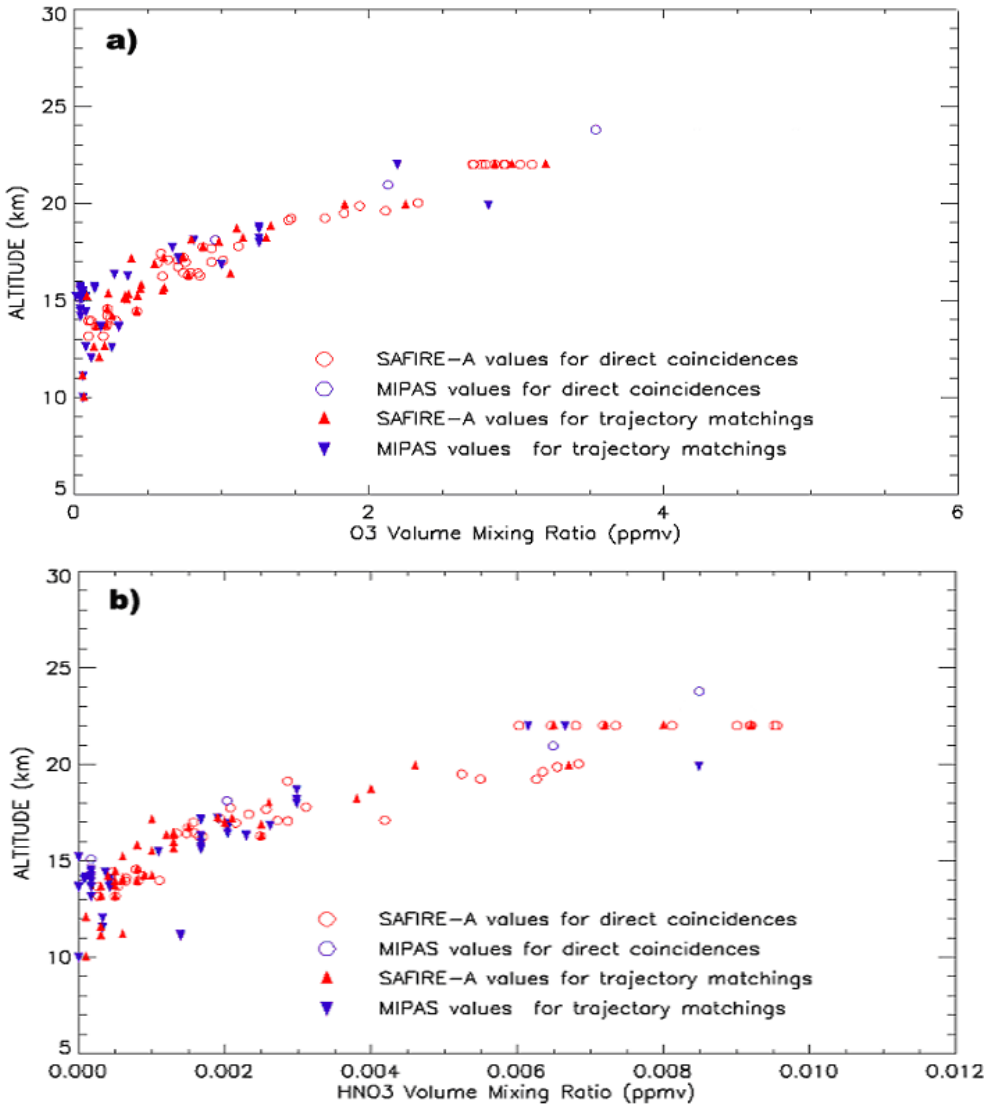

Figure 8.8: Plot of the two MIPAS-ENVISAT validation datasets derived by SAFIRE-A measurements 24th October, 2002, for (a) O_3 and (b) HNO_3.
VMR values from direct coincidences are marked with circles.
Triangles represent additional data obtained by trajectory matching.

8.1.1.5 Flight 24th October 2002: Conclusions

In case of O_3 and HNO_3 retrieval for the 24th October 2002, SAFIRE-A and MIPAS-ENVISAT profiles for the same air masses are in good agreement, therefore in case of mid-latitude atmosphere SAFIRE-A measurements validate MIPAS-ENVISAT products for these two species in the lower stratosphere. A similar result, is found when comparing O_3 and

HNO_3 mixing ratios obtained by the two instruments looking at the same air masses, as determined from backward and forward isentropic trajectories (produced by the University of L'Aquila) initialized at each of the SAFIRE-A tangent points.

8.2 ENVISAT Arctic Validation Campaign

The flights performed by the M-55 Geophysica aircraft from Kiruna in February - March 2003 aimed at the validation of level-2 products of the ENVISAT chemistry instruments in presence of strong horizontal and vertical gradients. In the following sections, I focus on the analysis of data collected during the flight performed on the 2nd March 2003, and their use for MIPAS-ENVISAT products validation at high latitude.

8.2.1 Flight 2nd March 2003: Arctic Campaign

On 2nd of March 2003, the limb sequences performed by the SAFIRE-A instrument were planned to sound the same air masses explored by MIPAS-ENVISAT scans 19, 20 and 21 of the orbit 5250.

The spatial and temporal overlapping of the aircraft and satellite profiles can be evaluated by looking at Figure 8.9, where the geolocation of MIPAS tangent points for the three scans of the selected overpass is indicated, along with the latitude and longitude of the tangent points for each of the limb sequences recorded by SAFIRE-A in the time period 19:10 – 22:13 UT. As evident from the figure, the best overlapping was obtained with the MIPAS scan at 20:35 UT (scan 20), whose tangent points in the altitude range 10-20 km correspond to the latitude and longitude region covered by SAFIRE-A observations during both the first and the second leg of the flight.

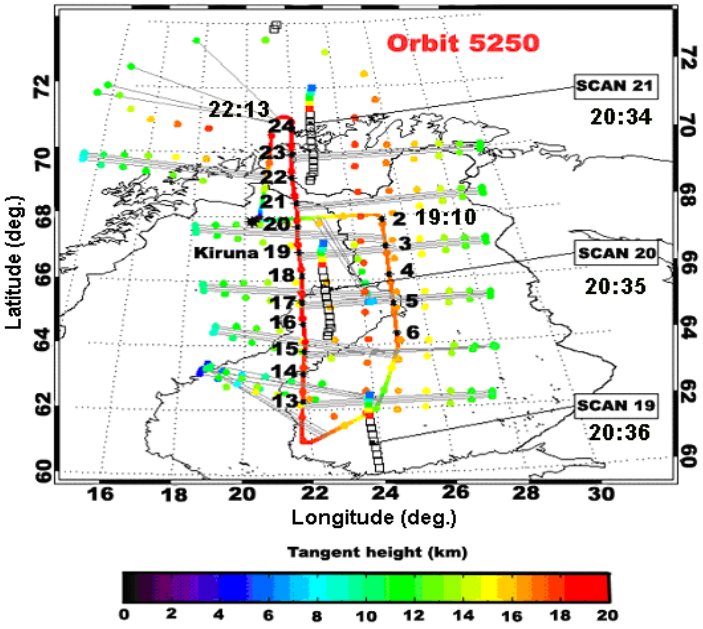

Figure 8.9: M-55 Geophysica flight track on 2nd March, 2003.

8.2.1.2 SAFIRE-A Measurements and Coincidence with MIPAS-ENVISAT scans

During the flight, the SAFIRE-A spectrometer acquired 24 limb scanning sequences. In Figure 8.10.a and Figure 8.10.b you can find the latitude-longitude position of each SAFIRE-A sequences during the first and second flight leg, while in Figure 8.10.c and Figure 8.10.d the sequences are reported respect to altitude and time. During the first part of the flight only

5 limb scanning sequences where performed, reaching a maximum altitude of 17 km. Then, after the dive, the instrument performed 12 limb sequences, from 13 to 24, with an altitude range from 19.5 to 10 km. During this flight, the selected configuration for SAFIRE-A measurements was to use the channel at 22-24 cm^{-1} and the channel at 124-126 cm^{-1}. This configuration permits the retrieval of O_3, HNO_3, N_2O, ClO, H_2O and HCl. The limb-scanning sequence for this flight was composed by 11 emission spectra with limb scanning angles: 80, 85, 87, 89, 90, 90.9, 91.35, 91.75, 92.1, 92.4, 92.7.
The analysis focused on the intercomparison with MIPAS level-2 products from scan 20 and particularly on O_3 and HNO_3, for SAFIRE-A sequences number 2, 3, 4, 19. Also for this flight, the choice of the sequences to be used in the intercomparison was made by evaluating the distance between the average location of MIPAS-ENVISAT tangent points in the range 10-25 km and the one of each SAFIRE-A scan and by calculating the time difference between the corresponding acquisition times.

8.2.1.3 Data Analysis

As for the flight described in the previous section, the data analysis was performed only for the limb sounding observations of the atmospheric emission over the frequency interval 22 - 24 cm^{-1} where spectral features of O_3, ClO, N_2O, and HNO_3 are present. All the input profiles for VMRs come from a model of high latitude atmosphere. Pressure and temperature profiles, used into the retrieval procedure, were obtained by NCEP (National Centers for Environmental predictions) data processed at University of L'Aquila. Temperature and geopotential height values at different pressure levels (from 10 to 1000 mbar) on a latitude-longitude grid (latitude step 1°, longitude step 1°) are provided every 6 hours (at 00, 06, 12 and 18 for each day). NCEP values for temperature and geopotential height were linearly interpolated in latitude and in time, in order to make use of the most suitable temperature and pressure values, on a given altitude grid, for each sequence.
The used microwindows for retrieved VMR profiles during this flight are the same used for the APE-GAIA data analysis.

8.2.1.4 SAFIRE-A Ozone and HNO_3 retrievals

Ozone retrieval was performed at all the tangent altitudes of the measurements with an added level at 20 km, in order to exploit the information contained in the measurements looking above the aircraft. In Figure 8.11.a you can find the retrieval result for sequences number 2.
As you can see, the used retrieval grid seems to be good providing 5.58 independent pieces of information over 6 retrieved points. The difference between biased and unbiased error is very small, with a ratio of 0.9 over the whole altitude range. Also the value of the integral, equal to one over the whole grid, and the values of the averaging kernels peaking at one, state that the information content for this retrieval comes mainly from measurements.
In the case of the HNO_3 retrieval, the chosen retrieval grid was composed by one point at 20 km and alternate tangent altitudes. An example of the used grid together with averaging kernel and quality parameters is reported in Figure 8.11.b for sequence number 2.
In this case, the number of total retrieved points is 4 and 2.55 are the independent pieces of information, the ratio between the biased and unbiased errors is 0.9 at higher altitudes and 0.4 at the lowermost point. The initial guess contribution to the last retrieved altitude is reflected also into the integral value (0.6 at this level and near one above). The shape of the averaging kernels is broad with FWHM above 2.5 km at each retrieved point. These grids were applied to all the 20 sequences performed by SAFIRE-A on the 2nd March.

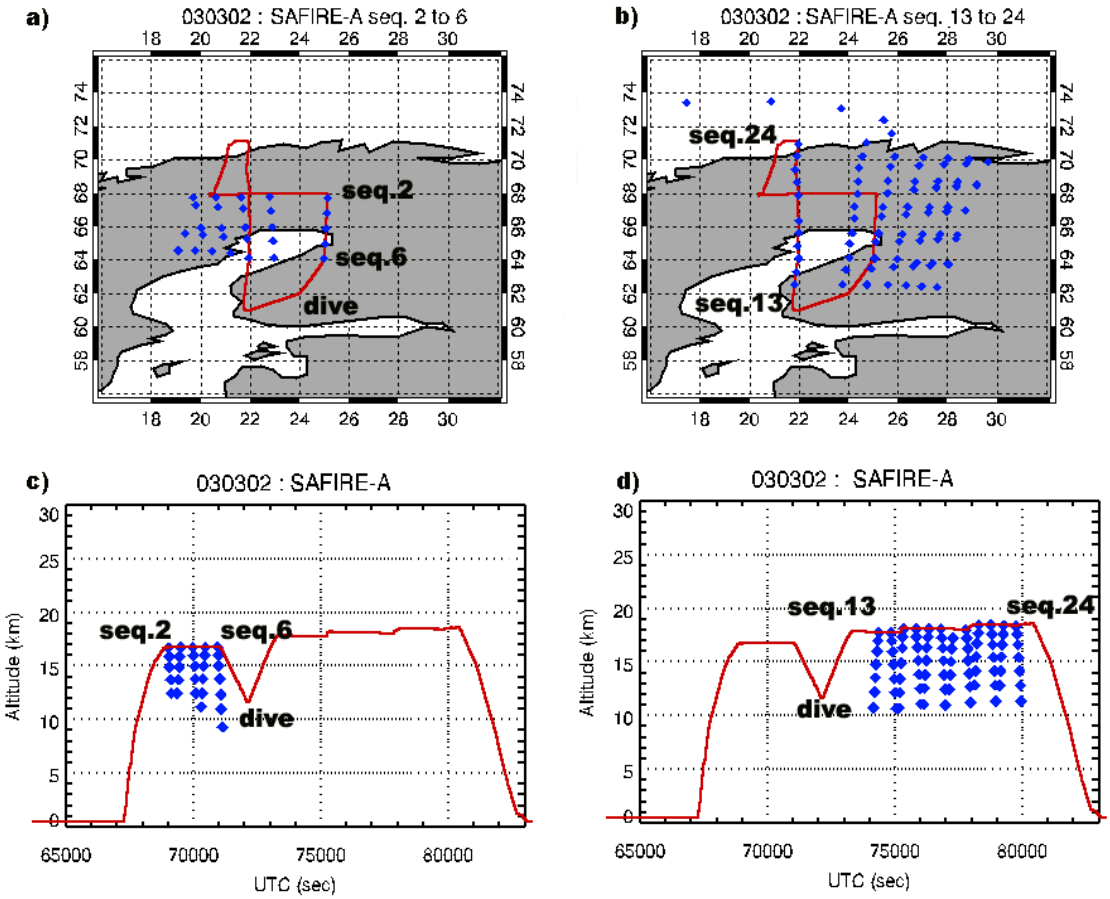

Figure 8.10: Location of SAFIRE-A tangent points and sequences in latitude-longitude domain for flight performed on 2nd March 2003 for the first (a) and second (b) part of the flight. Location of SAFIRE-A tangent points and sequences respect to altitude flight profile 2nd March 2003 for the first (c) and second (d) part of the flight.

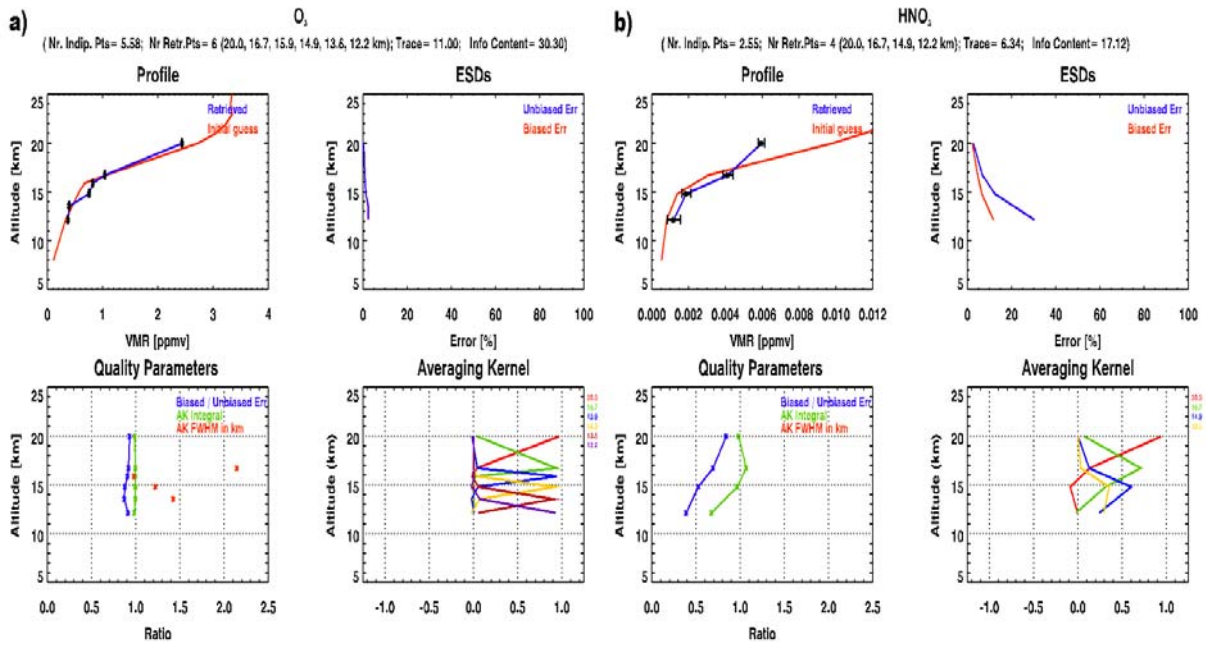

Figure 8.11: a) Ozone retrieval for sequence 2 on 2nd March 2003, b) HNO_3 retrieval for sequence 2 on 2nd March 2003.

8.2.1.5 Comparison with MIPAS-STR Ozone and HNO_3 profiles

During this flight both SAFIRE-A and MIPAS-STR achieved useful result for ozone and HNO_3 profiles. As already stated, the two sets of measurements are highly comparable, because the recorded spectra are spatially and temporally coincident. In Figure 8.12 you can find the exact location of both SAFIRE-A and MIPAS-STR measurements for this flight (red numbers and triangle symbols represent SAFIRE-A sequences, while black numbers represent the MIPAS-STR sequences). As can be noticed, MIPAS-STR measured more sequences than SAFIRE, for this reason in the table reported in the figure more than one MIPAS_STR sequence corresponding to each of the SAFIRE sequences can be found [52]. For the comparison I decided to use only one MIPAS-STR scan (the one with the lower time delay from the corresponding SAFIRE-A sequence) for each SAFIRE-A sequence

The result of this comparison for ozone is reported in Figure 8.13. From these figures it is possible to notice that MIPAS-STR retrieved ozone profiles are retrieved on a finer vertical grid with respect to the SAFIRE-A ones. The chosen vertical retrieval grid for MIPAS-STR is equally spaced with an altitude step of 0.5 km.

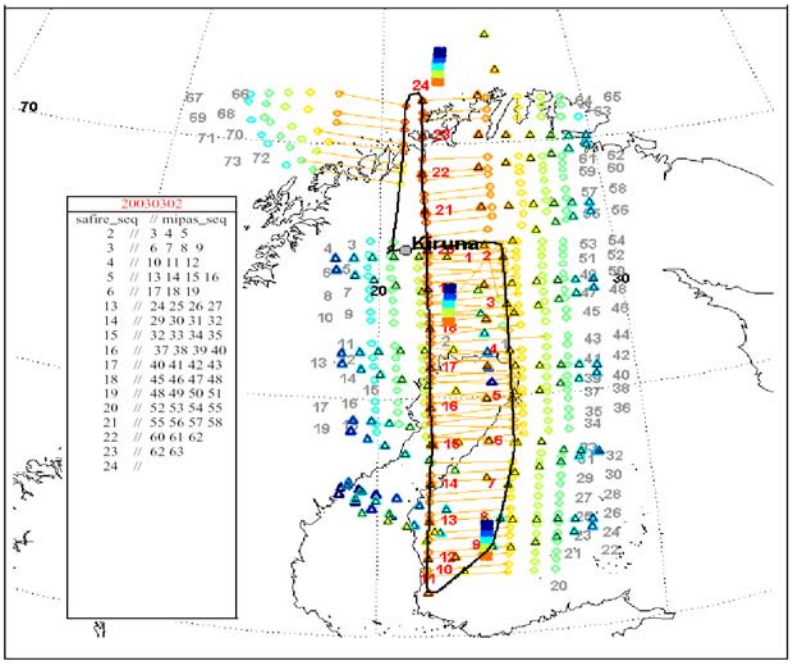

Figure 8.12:Tangent points of MIPAS-STR and SAFIRE-A measurements red numbers and triangle symbols are for SAFIRE-A sequences, black numbers for the MIPAS-STR sequences, in the table an overview of the possible coincidences between SAFIRE-A and MIPAS-STR scan is reported is reported [46].

Therefore some regualarization is necessary for each retrieved MIPAS-STR parameter because the chosen retrieval grid is much finer than the tangent altitude spacing and at lower tangent altitudes MIPAS-STR measurements are oversampling the atmosphere. The regularization strength of MIPAS-STR retrievals was adjusted just to avoid oscillations in the results [53]. For this reason the MIPAS-STR profiles appear to be very smooth, while SAFIRE-A profiles oscillates. In fact, in SAFIRE-A retrievals the chosen retrieval grid is equal to or coarser than the tangent altitude spacing and the applied regularization can be considered negligible (see also Figure 8.11.a). This approach can produce oscillations in the retrieval but doesn't reduce the degrees of freedom contained into the measurement (the information in the retrieved profiles comes mainly from the measurements). A part from the oscillations present into some sequences, SAFIRE-A ozone profiles are in a quite good agreement with the MIPAS-STR profiles.

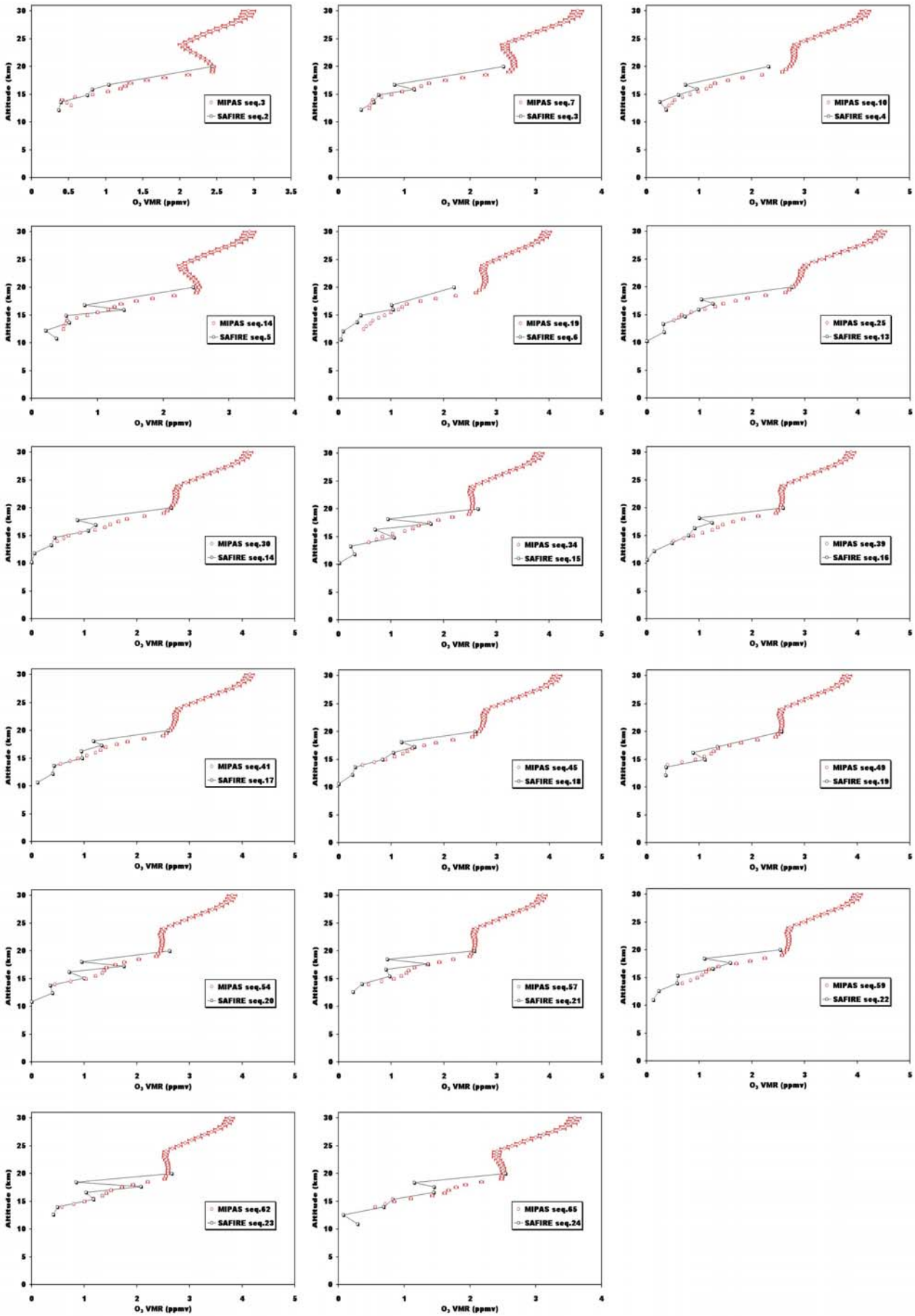

Figure 8.13:Comparison of SAFIRE-A and MIPAS-STR retrieved profiles for ozone on the 2nd March 2003.

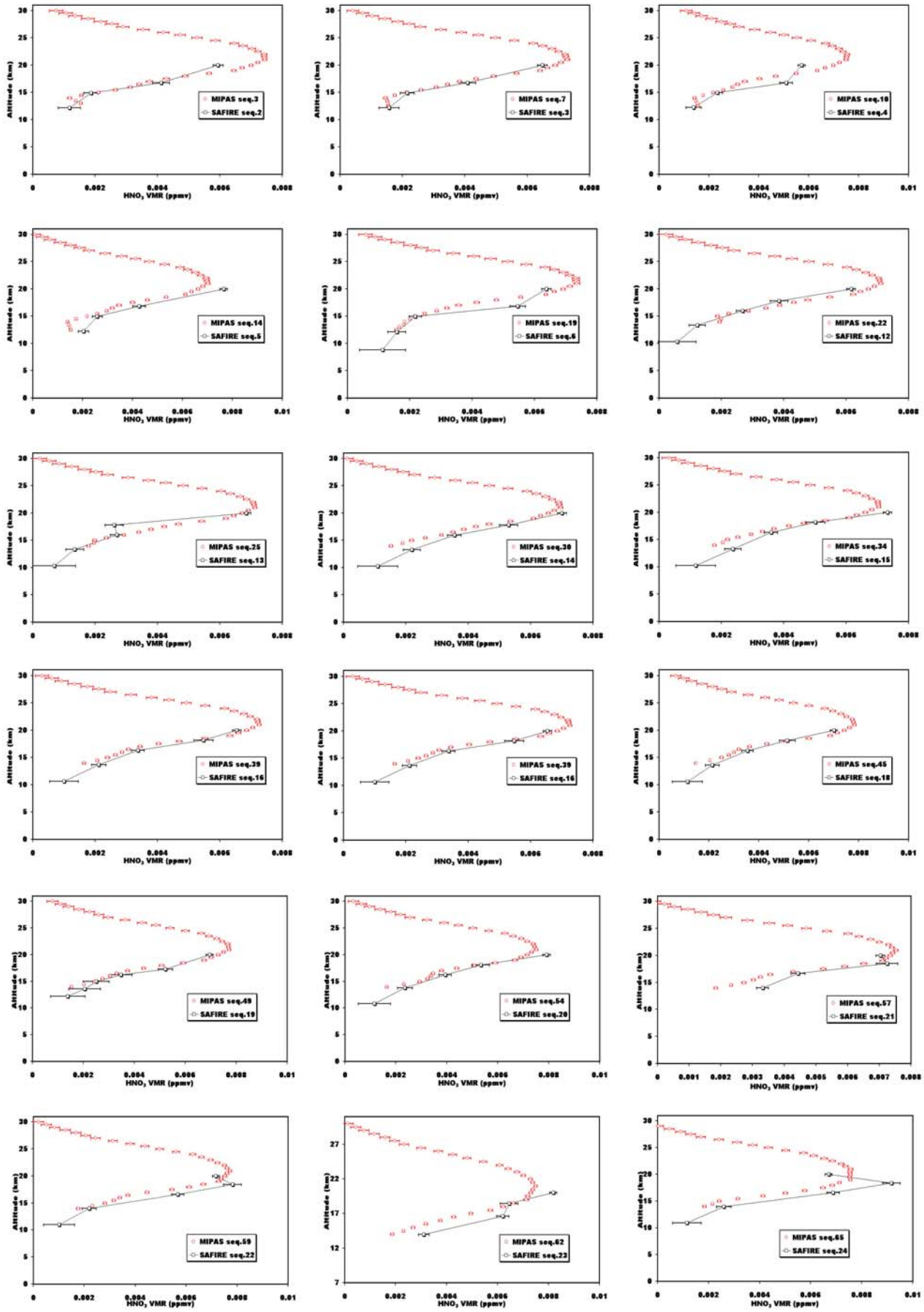

Figure 8.14: Comparison of SAFIRE-A and MIPAS-STR retrieved profiles for HNO_3 on the 2nd March 2003.

In the case of HNO_3 retrievals the agreement is very good. In Figure 8.14, you can find the results of this comparison. Even if the vertical resolutions of the corresponding profiles is very different (0.5 km for MIPAS-STR and more than 2 km for SAFIRE-A), the retrieved VMRs are very similar, with SAFIRE-A points that generally overlap the MIPAS-STR ones and with differences between the VMRs generally inside the error bars.
The possibility of comparing our results with profiles obtained from another limb sounding instrument onboard the Geophysica permits a more extensive validation of the achieved results. From this comparison it can be established that, the profiles obtained by SAFIRE-A during this flight for ozone and HNO_3 VMR, are a reliable estimate of the concentrations encountered during the exploration of the selected air masses. These profiles were used for the validation of MIPAS-ENVISAT measurements at high latitude, presented in the next section.

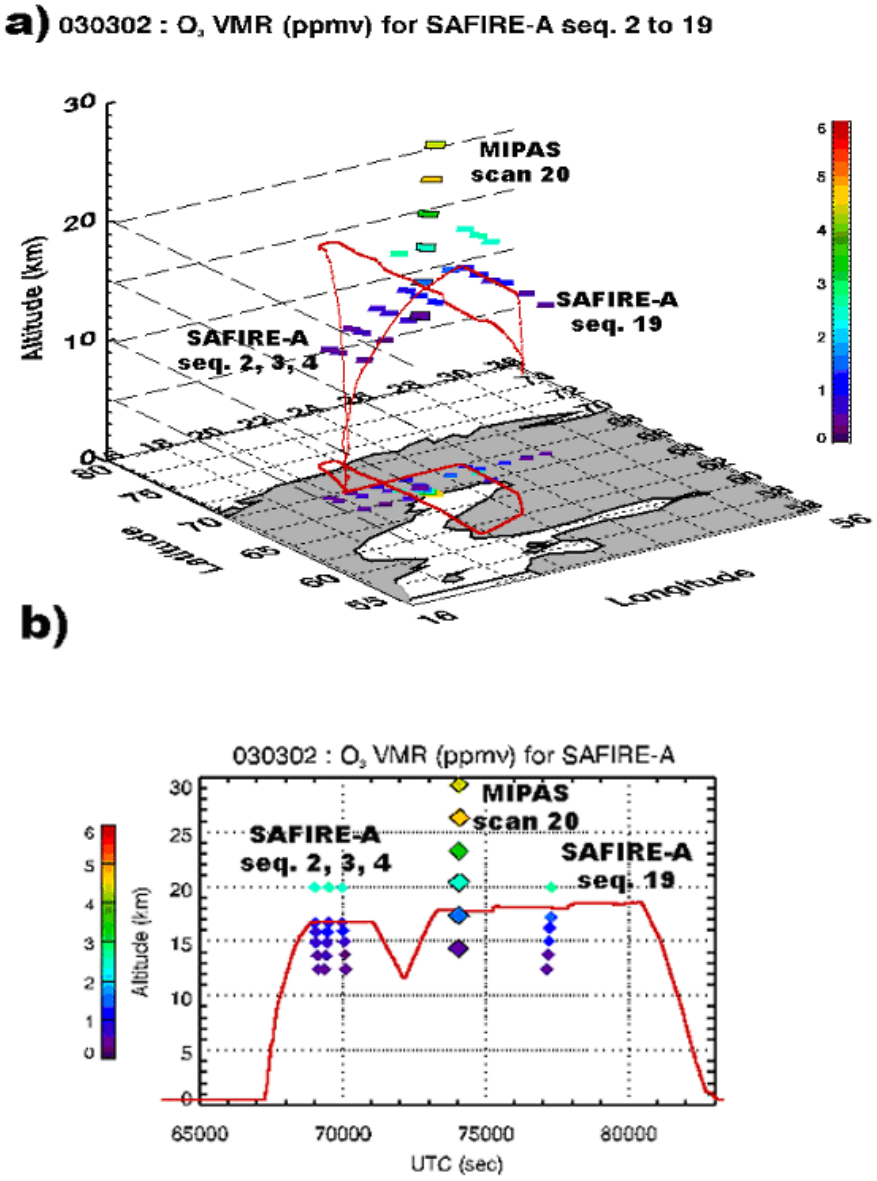

Figure 8.15: a) Location of SAFIRE-A sequences 2, 3, 4, 19 and MIPAS-ENVISAT scan 20 together with retrieved ozone values, b) Temporal collocation of SAFIRE sequences 2, 3, 4, 19 and MIPAS-ENVISAT scan 20 and ozone retrieved values.

8.2.1.6 Comparison with MIPAS-ENVISAT Ozone and HNO_3 profiles

As you can see from Figure 8.9, the better coincidence between SAFIRE-A and MIPAS-ENVISAT data is for MIPAS-ENVISAT scans 19 and 20, while scan number 21 has no direct matches with SAFIRE-a measurements. A larger number of coincidences can be found between MIPAS-ENVISAT scan 20 and SAFIRE-A scans 2, 3, 4, 19, and so, in the presented analysis, I focus on these matches more than on those of MIPAS-ENVISAT scan 19 and SAFIRE-A sequence number 13.

In Figure 8.15.a and Figure 8.15.b you can find a comparison between MIPAS-ENVISAT scan 20 and SAFIRE-A selected sequences in the case of ozone retrieval. In Figure 8.15.a the position of SAFIRE and MIPAS-ENVISAT measurements are reported in a 3D graph respect to longitude, latitude and altitude.

As can be seen in Figure 8.15.a, MIPAS-ENVISAT and SAFIRE-A data are spatially close, while they have a small time delay (see Figure 8.15.b) with a maximum time difference which is of the order of 45 minutes. Looking at these graphs a general good agreement for the retrieved ozone values is observed.

As discussed for the previous flight, in order to avoid differences arising from an altitude error, the profiles of O_3 and HNO_3 are compared in the pressure domain instead than in the altitude domain.

In Figure 8.16.a and Figure 8.16.b, a comparison between the O_3 and HNO_3 profile retrieved by MIPAS-ENVISAT and O_3 and HNO_3 VMR data obtained by SAFIRE-A for the best coincidences of scan 2, 3, 4 and 19 of the airborne instrument are shown, highlighting a quite good agreement. In case of ozone, some differences are reported around 100 hPa, while in case of HNO_3 retrievals the values are very similar at all the grid points but for the retrieved point at the altitude above the aircraft were MIPAS-ENVISAT provides an higher value.

In conclusion, in case of O_3 and HNO_3 retrieval for the 2nd March 2003, SAFIRE-A and MIPAS-ENVISAT profiles for the same air masses are in quite good agreement, even if some differences, possibly due to the variability of the polar atmosphere, are reported. Therefore, in case of polar atmosphere SAFIRE-A measurements validate MIPAS-ENVISAT products for these two species in the lower stratosphere.

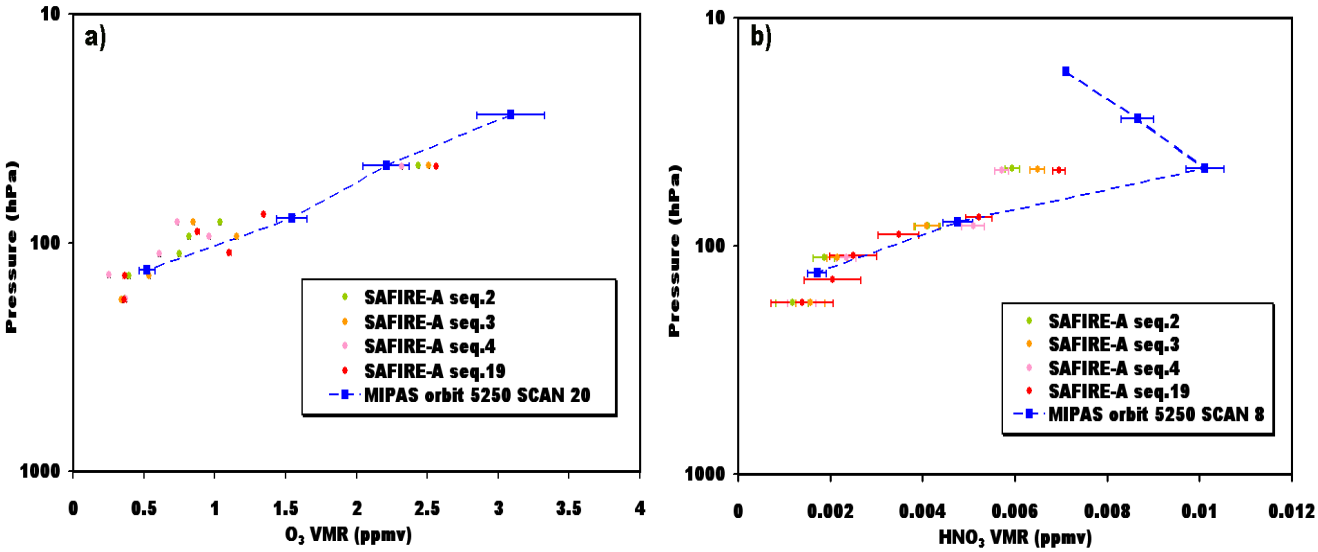

Figure 8.16: Comparison between SAFIRE-A and MIPAS O_3 and HNO_3 VMR profiles:
a) O_3 profiles comparison. SAFIRE-A sequences 2, 3, 4, 19
b) HNO_3 profiles comparison. SAFIRE-A sequences 2, 3, 4, 19.

8.3 Conclusions of ENVISAT Mid-Latitude and Arctic validation Campaigns

During both the ENVISAT mid-latitude validation campaign and the ENVISAT arctic campaign, the SAFIRE-A instrument provided results for ozone and HNO_3 profiles both in mid-latitude and in polar atmosphere. The obtained results were first checked using in situ measurements as well as assimilated and limb sounding measurements, and then used to validate MIPAS-ENVISAT products. The satellite profiles agree well with SAFIRE-A data. The agreement is better at mid latitude, while in polar regions, due to the presence of stronger gradients, the SAFIRE-A and MIPAS-ENVISAT profiles have some minor difference.

Conclusions

The main objective of this thesis was the development of an operational code to be used for the routine analysis of SAFIRE-A measurement and its exploitation for the analysis of several measurement campaigns performed by the instrument. SAFIRE-A is a Fourier Transform interferometer operating in the far infrared region, that is designed to measure the atmospheric emission using the limb-scanning technique. Starting from the recorded spectra and through the inversion procedure, the RAS (Retrieval Algorithm for SAFIRE-A) algorithm (chapter 5) is capable to retrieved the VMR profiles of minor gases in the lower stratosphere with spectral features into the far infrared.

The first part of this work was dedicated to the validation of the retrieval code. The validation procedure was composed of two parts. In the first part, tests were performed to prove the reliability of the retrieval procedure. To do so, the retrieval of VMRs profiles was operated analysing simulated spectra. These spectra were produced with the self standing forward model, named FAS (Forward Algorithm for SAFIRE-A). Starting from mid-latitude VMRs, temperature profiles, instrumental parameters and noise, all the spectra composing a limb scanning sequence were produced (simulated observations). In the retrieval algorithm, the simulated observations were analysed using, as initial guess for the target species, the profiles employed in the simulations perturbed by a quantity. If the retrieval procedure is correct, the difference between the retrieved profiles and the profiles used in the simulations (named reference profiles) has to be near 0 and inside the error bar. These tests have been performed for all the target quantities of SAFIRE-A instrument and the performance and the robustness of RAS code has been assessed.

The second part of the validation was performed through a comparison between the spectra simulated by SAFIRE-A forward model (FAS) and the MARSCHALS (Millimetre-wave Airborne Receivers for Spectroscopic CHaracterisation in Atmospheric Limb Sounding) Forward Model (MFM). In order to perform this comparison, it was necessary to apply some modification to the FAS code, because of the different spectral interval in which the two instruments operate. The first update was the use of a new partition functions for the cross section calculation, while the second was the implementation into the code of a new expression for the refraction index calculation. The refraction index update required the development of a simplified version of the expression used for the microwave region.

The comparison of the spectra obtained with the two models shows a good agreement. This results prove the reliability of the updates applied to the FAS code and validate both SAFIRE-A and MARSCHALS forward model (chapter 6).

After the forward model validation, new analysis features were implemented in the code.

The first new code feature was the possibility of retrieving the values of the pointing angles. I developed the part of the code necessary for this retrieval, then, after defining a new microwindow where an O_2 line is present for this calculation, I performed some tests on simulated data. These tests were carried out perturbing the value of one or more angles, and retrieving the pointing angles on their own or together with the instrumental offset. The obtained results were good and did validate the new part of the code. Finally this new feature was applied to real data (chapter 6) and also in this case the code seem to provide reliable results.

The second code feature that I developed, was the introduction in RAS of the calculation of the Averaging Kernel Matrix (AKM) of the retrieval together with the quality parameters. The Averaging Kernel Matrix and all the connected parameters were calculated according to the equations provided in chapter 4. In the thesis (chapter 6), two examples of the application of the AK to the retrieval results are reported. In the first example the AK are used to find the regularization parameter that represent the best compromise between the minimization of the spectral residuals and a smooth retrieved profile. In Tikhonov regularization, the regularization parameter value is commonly obtained through a method called of the L-curve.

For the reported case, the value that I found through the AK and quality parameters analysis and with the L-curve method was the same. The second example of AK application was the tuning of the vertical retrieval grid, and, more exactly the tuning of the number of the points added above the highest tangent altitude. The obtained results were, then, used for the data analysis.

The second part of the thesis consists on the SAFIRE-A data analysis for different campaigns.

The first analysed campaign was the APE-GAIA(Airborne Polar Experiment-Geophysica Aircraft in Antarctica) Campaign, held in Ushuaia (Terra del Fuoco, Argentina) in September-October 1999, and aiming at the analysis of the polar vortex stratosphere and of the ozone hole (chapter 7). The analysed spectra were recorded during two flights, the first performed inside the polar vortex during the ozone hole event, and the second performed outside the polar vortex and planned in order to explore a filament of the polar vortex air. For both the flights, the microwindows to be used for the retrieval of O_3, HNO_3, N_2O, ClO, HCl, and H_2O and retrieve the corresponding profiles for the measured limb scanning sequences have been retrieved. In order to validate the obtained profiles, the results were compared with in situ measurements performed by the Geophysica instrumentation. The good result of this comparison provided an indication of the reliability of the SAFIRE-A products. So SAFIRE-A retrieved profiles are a good estimate of the "true" state of the atmosphere and can be used to give an interpretation of the observed atmospheric scenario. For the first flight, SAFIRE-A profiles show evidence of the perturbed chemistry into the polar vortex region: the ozone depletion is reported along with enhanced ClO concentration in the inner most part of the vortex. The polar stratosphere appears to be a little dehydrated and denitrified, possibly as a consequence of sedimentation of PSCs (Polar Stratospheric Clouds) that took place previously to the flight. For the second flight SAFIRE-A measurements evidences both the position and the vertical extension of the filament of the polar vortex air (from 18 to 14 km). In this region the values of the ozone and HNO_3 were higher than outside, according to the fact that the air of the filament has higher PV value (air coming from higher altitudes). Into the filament air, no ozone depletion was observed in accordance with in situ measurements results.

The second analysed campaign was the ENVISAT (ENVIronmental SATellite) Validation Campaign, held in Forli' (Italy) and in Kiruna (Sweden) in 2002-2003, aiming at the validation of the ENVISAT satellite products (chapter 8). The validation procedure, in case of SAFIRE-A, focused especially on MIPAS (Michelson Interferometer for Passive Atmospheric Sounding)-ENVISAT products, more precisely on O_3 and HNO_3. The SAFIRE-A data for the mid-latitude campaign were used to retrieve the values of O_3 and HNO_3 VMRs. In this case a validation procedure of the retrieved profiles was carried out using both in situ measurements onboard the Geophysica and GOME (Global Ozone Monitoring Experiment) assimilated data at specified station. The comparison with MIPAS-ENVISAT products was carried out using both direct coincidences (finding SAFIRE-A measurements with minimum temporal and spatial distance from MIPAS data), and using trajectory calculations. In both cases the overall agreement was good. This provided a validation for MIPAS-ENVISAT data in case of mid-latitude atmosphere. In the case of the arctic validation campaign, the values of O_3 and HNO_3 VMRs were retrieved for the whole flight. This time, the SAFIRE-A retrieval validation was performed using profiles obtained by MIPAS/STR (Michelson Interferometer for Passive Atmospheric Sounding/STRatospheric aircraft) onboard the Geophysica. Even if some small differences, arising from a different regularization approach, can be found in the case of the ozone profiles, the two data sets were in good agreement. The SAFIRE-A data could, then be used for the comparison with MIPAS-ENVISAT products. The result of this comparison, using direct coincidences, for HNO_3 and O_3 provided quite good results with minor differences due to the presence of stronger gradients in the polar regions.

APPENDIX A: Some Basics of the Fourier Transform Spectrometry

Interferometry for chemical applications was first applied to the far infrared region. The main factors that influenced this choice were the relatively low energies emitted by the IR sources, relative simple optical requirements, and simplified mathematical requirements due to the fact that relatively few data points were required to perform the Fourier transformation. The purpose of this section is to highlight the theory behind the Fourier Transform Infrared (FT-IR) spectrometers.

A.1 The Michelson Interferometer

An FT-IR spectrometer is typically based on a Michelson Interferometer; an example is shown in Figure A.1. Michelson designed this device and together with Morley used it to disprove the existence of the ether, the hypothetical medium through which light waves were thought to propagate.

Michelson interferometer consists of a beam splitter, a fixed mirror, and a mirror that translates back and forth, very precisely. The beam splitter is made of a special material that transmits half of the radiation striking it and reflects the other half maintaining his phase. Radiation from the source strikes the beam splitter and separates into two beams. One beam is transmitted through the beam splitter to the fixed mirror and the second is reflected off the beam splitter to the moving mirror. The fixed and moving mirrors reflect the radiation back to the beamsplitter. Again, half of this reflected radiation is transmitted and half is reflected at the beam splitter, resulting in one beam passing to the detector and the second back to the source.

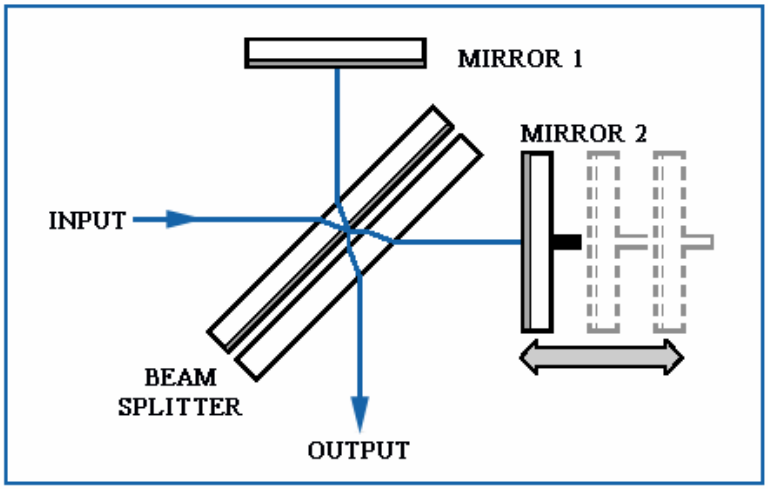

Figure A.1: Schematic of a generic Michelson interferometer.

Because of the effect of interference, the intensity of each beam reaching the detector and returning to the source depends on the path difference in the two arms of the interferometer. Both output beams contain equivalent information though the beam that returns to the source is rarely of some interest for spectrometry; it is usually difficult to distinguish it from the input beam unless for example it is directed toward a detector which may be the one already present in Figure A.1 (OUTPUT) or an additional one.

Let's suppose that the source is a perfect laser, i.e. a source of monochromatic (λ) and coherent light. The initial beam is split into two components by the beamsplitter, reflected by the mirrors; these two beams are combined back and are superimposed when they reach the detector and their energies add up. The result of the "summing" of the two waves (*interference*), depends on the energy of each wave but also on their relative phase: if two waves are in phase (their maxima coincide), then the resulting wave has a maximum

amplitude (*constructive interference*); all the light from the source reaches the detector and none returns back to the source. If the phases of the two waves differ by 180° (a maximum of one wave coincides with the minimum of the other wave), they cancel out and the result on the detector is null (*destructive interference*); all the light returns to the source and none reaches the detector. Any other combination will result in a wave that has an amplitude between 0 (no signal recorded) and the maximum [54]. As the moving mirror changes positions, it causes the waves that compose the infrared radiation to undergo constructive and destructive interference when they recombine at the beamsplitter, producing an interferogram (plot of the detector response, intensity in volts vs. the position of the moving mirror or retardation in cm, see Figure A.2). One scan taken with an FT-IR spectrometer is equivalent to a complete displacement of the moving mirror from the initial position to the final one. This change of position is referred to as the Optical Path Difference (OPD) or retardation because it sets the difference between the paths travelled by the two beams of light before recombination at the beam splitter location.

A.2 Monochromatic and Polychromatic Source

If we consider an idealized situation when a source of monochromatic radiation whose wavelength is indicated as λ, produces an infinitely narrow, perfectly collimated beam, the resulting interference pattern recorded at the detector is described by:

$$I'(\delta) = \frac{1}{2} I_{source}(\sigma)\{1 + \cos(2\pi\sigma\delta)\} \tag{A.1}$$

where σ is the reciprocal of λ (σ is the wavenumber) and $I_{source}(\sigma)$ is the intensity of the source (a delta-function centered on σ) and δ is the path difference (or retardation). Since the first term on the right side of eq.(A.2) is constant, the modulated component is usually referred to as the interferogram ($I(\delta)$) and it is described as an infinitely long cosine wave defined by the equation:

$$I\ (\delta) = \frac{1}{2} I_{source}(\sigma)\cos(2\pi\sigma\delta) \tag{A.2}$$

So eq.(A.2) is the interferogram of a monochromatic source when an ideal interferometer is considered. In reality the signal must be corrected to account for the beamsplitter actual efficiency (reflectance and transmittance cannot value exactly 50%), the detectors response which is not uniform for all the wavenumbers and the amplifiers response which is strongly wavenumber-dependent (the detected signal is amplified and filtered according to the spectral range of interest). All these factors are represented by a unique correction factor $H(\sigma)$:

$$I\ (\delta) = \frac{1}{2} H(\sigma) I_{source}(\sigma)\cos(2\pi\sigma\delta) = B(\sigma)\cos(2\pi\sigma\delta) \tag{A.3}$$

Where $B(\sigma)$ is the intensity of the source as modified by the instrumental characteristics.
When the source emits radiation of more than one wavenumber, the measured interferogram is the superimposition of the interferograms corresponding to each wavenumber. In the case of a continuum source, the interferogram can be expressed by:

$$I\ (\delta) = \int_{-\infty}^{+\infty} B(\sigma)\cos(2\pi\sigma\delta)d\sigma = FT[B(\sigma)] \tag{A.4}$$

A.3 The Interferogram

As we have already seen, interferogram is the name of the signal acquired by an FT-IR spectrometer. It is usually significantly more complex than a single sinusoid, which would be expected if radiation made of only a single wavelength was present. Figure A.2.a shows the beam path of a two wavelengths source; Figure A.2.b is the interferogram of a broadband light source, the X-axis of the interferogram representing the optical path difference. Note that at zero retardation, $\delta = 0$, all the waves are in phase, therefore, their contributions are all at maximum and a very strong signal is produced by the system's detector, this maximum is called the centerburst or the Zero Path Difference (ZPD) of the interferogram.

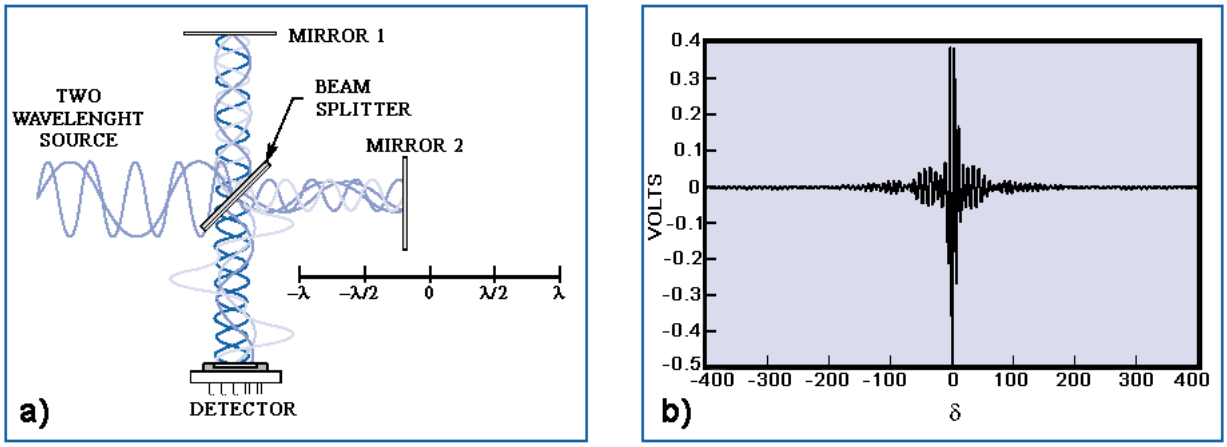

Figure A.2: a) Two wavelength source case. b) Broadband source interferogram.

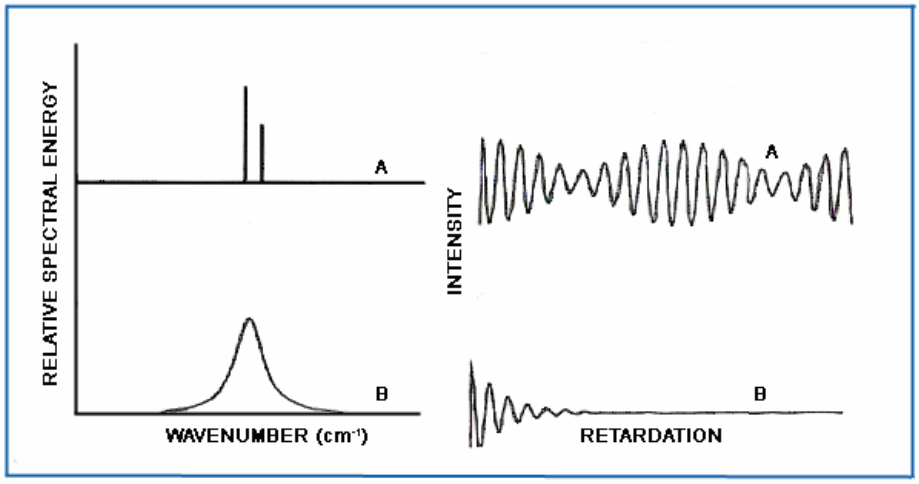

Figure A.3: Examples of simple spectra (left) and their interferograms (right). *Retardation* is the path difference δ. A:two infinitesimally narrow lines of different intensity; B:Lorentzian line centered at the mean wavenumber of the lines of the previous cases.

Moving away from the ZPD in either direction, causes the intensity of the interferogram, $I(\delta)$, to die off as contributions from the various frequencies go in and out of phase with each other. In fact, as the optical path difference, OPD, grows, different wavelengths reach their maxima at different positions and, in the case of a broadband signal, they never again reach their maxima simultaneously. Thus, moving away from the centerburst, the interferogram becomes a complex looking oscillatory signal with decreasing amplitude.

A.4 The Fourier Transform Algorithm

Once an interferogram is collected, it needs to be translated into a spectrum. As can be deduced from equation (A.4). The interferogram is the Fourier transform of the spectrum. So,

to obtain the spectrum from an interferogram, we need to perform the Fourier transform of the signal collected by the instrument as a function of the OPD. The Fourier Transform of the signal is a very time consuming computation. The algorithm usually used to perform this operation is called Fast Fourier Transform. The discovery of this method by J.W. Cooley and J.W. Tukey in 1965, followed by an explosive growth of computational power at affordable prices, has been the driving force behind the market penetration of FT-IR instruments.
The relationship between the interferogram and the spectrum is given by equation (A.5). This equation is the Fourier Transform pair of equation (A.4).
The source radiation can be expressed by the complementary Fourier integral, therefore, the Fourier Transform operation changes the domain of the original data into its reciprocal; in this way the space domain data (interferogram) is turned into a reciprocal space domain data (the spectrum):

$$B\ (\sigma) = \int_{-\infty}^{+\infty} I(\delta)\cos(2\pi\sigma\delta)d\delta = FT\left[I(\delta)\right] \qquad \text{(A.5)}$$

In theory, the spectrum can be measured from –∞ to ∞ at infinitely high resolution (eq.(A.4)); however this implies that the mirror has to be moved to infinitely long distances with δ varying from –∞ to ∞ (eq.(A.5)). In practice the interferogram can only be measured over a restricted range of δ values and this causes the spectrum to have a finite resolution; thus the spectral resolution depends on the maximum path difference (*L*): the longer the path, the finer the resolution (it is proportional to 1/L). In fact, for the Michelson interferometer, the interference appears as a cosinusoidal variations of intensity when expressed as a function of the path difference δ or the time difference $\tau = \delta/c$ for the two arms. From the coherence theory, if we consider as a source a spectral line with bandwidth Δν, the time difference for which fringes may be observed is related to the bandwidth of the line:

$$\Delta\nu\ \Delta\tau \sim 1 \qquad \text{(A.7)}$$

Where Δ τ is called coherence time of the radiation; a coherence length can also be defined as:

$$\delta = c\ \Delta\tau \qquad \text{(A.8)}$$

And this can be related to the bandwidth of the radiation, expressed as a wavenumber, by

$$\delta\ \Delta\sigma \sim 1 \qquad \text{(A.9)}$$

These results are said to show the temporal coherence of the radiation, which increases as the bandwidth is decreased [55]. From formula (A.9), we can obtain the relation between resolution and path difference. In order to obtain a very fine spectral resolution (Δσ) we have to increase the optical path difference reaching the higher resolution at the maximum path difference δ=L.
Limiting the δ values in the finite interval between –L and L can be thought of as the product of the interferogram with a boxcar truncation function *D(δ)* which is also called *modulation function*:

$$D(\delta) = \begin{cases} 1 & \delta \in [-L : L] \\ 0 & \delta > |L| \end{cases}$$

The corresponding spectrum becomes:

$$B\ (\sigma) = \int_{-\infty}^{+\infty} [I(\delta) * D(\delta)] \cos(2\pi\sigma\delta) d\delta = FT\left[I(\delta) * D(\delta)\right] \tag{A.10}$$

By applying one of the properties of the Fourier Transforms, eq.(A.10) can be expressed as follows:

$$B\ (\sigma) = FT\left[I(\delta) * D(\delta)\right] = FT\left[I(\delta)\right] \otimes FT\left[D(\delta)\right] \tag{A.11}$$

where $\otimes$ is the convolution product; the term $FT[I(\delta)]$ is the spectrum for an infinite path difference (eq.(A.5)) while the term $FT[D(\delta)]$, called Instrument Line Shape (ILS), corresponds to a *sinc(sinx/x)* function (Figure A.4):

$$FT\left[D(\delta)\right] = f(\sigma) = 2L * SINC(2\pi\sigma L) \tag{A.12}$$

A number of steps are involved in calculating the spectrum. Instrumental imperfections and basic scan limitations need to be accommodated by performing phase correction, that corrects for erroneous readings due to different time or phase delays of various spectral components and apodization. Apodization is used to correct the spectra for spectral leakage and for artificial creation of spectral features due to the truncation of the scan at its limits (a Fourier transform of sudden transition will have a very broad spectral content).

A.5 Apodization

Eq.(A.10) is the spectrum in the general case of a polychromatic source which accounts for the finite (realistic) values of the path differences. If the source is monochromatic (see section A.2), the term $FT[I(\delta)]$ corresponds to a delta function centered on the radiation wavenumber σ_0; hence the corresponding spectrum $B(\sigma_0)$ from eq.(A.11) coincides with the ILS (term $FT[D(\delta)]$) at the input wavenumber σ_0:

$$B(\sigma_0) = 2L * SINC(2\pi\sigma_0 L) \tag{A.13}$$

Eq.(A.13) tells that the finite dimensions of the instrument approximate the monochromatic beam to a *sinc* function: the ideal infinitesimally narrow line is "transformed" into a finite-width lineshape where sidelobes (called *feet*) are present (Figure A.4); these feet may appear as false sources of energy at nearby frequencies so it is desirable to reduce them. The process of removing these *feet* is called *apodization*: it consists of multiplying the interferogram by a Correction Function (CF) called the *apodizing function*; eq.(A.11) then becomes:

$$B\ (\sigma_0) = FT\left[I(\delta) * CF * D(\delta)\right] = FT\left[I(\delta)\right] \otimes FT\left[CF * D(\delta)\right] = FT\left[CF * D(\delta)\right]_{\sigma_0} \tag{A.14}$$

As an example, let's suppose that CF is a triangular function:

$$CF = 1 - \frac{|\delta|}{L} \tag{A.15}$$

Then eq.(A.11) returns:

$$B(\sigma_0) = L * SINC^2(2\pi\sigma_0 L) \tag{A.16}$$

Figure A.4 compares the *sinc* and $sinc^2$ functions, i.e. the unapodized and apodized solutions in the case of a monochromatic source: CF allows to reduce both the amplitude and the number of the sidelobes. The price to pay is the worse resolution of the measure caused by the broadening of the lineashape; this broadening effect introduces a correlation between any given spectral point and its nearest ones: for an unapodized spectrum sampled at the resolution intervals all spectral points are independent measurements with no statistical correlation, whereas when the spectrum is convoluted with the apodization function, a correlation between different spectral points is introduced.

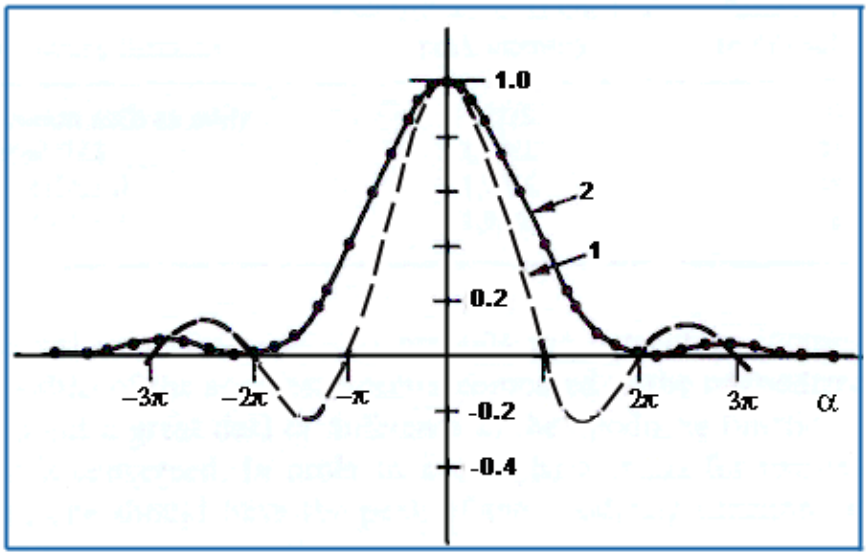

Figure A.4:Plot (1) shows $sinc(\alpha)$ versus α and plot (2) $sinc^2(\alpha)$ versus α [65].

A.6 Advantages of FT-IR instruments

In this section we present three significant advantages that FT-IR instruments hold over dispersive spectrometers.

A.6.1 Multiplex (Fellgett) Advantage

The Multiplex advantage was first discussed by Fellgett in 1951 in his doctoral thesis [56]: using a single detector, in an interferometer the whole spectral band is observed for the whole duration of the experiment, whereas in a grating (or any dispersive) spectrometer the spectral elements are observed sequentially for short periods which add up to give the total time of the experiment. Thus, the interferometer receives information about the entire spectral range during the entire scan, while the grating instrument receives information only in a narrow band at a given time. Fellgett gave the name *multiplex spectrometry* to the spectroscopic techniques in which all the spectral elements are simultaneously observed. The signal-to-noise obtained in the recovered spectrum is a factor of primary importance which determines the quality of the spectroscopic measurement. When spectra are collected under identical conditions (spectra collected in the same measurement time, at the same resolution, and with the same source, detector, optical throughput, and optical efficiency) on dispersive and FT-IR spectrometers, the signal-to-noise ratio of the FT-IR spectrum will be greater than that of the dispersive IR spectrum by a factor of $\sqrt{M}$, where $\sqrt{M}$ is the number of resolution elements. This means that a 2 cm^{-1} resolution 800 – 8000 cm^{-1} spectrum measured in 30 minutes on a dispersive spectrometer would be collected at equal S/N on an FT-IR spectrometer in 1 second, provided all other parameters are equal. The multiplex advantage is also shared by array of detectors (PDAs and CCDs) attached to spectrographs. However, the optimum

spectral range for these kinds of systems tend to be much smaller than FT-Irs and therefore the two techniques are mostly complementary to each other.

A.6.2 Throughput (Jacquinot) Advantage

Jacquinot pointed out in 1954 [57],[58] that an interferometer, being an instrument possessing circular symmetry, has an angular admission advantage over conventional grating spectrometers, which employ slits and consequently have not such symmetry. All spectrometers must have a limited angular acceptance if they have non-zero resolving power. For the interferometer, Jacquinot pointed out that the product of the infinitesimal area of any optical element and the infinitesimal solid angle subtended by the source is a constant for the instrument from the source to the detector (this product was called the *étendue* or *throughput*). He also emphasised that the Fourier method of interferometric spectrometry combines this advantage with the advantage of wide spectral range, which is lacking in the classical interferometric method of Fabry and Perot [59]. Jacquinot actually showed that when prism, grating, and interference spectrometers (e.g. Fabry-Perot, Amplitude and Polarization interferometers) were compared at equal resolving power and at equal instrument aperture, the radiant throughput of the interference spectrometer was much higher than that of the grating spectrometer (assuming that the instruments have the same entrance area). In reality there are some slit-like limits in the system, due to the fact that one needs to achieve a minimum level of collimation of the beams in the two arms of the interferometer for any particular level of resolution. This translates into a maximum useable detector diameter and, through the laws of imaging optics, it defines a useful input aperture.

A.6.3 High Resolution Advantage

Spectral resolution is a measure of how well a spectrometer can distinguish closely spaced spectral features. In a 2 cm^{-1} resolution spectrum, spectral features only 2 cm^{-1} apart can be distinguished. In FT-IR, the maximum achievable value of the OPD, determines the spectral resolution. Two transition one at 2000 cm^{-1} and one at 2002 cm^{-1} can be distinguished from each other with an interferometer whose maximum path difference is 0.5 cm or longer.

APPENDIX B: Radiative Theory and Spectroscopic Database

B.1 Introduction to the Radiative Theory

The emitted intensity (F_ν) of a medium may be represented as follows:

$$F_\nu = \alpha_\nu * B(\sigma, T) \tag{B.1}$$

In equation (B.1) α_ν is the "emissivity" coefficient and $B(\sigma, T)$ is the Planck function which describes the emission/absorption of a blackbody:

$$B(\sigma, T) = \frac{2hc^2\sigma^3}{\exp\left[\frac{hc\sigma}{k_B T}\right] - 1} \tag{B.2}$$

with h = Plank's constant ($6.626076*10^{-34}$ Js),
c = velocity of the light ($2.99792458*10^{10}$ cm/s)
k_b = Boltzmann's constant ($1.380658*10^{-23}$ J/K)
T = Kinetic temperature
σ = frequency (in cm^{-1})

Similarly, for the absorbed intensity of the medium (J_ν) an absorbivity coefficient may be defined (ε_ν) which binds J_ν to the Planck function

$$J_\nu = \varepsilon_\nu * B(\sigma, T) \tag{B.3}$$

In equilibrium conditions at a temperature T, absorption equals emission at each frequency ν. The Kirchoff law is directly derived from this assumption:

$$F_\upsilon = J_\upsilon$$

And so

$$\varepsilon_\upsilon = \alpha_\upsilon \tag{B.4}$$

Generally the atmospheric radiative field as a whole is not in equilibrium, so it is not possible to identify a uniform temperature. Nevertheless below 60 Km, i.e. for values of pressure higher than 0.01 mbar, it is possible to assess the temperature of a relatively small air volume with a good approximation. In this case we say that the Local Thermodynamic Equilibrium (LTE) applies: when a molecule absorbs a quantum of energy, before its re-emission a part of it is released through of the collisions with the surrounding molecules; this allows a redistribution of the initial energy in the air volume. When the radiation is emitted, the system has reached an intermediate energy between the level reached after the absorption and the level in which the molecule was before the absorption. If the mean time between the collisions (*relaxation time*) is significantly lower than the time period between absorption and emission (*lifetime of the excited states*), the collisions allow a uniform distribution of the energy: it is then possible to determine the temperature of the gas volume during the transition [1]. At altitudes lower than 60 km, most of the radiatively active gases respect this condition rather well; above, the equilibrium is no longer valid.

For atmospheric gases the emitted/absorbed radiation can be expressed by the *radiance* (dL_ν) which is the observed quantity (the spectrum).
The radiance is defined as the energy associated with a ray of light with solid angle $d\Omega$ which reaches the area dA at an incident angle θ with respect to its normal in the time dt (see Figure B.1):

$$dL_\nu = \frac{dE_\nu}{dt * d\nu * d\Omega * dA \cos \vartheta} \tag{B.5}$$

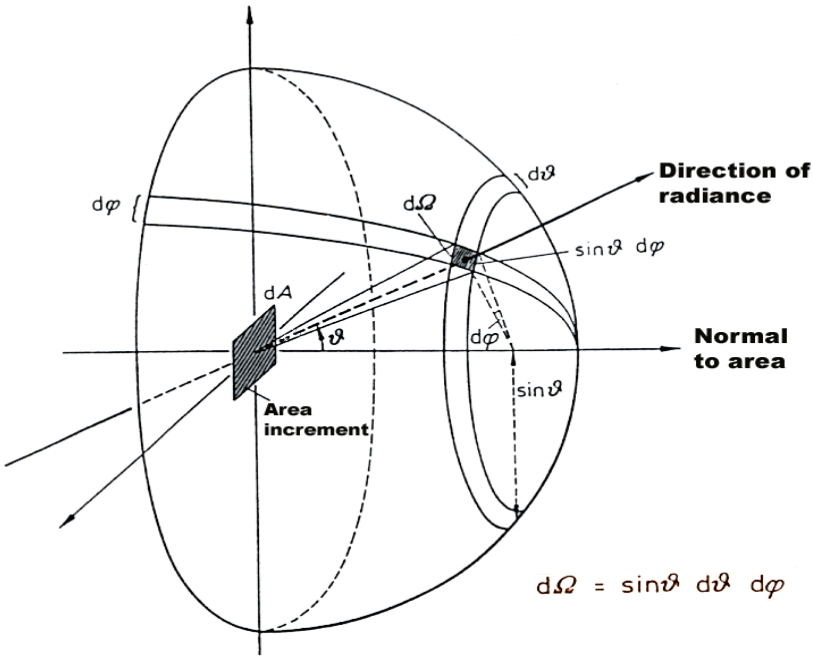

Figure B.1*:* Radiance associated with a ray of light.

In general, a molecule in gas phase can absorb and emit radiation only at given energies, that correspond to the difference between the energy levels of the molecule itself. Since the energy is related to the frequency of the radiation through the expression:

$$E = h\nu \tag{B.6}$$

Observing the atmospheric spectrum we can have informations about the composition of the atmosphere. The transitions are described by the quantum of energy which defines the energy step between the two levels involved:

$$\Delta E = h\nu_1 - h\nu_2 = h\nu_c \tag{B.7}$$

Where $h\nu_1$ e $h\nu_2$ are respectively the energies of the initial and final levels; ν_c is the central frequency of the spectral line that identifies the transition in the spectrum. Thus the spectral range in which a transition falls depends on the difference of energy between the two levels involved as summed up in the following table:

Type of transition	Spectral range
Rotational	far infrared – microwaves
Vibrational	middle to near infrared
Electronic	visible and ultraviolet

B.2 Radiative Transfer Theory

The radiative transfer equation states that the specific spectral intensity of radiation $L(\upsilon)$ (defined as the energy flux per unit time, unit frequency, unit solid angle and unit area normal to the direction of propagation, as a function of the frequency υ) during its propagation in a medium is subject to losses due to extinction and to gains due to emission:

$$\frac{dL(v)}{ds} = -\mu(v)\cdot L(v) + \rho \cdot j(v) \tag{B.8}$$

Where s is the position along the direction of propagation, positive in going from the source to the observer, $\mu(\upsilon)$ is the absorption coefficient, $j(\upsilon)$ is the emission coefficient per unit mass and ρ is the mass density; all this quantities are function of the position s. This dependence will be indicated only when necessary.
We introduce the source function defined as:

$$J(v) = \rho \cdot {j(v)}\big/{\mu(v)} \tag{B.9}$$

Using equations (B.9), equation (B.8) becomes:

$$\frac{dL(v)}{ds} = \mu(v)(J(v) - L(v)) \tag{B.10}$$

If we introduce the optical thickness $\tau(\upsilon)$, defined equal to:

$$\begin{aligned} d\tau(v) &= \mu(v)\cdot ds \\ \tau(v,s,s') &= \int_{s}^{s'} \mu(v,s)\cdot ds \end{aligned} \tag{B.11}$$

respectively as infinitesimal increment and as total value between points s and s', substituting ds in Eq. (B.10) we have:

$$\frac{dL(v)}{d\tau} = J(v) - L(v) \tag{B.12}$$

In Eq. (B.11) the optical thickness between two points must be considered as calculated along the optical path (that is not always a straight line). The general solution of equation (B.12) for a path between points s_1 and s' can be formally obtained by multiplying the differential equation given in point s' by $exp[\tau(\upsilon,s_1,s')]$

$$\begin{aligned} & e^{\tau(v,s_1,s')}\frac{dL(v,s')}{d\tau(v,s')} = e^{\tau(v,s_1,s')}\cdot J(v,s') - e^{\tau(v,s_1,s')}\cdot L(v,s') \\ & e^{\tau(v,s_1,s')}\frac{dL(v,s')}{d\tau(v,s')} + e^{\tau(v,s_1,s')}\cdot L(v,s') = e^{\tau(v,s_1,s')}\cdot J(v,s') \\ & \frac{d\left(e^{\tau(v,s_1,s')}\cdot L(v,s')\right)}{d\tau(v,s')} = e^{\tau(v,s_1,s')}\cdot J(v,s') \end{aligned} \tag{B.13}$$

Integrating Eq.(B.13) with s' that varies from point s_1 to point s_2 ($s_1 < s_2$), and τ that consequently varies from $\tau_1 = \tau(\upsilon, s_1, s_1) = 0$ to $\tau(\upsilon, s_1, s_2) = \tau_2$

$$
\begin{aligned}
& e^{\tau(v,s_1,s_2)} \cdot L(v,s_2) - e^{\tau(v,s_1,s_1)} \cdot L(v,s_1) = \int_{\tau 1}^{\tau 2} e^{\tau(v,s_1,s')} \cdot J(v,s') \cdot d\tau(v,s') \\
& e^{\tau(v,s_1,s_2)} \cdot L(v,s_2) = L(v,s_1) + \int_{\tau 1}^{\tau 2} e^{\tau(v,s_1,s')} \cdot J(v,s') \cdot d\tau(v,s') \\
& L(v,s_2) = L(v,s_1) \cdot e^{-\tau(v,s_1,s_2)} + \int_{\tau 1}^{\tau 2} e^{-\tau(v,s_1,s_2)} \cdot e^{\tau(v,s_1,s')} \cdot J(v,s') \cdot d\tau(v,s') \\
& L(v,s_2) = L(v,s_1) \cdot e^{-\tau(v,s_1,s_2)} + \int_{\tau 1}^{\tau 2} e^{-\tau(v,s',s_2)} \cdot J(v,s') \cdot d\tau(v,s')
\end{aligned}
\tag{B.14}
$$

Introducing the trasmittance (the *transparency* of the atmosphere: if it is 1, it means that the atmosphere is completely transparent; if it is 0 instead it means that the atmosphere is completely opaque to the radiation) $\Im(v,s',s) = e^{-\tau(v,s',s)}$, being $d\Im(v,s',s) = e^{-\tau(v,s',s)}\left[-\tau(v,s',s)\right]$ we finally obtain the integral expression of the radiative transfer equation:

$$
L(v,s_2) = L(v,s_1) \cdot \Im(v,s_1,s_2) - \int_{1}^{\Im_2} J(v,s') \cdot d\Im(v,s',s_2) \tag{B.15}
$$

with $\Im_1 = \Im_1(v,s_1,s_1) = e^{-\tau(v,s_1,s_1)} = e^0 = 1$, and $\Im_2 = e^{-\tau(v,s_1,s_2)}$. $L(\upsilon,s_1)$ is the radiance found at the boundary of the atmosphere; in case of limb measurements, it can be the solar radiation or the blackbody contribution from space; in the latter case its contribution is rather low, so it can be neglected [60] and the emission of the atmosphere is observed. So, in case of emission spectra the radiative transfer equation reduces to:

$$
L(v,s_2) = -\int_{1}^{\Im_2} J(v,s') \cdot d\Im(v,s',s_2) \tag{B.16}
$$

Eq. (B.16) can be slightly modified using the variables that are more appropriate to the limb sounding geometry. Let us characterise the geometry of observation with the altitude h and the limb angle θ^l of the observer and the optical path with the co-ordinate $s=s_2-s'$ that measures the distance from the observer. The observed atmospheric spectral intensity $I(\nu, \theta^l, h)$, i.e. the radiation specific intensity present in the atmosphere as a function of the optical frequency and of the observation parameters, is equal to:

$$
I(v,\theta^l,h) = \int_{\Im^b}^{1} J(v,s') d\Im(v,s') \tag{B.17}
$$

where ν = frequency,
θ^l = direction of the line of sight (limb angle),
h = altitude of the observer,
s = co-ordinate along the flight path
$J(v,s)$ = source function

$\Im(v,s')$ = transmittance of the path between the point *s=s'* and the observer located at *s=0*.

$\Im^b$ = trasmittance at the farthest point along the optical path that contributes to the signal observed by the instrument.

Under the local thermal equilibrium assumption, the source function *J(v,s)* coincides with the Planck function.

B.3 Cross section

The transmittance $\Im(v,s)$ is a key quantity in the inversion method whose aim is to get the VMR of the target species ($X_m(s)$) from the measured spectra (L_v). The combination of previous equations describes the way $\Im(v,s)$ is linked to the molecules VMRs:

$$\Im(v,s) = \exp\left[-\int_0^s \left(\overline{k(v,s')}\eta(s')\right)ds'\right] \tag{B.18}$$

with $\eta(s) = \dfrac{p(s)}{k^B T(s)}$ = number density of the air

$p(s)$ = pressure
$T(s)$ = temperature

and the weighted absorption cross section:

$$\overline{k(v,s)} = \sum_{m=1}^{molec} k_m(v,s)\mathrm{X}_m(s) \tag{B.19}$$

where
molec = number of different molecular species that absorb in the spectral region under consideration
$X_m(s)$ = volume mixing ratio (VMR) of the species *m* at the point *s*
$k_m(v, s)$ = absorption cross sections of the species *m*

The absorption cross section results from a line-by-line calculation of the absorption due to the spectroscopic transitions of the molecule, each with its intensity and line shape. In turn the intensity and line shape depends on the physical conditions of pressure and temperature that are encountered along the optical path. The absorption cross section of one molecular species *m* is a function of temperature and pressure and is given by the following sum over all lines of the species:

$$k_m(\sigma,T,p) = \sum_{l=1}^{lines} L_{m,l}(T)A_{m,l}(\sigma-\sigma_{m,l},T,p) \tag{B.20}$$

Where:

σ = frequency
$L_{m,l}(T)$ = line strength of line *l* of species *m*
$\sigma_{m,l}$ = central optical frequency of line *l* of species *m*
$A_{m,l}(\sigma-\sigma_{m,l},T,p)$ = line profile (line-shape function)

$\sigma_{m,l}$ is the central frequency of each l^{th} transition; if the molecular system was ideal (isolated and stationary), and the lifetime of the excited state was infinite, the spectrum of the molecule would be made up of "single" lines, each described by a Dirac delta at the central frequency $\sigma_{m,l}$. In the real case there are intrinsic phenomena (finite lifetime of the energy level, collisions, etc.), in particular of the absorption mechanisms, which generate a widening of the transition: in the spectrum the line is no longer a discrete entity as in the ideal case, but it covers a spectral range.

B.3.1 Lineshape

The lineshape is the function that describes the frequency dependence of the intensity of a transition; its mathematical expression depends on the type of phenomenon the molecule is undergoing. In the case of the atmosphere there are three processes that are responsible for the line broadening: the natural broadening, the pressure broadening and the Doppler broadening.

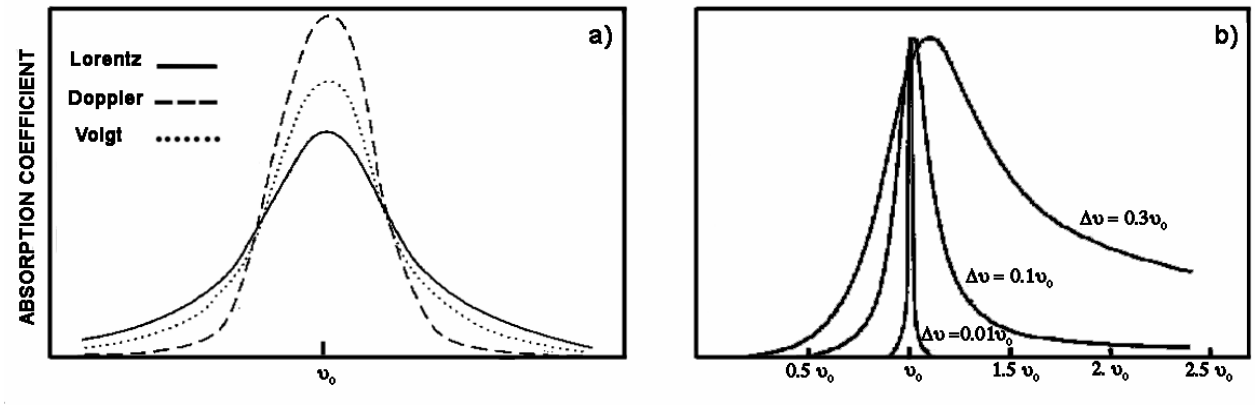

Figure B.2*: (a)* plots of Lorentz, Doppler and Voigt functions centered on the frequency ν_0 [1] *(b)* plots of Van Vleck-Weisskopf function in the case of NH_3 for various values of pressure in the microwave spectral region [61]; $\Delta\nu=\alpha^L_{m,l}$

B.3.1.1 Natural Broadening

The natural broadening is due to the finite lifetime of the excited states; the resulting lineshape can be described by the Lorentz function (Figure B.2.a):

$$A^L_{m,l}(\sigma-\sigma_{m,l},T,p)=\frac{1}{\pi}\frac{\alpha_{m,l}}{\alpha_{m,l}{}^2+(\sigma-\sigma_{m,l})^2} \qquad (B.21)$$

where $\alpha_{m,l}$ is the Lorentz HWHM equal to:

$$\alpha_{m,l}=\frac{1}{2\pi\omega} \qquad (B.22)$$

ω is the mean lifetime of the state and $\alpha_{m,l}$ is called broadening coefficient (that is the half width at the half maximum of the line). For vibrational and rotational transitions in the infrared spectral region, this effect is insignificant compared to other broadening sources.

B.3.1.2 Doppler Broadening

The Doppler broadening is generated by the molecule motion: when a molecule is moving with a velocity value *w* along the observer direction, the frequency by the emitted radiation as seen by the observer changes:

$$v = v_c\left(1+\frac{w}{c}\right) \tag{B.23}$$

In case of thermal equilibrium the probability that a molecule moves with the velocity *w* is ruled by the Boltzmann distribution:

$$P(w) = \sqrt{\frac{m}{2\pi * k_b T}}\, exp\left[-\frac{mw^2}{2k_b T}\right] \tag{B.24}$$

where *m* is the molecular mass.
Eqs.(B.23) and (B.24) allow to describe the lineshape as the Gauss function:

$$A^D_{m,l}(\sigma-\sigma_{m,l},T) = \sqrt{\frac{\ln 2}{\pi}}\frac{1}{\alpha^D_{m,l}}\exp\left[-\ln 2\frac{(\sigma-\sigma_{m,l})^2}{{\alpha^D_{m,l}}^2}\right] \tag{B.25}$$

where $\alpha^D_{m,l}$ is the Doppler half width at half maximum (HWHM) of the line equal to:

$$\alpha^D_{m,l} = \sigma_{m,l}\sqrt{2\ln 2\frac{k^B T}{M_m c^2}} \tag{B.26}$$

with M_m = molecular mass of species *m*

The Doppler line width depends on the temperature and on the frequency of the transition.

B.3.1.3 Pressure Broadening

The pressure broadening is due to the collisions of the molecule with the surrounding environment. The lineshape caused by the collisions can be described by the Van-Vleck-Weisskopf profile (Figure B.2.b):

$$A^{VVW}_{m,l}(\sigma-\sigma_{m,l},T,p) = \left(\frac{\sigma}{\sigma_{m,l}}\right)^2\frac{1}{\pi}\left[\frac{\alpha^L_{m,l}}{{\alpha^L_{m,l}}^2+(\sigma-\sigma_{m,l})^2}+\frac{\alpha^L_{m,l}}{{\alpha^L_{m,l}}^2+(\sigma+\sigma_{m,l})^2}\right] \tag{B.27}$$

where

$$\alpha^L_{m,l} = \sum_i \alpha^{L,i}_{m,l}\cdot P_i \tag{B.28}$$

where P_i is the partial pressure of the perturbing gas. For each perturbing gas :

$$\alpha_{m,l}^{L,i} = \alpha_{m,l}^{L_0,i} \frac{p}{p^0} \left[\frac{T^0}{T} \right]^{\gamma_{m,l}} \quad \text{(B.29)}$$

with $\alpha_{m,l}^{L_0,i}$ = Lorentz half width at reference temperature T^0 and reference pressure p^0 for the i-th gas

$\gamma_{m,l}$ = coefficient of temperature dependence of the half width (depends on the type of collisions considered)

As the pressure grows (Figure B.2.b), and consequently as $\alpha_{m,l}^{L}$ increase, the presence of both term will lead to a shift of the central frequency, so the symmetry of the low pressure lineshape is broken [61].

At high frequencies and/or for narrow lines (i.e. for $\sigma_{m,l} >> \alpha^{L}_{m,l}$) the Van Vleck-Weisskopf line shape reduces to the Lorentzian profile in (B.21) with broadening coefficient as in (B.29).

The Van Vleck-Weisskopf line shape is an approximation of the collision induced broadening that is valid under the assumption that the collisions are infrequent (the time between collision is long compared with the duration of the collisions) and at the same time sufficiently strong to change the orientation of the dipole moment of the molecule in a fully random way [62] and sufficiently weak to induce only linear deformations and that the involved energy levels are sufficiently isolated.

The Van Vleck-Weisskopf line shape can be considered as the classical Lorentz line shape with an additional feature at the negative frequency side and a correction factor $\left(\sigma / \sigma_{m,l} \right)^2$.

B.3.1.4 Voight shape

In the case of far infrared measurements, the natural broadening has a negligible contribution; so the broadening effects are mainly ruled by the pressure and the temperature ($\alpha_{m,l}^{L}$ and $\alpha_{m,l}^{D}$): when we deal with low altitudes (where the pressure values are very high), the impact of the collisions dominates; at high altitudes where the density of the air is very low, the temperature broadening becomes more and more important (Figure B.3). So at low altitudes the broadening effect of collisions dominates while at higher altitudes the number of collisions experimented by each molecule decreases so that collisional and Doppler broadening assume comparable values. In this case the lineshape can be expressed as the convolution of the Lorentz and Doppler functions; this shape is called Voigt function (Figure B.2.a, and (B.31)); when the Doppler and Lorentz broadening coefficients are comparable, the Doppler lineshape dominates in the central part of the line while the tails are mainly due to the Lorentz function.

Figure B.3 provides a comparison of the Doppler and the Lorentz HWHM for a typical spectroscopic case. The Doppler effect varies with the frequency and depends, through the temperature, weakly on altitude. The Lorentz broadening varies with the altitude, through the pressure, it depends on the transition but does not vary explicitly with the frequency. Figure B.3 shows how in the altitude range (below 40-50 km) and in the frequency range (at 20 cm^{-1} and near 100 cm^{-1}) that is of interest for SAFIRE-A, the main broadening effect is the pressure broadening.

Despite the fact that pressure broadening is the dominant effect, the line shape function to be modelled for a rigorous radiative transfer calculation is the profile given by equation (B.30): in the assumption that Doppler and pressure broadening are independent effects, the line

shape function is described by the function $A^{A}_{m,l}(\sigma-\sigma_{m,l},T,p)$ that results from the convolution of the Doppler profile $A^{D}_{m,l}(\sigma-\sigma_{m,l},T)$ and the Van-Vleck-Weisskopf profile $A^{VVW}_{m,l}(\sigma-\sigma_{m,l},T,p)$:

$$A^{A}_{m,l}(\sigma-\sigma_{m,l},T,p)=A^{D}_{m,l}(\sigma-\sigma_{m,l},T)*A^{VVW}_{m,l}(\sigma-\sigma_{m,l},T,p) \tag{B.30}$$

If the Van Vleck-Weisskopf line shape can be approximated by a Lorentz line shape, the line shape of equation (B.30) reduces itself to the Voight line shape:

$$A^{V}_{m,l}(\sigma-\sigma_{m,l},T,p)=A^{D}_{m,l}(\sigma-\sigma_{m,l},T)*A^{L}_{m,l}(\sigma-\sigma_{m,l},T,p) \tag{B.31}$$

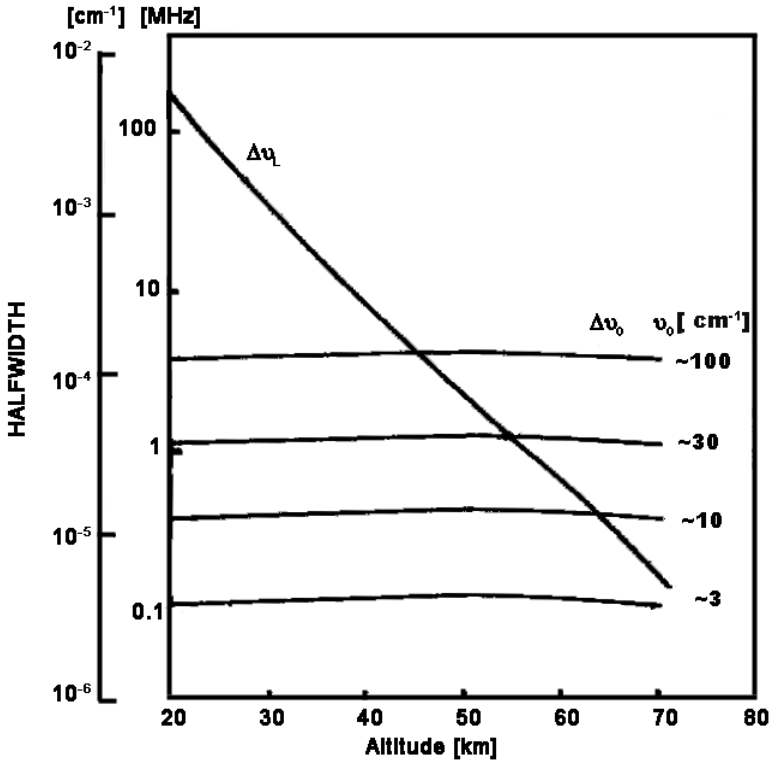

Figure B.3*:* Behaviour of the pressure ($\Delta\nu_L$) and Doppler broadening coefficients ($\Delta\nu_D$) with respect to height in case four different frequencies (100, 30, 10, 3 cm^{-1}) are taken into account [5].

B.3.2 Line intensity

$L_{i,l}\ (T)$ is the transition peak intensity and it is usually called *line strength* in literature; it is defined as:

$$L_{i,l}=\int_{-\infty}^{+\infty}k_i d\nu \tag{B.32}$$

In the case of a gas at a certain temperature T, the transition of the i^{th} molecule between two roto-vibrational states *n* and *n'*, $L_{i,l}(T)$ becomes:

$$L_{i,l}(T)=\frac{h\nu^{c}_{l}}{c}\frac{\rho_n}{N}\left(1-\frac{g_n\rho_{n'}}{g_{n'}\rho_n}\right)B_{nn'}\ *\ isot \tag{B.33}$$

where N is the number of molecules of the gas per cm^3 (*number density*), ρ_n and $\rho_{n'}$ are the populations respectively of the lower and higher energy states involved in the transition, g_n and $g_{n'}$ are the statistical weights of each level accounting for the electronic, vibrational and rotational structure of the molecule, and finally *isot* is the isotopic abundance of the species. H is the Planck constant and c is the vacuum speed light. $B_{nn'}$ is the Einstein coefficient for the induced absorption; it is bound to the probability of the transition that is to the square of the dipole moment $|M_{nn'}|^2$:

$$| M_{nn'} |^2 = \frac{3h^2}{8\pi^3} * B_{nn'} * 10^{36} \qquad \text{(B.34)}$$

$|M_{nn'}|^2$ is the sum of the square values of the dipole matrix terms weighted by g_n and it depends on the electronic structure of the molecule.
In case of LTE, it is possible to apply the Boltzmann statistics at the temperature T to calculate the population of the energy levels involved in the transition and therefore to obtain:

$$L_{i,l}(T) = \frac{h\nu^c_l}{c} \frac{g_n \exp\left(-uc * E_n / T\right)}{Q(T)} \left[1 - \exp\left(-uc * \nu^c_l / T\right)\right] B_{nn'} * isot \qquad \text{(B.35)}$$

$$Q(T) = \sum_s \exp\left(-uc * E_s / T\right) = \sum_m g_m * \exp\left(-uc * E_m / T\right) \qquad \text{(B.36)}$$

where E_n: lower state energy, $uc = hc / k_b$, $Q(T)$: total partition function [32], s: index for the molecule possible states, g_m and E_m: degeneracy and energy of the state m.

B.4 Spectroscopic Database

The explicit calculation of the cross sections requires the knowledge of the main spectroscopic parameters of each involved transition (such as for example the central frequency, the line strength at a reference temperature, the broadening coefficients). These quantities can be found in the spectroscopic databases. The progressive evolution of the analysis of molecular spectroscopy has led to the growth of quite accurate spectroscopic databases for different scientific purposes. In literature there are several spectroscopic databases according to the specific applications and the spectral ranges, being HITRAN the reference database for our studies you can find here a brief description of this database.

B.4.1 HITRAN

HITRAN stands for High-resolution TRANsmission; the project of building such a spectroscopic database started at the end of the sixties at the *Air Force Cambridge Research Laboratory* [63]. The first edition, dated 1973, contained data just for 7 of the major atmospheric absorbers in the spectral range 0-100 μm with few characteristics of their transitions. During the followings years a lot of developments have improved its quality by increasing the number of molecules, the spectral coverage, the number of parameters and also their accuracy; today its evolution and maintenance is under the supervision of the *Atomic and Molecular Physics Division* of the *Harvard Smithsonian Center for Astrophysics*. Along with the line-by-line catalogue HITRAN provides also the aerosol refraction indexes and the heavy molecules tabulated cross sections both in the ultraviolet and infrared.
For each molecule in the database you can find:

1) a species identification code (MOL) whose value does not follow any specific criteria but the chronological order in which the molecule has been introduced in the database

2) an isotope code using the AFGL (Air Force Geophysics Laboratory) notation that follows the natural abundances of the isotopes which allow to organize them in the database: a code 1 (ISO=1) is associated with the most abundant isotope, 2 with the second abundant isotope and so on. So in the database each species is described by two identification codes: MOL and ISO. For example: the most abundant isotope for the molecular oxygen (O_2^{16}) corresponds to MOL=7, ISO=1; the second most abundant ($O^{16}O^{18}$) to MOL=7, ISO=2.

3) nu_{ij} is the central frequency expressed in cm^{-1}

4) S_{ij} is the line strength (previously called $L_{i,l}(T)$) expressed in $cm^{-1}/(molec*cm^{-2})$ for a reference temperature T_0=296K

5) R_{ij} is the square of the dipole momentum ($|M_{nn}|^2$ in eq.(B.34)) expressed in $Debye^2=10^{-36}$ * erg * cm^3

6) gam_{air} is the pressure broadening coefficient $(\delta\nu)_L$ for collision with nitrogen in cm^{-1}/atm; its value is valid for a reference temperature T_0=296K and a reference pressure p_0=1atm

7) gam_{self} is the *self broadening* coefficient, i.e. the pressure broadening coefficient $(\delta\nu)_L$ due only to the analysed gas itself; reference temperature and pressure are the same as gam_{air}

8) *E"* is the energy of the lower level (in cm^{-1})

9) *n* is the temperature dependence coefficient for gam_{air} (γ in eq.(B.29))

10) *delta* is the pressure shift of nu_{ij} due to the air at T_0=296K and p_0=1atm; it is in cm^{-1}/atm.

APPENDIX C: Hints on the Ozone Chemistry

The stratospheric ozone plays a major role in absorbing the ultraviolet radiation which otherwise would reach the Earth surface and then negatively affect the health of humans, animals and plants. In fact, the evolution of the Earth's atmosphere and the formation of the ozone layer are thought to be closely related to the development of life on Earth.

C.1 Ozone Chemistry

Geological evidence suggests that primitive forms of plant life developed *in aqua* deep in the oceans, at a time when the Earth's atmosphere contained little or no oxygen and damaging UV radiation passed freely to the planet's surface. Through photosyntesis, these early forms of life are thought to have liberated oxygen, which then passed to the surface where it was dissociated by UV radiation according to the reaction:

$$O_2 + h\nu \rightarrow 2O \qquad (C.1)$$

Atomic oxygen produced by (C.1) could then recombine with O_2 to form ozone in the molecular reaction.

$$O_2 + O + M \rightarrow O_3 + M_+ \qquad (C.2)$$

Where M represents a third body needed to carry off excess energy liberated by the combination of O and O_2. Ozone created in (C.2) is dissociated by UV radiation according to the reaction

$$O_3 + h\nu \rightarrow O_2 + O \qquad (C.3)$$

If third bodies are abundant, atomic oxygen produced by (C.3) recombines almost immediately with O_2 lines in (C.2) to again form ozone. Thus, reactions (C.2) and (C.3) constitute a "closed cycle" that involves no net loss of components. Since the only result is the absorption of solar energy, this cycle can process UV radiation very efficiently. By removing harmful UV from the solar spectrum, ozone is thought to have allowed life to spread upward to the oceans surfaces, where it had greater access to visible radiation, could produce more oxygen through photosyntesis, and was then able to evolve into more sophisticated forms.

C.2 Ozone Distribution

The zonal-mean distribution of ozone mixing ratio is shown in Figure C.1 as a function of latitude and altitude. Whereas atmospheric water vapour is confined to the troposphere, ozone is concentrated in the stratosphere. Ozone mixing ratio increases sharply above the tropopause, reaching a maximum of about 10 ppmv near 30 km (10 mb). The zonal-mean ozone mixing ratio is largest in the tropics, where the flux of solar UV and photodissociation of O_2 are large.

The photochemical lifetime of ozone varies sharply with altitude. In the lower stratosphere, ozone has a photochemical lifetime of several weeks. Since this is long compared to the characteristic time scale of air motion (~ 1 day), ozone behaves as a tracer at these altitudes and its distribution is controlled by dynamical influences. Should ozone find its way into the troposphere, it is quickly destroyed. Its water solubility makes O_3 readily absorbed by convective systems, which precipitate it to the surface, where it can be destroyed by a variety of oxidation processes. Thus, the troposphere serves as a sink of stratospheric ozone. The photochemical lifetime of ozone also decreases upward, to the order of 1 day by 30 km and

only 1 h by the stratopause. For this reason, the distribution of ozone in the upper stratosphere and mesosphere is controlled mainly by photochemical influences.

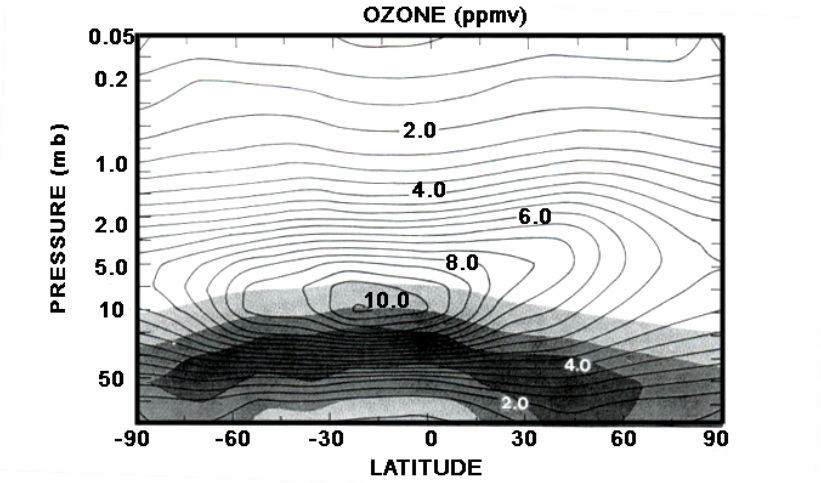

Figure C.1: Zonal-mean mixing ratio of ozone (contoured) and density of ozone (shaded) averaged over January-February 1979, as functions of latitude and pressure, obtained from the Limb Infrared Monitor of the Stratosphere (LIMS) on board Nimbus 7. The shaded levels correspond to 20, 40, and 60 % of the maximum value.

Even though its mixing ratio maximizes near 30 km, atmospheric ozone is concentrated in the lower stratosphere. Because air density decreases exponentially with altitude, the density of ozone (shaded area) is concentrated at altitudes of 10 to 20 km. Largest values are found in a shallow layer near 30 mb in the tropics, which descends and deepens in extratropical regions. The column abundance, or total ozone, is expressed in Dobson Units (DU), which measure in thousandths of a centimeter the depth the ozone column would assume if brought to standard temperature and pressure:

1 Dobson Unit (DU)=0.01mm at standard pressure and temperature

The entire ozone column measures less than one-half of 1cm at standard temperature and pressure [1].

C.3 The Ozone Hole

The discovery of the *ozone hole* in Antarctica in the 70s has led to a great number of research studies to understand the underlying causes and to analyse the possible occurrence of the phenomenon also at other latitudes. Since the beginning of the 20th century when the first observations of the total integrated column of ozone (based on ultraviolet absorption) were made, several systematic measurements have revealed that the total ozone abundance was actually decreasing over many regions since about 1980 [64].
The progressive comprehension of the Antarctic ozone hole chemistry has showed the great importance of the reactions of chlorine compounds on and within surfaces (heterogeneous chemistry), mainly under the very cold conditions of the polar regions; water ice, nitric acid hydrates and liquid sulfuric acid/water stratospheric surfaces are all centers of this crucial chemistry.

C.3.1 Polar Stratospheric Clouds (PSCs)

It is now widely accepted that PSCs (Polar Stratospheric Clouds) provide the surfaces on which certain reactions proceed much faster that they can in gas phase alone.

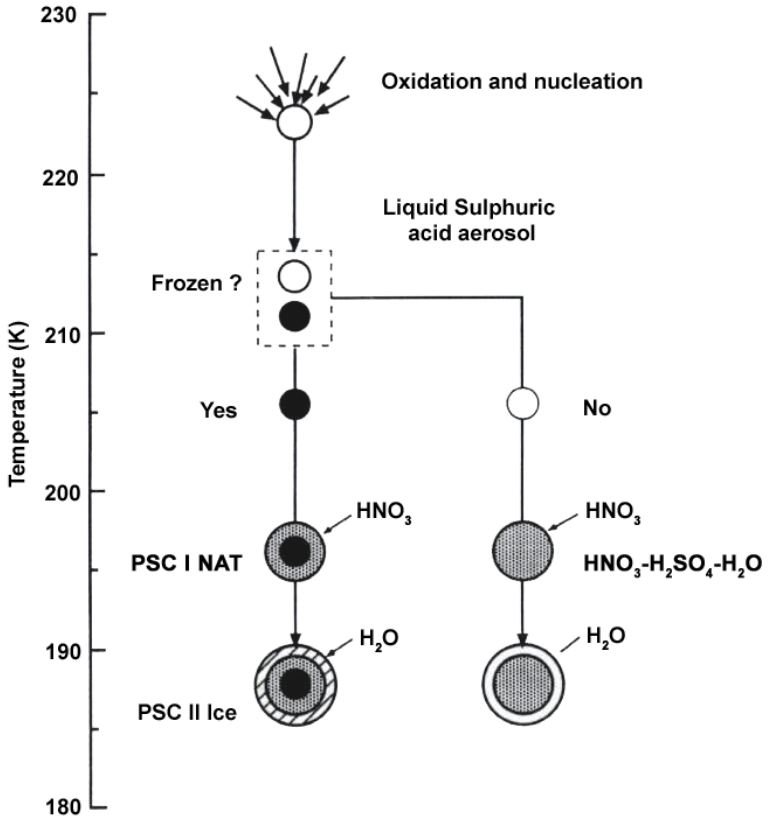

Figure C.2: Polar stratospheric cloud formation and composition. The left-hand path represents the conventional three-stage concept, while in the right-hand path, the aerosol remains liquid, and takes up HNO_3 to a form of supercooled ternary (HNO_3-H_2SO_4-H_2O) solution (European research in the stratosphere, Luxembourg 1997).

The stratosphere is isolated from convective motions and therefore from the source of water vapour at the Earth's surface. Consequently, clouds rarely form above the tropopause. Exceptional are nacreous clouds that develop in connection with the mountain wave. Nacreous clouds are through to be a subset of more ubiquitous PSCs. Because the stratosphere is very dry, PSCs form only under very cold conditions. Zonal-mean temperatures over the Antarctic fall below 190 K during Austral winter, more than 20 K colder than temperatures over the wintertime Arctic. For this reason, PSCs occur over the Antarctic with much greater frequency and depth than over Arctic.

Their optical properties suggest two main classes of PSCs. Type I PSCs are small (< 1μm diameter) HNO_3-rich particles, and have a mass mixing ratio of about 10 ppbm (parts per billion by mass). Type II PSCs are larger (from 10 μm to perhaps more than 1 mm diameter), are composed primarily of H_2O-ice together with a small amount of HNO_3 as hydrates, and can constitute up to 1000 ppbm of the stratosphere when they are present. Several hydrates of the acids may be present in the PSC particles. Type I PSCs often appear to belong to one of two sub-categories, Type Ia solid particles consisting of nearly pure NAT (nitric acid trihydrate) and Type Ib particles , which are supercooled liquid ternary solutions of HNO_3-H_2SO_4-H_2O.

Figure C.2 shows that Type I PSCs are formed at substantially higher temperatures –by 5 to 10 K- than the Type II PSCs. Both physical size and chemical composition are thus temperature dependent. The extent of denitrification (and dehydration) will be affected by the rate of sedimentation, itself obviously more rapid for larger particles. Subsidence of NAT-ice mixtures to the troposphere in Type II PSCs removes NO_y permanently, and the atmosphere is denitrified.

Moreover, the presence of PSCs shifts catalytic destruction of ozone column, to the lower stratosphere, where O_3 is concentrated.

C.3.2 Polar Vortex

Figure C.3 shows profiles of ozone concentration over Antarctica during Austral winter (solid line) and shortly after equinox (dashed line), when the sun rises above the horizon. A marked reduction of ozone has occurred between 10 and 20 km, where most of the ozone column resides.

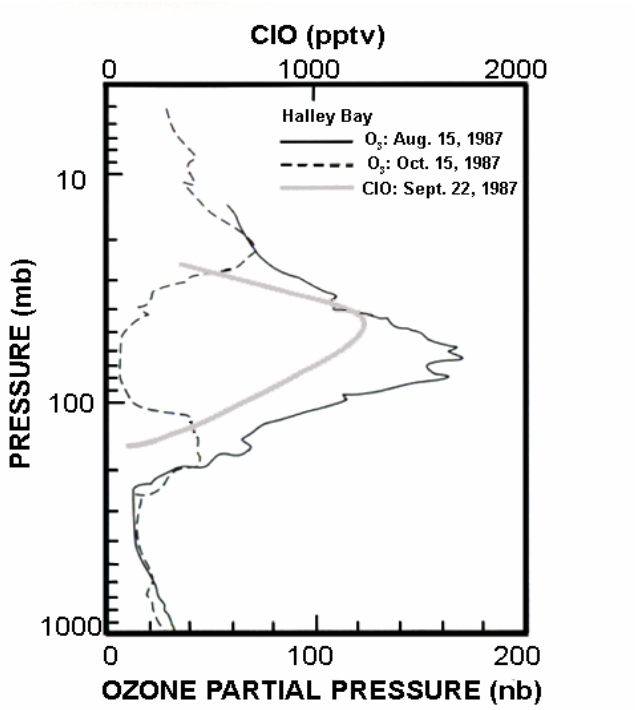

Figure C.3: Profiles of ozone partial pressure over Antarctica during Austral winter (solid line) and shortly after spring equinox (dashed line). A profile of the chlorine monoxide mixing ratio (shaded line) after equinox is superposed. Sources: WMO (1988), Solomon (1990).

Decreases in ozone mixing ratio of 50% are observed at this time year, with column abundances as low as 100 DU having been recorded. Superposed in Figure C.3 is the profile of ClO (shaded line), which is produced by the destruction of ozone:

$$Cl + O_3 \rightarrow ClO + O_2 \qquad \text{(C.4.1)}$$

$$ClO + O \rightarrow Cl + O_2 \qquad \text{(C.4.2)}$$

Which has the net effect

$$O_3 + O \rightarrow 2O_2 \qquad \text{(C.4.3)}$$

This closed cycle leaves Cl + ClO unchanged, so one atom of chlorine can destroy many atoms of ozone.

Consistent with the observed ozone depletion, ClO mixing ratio maximizes between 10 and 25 km-precisely where PSCs are sighted. A correspondence between reduced O_3 and increased ClO is also apparent across the edge of the polar –night vortex (Figure C.4). Ozone decreases sharply and chlorine monoxide increases sharply where temperature becomes colder than 196 K, which is close to the threshold temperature for the formation of PSCs.

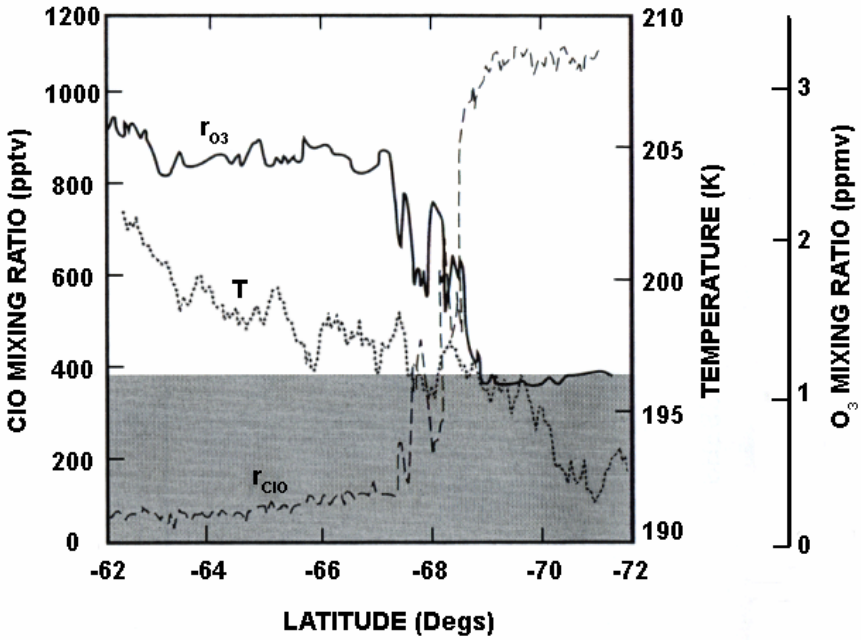

Figure C.4: Mixing ratio of ozone (solid line) and chlorine monoxide (dashed line) and temperature (dotted line) along a flight path into the Antarctic polar-night vortex. Temperatures colder than about 196 K (shaded) coincide with the formation of PSCs. Source of O_3 and ClO profiles.

The reactions now recognized to be primarily responsible for the ozone loss involve two stages: First, inactive chlorine species such as HCl and $ClONO_2$ are converted to reactive forms of Cl_x through heterogeneous reactions like

$$HCl_{(s)} + ClONO_{2(g)} \rightarrow Cl_{2(g)} + HNO_{3(s)} \quad (C.5.1)$$

and

$$H_2O_{(s)} + ClONO_{2(g)} \rightarrow HOCl_{(g)} + HNO_{3(s)} \quad (C.5.2)$$

Which involve solid (s) as well as gas (g) phase. These reactions proceed rapidly on ice, but slowly in the gas phase alone. Once produced, Cl_2 and HOCl are readily photolyzed by sunlight to release free chlorine

$$Cl_2 + h\nu \rightarrow 2Cl \quad (C.6.1)$$

$$HOCl + h\nu \rightarrow OH + Cl \quad (C.6.2)$$

Which is a reactive form of Cl_x. Then the sequence of reactions

$$Cl + O_3 \rightarrow ClO + O_2 \quad (C.7.1)$$

$$2ClO + M \rightarrow Cl_2O_2 + M \quad (C.7.2)$$

$$Cl_2O_2 + h\nu \rightarrow Cl + ClO_2 \quad (C.7.3)$$

$$ClO_2 + M \rightarrow Cl + O_2 + M \quad (C.7.4)$$

Destroys ozone catalytically with the net effect of

$$2O_3 + h\nu \rightarrow 3O_2 \qquad (C.7.5)$$

With established reaction rates, observed mixing ratios of ClO of about 1 pptv are adequate to explain the observed ozone depletion rate of about 2% per day. This concentration of ClO is two orders of magnitude greater than that predicted by gas-phase alone. However, it is consistent with calculations that include heterogeneous reactions.

The catalytic sequence (C.7) is initiated by free chlorine, which originates largely from photolysis of CFCs. Produced exclusively by industry, CFCs have led to steadily increasing levels of atmospheric chlorine. They are not destroyed in the troposphere: indeed they are not significantly soluble in water (hence not removed by rain and washout processes like acid rains), they do not react with soil surfaces or with any other chemical species in the lower atmosphere; so they tend to be inert in the troposphere. They are instead broken up by the ultraviolet light in the upper atmosphere, yielding Cl which destroys ozone in catalytic cycles. Atmospheric chlorine has increased fivefold since the 1950s-shortly after the introduction of CFCs in industrial applications. Tending in the opposite sense, the signature of ozone depletion over Antarctica emerges clearly after 1980, presumably when chlorine levels exceeded a threshold for reactions (C.7) to become an important sink of O_3 (Solomon, 1990).

While converting inert forms of chlorine into reactive Cl_x, heterogeneous reactions have the opposite effect on reactive nitrogen. They convert NO_x into relatively inactive nitric acid. This bears importantly on the ozone depletion because NO_x regulates the abundance of reactive chlorine. The principal means by which Cl_x is converted back to inactive forms is via reaction with nitrogen dioxide

$$ClO + NO_2 + M \rightarrow ClONO_2 + M \qquad (C.8)$$

The abundance of NO_2 thus controls the duration over which reactive chlorine is available to destroy ozone in (C.7). Since PSCs are composed of hydrated forms of nitric acid, their formation removes NO_x from the gas phase. Should PSC particles become large enough to undergo sedimentation, NO_x is removed entirely. The stratosphere is then denitrified, leaving reactive chlorine available much longer to destroy ozone.

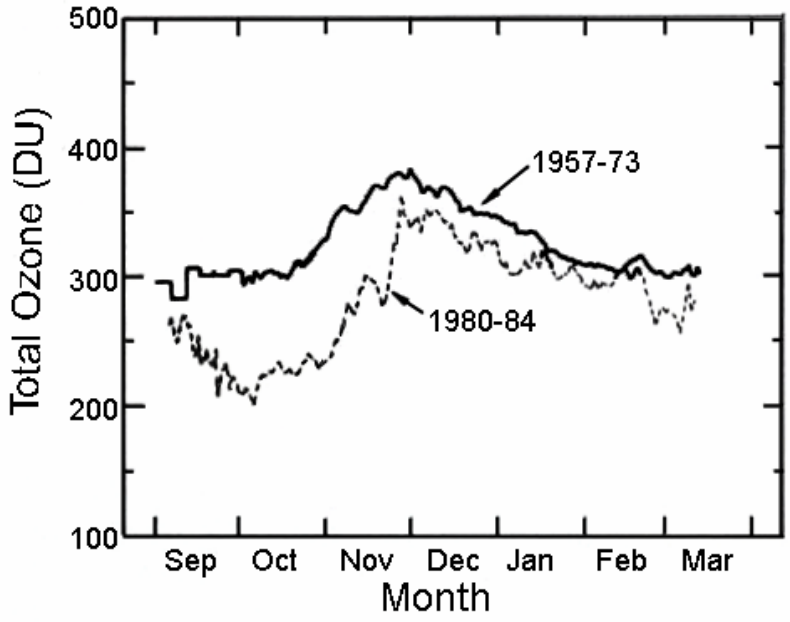

Figure C.5: Seasonal cycle of total ozone over Halley Bay, Antarctica, based on the historical record since 1957 and on years since the appearance of the Antarctic ozone hole.

Figure C.5 compares the seasonal cycle of ozone over Antarctica based on the historical record against that based on years since the appearance of the ozone hole. The two evolutions diverge near Austral spring, when solar radiation triggers reactions (C.6.1) and (C.6.2), which release reactive chlorine. Minimum ozone column abundance are observed in mid-October. By November, increasing values restore ozone towards historical levels, when ozone-rich air is imported from low latitudes during the final warming. But even then, values remain below historical levels due to the dilution of subpolar air with ozone depleted air from inside the polar vortex. During Austral spring the break down of the vortex involves a complex rearrangement of air.

Airborne observations have established that the same reactions operating over the Antarctic occur in the Arctic stratosphere. But, owing to the warmer temperature of the Arctic polar-night vortex, PSCs are a relatively infrequent phenomenon. Moreover, free chlorine that is produced in isolated PSCs is quickly acted on by dynamical effects that, by elevating temperature, reverse the process through other chemical reactions. This limits the amount of active chlorine available when the sun rise over Arctic. Similar considerations apply to mid-latitudes, where ozone depletions of 5 to 10% have been documented (WMO, 1991). Occurring at temperatures too warm to support cloud formation, those depletions may also follows from heterogeneous reactions, but involving sulfuric acid aerosols of volcanic origin.

The limiting factor in ozone depletions appears to be temperature, which controls the formation of stratospheric clouds. Indeed, the deepest reductions of Antarctic ozone are observed during the coldest winters, in agreement with the sharp correspondence between temperature and perturbed photochemistry. Consequently, dynamical disturbances that control temperature inside the vortex through diabatic effects are a key ingredient that regulates ozone depletion at high latitudes.

Since 1996 temperatures over Antarctica during October are cooler than those in the historical record. Evidence suggests that those depressed temperatures follow from diminished ozone heating associated with anomalously low ozone concentrations. By steepening the meridional temperature gradient, this response reinforces the vortex, which in turn acts to postpone the final warming that eventually restores the circulation toward normal conditions.

Acronyms

SAFIRE-A	Spectroscopy of the Atmosphere using Far InfraRed Emission—Airborne
APE	Airborne Polar Experiment
RAS	Retrieval Algorithm for SAFIRE-A
AK	Averaging Kernel
LOS	Line of Sight
ESA	European Space Agency
CODM	Cold Optics and Detector Module
ENVISAT	Environmental SATellite
MIPAS	Michelson Interferometer for Passive Atmospheric Sounding
MIR	Middle IfraRed
FIR	Far InfraRed
VMR	Volume Mixing Ratio
FTI	Fourier Transform Interferometer
ANS	Aircraft Navigation System
ILS	Instrumental Line Shape
S/N	Signal-to-noise
NESR	Noise-Equivalent Spectral Radiance
ENEA	Ente nazionale per le Nuove tecnologie, l'Energia e l'Ambiente
PNRA	Programma Nazionale di Ricerche in Antartide
MDB	Myasishchev Design Bureau
CAO	Central Aerological Observatory
MIPAS-STR	Michelson Interferometer for Passive Atmospheric Sounding/STRatospheric aircraft
GASCOD	Gas Absorption Spectrometer Correlating Optical Differences-Airborne
ECOC	ElectroChemical Ozone Cell
FISH	Fast In-Situ Stratospheric Hygrometer
FLASH	Fluorescent Airborne Stratospheric Hygrometer
ACH	Aircraft Condensation Hygrometer
HAGAR	High Altitude Gas chromatograph for Atmospheric Research
HALOX	HALogen Oxide Monitor
FSSP-300	Forward Scattering Spectrometer Probe
MAS	Multi-wavelength Aerosol Spectrometer
Mini-COPAS	Condensation Particle System
ABLE	AirBorne Lidar Experiment
MAL	Microjoule Airborne Lidar
FOZAN	Fast Ozone Analyzer
APE-GAIA	Airborne Polar Experiment-Geophysica Aircraft in Antarctica
ESABC	ESA Balloon Campaign
LSM	Least Square Method
AKM	Averaging Kernel Matrix
FWHM	Full Width at Half Maximum
LSF	Least Squares Fit
NLSF	Non-linear Least Squares Fit
FOV	Field Of View
ECMWF	European Centre for Medium-Range Weather Forecasts
NCEP	National Centers for Environmental Predictions

LBL	Line By Line
VCM	Variance-Covariance Matrix
MARSCHALS	Millimetre-wave Airborne Receivers for Spectroscopic CHaracterisation in Atmospheric Limb Sounding
FAS	Forward Algorithm for SAFIRE
MFM	MARSCHALS Forward Model
RAL	Rutherford and Appleton Laboratories
MASTER	Millimetre-wave Acquisition for Stratosphere-Troposphere Exchange Research
ACHEM	Atmospheric Composition Explorer for CHEMistry and climate
TIPS	Total Internal Partition Sum
RFM	Reference Forward Model
ESD	Estimated Standard Deviation
PV	Potential Vorticity
TOMS	Total Ozone Mapping Spectrometer
GOME	Global Ozone Monitoring Experiment
RDFT	Reverse Domain Filling Trajectory
UTC	Universal Time Co-ordinate
TM3-DAM	Data Assimilation Model
UKMO	United Kingdom Met Office
GMT	Global Trajectory Model
NIR	Near InfraRed
ZPD	Zero Path Difference
OPD	Optical Path Difference
CF	Correction Function
LTE	Local Thermal Equilibrium
DU	Dobson Unit
pdf	*p*robability *d*ensity *f*unction
VVW	Van-Vleck-Weisskopf
HWHM	Half Width at Half Maximum
HITRAN	HIgh-resolution TRANsmission
AFGL	Air Force Geophysics Laboratory
PSC	Polar Stratospheric Cloud
LIMS	Limb Infrared Monitor of the Stratosphere

Bibliography

[1] Murry L. Salby: “FUNDAMENTALS OF ATMOSPHERIC PHYSICS”, *Academic Press*, 1996

[2] J. Gille: “INSTRUMENTS AND TECHNIQUES FOR STRATOSPHERIC RESEARCH”, *Atmospheric Technology* No. 9 - Spring 1978, N.C.A.R., Bouldeder, Co.,1978

[3] D. H. Ehhalt: “IN SITU OBSERVATIONS*”, Phil. Trans. Roy. Soc., London,* A296, 175,1980

[4] Giovanni Bianchini, Ugo Cortesi, Bruno Carli: “EMISSION FOURIER TRANSFORM SPECTROSCOPY FOR REMOTE SENSING OF THE EARTH'S ATMOSPHERE”, *Geophysica annales*

[5] B. Carli and M Carlotti: "FAR-INFRARED AND MICROWAVE SPECTROSCOPY OF THE EARTH'S ATMOSPHERE", *in Spectroscopy of the Earth's Atmosphere and the Interstellar Medium* (Eds. K Narahari Raom and A Weber). Academic Press, 1992.

[6] B. Carli, H. Fischer, and J. Pyle, 1992, "LIMB SOUNDING TECHNIQUES FOR ENVIRONMENTAL MONITORING IN THE NINETIES", ESA SP-1140, ESA Publication Division, ESTEC, Noordwijk, the Netherlands.

[7] C. Cecchi Pestellini B.M. Dinelli M. Gai P. Raspollini L. Santurri: “MARSCHALS LEVEL 2 ALGORITHM THEORETICAL BASELINE DOCUMENT”, Technical note , 2004.

[8] B. Carli, P. A. R. Ade, U. Cortesi, P. Dickinson, M. Epifani, F. C. Gannaway, A. Gignoli, C. Keim, C. Lee, J. Leotin, F.Mencaraglia, A. G. Murray, I. G. Nolt, and M. Ridolfi: “SAFIRE_A—SPECTROSCOPY OF THE ATMOSPHERE USING FAR INFRARED EMISSION_AIRBORNE”, *J. Atmos. Oceanic Technol*. 16, pp.1313–1328 (1999).

[9] Martin, D. H., and E. Puplett, 1969: “POLARISED INTERFEROMETRIC SPECTROMETRY FOR THE MILLIMETRE AND SUBMILLIMETRE SPECTRUM”. *InfraredPhys.,* Vol. 10, pp. 105–109.

[10] Bianchini G., U. Cortesi, L. Palchetti, E. Pascale: “SAFIRE-A SPECTROSCOPY OF THE ATMOSPHERE BY FAR-INFRARED EMISSION—AIRBORNE: OPTIMIZED INSTRUMENT CONFIGURATION AND NEW ASSESSMENT OF IMPROVED PERFORMANCE”, *Applied Optics*, Vol. 43, No. 14, 10 May 2004.

[11] G. Bianchini, M. Lanfranchi, and U. Cortesi: “FLIGHT QUALIFICATION OF A DIODE LASER FOR PATH DIFFERENCE DETERMINATION OF A HIGH-RESOLUTION FOURIER TRANSFORM SPECTROMETER” *Appl. Opt*., Vol. 39, pp. 962–965, 2000.

[12] Stefanutti L., Sokolov L., Balestri S., MacKenzie A. R., Khattatov V. : “THE M-55 GEOPHYSICA AS A PLATFORM FOR THE AIRBORNE POLAR EXPERIMENT”, *Journal of Atmospheric and oceanic technology*, vol.16, October 1999

[13] L. Stefanutti et al. "APE-POLECAT-RATIONALE, ROAD MAP AND SUMMARY OF EARLY RESULTS", *Journal of Geophysical Research*, Vol 104 No. D19 Pages 23941-23959, October 1999.

[14] Cortesi U., B. Carli, C.E. Blom, G. Redaelli, M. Chipperfield "THE APE-GAIA CAMPAIGN: AIRBORNE POLAR EXPERIMENT - GEOPHYSICA AIRCRAFT IN ANTARCTICA" PROCEEDINGS OF THE SPARC 2000 2nd GENERAL ASSEMBLY OF THE SPARC/WCRP PROJECT, Mar Del Plata, Argentina - November 6-10, 2000.

[15] Patrick Wursteisen: "THE VALIDATION OF THE ENVISAT CHEMISTRY INSTRUMENTS BY USE OF STRATOSPHERIC BALLOONS AND AIRCRAFT" *Proc. of Envisat Validation Workshop*, Frascati, Italy, 9 – 13 December 2002 (ESA SP-531, August 2003)

[16] Blom C., U. Cortesi , G. Redaelli: "ENVISAT VALIDATION: INTRODUCTION TO THE CORRELATIVE MEASUREMENTS BY THE CHEMISTRY PAYLOAD ON BOARD THE M-55 GEOPHYSICA", *Proceedings of 16th ESA Symposium on European Rocket and Balloon Programmes and Related Research*, 2 to 5 June 2003, St. Gallen, Switzerland.

[17] C. D. Rodgers :"INVERSE METHODS FOR ATMOSPHERIC SOUNDING:THEORY AND PRACTICE*"* Ed. F. W. Taylor (University of Oxford), *World Scientific Publishing* Co. Pte. Ltd. (2000).

[18] D.S.Sivia "DATA ANALYSIS: A BAYESIAN TUTORIAL " *Clarendon*, Oxford, UK (1998).

[19] K.Levenberg, "A METHOD FOR THE SOLUTION OF CERTAIN NON-LINEAR PROBLEMS IN LEAST SQUARES" Quart. Appl. Math., vol.2, 164 (1944).

[20] D.W.Marquardt "AN ALGORITHM FOR THE LEAST-SQUARES ESTIMATION OF NONLINEAR PARAMETERS "*J. Soc. Appl. Math*., vol.11, 431 (1963).

[21] Press et al. "NUMERICAL RECIPES: THE ART OF SCIENTIFIC COMPUTING*"* Second Edition, *Cambridge University Press* (1995).

[22] S.Twomey "ON THE NUMERICAL SOLUTION OF FREDHOLM INTEGRAL EQUATION OF THE FIRST KIND BY THE INVERSION OF THE LINEAR SYSTEM PRODUCED BY QUADRATURE*" J. Ass. Comput. Mach*., vol. 10, 97 (1963).

[23] A.N.Tikhonov "ON THE SOLUTION OF INCORRECTLY STATED PROBLEMS AND A METHOD OF REGULARIZATION*" Dokl. Acad. Nauk* SSSR, vol. 151, 501 (1963).

[24] M. Carlotti "GLOBAL-FIT APPROACH TO THE ANALYSIS OF LIMB-SCANNING ATMOSPHERIC MEASUREMENTS*"*, *Applied Optics*, Vol. 27 No. 15, pp.3250 (1988)

[25] A. Goldman and R. S. Saunders "ANALYSIS OF ATMOSPHERIC INFRARED SPECTRA FOR ALTITUDE DISTRIBUTION OF ATMOSPHERIC TRACE CONSTITUENTS", I. Method of Analysis, *J. Quant. Spectrosc. Radiat. Transfer*, Vol. 21, pp.155 (1979)

[26] Born, M., E. Wolf, *"*PRINCIPLES OF OPTICS*",* Oxford, *Pergamon Press*, 5th edition, p. 87, 1975.

[27] J. T. Houghton, "THE PHYSICS OF ATMOSPHERES*"* 2nd Ed, *CUP*, Cambridge, (1986)

[28] Clough, S. A., F. X. Kneizys and R. W. Davies, *"*LINE SHAPE AND THE WATER VAPOR CONTINUUM*"*, *Atmospheric Research*, 23 229-241, 1989**.**

[29] R.J.Bell "INTRODUCTORY FOURIER TRANSFORM SPECTROSCOPY*"* *Academic Press*, New York and London (1972)

[30] Matthew Oldfield, Brian Moyna, Elie Allouis, Robert Brunt, Ugo Cortesi, Brian Ellison, JohnEskell, Tony Forward, Tony Jones, Daniel Lamarre, Joerg Langen, Peter de Maagt, David Matheson, Ivor Morgan, Jolyon Reburn, Richard Siddans, "MARSCHALS: DEVELOPMENT OF AN AIRBORNE MILLIMETRE WAVE LIMB SOUNDER" *Proc. SPIE* Vol.4540 pp.221-228 Dec 2001.

[31] L. Essen and K.D. Froome, "THE REFRACTIVE INDICES AND DIELECTRIC CONSTANTS OF AIR AND ITS PRINCIPAL CONSTITUENTS AT 24,000 MC/S", *Proc.Phys. Soc*. (London), B, vol. 64, p.862 (1951).

[32] Gamache R., R. L. Hawkins, L. S. Rothman, "TOTAL INTERNAL PARTION SUMS IN THE TEMPERATURE RANGE 70-3000 K: ATMOSPHERIC LINEAR MOLECULES", *Journal of molecular spectroscopy*, vol.142, pp. 205-219, 1990

[33] Chipperfield, M. P., Redaelli, G., "SCIENCE ISSUES AND TEORETHICAL/MODELLING WORK FOR APE-GAIA", internal report, September 1999.

[34] Carli et al. ,"AIRBORNE POLAR EXPERIMENT GEOPHYSICA AIRCRAFT IN ANTARCTICA (APE-GAIA)" *Sparc Newsletter*, 15 July 2000.

[35] U. Cortesi, G. Bianchini, E. Castelli, and B.M. Dinelli: *"*MEASUREMENTS OF MINOR STRATOSPHERIC CONSTITUENTS GEOGRAPHICAL AND VERTICAL DISTRIBUTION ACROSS THE BORDER OF THE SOUTHERN POLAR VORTEX BY LIMB SOUNDING OBSERVATION WITH THE SAFIRE-A SPECTROMETER", *Workshop on the Observation, Transport Modelling and Climatology of the Southern Hemisphere Stratosphere*, Buenos Aires (Argentina) - December 9-11, 2003.

[36] Dinelli B.M., E. Castelli, U: Cortesi, G. Bianchini, L. Palchetti :"LIMB SOUNDING EMISSION MEASUREMENTS OF LOWER STRATOSPHERIC CONSTITUENTS FROM HIGH ALTITUDE AIRCRAFT: AN OVERVIEW OF SAFIRE-A CAMPAIGNS AT MID-LATITUDE AND IN THE POLAR REGIONS", *Proceedings of Quadrennial Ozone Symposium 2004*, Kos Greece, 1-8 June 2004, vol.2, pag. 949-950, 2004.

[37] G. Giovanelli, D. Bortoli, A. Petritoli, E. Castelli, I. Kostadinov, F. Ravegnani, G. Radaelli, C. M. Volk, U. Cortesi, G. Bianchini and B. Carli, "STRATOSPHERIC MINOR GAS DISTRIBUTION OVER THE ANTARCTIC PENINSULA DURING THE APE-GAIA CAMPAIGN" accepted by IJRS Special Issue on "Atmospheric ozone: The Ozone Hole in the Context of Global Change".

[38] Giovanelli G., A. Petritoli, E. Castelli, D. Bortoli, I. Kostadinov, F. Ravegnani, G. Redaelli, C. M. Volk, U. Cortesi, G. Bianchini and B. Carli : "STRATOSPHERIC MINOR GAS DISTRIBUTION OVER THE ANTARCTIC PENINSULA DURING THE APE-GAIA CAMPAIGN.", Proceedings of Quadrennial Ozone Symposium 2004, Kos Greece, 1-8 June 2004, vol.2, pag. 960-961 (2004).

[39] Richard P. Wayne, "CHEMISTRY OF THE ATMOSPHERES 3RD ED." 2000, *Oxford University Press*, Oxford, UK.

[40] Chipperfield M., H. Roscoe "OBSERVATION FROM THE APE-GAIA CAMPAIGN SEPTEMBER/OCTOBER 1999"

[41] Darryn W. Waugh, Timothy M. Hall: "AGE OF STRATOSPHERIC AIR:THEORY, OBSERVATIONS, AND MODELS", *Reviews of Geophysics*, 40, 4 / December 2002.

[42] Proffitt, M.H., *al.*, "OZONE LOSS IN THE ARCTIC POLAR VORTEX INFERRED FROM HIGH-ALTITUDE AIRCRAFT MEASUREMENTS", *Nature*, **347**, 31-36, 1990.

[43] Michael Volk C., Oliver Riediger, Martin Strunk, Ulrich, Fabrizio Ravegnani , Alexey Ulanovsky, Gianluca Redaelli "AIRBORNE IN SITU OBSERVATIONS OF TRACERS AND OZONE INSIDE AND OUTSIDE THE ANTARCTIC VORTEX DURING APE-GAIA", Palermo, 2000.

[44] U. Cortesi, G. Bianchini, E. Castelli, B. M. Dinelli: "SAFIRE-A MEASUREMENTS DURING THE ESABC CAMPAIGN", *ENVISAT validation Workshop: validation by ballons and aircraft*, Esrin (Frascati), 9-13 December 2002.

[45] U. Cortesi ,G. Bianchini , L. Palchetti, E. Castelli, B.M. Dinelli, G. Redaelli "RESULTS OF MID-LATITUDE MIPAS VALIDATION MEASUREMENTS OBTAINED BY THE SAFIRE-A AIRBORNE SPECTROMETER", *proceeding of the second workshop on the Atmospheric Chemistry Validation of ENVISAT*, ESA-ESRIN, Frascati, Italy, 3-7 May 2004.

[46] U. Cortesi, G. Bianchini, L. Palchetti, B. M. Dinelli, E. Castelli, C. Lee: "SAFIRE-A MEASUREMENTS OF O_3, HNO_3 and N_2O VERTICAL DISTRIBUTION FOR MIPAS-ENVISAT VALIDATION, *EGS-AGU-EUG Joint Assembly*, Nice, 6-12 April, 2003.

[47] E. Castelli, U. Cortesi, G. Bianchini, and B.M. Dinelli: "MEASUREMENT CAPABILITIES AND APPLICATIONS OF THE HIGH RESOLUTION FOURIER TRANSFORM SPECTROMETER SAFIRE-A (SPECTROSCOPY OF THE ATMOSPHERE BY USING FAR-INFRARED EMISSION - AIRBORNE) ", *ASSFTS, Bad Wildbad (Black Forest)*, Germany, 7 to 10 October 2003.

[48] Cortesi U., G. Bianchini, L. Palchetti, E. Castelli, B.M. Dinelli, G. Redaelli :"MIPAS-ENVISAT VALIDATION MEASUREMENTS WITH THE HIGH RESOLUTION FT-FIR SPECTROMETER SAFIRE-A ABOARD THE STRATOSPHERIC AIRCRAFT M-55 GEOPHYSICA", *Proceedings of Quadrennial Ozone Symposium 2004*, Kos Greece, 1-8 June 2004, vol.1, pag. 526-527 (2004).

[49] U. Cortesi, G. Bianchini, L. Palchetti, E. Castelli, B.M. Dinelli, G. Redaelli: "RESULTS OF MID-LATITUDE MIPAS VALIDATION MEASUREMENTS OBTAINED BY THE SAFIRE-A AIRBORNE FT-FIR SPECTROMETER", Second Workshop on the Atmospheric Chemistry Validation on ENVISAT (ACVE-2), Esrin, Frascati, Italy, 3-7 May 2004.

[50] Redaelli G., "LAGRANGIAN TECHNIQUES FOR THE ANALYSIS OF STRATOSPHERIC MEASUREMENTS", *PhD thesis*, Univ. Of L'Aquila, Italy, 1997.

[51] U. Cortesi ,G. Bianchini , L. Palchetti, E. Castelli, B.M. Dinelli, G. Redaelli "RESULTS OF MID-LATITUDE MIPAS VALIDATION MEASUREMENTS OBTAINED BY THE SAFIRE-A AIRBORNE SPECTROMETER", *proceeding of the ENVISAT Symposium*, Salzburg, September 2004.

[52] Liu, C. E. Blom,: "PREMINARY COMPARISON OF MIPAS-STR AND SAFIRE-A FOR THE ARCTIC VALIDATION CAMPAIGN" (IMK-ASF, Mar. 24, 2004), private communication

[53] C. Keim, C.E. Blom,"VALIDATION OF MIPAS-ENVISAT BY CORRELATIVE MEASUREMENTS OF MIPAS-STR", *proceeding of the second workshop on the Atmospheric Chemistry Validation of ENVISAT*, ESA-ESRIN, Frascati, Italy, 3-7 May 2004.

[54] ORIEL "INSTRUMENTS MANUAL: INTRODUCTION TO FT-IR SPECTROSCOPY"

[55] W. H. Steel: "INTERFEROMETRY", *Cambridge University Press*, 1967

[56] P. B. Fellgett, Doctoral Thesis (unpublished), *Univ. of Cambridge*, 1951.

[57] P. Jacquinot, J. Opt. Soc. Amer. **44**, 761 (1954)

[58] P. Jacquinot, Rep. Progr. Phys. **23**, 267 (1960)

[59] C. Fabry and A. Perot, Ann. Chim. Phys. (7) **12**, 459 (1897), Ann. Chim. Phys. (7) **16**, 115, 289, 331 1899.

[60] B. Carli, M.Carlotti "FAR INFRARED AND MICROWAVE SPECTROSCOPY OF THE EARTH'S ATMOSPHERE*", Academic Press*, 1992.

[61] C.H. Townes, A.L. Schawlow*:* "MICROWAVE SPECTROSCOPY"*, Dover Publications*, Inc., New York, 1975

[62] Turner, D. S., "ABSORPTION COEFFICIENT ESTIMATION USING A TWO-DIMENSIONAL INTERPOLATION PROCEDURE »*, J. Quant. Spectrosc. Radiat. Transfer*, 55, 633-637, 1995.

[63] Rothman, Rinsland, Goldman, Massie, Edwards, Flaud, Perrin et al., "THE HITRAN MOLECULAR SPECTROSCOPIC DATABASE AND HAWKS (HITRAN ATMOSPHERIC WORKSTATION): 1996EDITION*", Journal of Quantitative Spectroscopy and Radiative Transfer*, vol. 60, pp. 665-710 (1998).

[64] S. Solomon: "STRATOSPHERIC OZONE DEPLETION: A REVIEW OF CONCEPTS AND HISTORY*"*, *Reviews of Geophysics*,37,3, 275-316, August 1999.

[65] R. J. Bell: "INTRODUCTORY FOURIER TRANSFORM SPECTROSCOPY*",* *Academic Press*, New York and London (1972)